2015

The Influence of Alloying Additions on Diffusion and Strengthening of Magnesium

Catherine Kammerer
University of Central Florida

THE INFLUENCE OF ALLOYING ADDITIONS ON DIFFUSION AND STRENGTHENING OF MAGNESIUM

by

CATHERINE C. KAMMERER
B.S. Missouri University of Science and Technology, 1994
M.S. University of Central Florida, 2013

A dissertation submitted in partial fulfillment of the requirements
for the degree of Doctor of Philosophy
in the Department of Materials Science and Engineering
in the College of Engineering and Computer Science
at the University of Central Florida
Orlando, Florida

Summer Term
2015

Major Professor: Yongho Sohn

ABSTRACT

Magnesium alloys are being developed as advanced materials for structural applications where reduced weight is a primary motivator. Alloying can enhance the properties of magnesium without significantly affecting its density. Essential to alloy development, inclusive of processing parameters, is knowledge of thermodynamic, kinetic, and mechanical behavior of the alloy and its constituents. Appreciable progress has been made through conventional development processes, but to accelerate development of suitable wrought Mg alloys, an integrated Materials Genomic approach must be taken where thermodynamics and diffusion kinetic parameters form the basis of alloy design, process development, and properties-driven applications.

The objective of this research effort is twofold: first, to codify the relationship between diffusion behavior, crystal structure, and mechanical properties; second, to provide fundamental data for the purpose of wrought Mg alloy development. Together, the principal deliverable of this work is an advanced understanding of Mg systems. To that end, the objective is accomplished through an aggregate of studies. The solid-to-solid diffusion bonding technique is used to fabricate combinatorial samples of Mg-Al-Zn ternary and Mg-Al, Mg-Zn, Mg-Y, Mg-Gd, and Mg-Nd binary systems. The combinatorial samples are subjected to structural and compositional characterization via Scanning Electron Microscopy with X-ray Energy Dispersive Spectroscopy, Electron Probe Microanalysis, and analytical Transmission Electron Microscopy. Interdiffusion in binary Mg systems is determined by Sauer-Freise and Boltzmann-Matano methods. Kirkaldy's extension of the

Boltzmann-Matano method, on the basis of Onsager's formalism, is employed to quantify the main- and cross-interdiffusion coefficients in ternary Mg solid solutions. Impurity diffusion coefficients are determined by way of the Hall method. The intermetallic compounds and solid solutions formed during diffusion bonding of the combinatorial samples are subjected to nanoindentation tests, and the nominal and compositionally dependent mechanical properties are extracted by the Oliver-Pharr method.

In addition to bolstering the scantly available experimental data and first-principles computations, this work delivers several original contributions to the state of Mg alloy knowledge. The influence of Zn concentration on Al impurity diffusion in binary Mg(Zn) solid solution is quantified to impact both the pre-exponential factor and activation energy. The main- and cross-interdiffusion coefficients in the ternary Mg solid solution of Mg-Al-Zn are reported wherein the interdiffusion of Zn is shown to strongly influence the interdiffusion of Mg and Al. A critical examination of rare earth element additions to Mg is reported, and a new phase in thermodynamic equilibrium with Mg-solid solution is identified in the Mg-Gd binary system. It is also demonstrated that Mg atoms move faster than Y atoms. For the first time the mechanical properties of intermetallic compounds in several binary Mg systems are quantified in terms of hardness and elastic modulus, and the influence of solute concentration on solid solution strengthening in binary Mg alloys is reported. The most significant and efficient solid solution strengthening is achieved by alloying Mg with Gd. The Mg-Nd and Mg-Gd intermetallic compounds exhibited better room temperature creep resistance than intermetallic compounds of Mg-Al. The correlation

between the concentration dependence of mechanical properties and atomic diffusion is deliberated in terms of electronic nature of the atomic structure.

ACKNOWLEDGMENTS

I write this acknowledgement with the deepest gratitude for the many people who have given me the opportunity to pursue this personal goal of earning my Ph.D. in Materials Science and Engineering. First and foremost, I give thanks to my family and friends who have endured my absence and given me never-ending support. It has been a long and arduous journey, and I recognize the sacrifices they have made for me.

I am grateful for the guidance, generosity, and scholarship provided by Dr. Yongho Sohn and my committee, Dr. K. Coffey, Dr. C. Suryanarayana, Dr. Y. Bai, and Dr. R. Blair. Many thanks to each of you! Many thanks are owed to my research cohorts for their comradery and friendship. It has gotten me through some of the biggest challenges, and their sustained support has made my work possible. Special thanks are given to Le Zhou for extensive TEM services, and to Felipe Betancor for enthusiastic metallographic work. Deep appreciation for the friendship and support of Karen Glidewell is offered.

I also express my gratitude to Kyu Cho and Anit Giri at the U.S. Army Research Laboratory (ARL). This work has been made possible by financial support of ARL under the Advanced Materials Design and Innovative Processing Development project, W911NF1120020.

"It's good to want; it gives you goals and objectives."

"It's all relative."

-- Catherine Carlisle Kammerer

TABLE OF CONTENTS

LIST OF FIGURES

LIST OF TABLES

LIST OF ACRONYMS

A	Contact area
bct	Body Centered Tetragonal crystal structure
BSE	Back-scattered electrons
η	Boltzmann parameter, $x/2\sqrt{t}$
C_i	Concentration of component i
C_i^o	Concentration of component i at Matano plane
C_i^∞	Concentration of component i at terminal end
cbco	c-base centered orthorhombic
d	nearest-neighbor jump distance
D	Diffusion coefficient (m^2/sec)
D_o (or k_o)	Pre-exponential factor of diffusion (or parabolic growth) (m^2/sec)
$\widetilde{D}$	Binary interdiffusion coefficient (m^2/sec)
$\widetilde{D}^{eff}$	Average effective interdiffusion coefficient (m^2/sec)
$\widetilde{D}^{int}$	Integrated interdiffusion coefficient (m^2/sec)
D_i^{Mg}	Impurity diffusion coefficient of component *i* in Mg (m^2/sec)
D_{ii}^k	Ternary interdiffusion main-coefficient in component k
D_{ij}^k	Ternary interdiffusion cross-coefficient in component k
ΔS	Change of entropy
EPMA	Electron Microprobe Analysis
ε_V	Volumetric (lattice) misfit factor

erf	Error function
E_r	Reduced modulus (GPa)
E_S	Young's modulus of sample
f	correlation factor
fcc	Face Centered Cubic crystal structure
FIB	Focused Ion Beam
H	Hardness (GPa)
h_c	contact depth
h_{max}	maximum contact depth
HAADF	High Angle Annular Dark Field
hcp	Hexagonal Close Packed crystal structure
ICME	Integrated Computational Materials Engineering
INLO	In-Situ Lift-Out technique
J_i	Diffusion flux of component I (mole·m^{-2} sec^{-1})
$\tilde{J}$	Interdiffusion flux (mole·m^{-2} sec^{-1})
k_p	Parabolic growth constant (m^2/sec)
MGI	Materials Genome Initiative
Mg(X)	Binary magnesium solid solution where X is solute
Mg(X,Y)	Ternary magnesium solid solution where X and Y are solutes
P	Indentation load
PI	Sensitivity to Pop-Ins
PLC	Portevin – Le Chatelier

Q	Activation energy (kJ/mole)
R	Ideal gas constant (8.314772 kJ/mole)
RE	Rare Earth
§	Section
S	Unloading stiffness
SAED	Select Area Electron Diffraction
SE	Secondary Electrons
SEM	Scanning Electron Microscope
SPM	Scanning Probe Microscopy
t	Time (seconds)
T	Temperature (Kelvin)
TEM	Transmission Electron Microscopy
T_M	Melting temperature
ν	Attempt frequency of exchange
ν_S	Poisson ratio of sample
V_M	Molar volume
WDS	Wavelength Dispersive Spectroscopy
X_i	Mole fraction of component i
x	Position (μm)
x_o	Matano plane position
x_{RE}	Relative extremum position
x_T	Terminal position

x_{ZFP}	Zero flux plane position
XEDS	X-ray Energy Dispersive Spectroscopy
ZAF	Atomic number, absorption, and fluorescence matrix correction factor
ZFP	Zero Flux Plane

CHAPTER 1: INTRODUCTION

1.1 General Background

Magnesium (Mg) is one of the lightest structural metals. Pure Mg is 50% less dense than aluminum (Al) alloys, and one-quarter the density of steel. As such, Mg alloys should have extensive applications where weight is proportional to fuel efficiency, power consumption, or functionality as in aerospace and automotive applications, or machine and prosthetic design. In the last two decades, intensive research and development has resulted in broader application of Mg alloys [1-6]. Alloys of Mg can be cast through various techniques (e.g. sand casting, die casting, squeeze casting) into near net shape products. Although the cold formability of Mg is hindered by its hexagonal close-packed (hcp) structure, wrought Mg alloys can be produced through elevated temperature processes such as extrusion, forging, and hot rolling. Unfortunately, Mg tends to exhibit macroscopically-appreciable basal texture upon plastic deformation of cold forming such as rolling, drawing, and stamping. This dichotomy exists because, at elevated temperatures, additional slip planes become available, and plastic deformation becomes easier. Despite the high dimensional stability and ease of machining and generally better overall mechanical properties of wrought Mg alloys, the deleterious consequences associated with high processing cost of hot working and strong anisotropy of mechanical properties has equated to the cast alloys domination over wrought alloys in terms of industrial application [5, 7]. To fully capitalize on the opportunities offered by Mg, alloys must be developed that reduce or mitigate the anisotropic properties.

Improvement of the cold formability of magnesium can be accomplished by reducing the c/a ratio of the hcp structure or through texture modification. Alloying can influence the c/a ratio and effect texture generation during hot working, therefore improve the availability of ambient deformation mechanisms. Precipitation of second phase particles in Mg alloys can also influence the room temperature ductility. Two of the most common alloying elements in magnesium alloys are aluminum and zinc (Zn). Al additions improve the strength through solid solution strengthening and precipitation hardening of $Mg_{17}Al_{12}$. In fact, high levels of $Mg_{17}Al_{12}$ precipitates impeded tensile twinning and enhanced dynamic recrystallization, resulting in weak deformation textures and improved formability [8]. Similarly, Zn is added, often times with Al, to improve room temperature properties and corrosion resistance. Magnesium alloyed with Zn can also be heat treated to form precipitates [9] offering significant strengthening. Nonetheless, these alloys do not possess the properties necessary for widespread implementation in wrought applications.

Improvements to the properties are expected through alloying with rare earth (RE) elements. RE elements are those of the Lanthanide series, such as cerium (Ce), neodymium (Nd) and gadolinium (Gd), along with yttrium (Y) and scandium (Sc). Mg–RE-based alloys exhibit both solution strengthening and precipitation hardening effects during decomposition of their supersaturated solid solutions, and have the ability to weaken texture evolution during wrought processing and forming. Lithium (Li) and the RE elements, in solid solution with Mg, decrease the c/a ratio giving rise to activation of the prismatic and pyramidal slip systems and the typical deformation anisotropy associated with Mg alloys is minimized [10, 11]. On the other hand, Al increases the c/a ratio while Zn

has no effect on the c/a ratio [12]. In addition, precipitation in Mg-RE alloys improves the strength and room-temperature plasticity by hindering tensile twinning [13] and promote particle-stimulated nucleation during recrystallization [14] and/or dynamic recrystallization during hot working [15].

Precipitation of the equilibrium phase is often accomplished incrementally through the nucleation of metastable, intermediate phases that preserve the coherency of the nucleus. Transition phases will often form because they have a lower activation barrier than the equilibrium phase and maintain some degree of coherency with the matrix. Peak strengthening is generally achieved with the transition phases because: the coherent precipitates induce significant lattice strain in the matrix thereby hindering dislocation motion; and the interprecipitate spacing between the initial fine precipitates is substantially small thus preventing dislocations from bowing around them. Overaging occurs when the precipitate is incoherent with the matrix and excessively coarsened (i.e. large interprecipitate spacing). In the overaged condition, the limit of strength of the alloy is controlled by the strength of the precipitate.

While the precipitation of the equilibrium γ-$Mg_{17}Al_{12}$ does proceed directly from supersaturated Mg solid solution, precipitates in Mg-Zn and Mg-RE binary systems have been shown to proceed through a sequence of transformations. These binary supersaturated solid solutions decompose in different sequences depending on the system [16, 17]. It should be noted from these sequences that stable equilibrium phases can be intermediary in the precipitation sequence, as indicated by the Pearson Symbol.

- Mg-Zn: α' (hcp, hP2) → G.P. Zones → β'$_1$ (Mg_4Zn_7, mC110) → β'$_2$ ($MgZn_2$, hP12) → β ($Mg_{21}Zn_{25}$, hR276)
- Mg-Nd: α' (hcp, hP2) → G.P. Zones → β" (Mg_3Nd, DO_{19}) → β' (Mg_7Nd, cbco) → β$_1$ (Mg_3Nd, cF16) → β ($Mg_{12}Nd$, bct) → β$_e$ ($Mg_{41}Nd_5$, tI92)
- Mg-Gd: α' (hcp, hP2) → β" (Mg_3Gd, DO_{19}) → β' (Mg_7Gd, cbco) → β$_1$ (Mg_3Gd, cF16) → β (Mg_5Gd, cF440)
- Mg-Y: α' (hcp, hP2) → β' (Mg_7Y, cbco) → β ($Mg_{24}Y_5$, cI58)

Alloy development has occurred primarily through empirical studies. Significant progress has been made through conventional experimentation, but to accelerate development of suitable wrought Mg alloys an integrated engineering approach must be taken. With multiple alloying elements, understanding the diffusional interactions in the multicomponent Mg alloy becomes important to the kinetics of and microstructural development during solidification, forming, and heat treatment.

In recent years, integrated computational materials engineering (ICME) has evolved and uses fundamental data to design optimum alloys and streamline alloy development [18]. In 2011, President Obama announced the Materials Genome Initiative (MGI) which aims to significantly reduce the time required for commercialization of advanced materials. Computational techniques are progressing from coupling phase diagrams with thermochemistry toward kinetic simulations integrated with thermodynamic calculations (i.e. simulation of phase transformations and prediction of microstructural evolution) and

onward linking multi-scaled relationships between structure, process, properties, and performance of new materials [19]. Requisite to this evolution is experimental data as a basis for and to validate the computational models.

1.2 Motivation

A limited understanding of the structure-behavior relationship has inhibited improvements to conventional Mg alloys. Over the past two decades, significant research efforts have focused on the correlation between the microstructure, process, and properties of wrought magnesium alloys. Still, relatively little is known about the properties of Mg alloys compared to Al alloys or steel. Long-range diffusion processes are important to microstructural evolution of alloys and hence mechanical properties.

It is well known that a thin plate-shaped precipitate will more effectively strengthen an alloy than spherical particles [20]. Precipitate plates that form on prismatic planes of the magnesium matrix phase have a lower inter-precipitate spacing than those formed on pyramidal or basal planes of the matrix phase [21]. Therefore, higher strengths are associated with microstructures that contain a high volume fraction of intrinsically strong precipitate plates with large aspect ratio and prismatic habit planes. Little work has been done to characterize the mechanical properties of the intermetallic phases independent of the solid-solution matrix. Similarly, systematic experimental data for diffusion are rare but necessary as a basis for alloy and process development and integrated computational materials engineering. Effective Mg-alloy design, both empirically and computationally,

requires data of the system kinetics and mechanical properties of the intermetallic compounds and solid solution.

The lack of mechanical-property data for the intermetallic compounds is partly due to the requirement for a bulk, homogeneous specimen for traditional mechanical property evaluation methods (e.g. tensile testing). While precipitation from supersaturated solid-solutions often results in metastable phases, and solidification from melt of intermetallic compounds results in microstructural gradients, solid-state synthesis of intermetallic compounds by isobaric, isothermal diffusion reaction between two metals has long been recognized as a means of eliciting intermediate phases occurring in the same sequence of the appropriate equilibrium phase diagram [22, 23], though metastable compounds can also form. In addition, the long-range thermally-activated solid-state kinetics between to the two metals can be characterized through the phenomenological description of diffusion. Using the measured concentration profile across a diffusion reaction zone, a diverse set of methods can be employed to calculate diffusion coefficients. For example, the Hall Method [24], which essentially fits just the most dilute portion of the concentration gradient to the error function solution of Fick's second law, is used to calculate impurity diffusion constants. Interdiffusion coefficients in binary systems, when molar volume can be neglected, can be computed using the Boltzmann-Matano analysis [25]. If molar volume changes are significant, the Sauer-Freise method can be employed. Similarly, when the concentration gradient is linear, the Heumann method can be utilized [26]. In the case of line compounds, were no gradient can be measured, an approach reported by Wagner may be more suitable [27]. Ternary interdiffusion coefficients typically require intersecting

diffusion paths in order to solve for the main and cross coefficients (i.e. two couples, four equations) [28]. In addition, growth constants can be determined.

Thus, solid-to-solid diffusion couples can serve as combinatorial specimens yielding:

1. an interdiffusion reaction zone with a discrete compositional profile from which descriptive diffusion coefficients can be quantified;
2. the nucleation and growth of equilibrium phases across the compositional spectrum of the terminal metals for isothermal assessment of the phase diagram;
3. and sufficiently thick layers of intermetallic phases and solid solutions to allow for nanomechanical testing and characterization of mechanical properties.

1.3 Objectives

The objective of this research effort is twofold: first is to codify the relationship between diffusion kinetics, crystal structure, and mechanical behavior; second is to provide fundamental data for the purpose of wrought Mg alloy development. The alloying elements of research focus are grouped as conventional (i.e. Al, Zn) and rare earth (i.e. Gd, Nd, Y). Together, the goal of this work is to advance the understanding of Mg systems. To that end, the objective is accomplished through an aggregate of studies.

This dissertation document is organized in terms of these individual studies. Chapter 2 presents the generalized experimental procedure common to all studies herein. Similarly, Chapter 3 provides the analytical framework exercised. Chapters 4 – 8 detail the

various studies constituent to this research. Each study provides unique and original contributions to the state of knowledge of Mg alloys. Specifically:

- Chapter 4: Examines the Al impurity diffusion response as a function of Zn solute concentration in Mg(Zn) solid solution
- Chapter 5: Quantifies interdiffusion in Mg(Al,Zn) ternary solid solution
- Chapter 6: Characterizes the change in lattice parameters due to homogeneity range in Mg_2Zn_{11}; provides crystallographic characterization of controversial Mg-Zn intermetallic compounds
- Chapter 7: Debunks recent claims of the existence of an equilibrium Mg_4Gd_6 phase and introduces a previously unidentified modulated hexagonal superstructure of approximate stoichiometry of Mg_6Gd in equilibrium with the Mg solid solution; reports diffusion kinetics for Gd and Y in polycrystalline Mg
- Chapter 8: Reports the mechanical properties of several intermetallic compounds in the Mg-Gd, Mg-Nd, Mg-Y, and Mg-Zn systems as determined through nanomechanical tests

A comprehensive summary of the findings, emphasizing the unifying relationships, is presented in Chapter 9. Appendix A offers suggestions for research directions which will serve to further advance the state of Mg alloy metallurgy. The datasets collected, analyzed, and described within this manuscript are presented in Appendix B for integration into the materials genome. Finally, Appendix C details the extensive publications and presentations that have come from this doctoral study.

CHAPTER 2: EXPERIMENTAL METHODS

2.1 Combinatorial Sample Fabrication

Combinatorial samples are composite specimens that can be used for the examination of materials across a compositional spectrum with a combination of techniques. This study capitalizes on products of diffusional reactions in binary and ternary systems obtained through solid-to-solid diffusion couples. In addition to facilitating the characterization of kinetic behavior, the diffusion couple technique offers a versatile alternative for phase diagram determination [29] and mechanical property evaluation of equilibrium phases. While the driving force for interdiffusion is the gradient of chemical potential across the diffusion reaction zone, local equilibrium is assumed at the interface between each evolved layer [23, 30]. It is possible, with the presence of impurities (i.e. O, C, N), for non-equilibrium phases to form in the diffusion reaction zone[31]. Impurity stabilized metastable phases typically will not grow parabolically once the impurity is consumed [32]. In this study, combinatorial samples were interrogated with an electron beam to ascertain structural and compositional information, as well as kinetic behavior. The samples were also physically prodded to determine mechanical behavior of pure metals, solid solutions, and intermetallic compounds in binary and ternary systems. Regardless of system, the combinatorial sample fabrication process is ostensibly universal. This section will describe the process and its minor modifications.

The high purity polycrystalline Mg, Gd, Al, Zn, Nd, and Y were commercially procured from Alfa Aesar while the magnesium alloys were produced by Magnesium

Elektron, North America. The purity of Al was 99.9965 wt.% while the purity of Mg and Zn was 99.9 wt.%. The Y purity was 99.9 wt.% excluding Ta. The Nd and Gd purity was 99.5 wt.% excluding tantalum (Ta). The primary impurity in the Gd was oxygen (0.46 wt.%). The chemical analysis for the alloys is identified in Table 1.

Table 1: Chemical analysis of Mg alloys in at.%

(at.%)	**Mg**	**Al**	**Zn**	**Others**	**Each**
Mg-3at.%Al	97.46	2.54	0.00	<0.02	<0.05
Mg-9at.%Al	91.27	8.72	0.01	<0.02	<0.005
Mg-1at.%Zn	99.01	0.00	0.99	<0.02	<0.005
Mg-3at.%Zn	97.58	0.01	2.41	<0.02	<0.005
Mg-3at.%Al-0.5at.%Zn	96.99	2.65	0.36	<0.02	<0.005
Mg-1at.%Al-1at.%Zn	97.98	0.89	1.13	<0.02	<0.005

The pure Mg and Mg alloys were subjected to a homogenization/grain-growth anneal roughly 40 – 50°C below their respective solidus for 8 – 16 hours. The grain size of all the Mg and Mg alloys employed in this investigation ranged from 100 to 500μm. The pure Gd rods were not subjected to a grain growth anneal. Grain size of the Gd was determined to be between 100 and 150μm. Pure Al, Zn, Y, Nd were not characterized prior to assembly because their application in previous internal studies [33-36]. The rods were sectioned into discs of 3 – 4 mm in thickness and 6 – 9 mm in diameter.

The discs were prepared for diffusion bonding by incrementally polishing the mating surface down to 1 μm using a non-oxidizing lubricant. Immediately prior to

assembly, the discs were wet abraded with ethanol and 1200 grit silicon carbide paper to remove any oxide formation. An intimate interface between two discs was achieved with the aid of a clamping jig. The jig consisted of two steel plates pulled together with three screws. Alumina spacers were used between the steel plates and sample discs and served to inhibit diffusion bonding between the steel and the disc. A schematic representation of the diffusion couple assembly is shown in Figure 1.

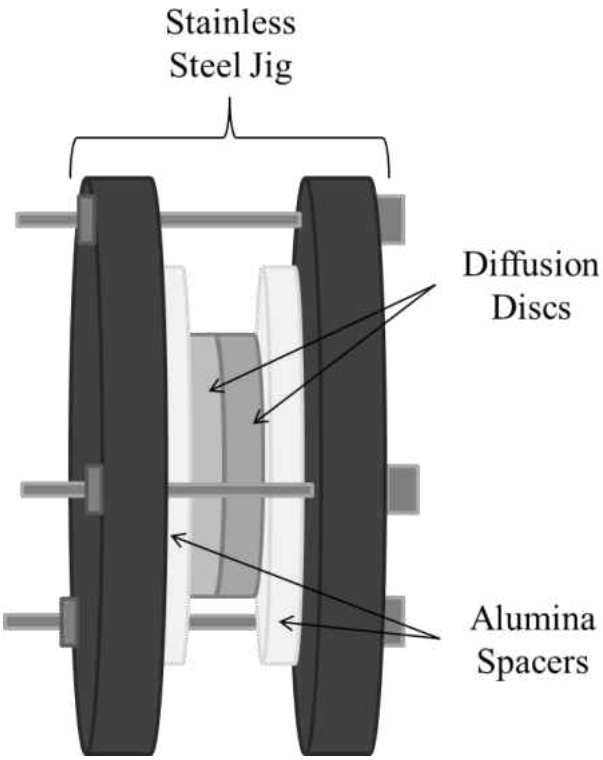

Figure 1: Diffusion couple assembly

The loaded jig was placed in a quartz ampoule with a tantalum oxygen getter. A quartz cap was welded onto the open end of the ampoule using standard flame-working techniques. The stem of the ampoule was attached to a custom built vacuum system

capable of pulling down to ~10^{-9} atm (10^{-6} Torr) as well as injecting hydrogen (H_2) or argon (Ar) gas. The ampoule was repeatedly flushed with argon and then hydrogen, and it was then fully evacuated to <$7.5x10^{-6}$ Torr. Before the ampoule was sealed and the stem removed, the Mg vs. pure metal couples were backfilled with a 96%Ar-4%H_2 mixture or ultra-high purity Ar so that at annealing temperature, the couple was in an inert atmosphere under ambient pressure (~760 Torr). The diffusion couples incorporating alloys were sealed under vacuum.

The encapsulated assembly was placed in either a Paragon Bluebird™ furnace or a Lindberg™ three-zone tube furnace preheated to the annealing temperature. The temperature of the diffusion couples was monitored via the independent thermocouple to verify furnace temperature stability. Furnace temperature was controlled to within 2°C of set point. Diffusion anneal temperatures and times for each system are presented in Table 2. After annealing, the capsule was quickly removed from the furnace and quenched in water. The couple was extracted from the jig and mounted in epoxy. Once cured, the couple was cross-sectioned and metallographically prepared down to 1μm finish, again using a non-oxidizing lubricant.

Table 2: Diffusion Anneal Parameters

Couple	Temperature (°C)	Time (hrs.)
Mg vs. Mg-9at.%Al	350	96
	400	17
	450	24
Mg vs. Mg-3at.%Zn	350	125
	400	8
	450	24
Mg-9at.%Al vs. Mg-3at.%Zn	400	8
	450	4
Mg-3at.%Al vs. Mg-1at.%Zn	400	20
	450	5
Mg vs. Mg-3at.%Al 0.5at.%Zn	350	168
	400	24
	450	4
Mg vs. Mg-1at.%Al 1at.%Zn	400	24
Mg vs. Al	300	720
Mg vs. Y	450	360
	500	240
	550	120
Mg vs. Nd	500	240
Mg vs. Zn	315	168
Mg vs. Gd	385	192
	425	166.5
	450	90
	475	96.5
	475	75
	490	72
	500	66

2.2 Interdiffusion Zone Characterization

The diffusion bond integrity and the interdiffusion microstructure of each diffusion couple was examined using optical and scanning electron microscopy (SEM) equipped with an X-ray energy dispersive spectrometer (XEDS). SEM analysis was accomplished using a Zeiss Ultra-55 field emission SEM with an angular selective backscattered electron detection system for maximum compositional contrast. The depth of interdiffusion and compositional boundaries of diffusion reaction products was determined with standardless semi-quantitative XEDS. When the diffusion reaction resulted in layer formation, the thickness of each phase was measured from multiple SEM fields of view using the image processing and analysis software, ImageJ™ (National Institutes of Health, http://imagej.nih.gov/ij/).

One of three different electron probe micro-analyzers (EPMA) equipped with wavelength-dispersive spectrometers (WDS) was utilized for x-ray emission spectral analysis. The precise quantitative determination of concentration profiles across the diffusion reaction zone was measured with a JEOL™ Superprobe 733, JEOL™ JXA-8200, or JEOL™ 8900R Superprobe EPMA. Point-to-point line scans were performed in the central region orthogonal to the interface with a 2 -10 μm step size and an accelerating voltage and probe current of 7.5 keV and 50 nA (Mg vs. Mg-9at.%Al, Mg-3at.%Al vs Mg-1at.%Zn, Mg-9at.%Al vs Mg-2at.%Zn, Mg vs Mg-3at.%Al-0.5at.%Zn), 15 keV and 50 nA (Mg vs. Mg-2at.%Zn), 15 keV and 20 nA (Mg vs Mg-1at.%Al-1at.%Zn, Mg vs Mg-3at.%Al, Mg vs. Zn), or 20 keV and 30 nA (Mg vs Y, Mg vs Nd, Mg vs Al). The measured x-ray intensities were corrected for matrix affects by applying the Heinrich ZAF correction factors. The Mg-Al-Zn

alloys and pure metals, Mg, Al, Zn, Y, Nd, Gd, were used as standards for equipment calibration prior to each scan. At least two independent line scans were performed on each couple. Fitted concentration profiles were extracted from the EPMA data using piecewise cubic smoothing splines in OriginPro™. These fitted concentration profiles were used for subsequent analysis.

In some instances (i.e. Mg vs Zn, Mg vs. Gd) the intermetallic compounds produced by interdiffusion were further examined using an FEI/Tecnai™ F30 transmission electron microscope (TEM) with a field-emission source working at 300 keV and equipped with a Fischione™ high angle annular dark field (HAADF) detector and XEDS. Site-specific specimens were prepared using an FEI TEM200 Focus Ion Beam (FIB) in-situ lift-out (INLO) technique [37, 38]. The spacing and orientation of the diffraction spots in a series of single crystal Selected Area Electron Diffraction (SAED) patterns, obtained through a range of tilt angles, were used to determine the interplanar spacing and lattice parameters of each phase. At least six orientations within each phase were obtained by tilting the specimens. High resolution electron microscopy was also employed to capture atomic-resolution images and ascertain greater details of the crystal structure of a previously unidentified intermetallic phase in the Mg-Gd system.

2.3 Nanomechanical Testing

Nanomechanical tests were performed by applying a force to drive an indenter probe into a sample surface and then reducing the force to withdraw the probe. The applied load, P, and indenter displacement, h, into the sample were continuously

monitored. Instrumented indentation tests were performed on select diffusion couples using a Hysitron™ TI Premier system with a 100 nm diamond Berkovich tip of an included angle of 142.3◦ and tip radius of ~100 nm and scanning probe microscopy (SPM) capabilities. The normal force versus penetration depth (i.e. load-displacement) curves were obtained in-situ with load and displacement resolutions of <1 nN and <0.02 nm, respectively. Point-to-point line scans and indent arrays were performed across the interdiffusion reaction zone and on the intermetallic phases, respectively. An average of 10 – 25 indents were obtained for each phase. The indentation loading profile consisted of ten-second loading to a peak load, followed by a three-second hold segment, and then a ten-second unloading segment. Typically, when the phase layer thickness exceeded 50 μm the peak load was 7 mN. For layers greater than 5 μm but less than 50 μm the peak load was reduced to 5 mN. Layers less than 5 μm in thickness were subjected to 3.5 mN peak loading. The reduction in peak load was necessary to ensure test results were not affected by the presence of an interface. Indent location on the narrow intermetallic phases were confirmed after nanoindentation with secondary and backscattered electron imaging. To reveal any concentration dependencies on the mechanical properties, multiple indentation line scans were performed on the central region of the sample, perpendicular to the interface and extending into the solid solution phases. The load profile remained the same as previously described however the peak load was 7 mN for the intermetallic phases and 5 mN for the solid solution phases; the step size was 5 - 10 μm depending on extent of interdiffusion.

All testing was performed in load-controlled feedback mode. Feedback controlled nanoindentation tests do not start at zero force and displacement due to the effects of the drift correction procedure. Therefore, data was collected by the system during drift correction and the test was begun from the air above the sample. As the probe approached the sample surface, the computer continued to collect data so the point where the probe made contact with the sample was clearly defined as the point where the force began to increase. The zero point was defined as the point where the measured force began to increase. The zero displacement and zero force points of the data were assigned individually to each data set in order to obtain accurate results. The zero point was verified by zooming in to the force onset region of the load vs. displacement profile and selecting the point where the force begins to increase.

The hardness and elastic modulus of the material were determined from indentation load–displacement data obtained during one cycle of loading and unloading according to the Oliver-Pharr method [39-41]. Hardness, H, was obtained from the peak load, P_{max}, divided by the contact area, which was calculated as a function of contact displacement, h_c. The contact area function, A, for the Berkovich tip, described by an n^{th} (n = 3 – 6) order polynomial, was determined through tip area calibration on a standard fused quartz substrate of known elastic modulus of 69.6 GPa and Poisson's ratio, $\upsilon = 0.17$ before testing.

The reduced elastic modulus, E_r, was determined from its relationship to contact area function and the initial unloading stiffness, S.

CHAPTER 3: ANALYTICAL FORMULAE

3.1 Parabolic Growth and the Integrated Interdiffusion Coefficient

With diffusion controlled growth in a solid-to-solid diffusion couple, the thickness of a growing phase, *x*, after time, *t*, can be described by the parabolic relationship [23, 42] as given by Equation 1.

$$k_p = \frac{x^2}{2t} \tag{1}$$

Under the assumption of diffusion controlled parabolic growth, the interface velocity is inversely proportional to the phase thickness therefore, the parabolic growth constant, k_p, is proportional to the interdiffusion coefficient and is often used as an indicator of kinetic behavior. The layer thickness and parabolic growth constant depends on the compositions of the neighboring phases, and can be used to determine the integrated interdiffusion coefficient, $\widetilde{D}^{\text{int}}_{A_mB_n}$, by adjusting for the chemical effects of the neighboring phases as described by Huang *et al*. [43] adopted from Wagner [27], as shown for A_mB_n intermetallic phase of thickness $x_2 - x_1$, where C_i is the atomic fraction of component *i* and the -∞ (+∞) denotes the left (right) side of the concentration profile (i.e. terminal ends), in Equation 2.

$$\widetilde{D}^{\text{int}}_{A_mB_n} = C_B^{A_mB_n}\left(1-C_i^{A_mB_n}\right)k_p^{A_mB_n} + \frac{\Delta x^{A_mB_n}}{2t}\left[\left(1-C_i^{A_mB_n}\right)\int_{-\infty}^{x_1} C_i dx + C_i^{A_mB_n}\int_{x_2}^{+\infty}\left(1-C_i\right)dx\right]_{C_i^{-\infty}=0, C_i^{+\infty}=1} \quad (2)$$

Dayananda [44] relates the integrated interdiffusion coefficient to the interdiffusion coefficient, $\widetilde{D}$, and interdiffusion flux of component *i*, $\widetilde{J}_i$, by Equation 3.

$$\widetilde{D}^{\text{int}}_{A_mB_n} = \int_{C_i^{x1}}^{C_i^{x2}} \widetilde{D} dC_i = -\int_{x_1}^{x_2} \widetilde{J}_i dx \quad (3)$$

In this equation, $C_i^{x_1}$ and $C_i^{x_2}$ represent the concentration of component *i* position of the left and right interphase of the for A_mB_n intermetallic compound.

3.2 Boltzmann-Matano Method

Boltzmann transformed Fick's Second Law into a much simplified nonlinear ordinary differential equation from the nonlinear partial differential equation by utilizing a scaling parameter of distance, x, over the square root of time [45]. Matano applied boundary conditions such that a mass balance exists at the Matano plane to solve the ordinary differential equation. The location of the Matano plane, x_o, is the position at which the boundary condition is satisfied, and is determined by integrating over the concentration profile [25], as shown in Equation 4,

$$\int_{C_i^{+\infty}}^{C_i^o} x dC_i + \int_{C_i^o}^{C_i^{-\infty}} x dC_i = 0 \tag{4}$$

where $C_i^{-\infty}$ and$C_i^{+\infty}$ refer to the composition at terminal ends of the diffusion couple and C_i^o is the composition at the Matano plane, assuming that the molar volume is constant.

The interdiffusion flux, $\tilde{J}_i$, is then calculated as shown in Equation 5 with respect to the position of the Matano plane [46].

$$\tilde{J}_i = \frac{1}{2t} \int_{C_i^{\pm\infty}}^{C_i^o} (x - x_o)\, dC_i \tag{5}$$

The interdiffusion coefficient, $\widetilde{D}$, can then be calculated by combining Fick's first law $\widetilde{J}_i = -\widetilde{D}(\partial C_i / \partial x)$ with Equation 5 to yield Equation 6.

$$\widetilde{D} = -\frac{\frac{1}{2t}\int_{C_i^{\pm\infty}}^{C_i^o}(x - x_o)\, dC_i}{\frac{\partial C_i}{\partial x}} \tag{6}$$

3.3 Sauer-Freise Method

The Boltzmann-Matano method presumes the molar volume is constant across the compositional range of the interdiffusion zone. This approach is only valid when the deviation in molar volume, V_M, from that of ideal solution, e.g. Vegard's law, is negligible.

Non-ideal solutions deviate from this rule. The Sauer-Freise Method [47] with Wagner's adaptation [27] can be used to calculate the interdiffusion coefficient when changes in molar volume occur as in the case of multicomponent, multiphase diffusion reactions [26]. This method [42] essentially normalizes the concentration such that $Y = \left(C - C^{+\infty}\right) / \left(C^{-\infty} - C^{+\infty}\right)$, and the concentration dependent diffusion coefficient is modified as demonstrated in Equation 7.

$$\widetilde{D}(Y^*) = -\frac{V_M^*}{2t\left(dY/dx\right)_{x^*}}\left[\left(1-Y^*\right)\int_{x^*}^{x^{+\infty}}\frac{Y}{V_M}dx + Y\int_{x^{-\infty}}^{x^*}\frac{1-Y}{V_M}dx\right] \tag{7}$$

The Sauer-Freise method is not subject to the error potentially introduced through the determination of the plane of mass balance in the Boltzmann-Matano method.

3.4 Effective Interdiffusion

While the interdiffusion coefficient varies over the composition range, the effective interdiffusion coefficient, $\widetilde{D}^{eff}$, provides a single nominal coefficient for a compositional spectrum and allows for comparison with other diffusion coefficients as a function of temperature [44]. Additionally, in ternary and higher order systems, the effective interdiffusion coefficient alone can provide some information about the nature of the main and cross interdiffusion coefficients [48]. Integrating the flux over an interval from x_1 to x_2, and dividing by the change in composition over the interval, yields the effective interdiffusion coefficient, Equation 8.

$$\widetilde{D}^{eff} = -\frac{\int_{x_1}^{x_2} \tilde{J}\, dx}{(C_{x_2} - C_{x_1})} \tag{8}$$

The effective interdiffusion coefficient is essentially an unbiased interdiffusion coefficient. Often times in literature, a numerical average interdiffusion coefficient is reported interchangeably as an average effective interdiffusion coefficient. The numerical average interdiffusion coefficient can be influenced or biased by the nature of the composition dependence. While these two values are comparable, they may not be equivalent.

3.5 Hall Method

According to Darken's relationship [49], the impurity diffusion coefficient is equal to the interdiffusion coefficient in infinitely dilute solutions. The Hall Method has been shown to be an effective approach to determining impurity diffusion coefficients from the extrapolation of interdiffusion coefficients [50]. Since time is constant for a given experiment, a probability plot of the concentration distribution yields a straight line whose slope and intercepts are used to solve the concentration dependent diffusion coefficient [24]. By treating C/C^{∞} as a probability and writing it in terms of the standard normal cumulative distribution function or $C/C^{\infty} = ½ + ½ \text{ erf}(u)$, where $u = h\eta + k$ and η is the Boltzmann variable, $x/2(t^{1/2})$, the diffusion equation can be rewritten in terms of h, k, and u [51] as shown in Equation 9.

$$\widetilde{D} = \frac{1}{h^2} + \frac{k\sqrt{\pi}}{h^2}(1 + \mathrm{erf}\,u)\exp(u^2) \tag{9}$$

The Hall Method puts the concentration gradient in terms of a probability distribution facilitating the accurate determination of the interdiffusion coefficient at impurity levels.

3.6 Kirkaldy's Extension

For any system consisting of n components, (n-1) independent concentrations and $(n-1)^2$ interdiffusion coefficients are necessary. Therefore, the composition dependent diffusion behavior of a ternary system, where there are two independent concentrations, must be described by four interdiffusion coefficients; two are the main coefficients, D_{ii}^3, and two are the cross coefficients, D_{ij}^3, where $i, j = 1,2$ and the dependent concentration is that of component 3. Based on Onsager's formalism, an extension of Fick's First Law as demonstrated by Kirkaldy, yields two equations but four unknowns as shown in Equation 10 [52, 53].

$$\begin{aligned}
\widetilde{J}_1 &= -\widetilde{D}_{11}^3 \frac{\partial C_1}{\partial x} - \widetilde{D}_{12}^3 \frac{\partial C_2}{\partial x} \\
\widetilde{J}_2 &= -\widetilde{D}_{21}^3 \frac{\partial C_1}{\partial x} - \widetilde{D}_{22}^3 \frac{\partial C_2}{\partial x} \\
\widetilde{J}_3 &= -\left(\widetilde{J}_1 + \widetilde{J}_2\right)
\end{aligned} \tag{10}$$

To describe a ternary system, Kirkaldy extended the Boltzmann-Matano method for multicomponent systems [54] as shown in Equation 11.

$$\int_{C_1(\pm\infty)}^{C_1(x)} (x - x_o) dC_1 = -2t\left[\tilde{D}_{11}^3 \frac{\partial C_1}{\partial x} + \tilde{D}_{12}^3 \frac{\partial C_2}{\partial x} \right]$$
$$\int_{C_2(\pm\infty)}^{C_2(x)} (x - x_o) dC_2 = -2t\left[\tilde{D}_{21}^3 \frac{\partial C_1}{\partial x} + \tilde{D}_{22}^3 \frac{\partial C_2}{\partial x} \right] \quad (11)$$

In order to solve for the four interdiffusion coefficients, Kirkaldy obtained four equations and four unknowns by examining the interdiffusion behavior of intersecting diffusion paths on ternary isotherm [54-56]. That is, each path of two independent diffusion paths, *A* and *B*, at one common intersecting composition provided two equations. Analysis of the concentration gradient at this common concentration allowed for the calculation of the main and cross coefficients, $\tilde{D}_{ij}^3$ as given in Equation 12.

$$\widetilde{D}_{11}^{3}=\frac{-\left(\frac{1}{2t}\int_{C_1(\pm\infty)}^{C_1(x)}(x-x_o)dC_1\right)_A-\widetilde{D}_{12}^{3}\left(\partial C_2/\partial x\right)_A}{\left(\partial C_1/\partial x\right)_A}$$

$$\widetilde{D}_{12}^{3}=\frac{\left(\frac{1}{2t}\int_{C_1(\pm\infty)}^{C_1(x)}(x-x_o)dC_1\right)_B\left(\partial C_1/\partial x\right)_A-\left(\frac{1}{2t}\int_{C_1(\pm\infty)}^{C_1(x)}(x-x_o)dC_1\right)_A\left(\partial C_1/\partial x\right)_B}{\left(\partial C_2/\partial x\right)_A\left(\partial C_1/\partial x\right)_B-\left(\partial C_2/\partial x\right)_B\left(\partial C_1/\partial x\right)_A}$$

$$\widetilde{D}_{21}^{3}=\frac{-\left(\frac{1}{2t}\int_{C_2(\pm\infty)}^{C_2(x)}(x-x_o)dC_2\right)_A-\widetilde{D}_{22}^{3}\left(\partial C_2/\partial x\right)_A}{\left(\partial C_1/\partial x\right)_A}$$

$$\widetilde{D}_{22}^{3}=\frac{\left(\frac{1}{2t}\int_{C_2(\pm\infty)}^{C_2(x)}(x-x_o)dC_2\right)_B\left(\partial C_1/\partial x\right)_A-\left(\frac{1}{2t}\int_{C_2(\pm\infty)}^{C_2(x)}(x-x_o)dC_2\right)_A\left(\partial C_1/\partial x\right)_B}{\left(\partial C_2/\partial x\right)_A\left(\partial C_1/\partial x\right)_B-\left(\partial C_2/\partial x\right)_B\left(\partial C_1/\partial x\right)_A} \quad (12)$$

Thus, four interdiffusion coefficients, namely the two main ($\widetilde{D}_{11}^{3}$ and $\widetilde{D}_{22}^{3}$) coefficients and two cross ($\widetilde{D}_{12}^{3}$ and $\widetilde{D}_{21}^{3}$) coefficients are required to describe the interdiffusion in ternary system at a fixed composition. Experimentally, two independent diffusion paths, from two independent diffusion couples, that intersect at a common composition are required to determine the four interdiffusion coefficients.

In ternary and multicomponent diffusion, concentration profiles can exhibit relative maxima and/or minima where the concentration gradient of the respective component is zero; similarly, near the terminal ends, the concentration gradient of one component may

go to zero (i.e. $\partial C_i / \partial x = 0$). In this case, Equation 12 may be employed to determine one main and cross interdiffusion coefficient without the need for an intersecting diffusion paths from two independent diffusion couples [57]. Furthermore, development of a zero-flux plane (ZFP) [58] can yield a ratio between the main and cross interdiffusion coefficients.

3.7 Ternary Interdiffusion Coefficient Transformation

In consideration of atomic mobility and the concept of lattice velocity, ternary interdiffusion coefficients can be transformed between the defined, dependent component [59]. Additional sets of interdiffusion coefficients corresponding to $\widetilde{D}^1_{cd}\ (c,d=2,3)$ and $\widetilde{D}^2_{mn}\ (m,n=1,3)$ can be calculated from the values of $\widetilde{D}^3_{ij}\ (i,j=1,2)$ on the basis of the relations of Equation 13 [60].

$$\begin{gathered}
\widetilde{D}^1_{22} = \widetilde{D}^3_{22} - \widetilde{D}^3_{21} \\
\widetilde{D}^1_{23} = -\widetilde{D}^3_{21} \\
\widetilde{D}^1_{32} = \widetilde{D}^3_{11} + \widetilde{D}^3_{21} - \widetilde{D}^3_{22} - \widetilde{D}^3_{12} \\
\widetilde{D}^1_{33} = \widetilde{D}^3_{11} + \widetilde{D}^3_{21} \\
\widetilde{D}^2_{11} = \widetilde{D}^3_{11} - \widetilde{D}^3_{12} \\
\widetilde{D}^2_{13} = -\widetilde{D}^3_{12} \\
\widetilde{D}^2_{31} = \widetilde{D}^3_{22} + \widetilde{D}^3_{12} - \widetilde{D}^3_{11} - \widetilde{D}^3_{21} \\
\widetilde{D}^2_{33} = \widetilde{D}^3_{22} + \widetilde{D}^3_{12}
\end{gathered} \tag{13}$$

3.8 Arrhenius Relationship

Solid-state diffusion is strongly dependent on temperature. In general, the diffusion rate increases with increasing temperature. The temperature dependence of diffusion coefficients and subsequent parabolic growth constants typically fit an Arrhenius model. For example, Equation 14 shows the relation between the interdiffusion coefficient and temperature.

$$\widetilde{D} = \widetilde{D}_o e^{-\frac{\tilde{Q}_D}{RT}} \tag{14}$$

$\widetilde{D}_o$ is the pre-exponential factor and $\tilde{Q}_D$ is the activation energy for interdiffusion. T is the absolute temperature and R is the gas constant. When the diffusion coefficient is plotted against the inverse of the temperature, the slope of the line will give the activation energy and the intercept will yield the pre-exponential as shown in Figure 2.

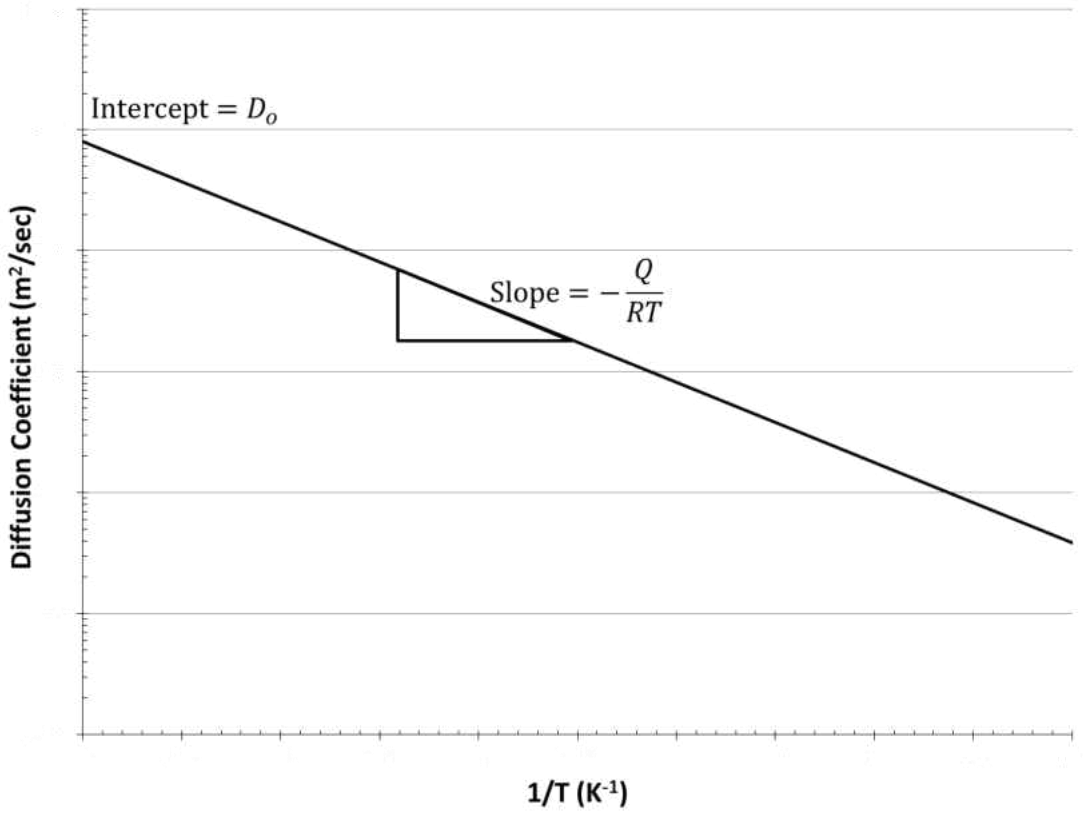

Figure 2: Schematic representation of the Arrhenius relationship between diffusivity and temperature

The pre-exponential factor and activation energy for diffusion depend on the diffusion mechanism, on the type of diffusion process, and on the lattice geometry [26]. In substitutional solid solutions, the attractive and repulsive forces between solute atoms and vacancies affect the probability of a vacancy existing on a nearest-neighbor position of a solute atom [26]. Additionally, there exists a correlation between the directions of consecutive jumps. The probability of making a jump depends on the direction of the preceding jump [61]. The predominant diffusion mechanism will govern the correlation

and frequency. The diffusion coefficient can provide some insight into the correlation factor, jump attempt frequency, and binding energy, when the vacancy mechanism is assumed. Stochastic diffusion theory defines the pre-exponential factor as the attempt frequency of atomic motion and can be quantified as given in Equation 15, where f is the correlation factor, d is the nearest-neighbor jump distance, and v_i is the attempt frequency of exchange with a solvent atom or a solute atom in different configurations [62].

$$D_o = f d^2 v_i \exp\left(\frac{\Delta S}{R}\right) \tag{15}$$

3.9 Oliver-Pharr Method

A load vs. displacement curve is generated from the collected data during instrumented indentation testing. Figure 3 depicts an example of a load vs. displacement curve in which the load is increased at a constant rate to some peak value (loading), held at that value for a set amount of time, and then decreased to zero (unloading). The sample hardness H and reduced elastic modulus E_r can then be calculated from the curve.

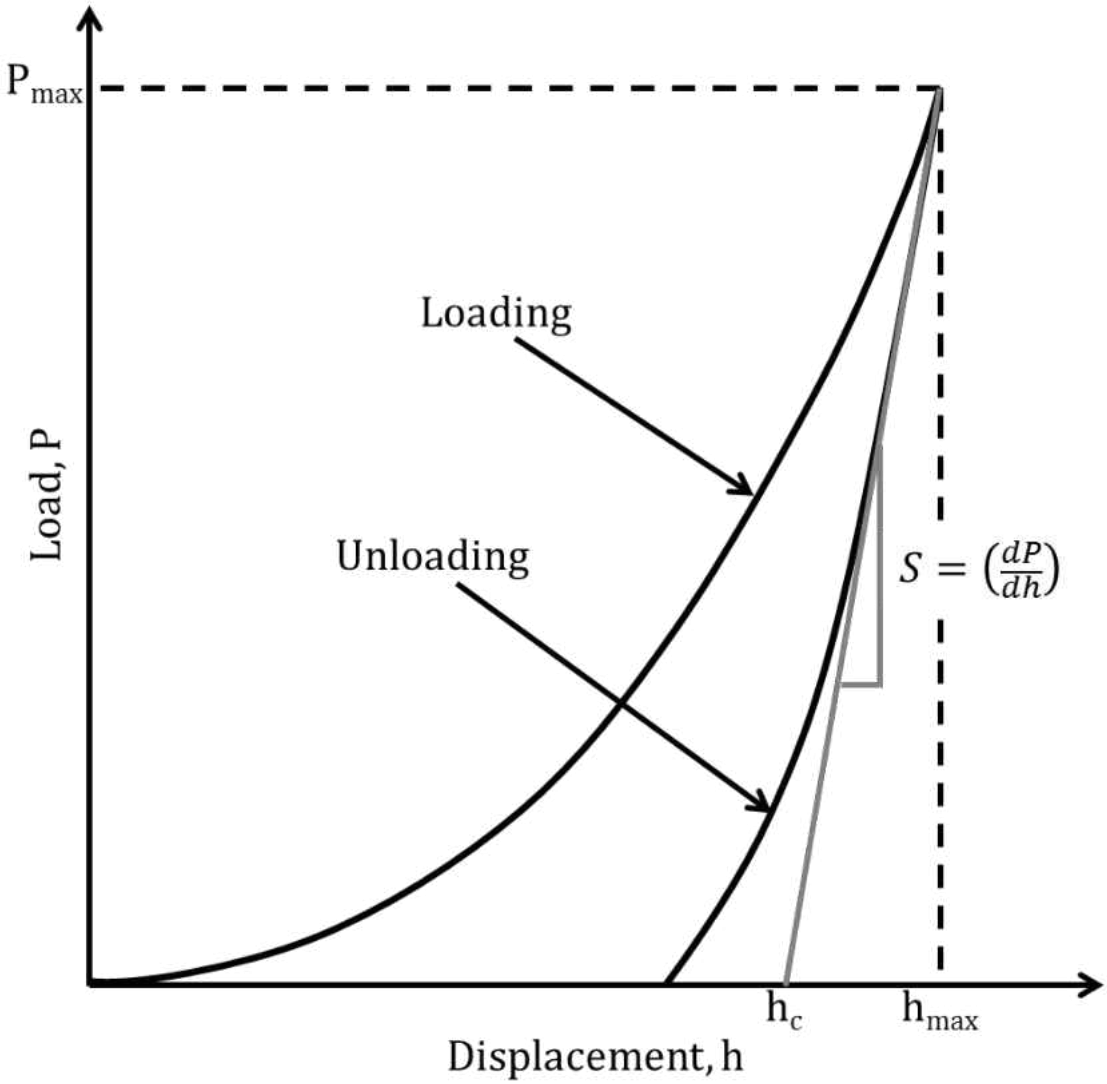

Figure 3: Load-Displacement profile

The reduced modulus is defined by Equation 16 where *S*, the unloading stiffness, is defined by slope of the initial portion of the unloading segment and *A*, the contact area, is determined from the shape of tip in the calibration process. [39, 41]

$$E_r = \frac{S\sqrt{\pi}}{2\sqrt{A}} \tag{16}$$

The unloading stiffness, S, is calculated by fitting the unloading curve to the power law relation $P = B\left(h - h_f\right)^m$ where B, h_f, and m are arbitrary fitting parameters. The stiffness at the peak of the unloading curve represents the elastic response of the material at the initial point of unloading, evaluated at $h = h_{max}$ as given in Equation 17.

$$S = \left.\frac{dP}{dh}\right|_{h=h_{\max}} = mB\left(h_{\max} - h_f\right)^{m-1} \tag{17}$$

The contact area, A, is a function of the probe's contact depth, h_c. The probe area function, unique for each probe, is determined through a calibration on a reference material (i.e. fused silica), and is mathematically described by an n^{th} order polynomial ($3 \leq n \leq 6$). The contact depth is calculated from the load vs. displacement curve according to Equation 18.

$$h_c = h_{\max} - \varepsilon \frac{P_{\max}}{S} \tag{18}$$

Equation 18 accounts for the fact that the contact depth is always less than the peak displacement due to deflection of the surface around the contact perimeter [41]. ε is a geometric constant taken to be 0.75 for most common probe geometries (e.g. Berkovich) [40].

The reduced modulus is related to the modulus of elasticity (E_S) through Equation 19 where the subscript *i* corresponds to the indenter material, the subscript *s* refers to the indented sample materials and *v* is Poisson's ratio [39, 41]. For a diamond indenter probe (e.g. Berkovich), E_i is 1140 GPa and v_i is 0.07. Poisson's ratio varies between 0 and 0.5 for most materials.

$$\frac{1}{E_r} = \frac{\left(1-\nu_i^2\right)}{E_i} + \frac{\left(1-\nu_S^2\right)}{E_S} \tag{19}$$

The hardness is defined by the ratio of the maximum load to the projected contact area as given by Equation 20 [39, 41]:

$$H = \frac{P_{\max}}{A} \tag{20}$$

CHAPTER 4: INFLUENCE OF SOLUTE CONCENTRATION ON IMPURITY DIFFUSION

4.1 Background

In terms of modern alloy and process design, it is the impurity diffusion coefficients which serve as the building blocks of subsequent computations and predictions. Conventional Mg alloys often contain more than one alloying element. As such, the influence of tertiary impurities must be incorporated into the models. Few experimental data is available.

The solute concentration-dependent impurity diffusion coefficient was determined for Zn impurity in Mg-*x*Al alloys by Čermák using conventional radioisotopic tracer techniques [63]. With increasing concentration of Al, the Zn impurity diffusion coefficient is slightly increased, and the change in the diffusion coefficient as a function of concentration is not affected by temperature. Čermák concluded that the activation energy for Zn impurity diffusion is independent of Al concentration while the pre-exponential factor is dependent on the concentration of Al. On the basis of Equation 15, Čermák rationalized that since the jump distance is only weakly influenced by the Al concentration and the correlation factor and attempt frequency can be considered constant, the entropy term must be the dominant contributor to the concentration-dependent pre-exponential factor. Therefore as the entropy increases, the pre-exponential factor will also increase. Furthermore, using Zener's approximation for entropy [64], based on elastic strain theory which states that pre-exponential factor is fractionally proportional to the ratio of activation energy to melting temperature [42], Čermák pointed out that as Al concentration

increases, the melting temperature of the alloy decreases and entropy of the alloy increases.

The objective of this study is to determine the impurity diffusion coefficients in binary Mg-rich solid solutions using solid-to-solid diffusion couples assembled with binary and ternary solid solutions. Interdiffusion coefficients are calculated by the Hall method [24, 51] and extrapolated to the impurity diffusion coefficient on the basis of Darken's relation [49]. The pre-exponential factor and activation energy of impurity diffusion are examined as a function of solute concentration.

4.2 Experimental Parameters

The chemical composition of the magnesium and magnesium alloys used in this investigation are given in Table 1. Diffusion couple assembly and anneal parameters used in this study are listed in Table 3. The Hall method described in §3.5, was used to extrapolate impurity diffusion coefficients.

Table 3: Diffusion anneal parameters for impurity diffusion study

Diffusion Couple	Anneal Temperature (°C)	Anneal Time (Hours)
Mg vs. Mg-9at.%Al	350	96
	400	17
	450	24
Mg vs. Mg-3at.%Zn	350	125
	400	8
	450	24
Mg-3at.%Al vs. Mg-1at.%Zn	400	20
	450	5
Mg-9at.%Al vs. Mg-3at.%Zn	400	8
	450	4
Mg vs.Mg-3at.%Al-0.5at.%Zn	350	168
	400	24
	450	4

4.3 Results and Discussion

Using the Hall interdiffusion coefficient at the infinitely dilute composition, the impurity diffusion coefficients were extracted from one or more concentration profiles for each diffusion couple. The Zn and Al impurity diffusion data is presented in Table 4 and Table 5, respectively. The activation energy and pre-exponential factor of the impurity diffusion in pure Mg was determined. For Zn in pure Mg, the impurity diffusion pre-exponential factor and activation energy are 1.86×10^{-4} m^2/sec and 130.0 kJ/mol. These results are slightly higher than the impurity diffusion coefficients determined in binary Mg alloys and previously reported [65] but are in good agreement with the results from tracer diffusion experiments , 1.00×10^{-4} m^2/sec and 125.2 kJ/mol [66]. The pre-exponential factor and activation energy for Al impurity diffusion in pure Mg are determined to be 2.02×10^{-5}

m^2/sec and 131.2 kJ/mol, respectively. These results are consistent with previously reported values, D_o = 6.25x10^{-5} m^2/sec and Q = 139.3 kJ/mol [65]. Zn impurities diffuse faster than self-diffusion of Mg atoms (D_o = 1.20x10^{-4} m^2/sec and Q = 134 kJ/mol [66]) which is, in turn, faster than Al impurity diffusion.

Table 4: Zn Impurity Diffusion Coefficients, D_{Zn}^{Mg}

	Couple	at.%Al	Average (Std. Dev.)	D_{Zn}^{Mg}	Average (Std. Dev.)
350°C	Mg vs.Mg-3at.%Al-0.5at.%Zn	0.00	0.00 (0.00)	7.45x10^{-16}	2.07x10^{-15} (1.36x10^{-15})
		0.00		4.87x10^{-16}	
	Mg vs. Mg-3at.%Zn	0.00		3.51x10^{-15}	
		0.00		2.91x10^{-15}	
		0.00		2.71x10^{-15}	
400°C	Mg vs.Mg-3at.%Al-0.5at.%Zn	0.00	0.00 (0.00)	2.06x10^{-14}	1.90x10^{-14} (5.62x10^{-15})
		0.00		1.14x10^{-14}	
	Mg vs. Mg-3at.%Zn	0.00		1.57x10^{-14}	
		0.00		2.15x10^{-14}	
		0.00		2.60x10^{-14}	
	Mg-3at.%Al vs. Mg-1at.%Zn	2.71	2.70 (0.01)	4.71x10^{-15}	9.11x10^{-15} (6.22x10^{-15})
		2.73		1.35x10^{-14}	
	Mg-9at.%Al vs. Mg-3at.%Zn	9.08	9.10 (0.01)	3.42x10^{-14}	3.35x10^{-14} (9.90x10^{-16})
		9.06		3.28x10^{-14}	
450°C	Mg vs.Mg-3at.%Al-0.5at.%Zn	0.00	0.00 (0.00)	6.01x10^{-14}	6.56x10^{-14} (8.40x10^{-15})
		0.00		5.35x10^{-14}	
	Mg vs. Mg-3at.%Zn	0.00		7.27x10^{-14}	
		0.00		7.07x10^{-14}	
		0.00		7.10x10^{-14}	
	Mg-3at.%Al vs. Mg-1at.%Zn	2.77	2.80 (0.01)	6.53x10^{-14}	5.80x10^{-14} (1.03x10^{-14})
		2.76		5.07x10^{-14}	
	Mg-9at.%Al vs. Mg-3at.%Zn	8.09	8.10 (--)	1.49x10^{-13}	1.49x10^{-13} (--)

Table 5: Al Impurity Diffusion Coefficients, D_{Al}^{Mg}

	Couple	at.%Zn	Average (Std. Dev.)	D_{Al}^{Mg}	Average (Std. Dev.)
350°C	Mg vs.Mg-3at.%Al-0.5at.%Zn	0.02	0.00 (0.01)	$7.76\text{x}10^{-17}$	$1.83\text{x}10^{-16}$ ($1.48\text{x}10^{-16}$)
		0.00		$4.39\text{x}10^{-16}$	
	Mg vs. Mg-9at.%Al	0.00		$8.49\text{x}10^{-17}$	
		0.00		$1.56\text{x}10^{-16}$	
		0.00		$1.51\text{x}10^{-16}$	
400°C	Mg vs.Mg-3at.%Al-0.5at.%Zn	0.02	0.02 (0.04)	$3.80\text{x}10^{-15}$	$1.64\text{x}10^{-15}$ ($1.44\text{x}10^{-15}$)
		0.08		$8.46\text{x}10^{-16}$	
	Mg vs. Mg-9at.%Al	0.00		$1.02\text{x}10^{-15}$	
		0.00		$8.87\text{x}10^{-16}$	
	Mg-3at.%Al vs. Mg-1at.%Zn	1.00	1.00 (0.02)	$3.57\text{x}10^{-15}$	$2.92\text{x}10^{-15}$ ($9.19\text{x}10^{-16}$)
		0.97		$2.27\text{x}10^{-15}$	
	Mg-9at.%Al vs. Mg-3at.%Zn	2.04	2.10 (0.11)	$2.09\text{x}10^{-15}$	$2.06\text{x}10^{-15}$ ($4.95\text{x}10^{-17}$)
		2.20		$2.02\text{x}10^{-15}$	
450°C	Mg vs. Mg-9at.%Al	0.00	0.00 (0.02)	$4.87\text{x}10^{-15}$	$5.97\text{x}10^{-15}$ ($9.24\text{x}10^{-16}$)
		0.00		$5.89\text{x}10^{-15}$	
		0.00		$6.96\text{x}10^{-15}$	
	Mg vs.Mg-3at.%Al-0.5at.%Zn	0.03		$6.85\text{x}10^{-15}$	
		0.05		$5.30\text{x}10^{-15}$	
	Mg-3at.%Al vs. Mg-1at.%Zn	0.90	1.00 (0.11)	$1.83\text{x}10^{-14}$	$2.69\text{x}10^{-14}$ ($1.22\text{x}10^{-14}$)
		1.06		$3.55\text{x}10^{-14}$	
	Mg-9at.%Al vs. Mg-3at.%Zn	2.01	2.00 (--)	$5.56\text{x}10^{-14}$	$5.56\text{x}10^{-14}$ (--)

The influence of solute concentration in Mg solid solutions on the impurity diffusion coefficient was examined. Figure 4 presents the Zn impurity diffusion coefficient, D_{Zn}^{Mg}, in Mg(Al) solid solutions. Open circle markers represent the average impurity diffusion coefficient at 450˚C; open square markers indicate the average impurity diffusion coefficients at 400˚C. The vertical and horizontal error bars represent one standard deviation in the diffusion coefficient and atomic concentration, respectively. No data is presented for impurity diffusion at 350˚C since coefficients were determined in only pure

Mg. With increasing concentration of Al, the Zn impurity diffusion coefficient is slightly increased. The change in the diffusion coefficient as a function of concentration is not affected by temperature, indicating that the activation energy for Zn impurity diffusion is independent of Al concentration. The results of this study agree well with the work of Čermák [63], indicated by the dashed lines in Figure 4. Čermák characterized the Zn impurity diffusion coefficient as a function of the aluminum concentration (in wt.%) through an Arrhenius relationship as:

$$D_{Zn}^{Mg} = \exp\left[(0.100 \pm 0.007)(wt.\%Al) - (9.16 \pm 0.33)\right]\exp\left(-\frac{125800 \pm 2100}{RT}\right) \qquad (21)$$

The solute concentration-dependent impurity diffusion coefficient determined in this study by the Hall Method is within the margin of error of that determined by Čermák using the tracers. As was pointed out by Čermák, the pre-exponential factor is concentration dependent while the activation energy is concentration independent [63].

The Al impurity diffusion coefficient, D_{Al}^{Mg}, in Mg(Zn) solid solutions is presented in Figure 5. Open circle markers represent the average impurity diffusion coefficient at 450˚C; open square markers indicate the average impurity diffusion coefficients at 400˚C. No data is presented for impurity diffusion at 350˚C since coefficients were determined in only pure Mg. At 400°C, the Al impurity diffusion coefficient remains relatively unchanged with increasing Zn concentration. The behavior of the diffusion coefficient is notably different at

450°C; the impurity diffusion coefficient increases by an order of magnitude when the Mg solid solution contains 2 at.%Zn. The divergence of the impurity diffusion coefficient with increasing concentration between the two studied temperatures is indicative that both the pre-exponential factor and energy of activation for Al impurity is dependent on the concentration of Zn in solution with Mg.

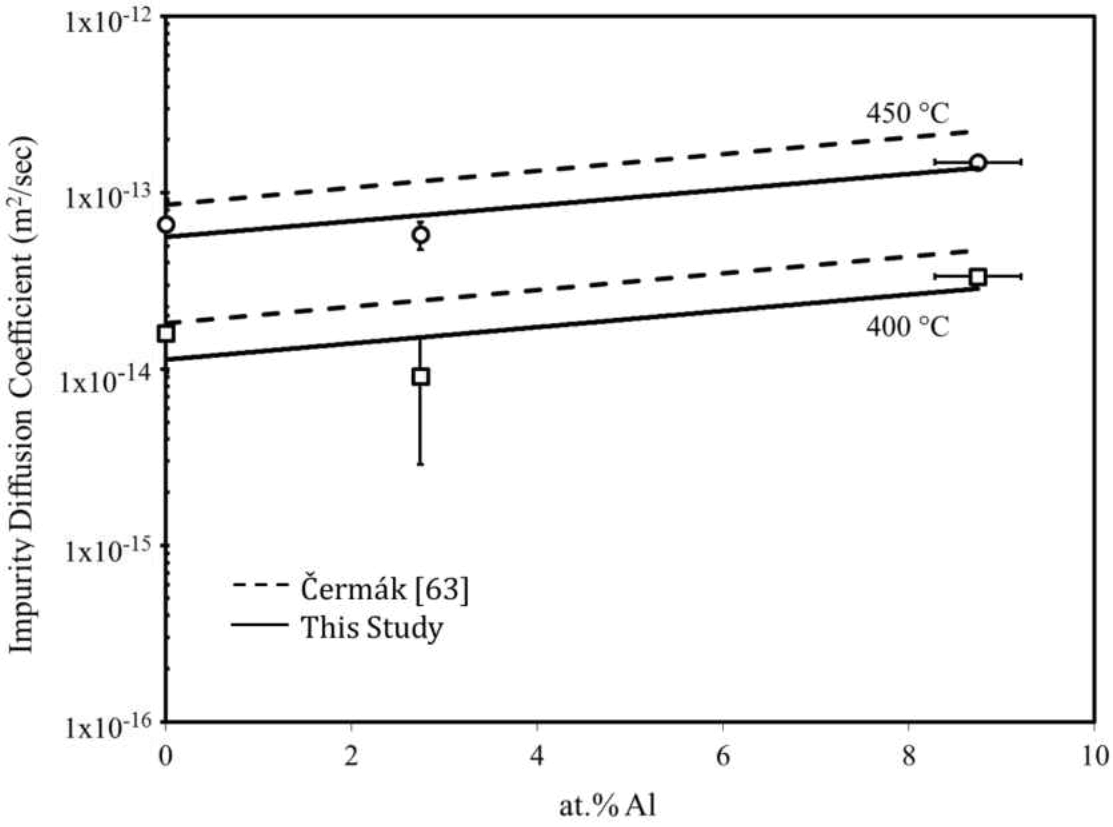

Figure 4: Influence of solute concentration on the Zn impurity diffusion coefficient in Mg(Al) solid solutions

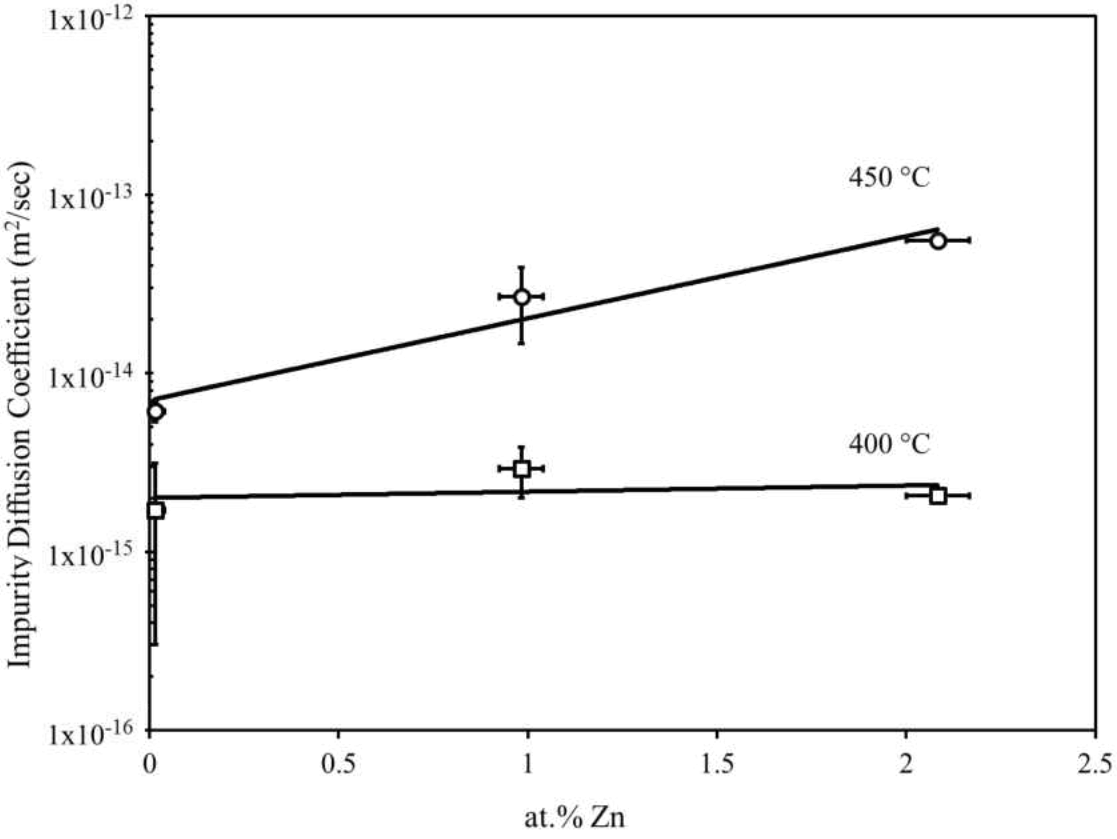

Figure 5: Influence of solute concentration on the Al impurity diffusion coefficient in Mg(Zn) solid solutions

To understand the underlying contributors on the concentration dependence of Al impurity diffusion in Mg(Zn) solid solutions, the available data is examined through an Arrhenius relationship, shown in Figure 6. The composition dependence of the Al impurity diffusion coefficient in Mg solid solution can be nominally expressed by the following relation:

$$D_{Al}^{Mg} = 1.4\times10^{-5}\exp\left[11.6\times at\%Zn\right]\exp\left(-\frac{1.32\times10^{5}\exp\left(at\%Zn/3\right)}{RT}\right) \quad (22)$$

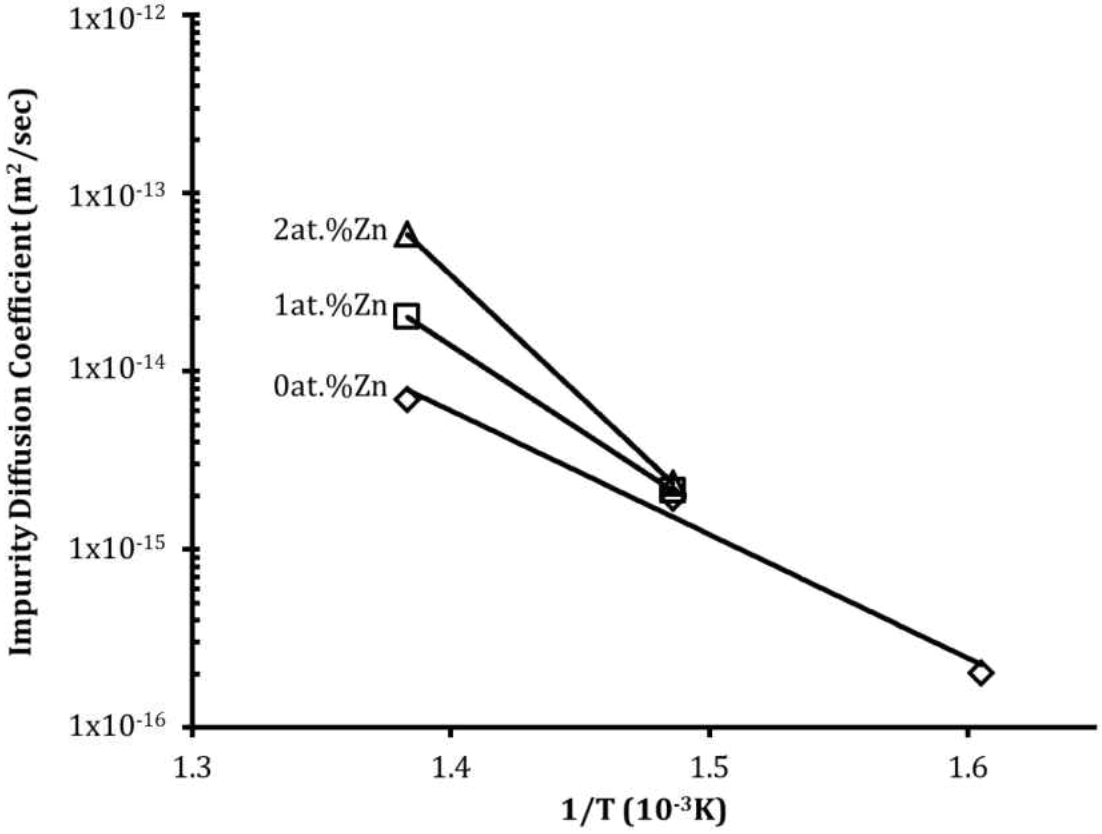

Figure 6: Temperature dependence of Al impurity diffusion coefficient in Mg(Zn) solid solution

Because only two data points are used to determine the pre-exponential factor and activation energy for Al impurity diffusion in Mg-1at.%Zn and Mg-2at.%Zn, Equation 22 is only an approximate relation. Ideally, three or more points should be used to determine the parameters of temperature dependence. Nonetheless, it is obvious from Equation 22 and

Figure 6 that the concentration dependence of D_{Al}^{Mg} is expressed in both the pre-exponential factor and the activation energy. As such, at lower temperatures, the presence of Zn in solid solution may limit Al impurity diffusion while at higher temperatures the presence of Zn promotes Al impurity diffusion.

In consideration of Equation 15 and analogous to Čermák's rationalization, the concentration dependence of the pre-exponential factor is derived predominately from the activated state entropy term, which is proportional to activation energy to melting temperature ratio. The correlation between atomic radius of the solute atom and the nearest-neighbor distance in Mg(Al) and Mg(Zn) solid solutions has been experimentally studied [67] and computationally examined from first principles [68, 69]. When alloyed with 2.77 at.%Zn, the jump distance between Mg and Zn is reduced only 2.14% from the nearest-neighbor distance in pure Mg [69]. As a result of these findings, a constant and compositionally independent jump distance is a valid presumption in this study, as was made by [63]. To a greater extent than that caused by the addition of Al, the melting temperature of the Mg solid solution significantly decreases with even small additions of Zn (i.e. $\left|\nabla T_M\left(C_{Zn}\right)\right| >> \left|\nabla T_M\left(C_{Al}\right)\right|$). Therefore, the entropy of activation sharply increases with increasing Zn concentration, and thus it follows the pre-exponential factor substantially increases with increasing Zn concentration.

It is also evident from Equation 22, there is an exponential concentration dependence of the Al impurity diffusion activation energy. For vacancy mediated diffusion, the diffusion coefficient is proportional to the vacancy concentration. The existence of

vacancies alone, however, is not sufficient for diffusion to occur; vacancies must also be able to move or migrate. In addition, vacancies interact with solutes and impurities according to their binding energy. The diffusion activation energy is the sum of the vacancy formation and migration energies [70]. The vacancy formation energy can be further decomposed to the difference between the energy of formation in pure Mg and the solute-vacancy binding energy [71]. Experimentally and through first principle computations, the solute-vacancy binding energy for Zn is more favorable than that for Al in Mg solid solution [72-74]. Furthermore, the c/a ratio in Mg solid solution is increased on the addition Al but decreased or unchanged with the addition of Zn. The variation in *a* parameter is dependent only on the atomic radius of the solute element, whereas the c/a ratio is proportional to the variation in electron concentration [75, 76]. Therefore, the increase in the Al impurity diffusion activation energy as a function of Zn concentration in Mg solid solution can be qualitatively rationalized on the basis of an increase in net Zn-vacancy binding energy and stronger attractive forces. It is interesting to note, the trend in the c/a ratio is parallel to trend in impurity diffusion coefficients (i.e. $(c/a)_{Zn} < (c/a)_{Mg} < (c/a)_{Al} \approx D_{Zn}^{Mg} < D_{Mg}^{Mg} < D_{Al}^{Mg}$).

4.4 Summary

Impurity diffusion coefficients for Al and Zn in pure Mg, Zn in Mg(Al) solid solution, and Al in Mg(Zn) solid solution were calculated by the Hall Method using solid-to-solid diffusion couples. Al impurity in Mg(Zn) solid solution have not been previously reported. The impurity diffusion coefficients in pure Mg are consistent with those determined

through other analytical techniques. Zn impurities diffuse faster than Al impurities in pure Mg.

The Zn impurity diffusion coefficient is only slightly affected by the presence of Al in Mg(Al) solid solution at the temperatures studied. Al impurity diffusion in Mg(Zn) solid solution is strongly influenced by the Zn concentration at 450˚C.

- The pre-exponential factor for Zn impurity diffusion is concentration dependent while the activation energy is independent of concentration of Al in solution with Mg.
- Both the pre-exponential factor and energy of activation for Al impurity diffusion is dependent on the concentration of Zn in solution with Mg.
- Zn in solid solution promotes Al impurity diffusion at high temperatures.

CHAPTER 5: INTERDIFFUSION IN TERNARY MAGNESIUM SOLID SOLUTIONS OF ALUMINUM AND ZINC

5.1 Background

The diffusion data available for Mg alloys is typically restricted to self/impurity diffusion and diffusion in binary Mg systems [34-36, 63, 65, 66, 71, 77-91]. While diffusion studies have been performed in the binary Mg-Al and Mg-Zn systems [35, 50, 63, 71, 77, 79, 80, 89, 92], little work has been done to study of interdiffusional behavior in the ternary Mg-Al-Zn system. In fact, due to the extent of aluminum alloy applications, most solid-state kinetic studies have focused on the Al-rich ternary alloys [93, 94]. The author is not aware of any ternary interdiffusion data available in literature for Mg-rich (hcp) Mg-Al-Zn ternary alloy. Regarding the diffusional interaction among Mg, Al, and Zn, limited data is available for the Al-rich (fcc) Mg-Al-Zn ternary alloy [83, 84, 94-97]. Most recently, Takahashi *et al*. [97] examined ternary and quaternary interdiffusion diffusion in 7000 series aluminum alloys (Al-Mg-Zn-Cu).

The objective of this study is to determine the ternary interdiffusion coefficients in Mg-rich (hcp) Mg-Al-Zn alloys at 400° and 450°C using solid-to-solid diffusion couples assembled with binary and ternary solid solutions. Analyses of the concentration profiles are based on Kirkaldy's extension [28, 54] of Fick's law on the basis of Onsager's formalism [52, 53] and Boltzmann-Matano method. The magnitude and sign of main- (diagonal) and cross- (off-diagonal) coefficients for the solutes Al and Zn were examined as a function of composition and ternary diffusional interaction.

5.2 Experimental Parameters

As listed in Table 3, four diffusion couple series were selected to explore interdiffusion in Mg solid solution of the Mg-Al-Zn ternary system. Four diffusion couples were annealed at 400°C and three diffusion couples were annealed at 450°C.

Table 6: Diffusion anneal parameters for ternary interdiffusion study

Series	Diffusion Couple	Anneal Temperature (˚C)	Anneal Time (Hours)
I	Mg-9at.%Al vs. Mg-3at.%Zn	400 450	8 4
II	Mg-3at.%Al vs. Mg-1at.%Zn	400 450	20 5
III	Mg vs. Mg-3at.%Al-0.5at.%Zn	400 450	24 4
IV	Mg vs. Mg-1at.%Al-1at.%Zn	400	24

The concentration profiles were determined by EPMA and fitted using a piecewise cubic smoothing spline. Kirkaldy's extension of Boltzmann-Matano analysis based on Onsager's formalism, as described in §3.6, was employed to calculate the interdiffusion coefficients at specific compositions.

5.3 Results

All diffusion couples exhibited good bonding as represented by a backscatter electron micrograph in Figure 7 from the Mg-9at.%Al vs. Mg-3at.%Zn couple annealed at 450°C for 4 hours.

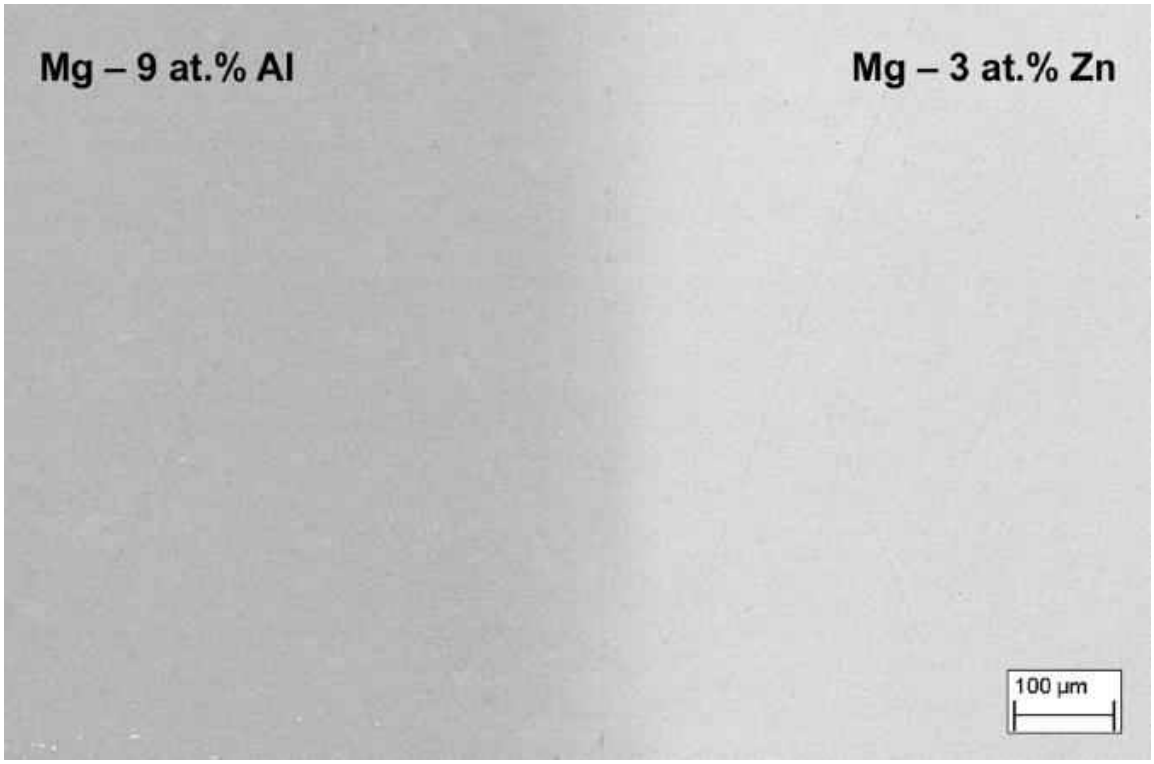

Figure 7: Backscatter electron micrograph from the diffusion couple Mg-9at.%Al vs. Mg-3at.%Zn annealed at 450°C for 4 hours

The interdiffusion fluxes of the individual components were calculated from the experimental concentration profiles using Equation 5. Typical concentration profiles and the corresponding interdiffusion flux profiles are presented in Figure 8, Figure 9, and Figure 10 for the diffusion couples, Mg-9at.%Al vs. Mg-3at.%Zn annealed at 450°C for 4 hours, Mg-3at.%Al vs. Mg-1at.%Zn annealed at 450°C for 5 hours, and Mg vs. Mg-1at.%Al-1at.%Zn annealed at 400°C for 24 hours, respectively. Qualitatively, from the concentration profiles, Al interdiffusion is observed to be slower than Mg and Zn. Also the concentration profile of Mg can exhibit relative maximum and minimum, and its redistribution appears to be largely influenced by interdiffusion of Zn.

As previously described in §3.6, there are several features within the profiles of concentrations and interdiffusion fluxes where additional determination of ternary interdiffusion coefficients without the necessity of the intersecting diffusion paths at a common composition. Specifically, relative maxima and minima exist in Mg concentration profiles, $\left(\partial C_{Mg}/\partial x\right)=0$ presented in Figure 8 and Figure 9, denoted by x_{RE}. In addition, diffusional depth of penetration for Al was typically smaller than those of Mg and Zn, and allowed for determination of ternary interdiffusion coefficients where $\left(\partial C_{Al}/\partial x\right)=0$, denoted by x_T in Figure 8, Figure 9, and Figure 10. Finally, the interdiffusion flux of a component may go to zero and reverse its direction at a Zero Flux Plane (ZFP) [58]. The activity of a component, Mg in Figure 8, at the composition of a ZFP is approximately the same as its activity in one of the terminal ends of the couple [58]. According to Eq. [11], the ratio of main to cross ternary interdiffusion coefficients can be calculated at ZFP denoted by x_{ZFP}.

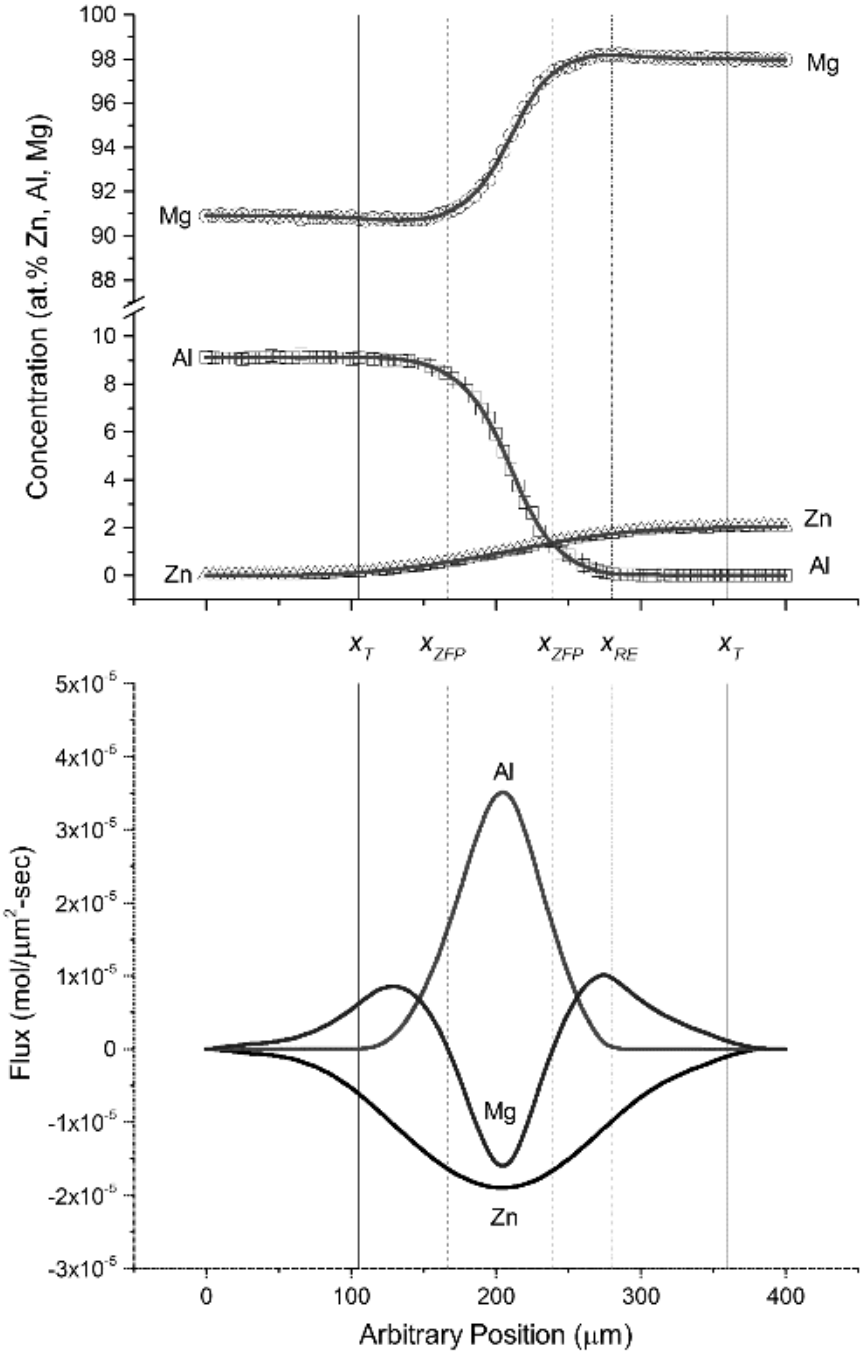

Figure 8: Concentration profile (top) and flux profile (bottom) across interdiffusion zone in the Mg-9at.%Al vs. Mg-3at.%Zn diffusion couple annealed at 450°C for 4 hours. Open markers denote raw EPMA measurements while solid lines represent the curve fitted profile. Zero flux planes (x_{ZFP}), relative extrema (x_{RE}), and terminal point (x_T) positions are indicated with vertical lines.

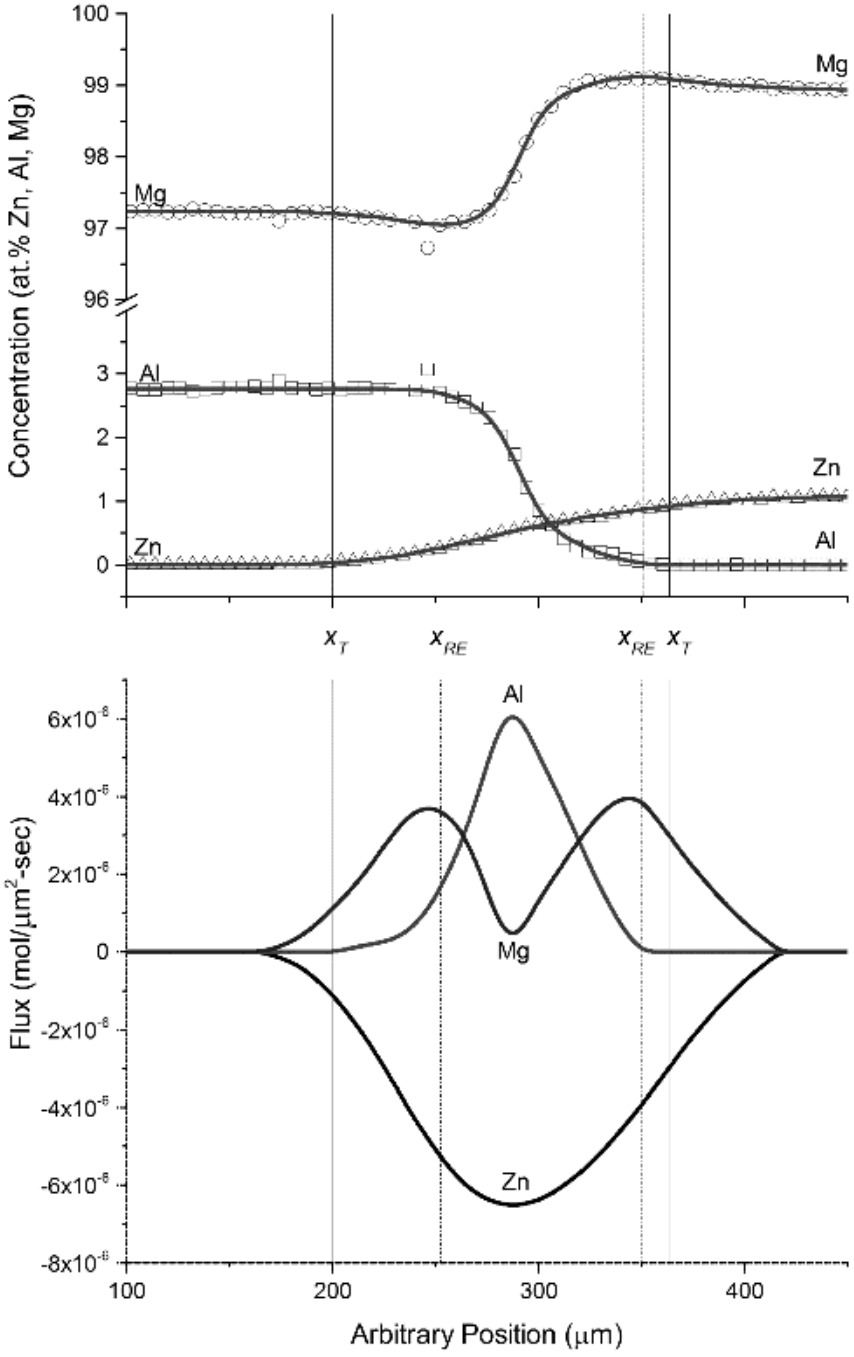

Figure 9: Concentration profile (top) and flux profile (bottom) across interdiffusion zone in the Mg-3at.%Al vs. Mg-1at.%Zn diffusion couple annealed at 450°C for 5 hours. Open markers denote raw EPMA measurements while solid lines represent the curve fitted profile. Relative extrema (x_{RE}) and terminal point (x_T) positions are indicated with vertical lines.

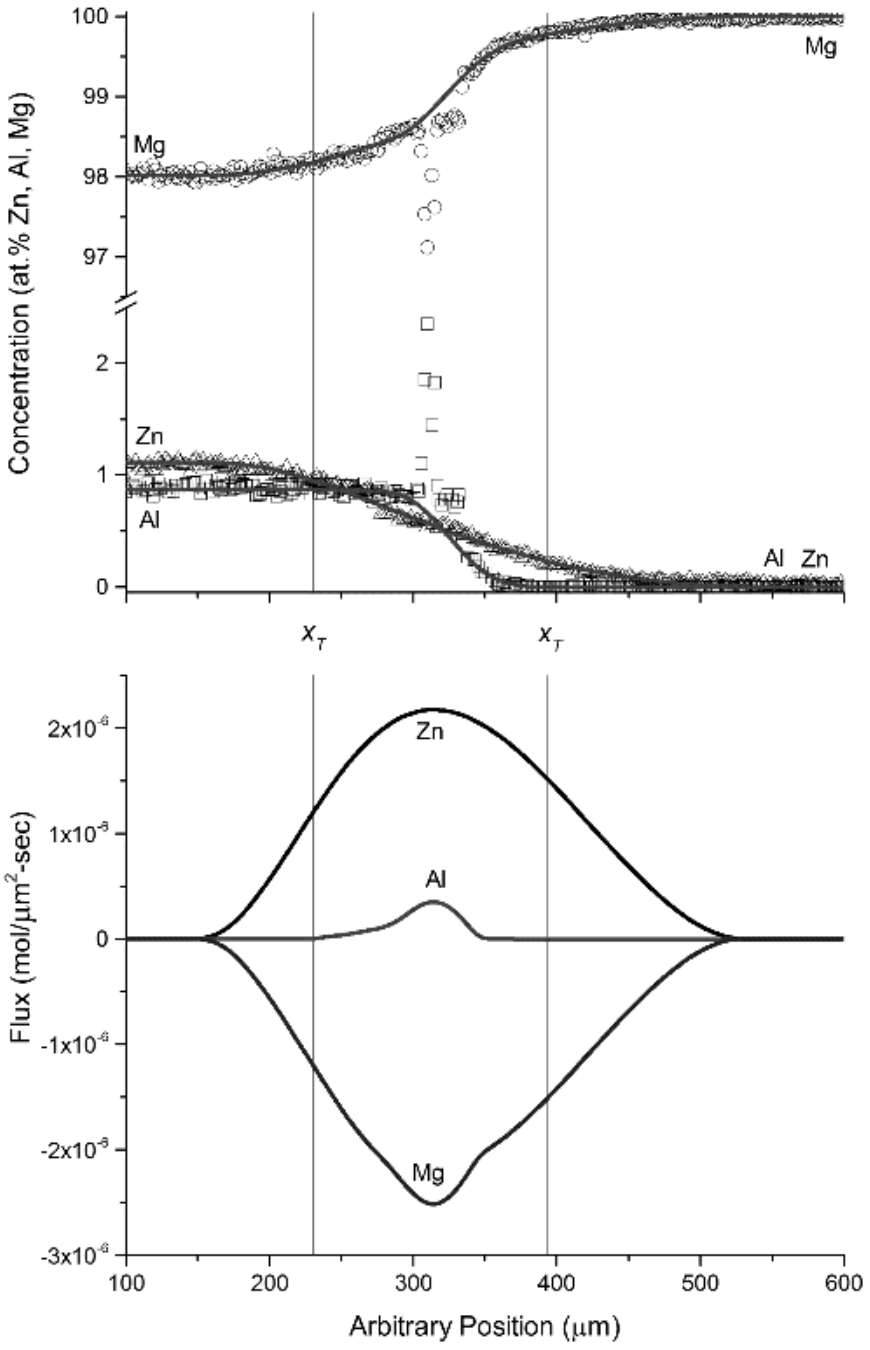

Figure 10: Concentration profile (top) and flux profile (bottom) across interdiffusion zone in the Mg vs. Mg-1at.%Al-1at.%Zn diffusion couple annealed at 400°C for 24 hours. Open markers denote raw EPMA measurements while solid lines represent the curve fitted profile. Terminal point (x_T) positions are indicated with vertical lines.

The diffusion paths determined from the experimental concentration profiles are presented in the Mg-Al-Zn isotherms presented in Figure 11. There are two sets of intersecting diffusion paths at 400°C, and one set at 450°C. At these common intersecting compositions, the four composition-dependent interdiffusion coefficients can be calculated using Equation 12. Unfortunately, the intersection compositions at 400°C were identified where the concentration gradient of one or two components were negligibly small (i.e., large uncertainty), and could not be utilized for determination of four composition-dependent interdiffusion coefficients.

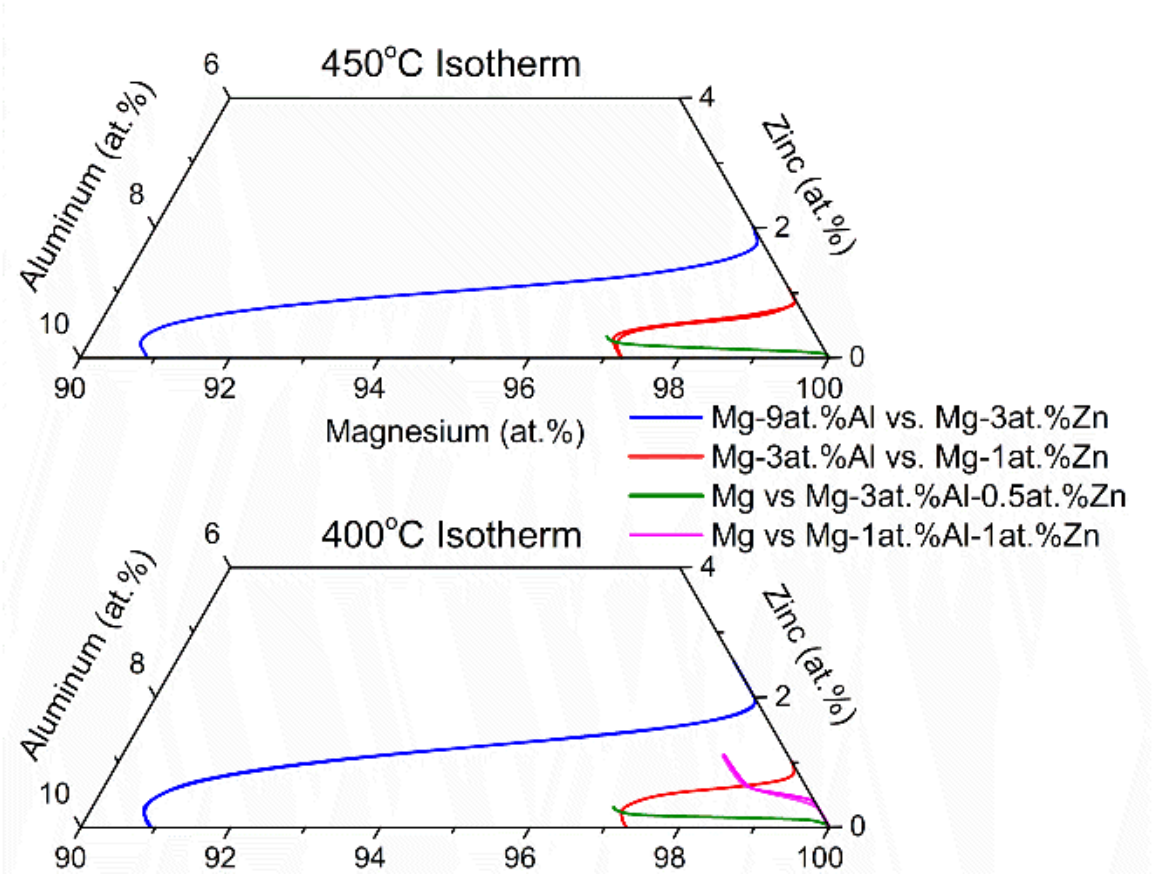

Figure 11: Mg-Al-Zn ternary isotherm at 450°C (top) and 400°C (bottom) with the diffusion paths determined from experimental concentration profiles

Table 7 reports the ternary interdiffusion coefficients calculated at common intersecting compositions and relative extrema in concentrations. Whenever possible, Equation 13 was employed to calculate additional ternary interdiffusion coefficients by changing the dependent component variables. Ratios of interdiffusion coefficients were also determined at ZFP's. In addition, Table 7 reports impurity diffusion coefficients determined in unary and binary compositions from previous studies by Kammerer [88] and Čermák [63]. Based on repeated experiments, ranging from repeated diffusion experiments, multiple EPMA scans, and concentration profile fitting, the uncertainties in the reported magnitude of interdiffusion coefficients are within ±20% for the main and ±50% for the cross ternary interdiffusion coefficients. The ternary interdiffusion coefficients with Mg as dependent concentration variable are presented on ternary Mg-Al-Zn isotherms at 450°C in Figure 12. Since the cross coefficients could not be determined at 400°C, a similar figure is omitted.

Table 7: Ternary main- and cross- interdiffusion coefficients in Mg solid solution of Mg-Al-Zn system at 400°C and 450°C calculated by Boltzmann-Matano analysis (1 = Al, 2 = Zn, 3 = Mg)

	Series / Source	Remarks	C_{Al} (at.%)	C_{Mg} (at.%)	C_{Zn} (at.%)	$\widetilde{D}^3_{ij}$ (x10^{-15} m^2/sec)				$\frac{\widetilde{D}^3_{21}}{\widetilde{D}^3_{22}}$	$\frac{\widetilde{D}^3_{12}}{\widetilde{D}^3_{11}}$	$\widetilde{D}^2_{mn}$ (x10^{-15} m^2/sec)				$\frac{\widetilde{D}^2_{13}}{\widetilde{D}^2_{11}}$	$\frac{\widetilde{D}^2_{31}}{\widetilde{D}^2_{33}}$	$\widetilde{D}^1_{cd}$ (x10^{-15} m^2/sec)				$\frac{\widetilde{D}^1_{23}}{\widetilde{D}^1_{22}}$	$\frac{\widetilde{D}^1_{32}}{\widetilde{D}^1_{22}}$
						$\widetilde{D}^3_{11}$	$\widetilde{D}^3_{12}$	$\widetilde{D}^3_{21}$	$\widetilde{D}^3_{22}$			$\widetilde{D}^2_{11}$	$\widetilde{D}^2_{13}$	$\widetilde{D}^2_{31}$	$\widetilde{D}^2_{33}$			$\widetilde{D}^1_{22}$	$\widetilde{D}^1_{23}$	$\widetilde{D}^1_{32}$	$\widetilde{D}^1_{33}$		
400°C	I	Terminal	9.08	90.83	0.09	—	—	—	38.22	—	—	—	—	—	38.22	—	—	—	—	—	—	—	—
		Terminal	9.06	90.78	0.16	—	—	—	39.75	—	—	—	—	—	39.75	—	—	—	—	—	—	—	—
		Relative	8.99	90.70	0.31	—	—	—	—	—	—	9.97	—	33.02	—	—	—	42.99	—	-33.02	—	—	—
		Relative	8.96	90.72	0.32	—	—	—	—	—	—	16.41	—	31.18	—	—	—	47.60	—	-31.18	—	—	—
		ZFP	8.12	91.19	0.69	—	—	—	—	—	—	—	—	—	—	—	0.75	—	—	—	—	—	-2.98
		ZFP	8.16	91.15	0.69	—	—	—	—	—	—	—	—	—	—	—	0.74	—	—	—	—	—	-2.77
		ZFP	2.77	95.86	1.37	—	—	—	—	—	—	—	—	—	—	—	0.90	—	—	—	—	—	-8.65
		ZFP	2.61	95.99	1.39	—	—	—	—	—	—	—	—	—	—	—	0.89	—	—	—	—	—	-8.32
		Relative	0.06	98.05	1.89	—	—	—	—	—	—	0.40	—	21.25	—	—	—	21.67	—	-21.25	—	—	—
		Relative	0.00	97.92	2.08	—	—	—	18.62	—	—	—	—	—	18.61	—	—	—	—	—	—	—	—
		Terminal	0.00	97.90	2.10	—	—	—	20.17	—	—	—	—	—	20.17	—	—	—	—	—	—	—	—
	II	Terminal	0.00	99.98	0.02	—	—	—	19.48	—	—	—	—	—	19.48	—	—	—	—	—	—	—	—
		Terminal	0.00	99.95	0.05	—	—	—	16.83	—	—	—	—	—	16.83	—	—	—	—	—	—	—	—
		Terminal	2.71	97.22	0.07	—	—	—	6.58	—	—	—	—	—	6.58	—	—	—	—	—	—	—	—
		Terminal	2.73	97.14	0.13	—	—	—	7.74	—	—	—	—	—	7.74	—	—	—	—	—	—	—	—
		Relative	2.72	97.12	0.16	—	—	—	—	—	—	0.50	—	6.59	—	—	—	7.11	—	-6.60	—	—	—
		Relative	2.65	97.10	0.26	—	—	—	—	—	—	1.10	—	4.52	—	—	—	5.63	—	-4.52	—	—	—
		Relative	0.08	99.10	0.82	—	—	—	—	—	—	2.39	—	10.78	—	—	—	13.16	—	-10.78	—	—	—
		Relative	0.04	99.07	0.88	—	—	—	—	—	—	1.87	—	9.80	—	—	—	11.67	—	-9.80	—	—	—
	III	Terminal	2.73	96.98	0.29	—	—	—	6.93	—	—	—	—	—	6.93	—	—	—	—	—	—	—	—
	Ref [63]*	Binary Impurity	0.00	100.0	0.00	—	—	—	18.10	—	—	—	—	—	—	—	—	—	—	—	—	—	—
			6.00	94.00	0.00	—	—	—	32.97	—	—	—	—	—	—	—	—	—	—	—	—	—	—
			8.00	92.00	0.00	—	—	—	40.27	—	—	—	—	—	—	—	—	—	—	—	—	—	—
	Ref [63]#		2.00	98.00	0.00	—	—	—	10.77	—	—	—	—	—	—	—	—	—	—	—	—	—	—
			4.00	96.00	0.00	—	—	—	12.97	—	—	—	—	—	—	—	—	—	—	—	—	—	—
	Ref. [88]		0.00	100.0	0.00	—	—	—	16.0	—	—	—	—	—	—	—	—	—	—	—	—	—	—
			2.70	97.30	0.00	—	—	—	9.11	—	—	—	—	—	—	—	—	—	—	—	—	—	—
			9.10	90.90	0.00	—	—	—	33.5	—	—	—	—	—	—	—	—	—	—	—	—	—	—
			0.00	99.98	0.02	1.71	—	—	—	—	—	—	—	—	—	—	—	—	—	—	—	—	—
			0.00	99.00	1.00	2.92	—	—	—	—	—	—	—	—	—	—	—	—	—	—	—	—	—
			0.00	97.90	2.10	2.06	—	—	—	—	—	—	—	—	—	—	—	—	—	—	—	—	—

	Series / Source	Remarks	C_{Al} (at.%)	C_{Mg} (at.%)	C_{Zn} (at.%)	$\widetilde{D}^3_{ij}$ (x10^{-15} m^2/sec)				$\frac{\widetilde{D}^3_{21}}{\widetilde{D}^3_{22}}$	$\frac{\widetilde{D}^3_{12}}{\widetilde{D}^3_{11}}$	$\widetilde{D}^2_{mn}$ (x10^{-15} m^2/sec)				$\frac{\widetilde{D}^2_{13}}{\widetilde{D}^2_{11}}$	$\frac{\widetilde{D}^2_{31}}{\widetilde{D}^2_{33}}$	$\widetilde{D}^1_{cd}$ (x10^{-15} m^2/sec)				$\frac{\widetilde{D}^1_{23}}{\widetilde{D}^1_{22}}$	$\frac{\widetilde{D}^1_{32}}{\widetilde{D}^1_{22}}$
						$\widetilde{D}^3_{11}$	$\widetilde{D}^3_{12}$	$\widetilde{D}^3_{21}$	$\widetilde{D}^3_{22}$			$\widetilde{D}^2_{11}$	$\widetilde{D}^2_{13}$	$\widetilde{D}^2_{31}$	$\widetilde{D}^2_{33}$			$\widetilde{D}^1_{22}$	$\widetilde{D}^1_{23}$	$\widetilde{D}^1_{32}$	$\widetilde{D}^1_{33}$		
450°C	I	Terminal	9.10	90.78	0.12	—	—	—	145.95	—	—	—	—	—	145.95	—		—	—	—	—	—	—
		Relative	9.04	90.69	0.28	—	—	—	—	—	—	26.66		125.11	—	—		151.77	—	-125.11	—	—	—
		ZFP	8.38	91.06	0.56	—	—	—	—	—	—	—	—	—	—	0.75		—	—	—	—	-3.06	—
		ZFP	1.30	97.33	1.37	—	—	—	—	—	—	—	—	—	—	0.83		—	—	—	—	-4.81	—
		Relative	0.09	98.16	1.74	—	—	—	—	—	—	1.39	—	129.41	—	—		130.81	—	-129.41	—	—	—
		Terminal	0.00	97.99	2.01	—	—	—	80.53	—	—	—	—	—	80.53	—		—	—	—	—	—	—
	II	Terminal	2.77	97.21	0.03	—	—	—	59.70	—	—	—	—	—	59.70	—		—	—	—	—	—	—
		Terminal	2.77	97.13	0.09	—	—	—	81.74	—	—	—	—	—	81.74	—		—	—	—	—	—	—
		Relative	2.69	97.05	0.26	—	—	—	—	—	—	18.43	—	53.76	—	—		72.19	—	-53.76	—	—	—
		Relative	2.72	96.97	0.31	—	—	—	—	—	—	34.18	—	68.83	—	—		103.02	—	-68.83	—	—	—
		ZFP	2.46	97.12	0.42	—	—	—	—	—	—	—	—	—	—	0.77		—	—	—	—	-3.24	—
		ZFP	0.82	98.54	0.65	—	—	—	—	—	—	—	—	—	—	0.85		—	—	—	—	-5.42	—
		Relative	0.04	99.12	0.84	—	—	—	—	—	—	17.73	—	137.38	—	—		154.65	—	-136.98	—	—	—
		Relative	0.02	99.11	0.87	—	—	—	—	—	—	1.74	—	92.25	—	—		93.99	—	-92.25	—	—	—
		Terminal	0.00	99.08	0.92	—	—	—	70.14	—	—	—	—	—	70.14	—		—	—	—	—	—	—
	III	Terminal	2.80	96.90	0.30	—	—	—	92.49	—	—	—	—	—	92.49	—		—	—	—	—	—	—
	II x III	Intersect	2.71	97.05	0.24	14.21	-9.11	-3.13	72.18	-0.64	-0.04	23.32	9.11	52.65	63.73	0.39	0.83	75.98	3.13	-52.65	11.08	0.04	-4.75
		Intersect	2.75	97.00	0.25	20.84	-11.81	-10.52	95.92	-0.57	-0.11	32.65	11.81	73.79	84.11	0.36	0.88	106.44	10.52	-73.79	10.32	0.10	-7.15
	Ref. [63]*	Binary Impurity	0.00	100.0	0.00	—	—	—	85.67	—	—	—	—	—	—	—		—	—	—	—	—	—
			2.00	98.00	0.00	—	—	—	104.64	—	—	—	—	—	—	—		—	—	—	—	—	—
	Ref. [63]#		3.00	97.00	0.00	—	—	—	57.41	—	—	—	—	—	—	—		—	—	—	—	—	—
			8.00	92.00	0.00	—	—	—	91.40	—	—	—	—	—	—	—		—	—	—	—	—	—
	Ref. [88]		0.00	100.0	0.00	6.11	—	—	66.40	—	—	—	—	—	—	—		—	—	—	—	—	—
			2.80	97.20	0.00	—	—	—	58.00	—	—	—	—	—	—	—		—	—	—	—	—	—
			8.10	91.90	0.00	—	—	—	149.00	—	—	—	—	—	—	—		—	—	—	—	—	—
			0.00	99.00	1.00	26.90	—	—	—	—	—	—	—	—	—	—		—	—	—	—	—	—
			0.00	98.00	2.00	55.60	—	—	—	—	—	—	—	—	—	—		—	—	—	—	—	—

* Nominal value of Equation 21

\# Minimum value of Equation 21

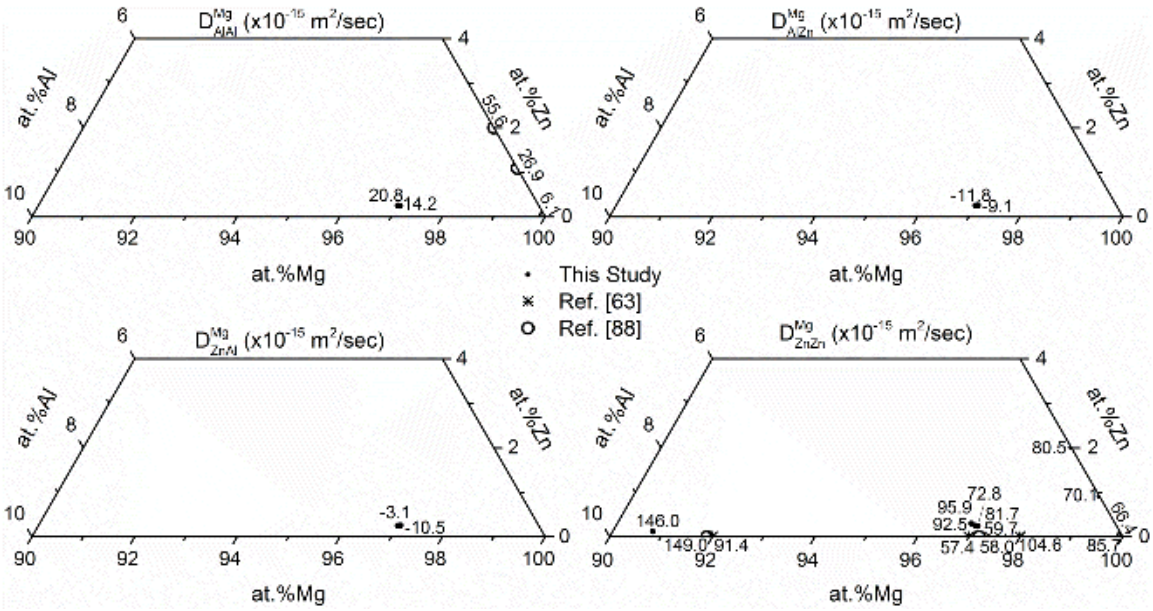

Figure 12: Mg-dependent ternary interdiffusion coefficients at 450°C are presented on Mg-Al-Zn ternary isotherms. Binary impurity [63, 88] data is included with the main coefficients

5.4 Discussion

The diffusion path plotted on a ternary isotherm can provide qualitative insight into the diffusional behavior of the individual components [98]. The diffusion path for a ternary single-phase diffusion couple is generally characterized as serpentine in shape based on mass balance requirement. For all diffusion couples in this study, the terminal-ends of the diffusion paths were observed to be along a constant concentration of the slowest diffusing species, i.e., Al. From Figure 11, as the diffusion paths approach their terminal compositions, the serpentine curve is collinear with a fixed Al concentration. Similarly, near the terminal compositions, the path is nearly parallel to the Zn axis, indicating Zn is the

fastest species. Quantitative results presented in Table 7 and Figure 12 clearly demonstrate that $\tilde{D}^{Mg}_{ZnZn}$ is greater than $\tilde{D}^{Mg}_{AlAl}$, and $\tilde{D}^{Al}_{ZnZn}$ is great than $\tilde{D}^{Al}_{MgMg}$.

The Zn, as the fast diffusing species, also has a significant influence on the interdiffusion of both Al and Mg. Table 7 and Figure 12 report that the cross interdiffusion coefficients, $\tilde{D}^{Mg}_{AlZn}$ are negative and appreciable in magnitude, in comparison to the magnitude of main interdiffusion coefficients $\tilde{D}^{Mg}_{AlAl}$. The influence of Zn interdiffusion on Mg is also signified by negative $\tilde{D}^{Al}_{MgZn}$ coefficients with magnitude *much* larger than $\tilde{D}^{Al}_{MgMg}$ as reported in Table 7, i.e., large negative ratios of $\tilde{D}^{Al}_{MgZn}/\tilde{D}^{Al}_{MgMg}$. These results imply that the Zn may reduce the thermodynamic activities of both Al and Mg, and can significantly influence the interdiffusion of both Al and Mg. Figure 9 for example shows that the overall interdiffusion flux of Mg is positive against the interdiffusion flux of Zn in the negative direction.

The slow diffusing Al had an appreciable influence on the Mg interdiffusion, but did not significantly influence the Zn interdiffusion based on ternary interdiffusion coefficients reported in Table 7. The $\tilde{D}^{Zn}_{MgAl}$ coefficients were positive and significant in magnitude, yielding appreciable $\tilde{D}^{Zn}_{MgAl}/\tilde{D}^{Zn}_{MgMg}$ ratios. The $\tilde{D}^{Mg}_{ZnAl}$ cross interdiffusion coefficients were negative, but much smaller than the $\tilde{D}^{Mg}_{ZnZn}$ coefficients in magnitude. Correspondingly, the ratios $\tilde{D}^{Mg}_{ZnAl}/\tilde{D}^{Mg}_{ZnZn}$ were negative but very small.

Table 7 also reports that Mg had an influence on the Al interdiffusion, but not on the Zn interdiffusion. The $\tilde{D}^{Zn}_{AlMg}$ cross interdiffusion coefficients were positive and had

appreciable magnitude comparable to $\widetilde{D}_{AlAl}^{Zn}$, i.e., $\widetilde{D}_{AlMg}^{Zn} \Big/ \widetilde{D}_{AlAl}^{Zn} \approx 0.35 \sim 0.40$. On the contrary, positive $\tilde{D}_{ZnMg}^{Al}$ coefficients were an order of magnitude smaller than the $\tilde{D}_{ZnZn}^{Al}$ coefficients.

5.5 Summary

Solid-to-solid diffusion couple experiments were carried out to determine the composition-dependent ternary interdiffusion coefficients and examine the diffusional interactions of Al and Zn in ternary Mg solid-solution at 400° and 450°C. Concentration profiles of Mg-Al-Zn ternary alloys were determined by electron probe microanalysis, and analyzed using Kirkaldy's extension of Fick's law based on Onsager's formalism. Findings from this investigation were:

- Magnitude of $\widetilde{D}_{ZnZn}^{Mg}$ ternary interdiffusion coefficients was greater than that of $\tilde{D}_{AlAl}^{Mg}$. Magnitude of $\tilde{D}_{ZnZn}^{Al}$ ternary interdiffusion coefficients was greater than that of $\tilde{D}_{MgMg}^{Al}$. Finally, magnitude of $\tilde{D}_{MgMg}^{Zn}$ was greater than that of $\tilde{D}_{AlAl}^{Zn}$. Based on these results, Zn is determined to interdiffuse the fastest, followed by Mg, then Al, in hcp-Mg solid solution.
- Zn was observed to have a significant influence on the interdiffusion of Mg, signified by the large magnitude of $\tilde{D}_{MgZn}^{Al}$ coefficients. Zn also had an influence of the interdiffusion of Al, signified by appreciable magnitude of $\tilde{D}_{AlZn}^{Mg}$ coefficients. Both $\tilde{D}_{MgZn}^{Al}$ and $\tilde{D}_{AlZn}^{Mg}$ coefficients were negative.

- Al was found to have an appreciable influence on the Mg interdiffusion, but not on the Zn interdiffusion. The $\tilde{D}^{Zn}_{MgAl}$ coefficients were positive. Mg was observed to have an influence on the Al interdiffusion, but not on the Zn interdiffusion. The $\tilde{D}^{Zn}_{AlMg}$ coefficients were positive.

CHAPTER 6: DIFFUSION KINETICS AND CRYSTALLOGRAPHIC CHARACTERIZATION OF INTERMETALLIC COMPOUNDS IN THE MAGNESIUM-ZINC BINARY SYSTEM

6.1 Background

Zn is one of the two most common alloying elements in Mg. As shown in the phase diagram in Figure 13 [99], there are five intermetallic compounds in the Mg-Zn system – $Mg_{51}Zn_{20}$, $Mg_{21}Zn_{25}$, Mg_4Zn_7, $MgZn_2$, and Mg_2Zn_{11}. The $Mg_{51}Zn_{20}$ phase is not stable at room temperature. While $Mg_{21}Zn_{25}$ is the equilibrium intermetallic with Mg solid-solution (α-Mg), formation of Guinier-Preston (GP) zones and metastable precipitates of $MgZn_2$ and Mg_4Zn_7 take place during artificial aging in commercial Mg alloys containing Zn [17, 100]. There is considerable debate on the exact stoichiometry and solubility limits of the intermediate phases in the Mg-Zn system. Similarly, there is uncertainty in the specific details of the crystal structure of the Mg-Zn intermetallic compounds. In recent years, investigation into the stoichiometry and crystal structure of the phases has been conducted [99, 101-103]. In fact, the phase diagram given in Figure 13 is based on the 2012 work of Ghosh *et al*. [101] in which all available experimental and computational data for thermodynamic properties and phase boundaries of the Mg-Zn system were modeled. Nonetheless, little corroborating data is available to resolve the precise stoichiometry, extent of homogeneity, and crystal structure of the room-temperature equilibrium intermetallic phases.

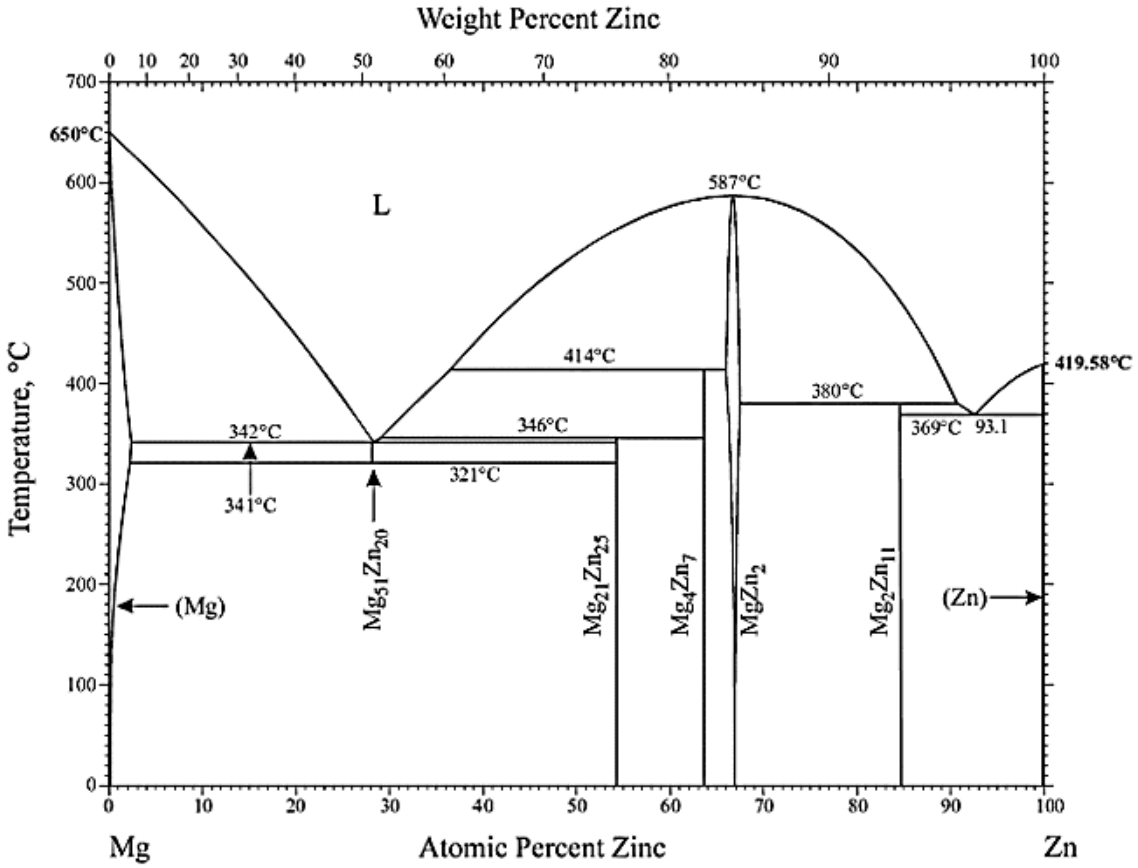

Figure 13: Mg-Zn phase diagram taken from the 2013 review by Okamoto [99] and based on the work of Ghosh *et al*. [101]

The first interdiffusion study of the Mg-Zn system was conducted by Sakakura and Sugino [104] via polycrystalline solid-to-solid diffusion couples annealed between 200°C and 300°C. They observed only the $MgZn_2$ and Mg_2Zn_{11} phases and calculated interdiffusion coefficients and parabolic growth constants. More recently, Brennan *et al*. [35] determined the parabolic growth constants for phases evolved during diffusion anneals between 295°C and 325°C of polycrystalline couples of pure Mg and Zn. Only four of the five phases were reported; as expected, $Mg_{51}Zn_{20}$ was observed in only the couple

annealed at 325°C, but $Mg_{21}Zn_{25}$ was not observed in any couple. In the most comprehensive diffusion study to date, Das *et al*. [82] examined the anisotropic diffusion behavior in the Mg-Zn system. Couples of single crystal Mg and polycrystalline Zn were annealed at 280°C to 330°C. All intermediate phases were observed, thicknesses measured, and parabolic growth constants computed. Interdiffusion coefficients for Mg_4Zn_7 (reported in [82] as Mg_2Zn_3), $MgZn_2$ and Mg_2Zn_{11} were experimentally determined while those for $Mg_{21}Zn_{25}$ (reported in [82] as $Mg_{12}Zn_{13}$) and $Mg_{51}Zn_{20}$ were calculated from a multiphase diffusion model. Most recently Mostafa and Medraj [90] annealed solid-to-solid Mg-Zn diffusion couples between 250°C and 300°C. They observed and measured the thickness of all phases indicated by the phase diagram for the studied temperature range. Still, there is limited data which can be used to offer consensus on the kinetic behavior in the intermetallic phases.

The objective of this study was to examine the structure and kinetic properties of the equilibrium phases in the technologically relevant Mg-Zn system.

6.2 Experimental Parameters

In this study, a solid-to-solid diffusion couple consisting of pure Mg diffusion bonded to pure Zn at 315°C for 168 hours was assembled. Resulting phases were subjected to Electron Probe Micro Analysis (EPMA), and Selected Area Electron Diffraction (SAED) via Transmission Electron Microscopy (TEM). Crystallographic characteristics for $Mg_{21}Zn_{25}$, Mg_4Zn_7, and Mg_2Zn_{11} are examined and reported. Parabolic growth constants and interdiffusion coefficients for the phases are computed, as described in §3.1, and compared

to literature values. Composition dependent interdiffusion coefficients were determined by both the Boltzmann-Matano Method and the Sauer-Freise Method as described in §3.2 and §3.3, respectively.

6.3 Phase Constituents and Crystallography

A backscattered electron micrograph of the diffusion reaction products from the Mg vs. Zn couple annealed at 315°C for 168 hours is presented in Figure 14. All room-temperature equilibrium compounds are present. A natural marker plane from oxidation is observed within the Mg_2Zn_{11} phase [35, 90]; as a consequence this phase was more susceptible to cracking and pull out during subsequent processing. In addition, there is a slight contrast in the Mg_2Zn_{11} phase on either side of the marker plane.

The composition across the diffusion reaction zone was determined via EPMA, and the concentration profiles were curve fit for each phase. Figure 15 presents the EPMA data along with the fitted concentration profile. The scatter within the Mg_2Zn_{11} phase is assumed to be due to pull-out at the marker plane during polishing. Mg_4Zn_7, $MgZn_2$, and Mg_2Zn_{11} are all present with definite concentration gradients $\partial C/\partial x \neq 0$. With the exception for Mg solid solution, the concentration profiles for each phase were best fit with a simple linear least squares regression. The Zn concentration in Mg was fit with an exponential function. There was no apparent solubility of Mg in Zn therefore the concentration profile was not fit for this phase.

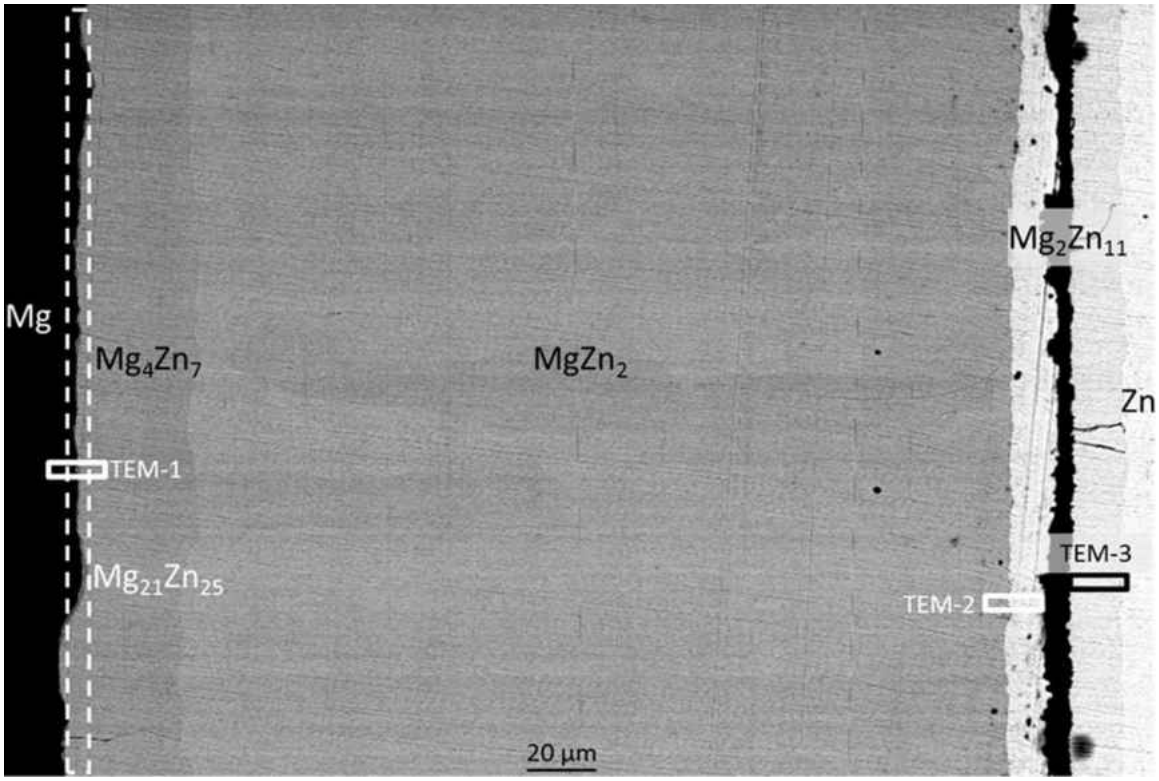

Figure 14: Backscattered electron micrograph in the interdiffusion zone from the diffusion couple Mg vs. Zn annealed at 315°C for 168 hours: phases and approximate location of TEM specimens are annotated

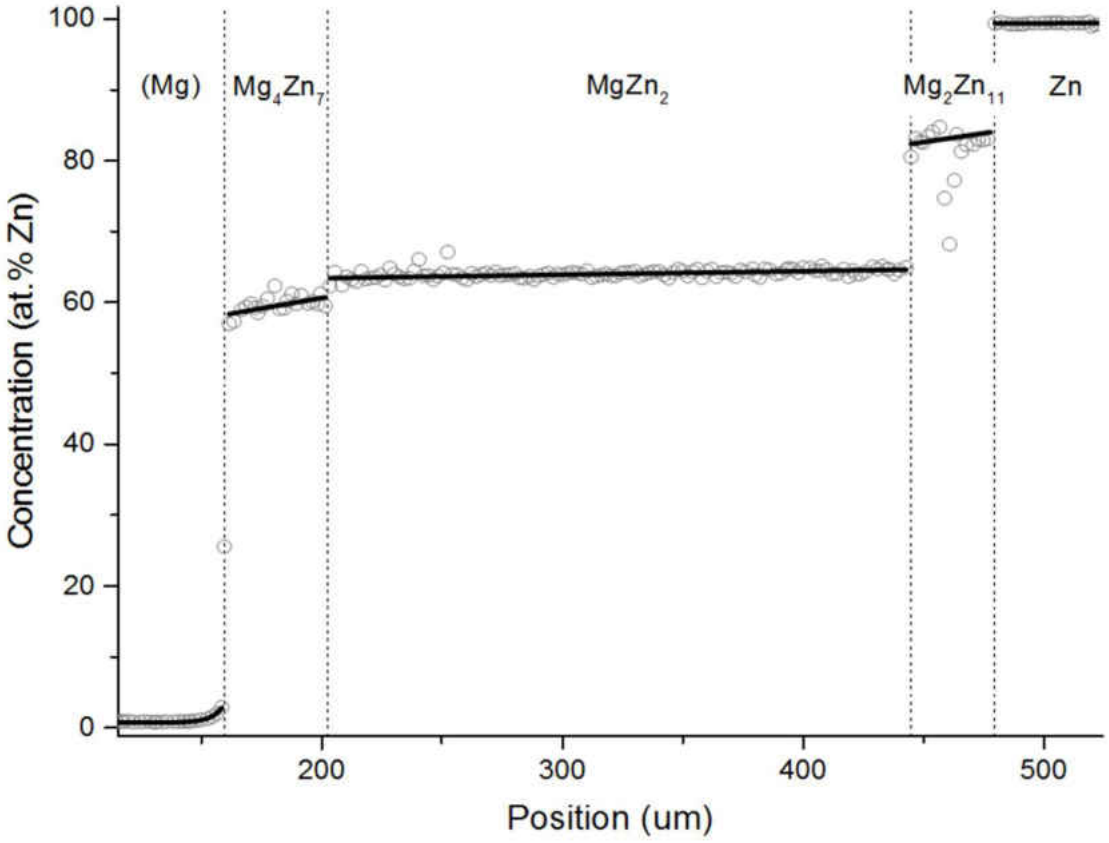

Figure 15: Concentration profile across the interdiffusion zone from the diffusion couple Mg vs. Zn annealed at 315°C for 168 hours. Open symbols are from the measured EPMA data and solid line is the fitted profile. The large scatter in the Mg_2Zn_{11} phase is an artifact caused by the crack at the marker plane.

From EPMA line scans shown in Figure 15, the line compounds, Mg_4Zn_7 and Mg_2Zn_{11}, have a homogeneity range of 2.4 at.%Zn and 1.6 at.%Zn, respectively. The absolute composition for each phase presents with slightly lower Zn concentration than stoichiometry would suggest. EPMA can precisely determine concentration gradient which is essential for diffusion and relative concentration studies, but the technique can have

increased error in the absolute concentration; EPMA is precise to the ppm level but only accurate within ~2% [105].

To examine the crystal structure of the intermetallic compounds, three samples were extracted from the interdiffusion zone for TEM. The locations of the extracted specimens are annotated in Figure 14 as TEM-1, TEM-2, and TEM-3. A bright field micrograph from TEM-1 specimen, shown in Figure 16a, reveals the α-Mg, $Mg_{21}Zn_{25}$, and Mg_4Zn_7 phases. A bright field micrograph from TEM-3 showing Mg_2Zn_{11} phase is presented in Figure 16b. TEM-3 with Mg_2Zn_{11} was indistinguishable from TEM-2 other under bright field imaging and is therefore not presented.

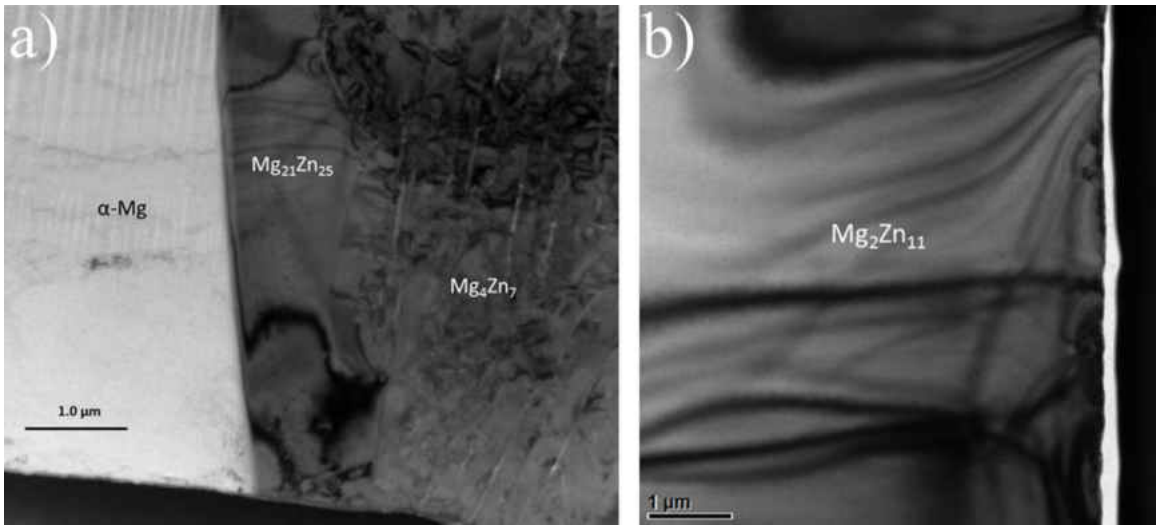

Figure 16: Bright field micrographs: a) TEM-1 showing the α-Mg, $Mg_{21}Zn_{25}$, and Mg_4Zn_7 phases; b) TEM-3 specimens showing Mg_2Zn_{11} phase

The intermetallic compound in equilibrium with Mg solid-solution is $Mg_{21}Zn_{25}$; it has also been described as $Mg_{12}Zn_{13}$ or the equiatomic MgZn despite the composition being Zn rich. Casting further doubt on the exact stoichiometry of this phase is the fact that the

crystal structure of MgZn or $Mg_{12}Zn_{13}$ has not been decidedly reported [17, 99, 106, 107]. Tilting series SAED patterns were obtained for $Mg_{21}Zn_{25}$ from TEM-1, four of which are shown in Figure 17. From the SAED study, the $Mg_{21}Zn_{25}$ was found to have a trigonal symmetry (space group *R3ch*) with lattice parameters of a = 2.5518 nm and c = 0.8713 nm. In 2002, Cerńy and Renaudin [102] identified, using single crystal XRD, a Mg-Zn compound that is isomorphous with $Zr_{21}Re_{25}$. From their work, it was shown $Mg_{21}Zn_{25}$ nucleates and grows in a trigonal structure with 6 formula units per unit cell and lattice parameters of a = 2.5776 nm and c = 0.8762 nm. In another study, the $Mg_{21}Zn_{25}$ phase, formed during mechanical alloying and annealing of pure Mg, Zn and Si powders, was characterized by De Negri *et al*. [108] via powder XRD. The crystal structure was likewise identified as trigonal with cell parameters of a = 2.5640 nm and c = 0.8714 nm. The results obtained in this study by electron diffraction for $Mg_{21}Zn_{25}$, summarized in Table 8, agree well with those determined by XRD [102, 108] and validate the stoichiometry of $Mg_{21}Zn_{25}$.

Similarly, Mg_4Zn_7 had generally been accepted as Mg_2Zn_3 as originally reported by Takei [109], Laves [110], and later Clark and Rhines [111]. The crystal structure of Mg_2Zn_3 was thought to be triclinic (a = 1.724 nm, b = 1.445 nm, c = 0.520 nm, α = 96°, β = 89°, γ = 138°) [17]. In 1975, Yarmolyuk *et al*. [103] determined the crystal structure and ideal stoichiometry of the intermetallic phase as having monoclinic symmetry with cell parameters of a = 2.596 nm, b = 0.524 nm, c = 1.428 nm, and β = 102.5° and 10 formula units per unit cell; stoichiometry was identified as Mg_4Zn_7. Nonetheless, consensus on the crystal structure and stoichiometry of Mg_4Zn_7 has remained unresolved [99, 112]. In the present study, tilting series SAED patterns were obtained for Mg_4Zn_7 as shown in Figure 18.

A monoclinic structure (space group *B2/m*) with lattice parameters *a* = 2.669 nm, *b* = 0.511 nm, *c* = 1.411 nm, and β = 101.85° were determined. These results are in good agreement with those of Yarmolyuk *et al*. [103].

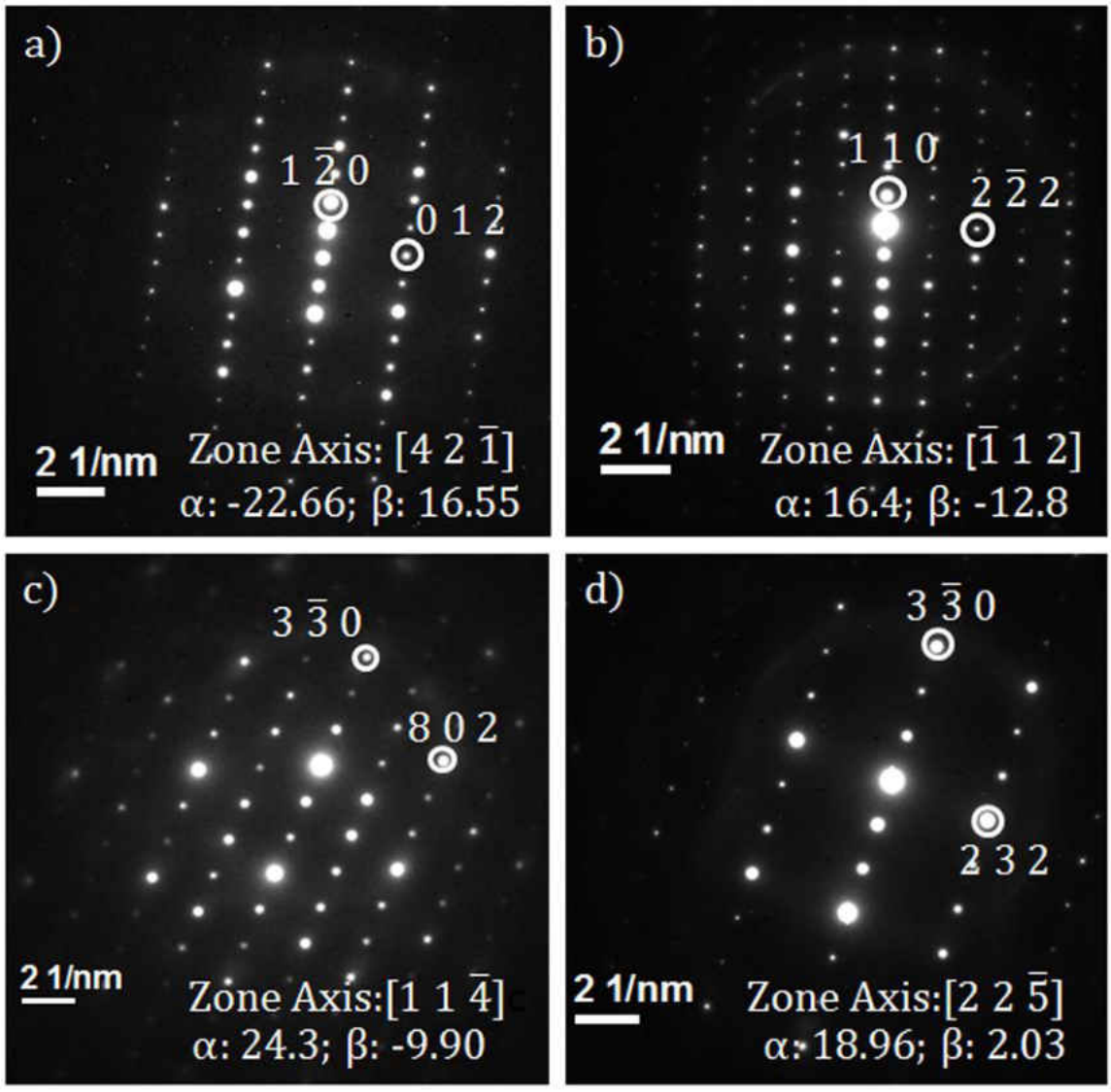

Figure 17: Tilting series SAED patterns from the $Mg_{21}Zn_{25}$ phase in TEM-1 indicating the trigonal symmetry (space group $R\bar{3}ch$) and lattice parameters of *a* = 2.5518 nm and *c* = 0.8713 nm: zone axis a) [42 $\bar{1}$]; b) [$\bar{1}$ 12]; c) [11 $\bar{4}$]; d) [22 $\bar{5}$]

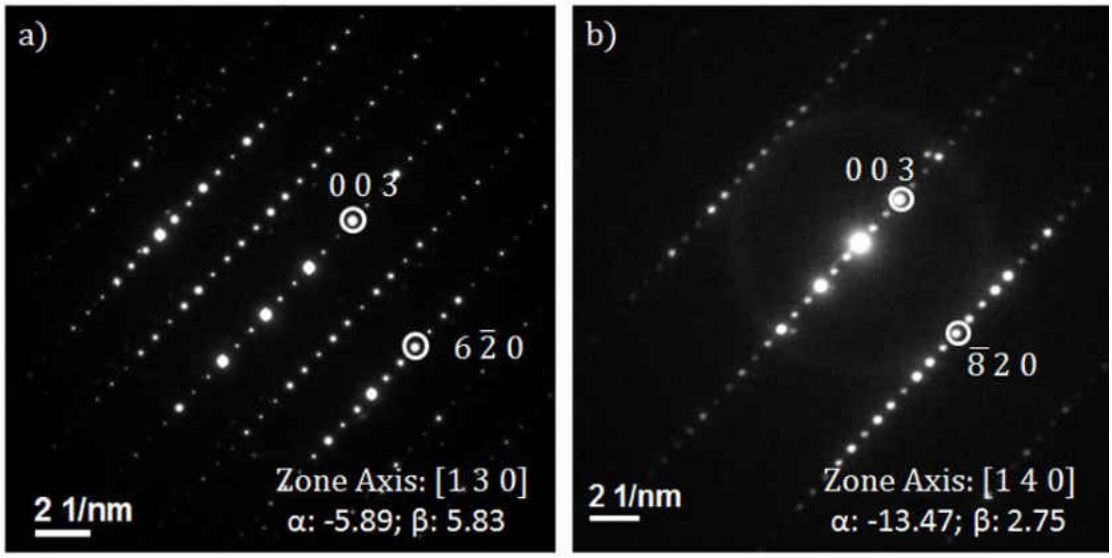

Figure 18: SAED patterns for Mg_4Zn_7 from TEM-1 indicates a monoclinic structure (space group *B2/m*) with lattice parameters of *a* = 2.669 nm, *b* = 0.511 nm, *c* = 1.411 nm, and β = 101.85°: zone axis a) [130] and b) [140]

Mg_2Zn_{11} has been cited as a line compound with cubic symmetry and *a* = 0.8552 nm [99, 113]. To study influence of concentration on lattice parameter in Mg_2Zn_{11}, SAED patterns from TEM-2 and TEM-3 specimens, presented in Figure 19, were analyzed. Both specimens exhibit a cubic structure (space group *Pm3*) with slightly different lattice parameters *a* = 0.8462 nm (TEM-2) and *a* =0.8415 nm (TEM-3). A smaller lattice parameter is observed for Mg_2Zn_{11} near the Zn side. The molar volume of Mg is 13.99 cm^3/mol while the molar volume of Zn is 9.15 cm^3/mol. Thus, consistent with Vegard's law [114], an increase in Zn content would decrease the molar volume of the phase and hence the lattice parameter. This finding is consistent with the homogeneity range determined by EPMA. The results of SAED and EPMA strongly suggest that the Mg_2Zn_{11} has a range of solubility with a corresponding variation in lattice parameter.

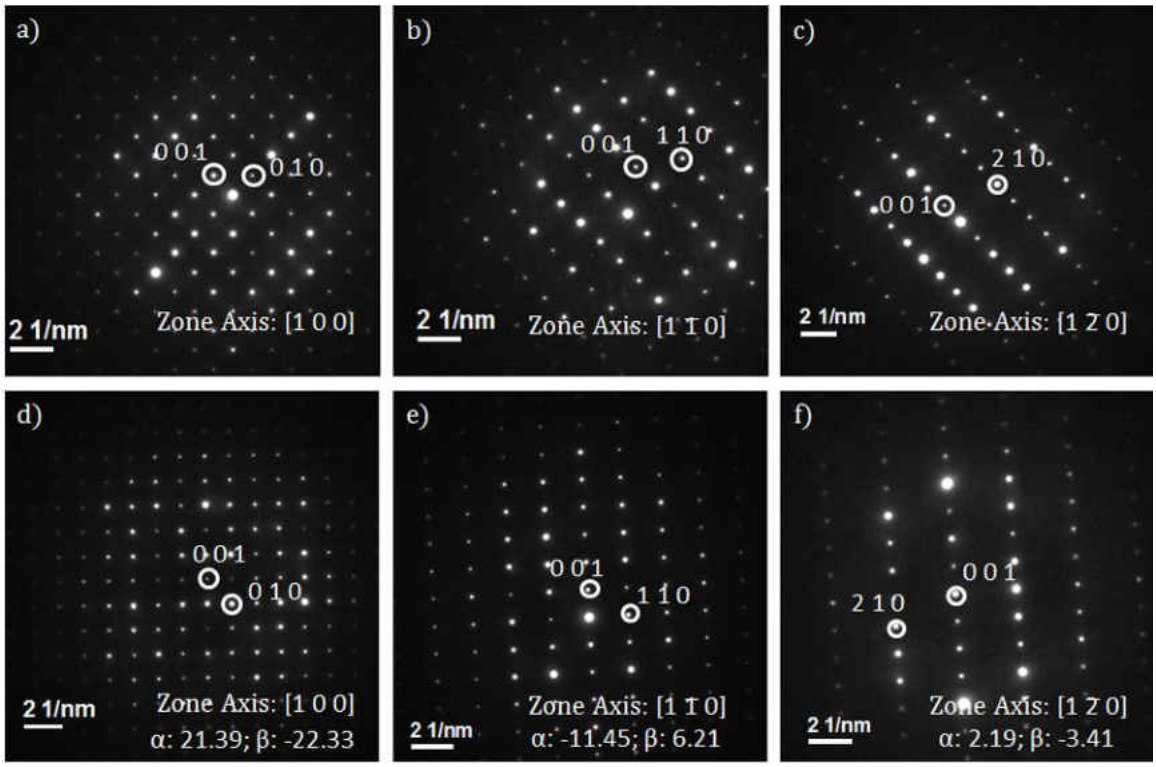

Figure 19: SAED patterns for Mg_2Zn_{11} from TEM-2 (top row: a - c) and TEM-3 (bottom row: d - f) reveal a cubic structure (space group *Pm3*) with a variation in lattice parameters a = 0.8462 nm (TEM-2) and a =0.8415 nm (TEM-3): zone axis a) [100], b) [1 $\bar{1}$ 0], c) [1 $\bar{2}$ 0], d) [100], e) [1 $\bar{1}$ 0], f) [1 $\bar{2}$ 0]

The crystal structure of $MgZn_2$ is well established as the prototypical C14 Laves Phase [110, 115, 116]. Therefore, no TEM was carried out. Table 8 provides a summary of the crystallographic parameters determined in this study along with that for $MgZn_2$ from PDF#04-003-2083 [116].

Table 8: Experimentally determined room-temperature equilibrium phase crystallographic parameters for intermetallic compounds in Mg-Zn system

	Structure	***a*** **(nm)**	***b*** **(nm)**	***c*** **(nm)**	***α***	***β***	***γ***	**Formula Units**	**Molar Volume (cm^3/mol)**
$Mg_{21}Zn_{25}$	trigonal	2.564		0.8714	90°		120°	6	10.74
Mg_4Zn_7	monoclinic	2.669	0.511	1.411	90°	101.85°	90°	10	10.31
***$MgZn_2$**	C14 Laves	0.5223		0.8566	90°		120°	4	10.15
Mg_2Zn_{11}	cubic	0.8462 – 0.8415			90°			3	9.20 – 9.35

*$MgZn_2$ data taken from PDF#04-003-2083 [116]

6.4 Diffusion Kinetics Characteristics

The concentration dependent interdiffusion coefficient was calculated by applying both the Boltzmann-Matano approach, Equation 6, and the Sauer-Freise approach, Equation 7, using the molar volumes estimated from the lattice parameters determined by TEM. The results of the two analytical approaches are compared in Figure 20. The observed molar volume variation of Mg_2Zn_{11} has negligible influence on the computed interdiffusion coefficients as demonstrated in Figure 20. In addition to the congruency of results obtained, an examination of Figure 20 reveals that there is no appreciable concentration dependence on the interdiffusion coefficients for Mg_4Zn_7 and $MgZn_2$, while there is a slight concentration dependence in Mg_2Zn_{11}.

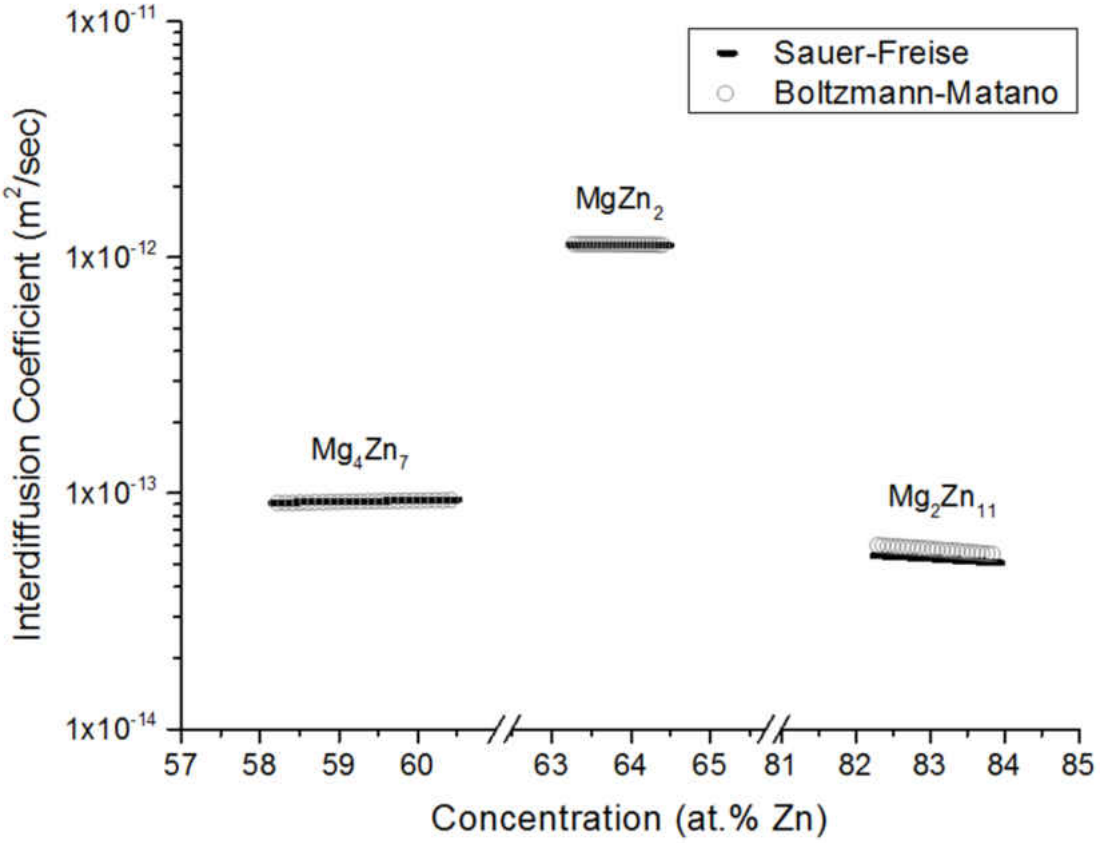

Figure 20: Interdiffusion coefficients determined using Sauer-Freise and Boltzmann-Matano methodologies and plotted as a function of composition

The thickness of each phase was measured as previously described. The phase-specific growth constant, k_p, was calculated using Equation 1, and reported in Table 9. $MgZn_2$ phase grew the thickest while $Mg_{21}Zn_{25}$ did not form a layer of substantial thickness. Mg_4Zn_7 was thicker than Mg_2Zn_{11}. The integrated interdiffusion coefficient for $Mg_{21}Zn_{25}$ was determined using Equation 2, while the integrated interdiffusion coefficient for Mg_4Zn_7, $MgZn_2$, and Mg_2Zn_{11} were calculated by using Equation 3. The effective interdiffusion coefficients was calculated using Equation 8, where the flux was determined

using the Boltzmann-Matano approach. The interdiffusion coefficients are reported in Table 9 as well. Interdiffusion in $MgZn_2$ is orders of magnitude faster than in the other intermetallic phases. $Mg_{21}Zn_{25}$ has the lowest interdiffusion coefficient.

Table 9: Thickness, parabolic growth constant, integrated interdiffusion coefficients, and average effective interdiffusion coefficients of intermetallic phases in Mg-Zn system

	$Mg_{21}Zn_{25}$	**Mg_4Zn_7**	**$MgZn_2$**	**Mg_2Zn_{11}**	**Source**
Thickness (μm)	0.94 (±0.32)	33.7 (±3.3)	237.0 (±2.4)	30.8 (±1.7)	This Study
k_p **(m^2/s)**	1.6×10^{-18}	1.9×10^{-15}	9.3×10^{-14}	1.6×10^{-15}	This Study
k_p **(m^2/s)**	--	1.1×10^{-15}	4.9×10^{-14}	1.2×10^{-15}	[35]
k_p **(m^2/s)** ***a*-axis** ***c*-axis**	7.24×10^{-19} 3.27×10^{-18}	2.21×10^{-15} 2.36×10^{-15}	6.17×10^{-14} 9.21×10^{-14}	2.12×10^{-15} 2.35×10^{-15}	[82]
$\widetilde{D}^{\text{int}}$ **(m^2/sec)**	4.74×10^{-17}	2.31×10^{-15}	1.53×10^{-14}	9.97×10^{-16}	This Study
$\widetilde{D}^{eff}$ **(m^2/sec)**	--	9.76×10^{-14}	1.13×10^{-12}	6.02×10^{-14}	This Study
$\overline{\widetilde{D}}^{eff}$ ***a*-axis** **(m^2/sec)** ***c*-axis**	8.13×10^{-15} 7.72×10^{-15}	1.19×10^{-13} 1.12×10^{-13}	5.07×10^{-13} 4.83×10^{-13}	4.70×10^{-14} 4.66×10^{-14}	[82]
$\widetilde{D}^{eff}$ **(m^2/sec)**	--	1.44×10^{-14}	2.87×10^{-13}	2.55×10^{-13}	[104]

With due consideration for other researchers, Table 9 also presents comparative data for growth and interdiffusion at 315°C. Nominal pre-exponential factor and activation energy were used to compute average interdiffusion coefficients, $\overline{\widetilde{D}}$. Mostafa [90] computed interdiffusion coefficient of each interphase boundary (i.e. $Mg/Mg_{21}Zn_{25}$, $Mg_{21}Zn_{25}/Mg_4Zn_7$, $Mg_4Zn_7/MgZn_2$, $MgZn_2/Mg_2Zn_{11}$, and Mg_2Zn_{11}/Zn) as a fixed-frame of reference, and therefore they are not comparable to the present work, and have been

omitted from Table 9. There is good agreement in the parabolic growth constants determined by Brennan [35] and Das [92] with those calculated in this study. On the other hand, there is some difference on the interdiffusion coefficients determined in this study. Disagreement in the interdiffusion coefficients can be attributed to the different analytical formulae employed. Das used the Heumann-Matano method and Sakakura exercised the Boltzmann-Matano method; both calculate the "numerical average value" of the measured interdiffusion coefficients over a composition range, $\widetilde{\overline{D}}$, which is comparable but not equivalent to the effective interdiffusion coefficient, determined in this study.

6.5 Summary

Pure Mg was diffusion bonded to pure Zn in order to nucleate and grow equilibrium intermetallic compounds; all room-temperature equilibrium phases formed during diffusion anneal. Analytical techniques yielded concentration profiles and electron diffraction patterns which were used to characterize the phase constituents, crystallography, and diffusion kinetics of the intermetallic compounds.

The phase in equilibrium with Mg solid solution was found to be $Mg_{21}Zn_{25}$ with a trigonal structure and lattice parameters, a = 2.5518 nm and c = 0.8713 nm. The crystal symmetry and lattice parameters established in this study agreed well with those determined by the recent XRD studies and validated the stoichiometry of the phase. Mg_4Zn_7 was found to have monoclinic symmetry with structural lattice parameters of a = 2.669 nm, b = 0.511 nm, c = 1.411 nm, and β = 101.85°, consistent with the structure and symmetry of the Mg_4Zn_7 reported in literature. This study found Mg_4Zn_7 to have a 2.4 at.%Zn range of

solubility rather than being a fixed line compound as indicated on the most recent phase diagram. This study also found that the Mg_2Zn_{11} phase has a 1.6 at.%Zn range of solubility with a corresponding variation in cubic lattice parameter (0.8415 ~ 0.8462 nm).

Kinetic properties were examined through Boltzmann-Matano and Sauer-Freise methods. The observed variation in molar volume did not influence the magnitude of interdiffusion coefficients determined for the Mg-Zn system. Interdiffusion and growth rates followed the same trend; $MgZn_2$ (k_p = 9.3x10^{-14}) was greatest while Mg_4Zn_7 (k_p = 1.9x10^{-15}) and Mg_2Zn_{11} (k_p = 1.6x10^{-15}) were an order of magnitude smaller, and $Mg_{21}Zn_{25}$ (k_p = 1.6x10^{-18}) was substantially less than all other equilibrium phases. The interdiffusion coefficients within each intermetallic phase did not vary significantly as a function of composition.

CHAPTER 7: PHASE EQUILIBRIUM AND DIFFUSION IN MAGNESIUM-RARE EARTH BINARY SYSTEMS

7.1 Background

The Mg-Rare Earth (RE) systems may well be the "lost alloys" of Mg. RE elements include, Sc, Y, and the Lanthanide Series (i.e. La, Ce, Pr, Nd, Pm, Sm, Eu, Gd, Tb, Dy, Ho, Er, Tm, Tb, and Lu). A spark of research was carried out by Krishan Lal in the mid-1960's as he pursued his doctorate studying impurity diffusion of various elements including Ce and La in Mg which represented a significant fraction of the fission products [117]. Beyond reporting the diffusion coefficients, activation energy, and pre-exponential factor, Lal offered no insightful description of the diffusion behavior. Only in the past few years, with the emergence of interest in rare earth elements as alloying agents, have interdiffusion studies in Mg-RE systems been published. The Mg-Nd system was empirically examined and the intermetallic phases formed during isothermal diffusion anneals were characterized with growth constants; however, interdiffusion coefficients were not reported [36]. Similarly, intermetallic phase growth constants were also determined through solid-to-solid diffusion couples utilizing polycrystalline Mg and Y [33, 118]. Most recently, single-crystal Mg was coupled to Y and to Gd; interdiffusion coefficients and growth constants were determined for the intermediate phases [81]. Consistent amongst these studies is that the least thermodynamically stable phase (i.e. lowest T_m) grew the thickest while the most thermodynamically stable phase did not form or grew the least. Additionally, the solubility limits of the intermetallic phases tend to be greater than the stoichiometric line compounds represented in the phase diagrams [118]. In the Mg-Gd

system, Mg_3Gd was reported to have an activation energy for diffusion 50% greater than its activation energy for growth [81]. This may indicate that the growth constant is dependent on the growth of other phases.

In addition to the impurity diffusion coefficients of Ce and La in Mg empirically determined by Lal [89], impurity diffusion coefficients of Gd and Y in single crystal Mg were computationally determined through multiphase diffusion simulations and using self-diffusion coefficients, expressed in terms of the mobility, and in combination with the thermodynamic potential [81]. The mobility terms for Mg and Y were derived from their self-diffusion coefficients and, due to the lack of experimental data, the mobility of Mg in Y was assumed to be two orders of magnitude lower than the self-diffusivity of Mg. Correspondingly, without experimental data for Gd, it was assumed that Gd has the same mobility values as Y on the basis of their similar physical and chemical properties. For both Gd and Y, the impurity diffusion coefficients along the a-axis are reported to be slightly higher than along the c-axis of the Mg crystal, and the anisotropy of diffusivity becomes smaller with increasing temperature. Not surprisingly, the diffusion coefficients of Y and Gd were found to be similar to each other [81]. The Gd and Y impurity diffusion coefficient are reported to be almost an order of magnitude lower than Mg self-diffusion as well as Al and Zn impurity diffusion coefficients. This is the case at temperatures approaching the melting point of Mg (650°C), but at hot working temperatures of 350°C both Gd and Y are faster diffusers than Al according to the multiphase diffusion simulations [81].

The objective of this study is twofold. First, this study aims to determine the interdiffusion coefficients in Mg-RE systems by means of the Boltzmann-Matano Method as

described in §3.2. Second, RE impurity diffusion coefficients in Mg solid solutions are evaluated from the Hall Method, described in §3.5.

7.2 Experimental Parameters

Two different RE metals were coupled to Mg to form solid-to-solid diffusion couples. The diffusion anneal parameters are given in Table 10.

Table 10: Diffusion anneal parameters for Mg-RE study

Diffusion Couple	Anneal Temperature (˚C)	Anneal Time (Hours)
Mg vs. Y	450	360
	500	240
	550	120
Mg vs. Gd	385	192
	425	166.5
	450	90
	475	96.5
	475	75
	490	72
	500	66

The thicknesses were measured for each intermetallic phase to calculate the parabolic growth constants using Equation 1. Integrated interdiffusion coefficients were calculated using Equation 2. Composition profiles were measured by EPMA. Boltzmann-Matano analysis was employed to calculate the interdiffusion coefficients of each phase with a non-zero concentration gradient ($\partial C/\partial x \neq 0$). The average effective interdiffusion coefficient for each phase was calculated from Equation 8. Impurity diffusion coefficients

were extracted from the concentration profile by means of the Hall Method. The temperature dependence of the growth constants and diffusion coefficients were examined via the Arrhenius Relationship, and the activation energies and pre-exponential factors determined.

7.3 Mg-Y System

7.3.1 Diffusion Zone Composition and Morphology

The binary phase diagram for the Mg-Y system is presented in Figure 21 [119]. The diffusion anneal temperatures were held just below the eutectic temperature as indicated by the dashed isothermal lines, and five phases are present at equilibrium – two terminal solid solutions and three intermediate phases. Crystallographic data for each intermediate phase is summarized in Table 11.

Table 11: Crystallographic parameters for intermetallic compounds in Mg-Y system

	Structure	**Pearson Symbol**	***a* (Å)**	***b* (Å)**	***c* (Å)**	***α***	***β***	***γ***	**Molar Volume (cm^3/mol)**	**Source**
MgY	Cubic	cP2	3.797			90°			16.48	[120]
δ-Mg_2Y	C14 Laves	hP12	6.037		9.752	90°		120°	15.44	[121]
ε-$Mg_{24}Y_5$	Cubic	cI58	11.25			90°			14.77	[122]

Backscatter electron micrographs of each diffusion couple and corresponding concentration profiles are presented in Figure 22. Two distinct intermediate phases between the terminal Mg and Y solid solutions can be seen. The phase near Mg solid

solution is ε-$Mg_{24}Y_5$, and δ-Mg_2Y is near the Y. Though present on the Mg-Y equilibrium phase diagram, the MgY phase is not easily observed in any of the diffusion couples. The very thin layer of the MgY phase was almost completely lost during polishing. However, some regions of the phase remained intact in each of the couples as shown in the backscatter electron micrographs in Figure 23. Due to the diminutive thickness, compositional information could not be obtained by EPMA.

The compositional boundaries and homogeneity ranges of the Mg solid solution and intermediate phases, determined from the EPMA profiles, were generally consistent with the phase diagram. These are shown on the phase diagram in Figure 21 with black markers. On the other hand, no solid solubility of Mg in Y was observed in the diffusion couples. These results generally agree with the EPMA results of solid-to-solid diffusion couples in another investigation [81, 118], and other experimental data [121, 123, 124]. The compositional boundaries of Mg solid solution and the observed intermediate phases are also consistent with the calculated phase boundaries based on optimized parameters from experimental results [125]. The lack of solubility of Mg in Y, combined with the diffusion couple morphology, provides some qualitative implications about the kinetics of the individual components of the system.

A secondary electron micrograph of the diffusion couples is presented in Figure 24. Large voids can be seen in the Mg solid solution of the diffusion couples. Kirkendall voids [126] form on the side of the fastest diffusing species, and show a temperature dependence as evident by the size and quantities present. The reduction in void formation suggests that as temperature increases the difference between the magnesium and yttrium intrinsic

diffusivities decreases. However, no marker plane was found in the diffusion couple to qualitatively analyze the intrinsic diffusivities of Mg and Y. Qualitatively, Mg is diffusing faster than Y.

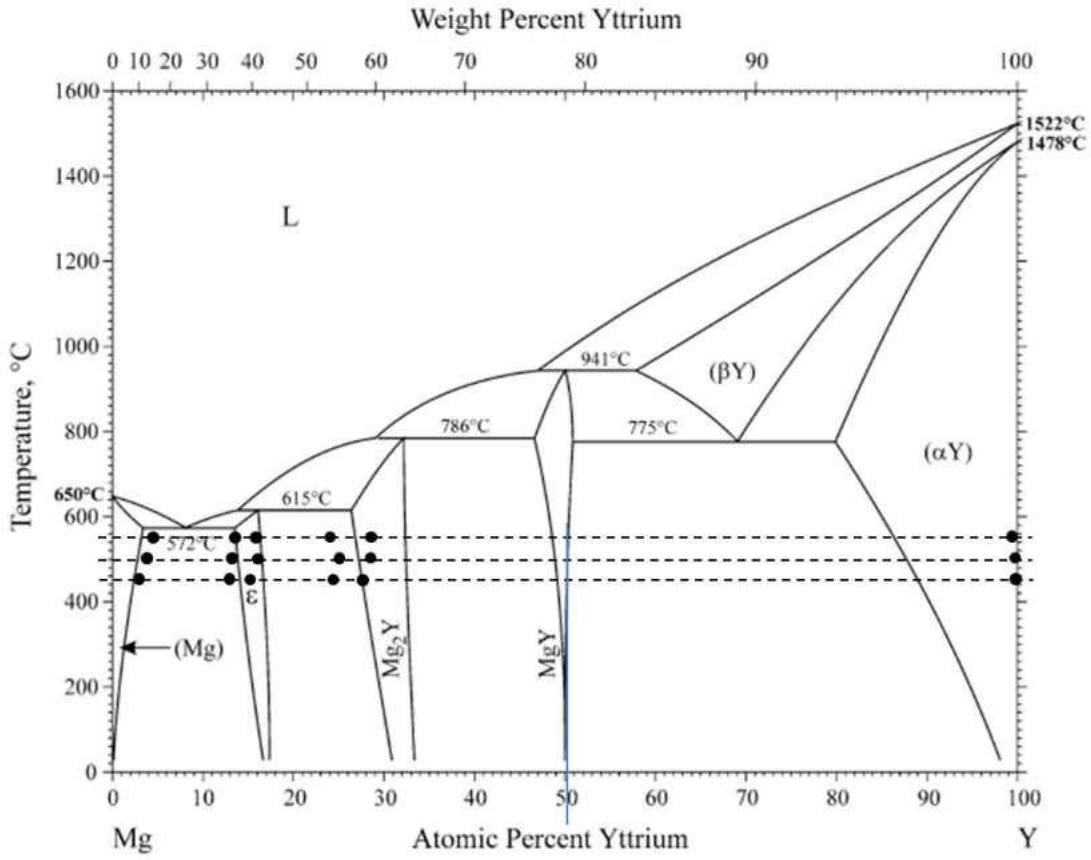

Figure 21: Equilibrium Mg-Y phase diagram with diffusion anneal temperatures and measured compositional boundaries of evolved phases [119]

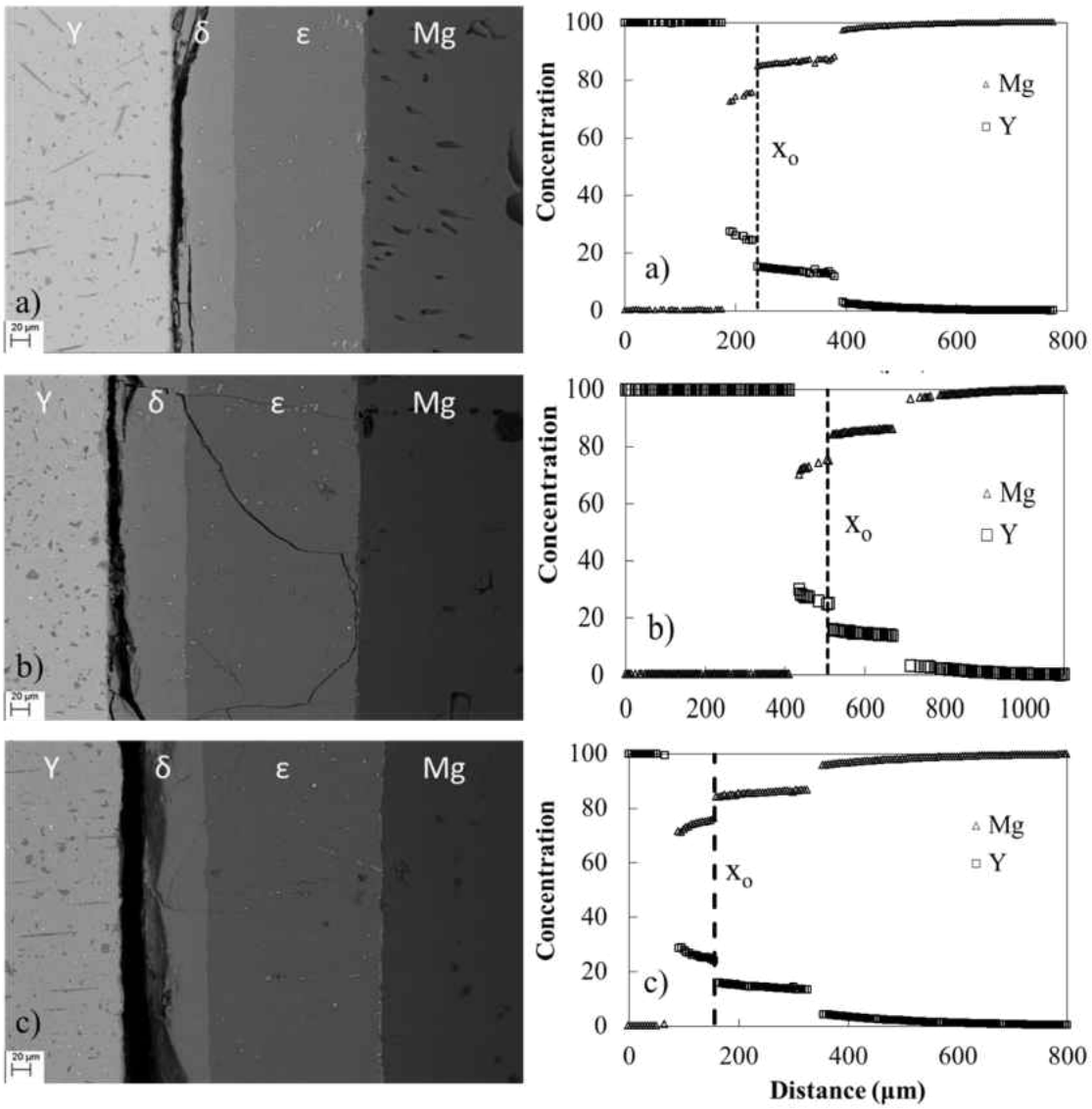

Figure 22: Backscatter electron micrograph and concentration profile of Mg-Y diffusion couples annealed at a) 450°C for 360 hours, b) 500°C for 240 hours and c) 550°C for 120 hours

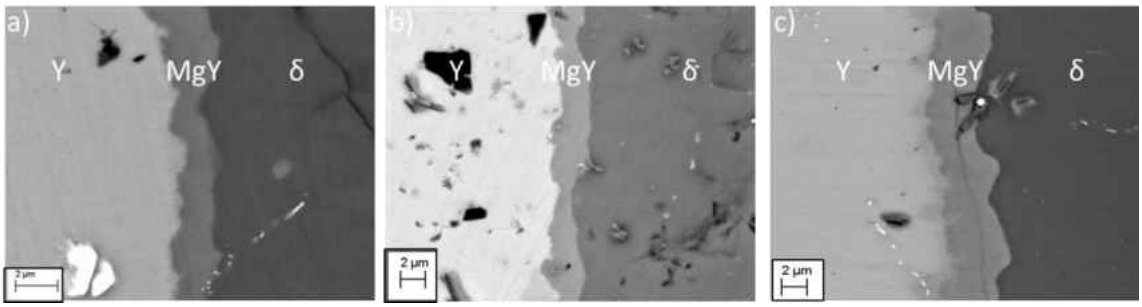

Figure 23: High magnification backscatter electron micrograph revealing MgY phase in diffusion couples annealed at a) 450°C for 360 hours, b) 500°C for 240 hours, and c) 550°C for 120 hours

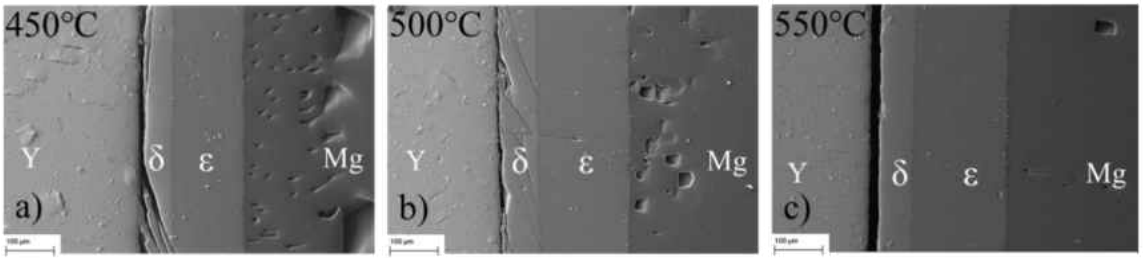

Figure 24: Secondary electron micrograph of Mg-Y diffusion couples annealed at a) 450°C for 360 hours, b) 500°C for 240 hours and c) 550°C for 120 hours

7.3.2 Parabolic Growth Constants and Interdiffusion

The thickness of each intermediate phase was measured, and the parabolic growth constants were calculated. The temperature dependence of the growth constants was examined, as shown in Figure 25, and the activation energy for growth was calculated. The quantitative growth results are reported in Table 12. The ε-$Mg_{24}Y_5$ phase grew to a much thicker layer than the δ-Mg_2Y in all diffusion couples, but the activation energy for ε-$Mg_{24}Y_5$ is only slightly greater than the energy for δ-Mg_2Y. The thinnest layer, MgY, has the largest

activation energy. These results are in good agreement with the results presented by Das *et al*. [81] as reported in Table 12.

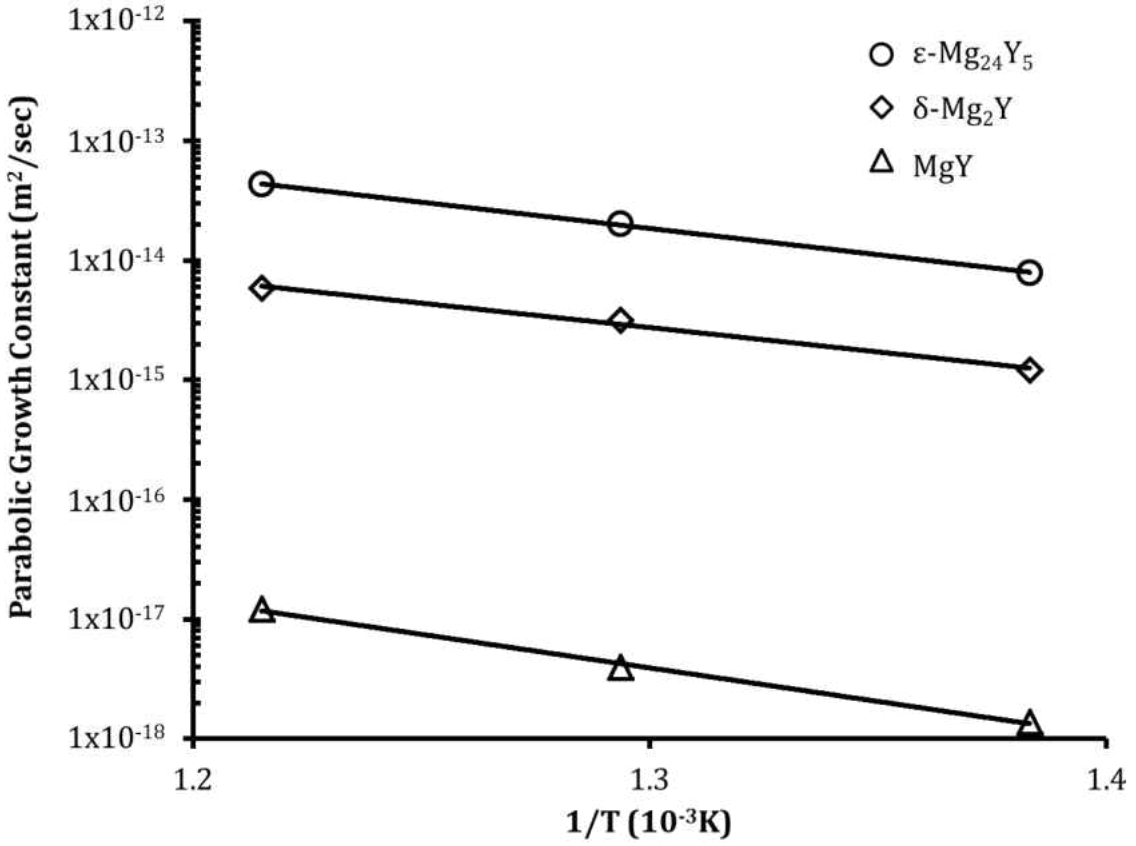

Figure 25: Parabolic growth constants for δ-Mg_2Y and ε-$Mg_{24}Y_5$ phases as a function of temperature

Table 12: Thickness and parabolic growth constants of intermediate phases in the Mg-Y system

		MgY	δ-Mg_2Y	ε-$Mg_{24}Y_5$	Source
Thickness (μm)	450°C	1.9 (±0.6)	56 (±4)	143 (±5)	This Study
k_p **(m²/s)**		1.51×10^{-18}	1.21×10^{-15}	7.89×10^{-15}	
Thickness (μm)	500°C	2.6 (±0.6)	74 (±2)	187 (±3)	
k_p **(m²/s)**		3.99×10^{-18}	3.17×10^{-15}	2.02×10^{-14}	
Thickness (μm)	550°C	3.2 (±0.6)	71 (±2)	193 (±1)	
k_p **(m²/s)**		1.22×10^{-17}	5.83×10^{-15}	4.31×10^{-14}	
k_o **(m²/s)**		7.85×10^{-11}	5.52×10^{-10}	9.51×10^{-9}	
Q **(kJ/mol)**		107.5	78.1	84.1	
k_o **(m²/s)**	***a*-axis** ***c*-axis**	2.02×10^{-8} 3.36×10^{-8}	4.02×10^{-10} 4.14×10^{-10}	6.39×10^{-10} 5.65×10^{-10}	[81]
Q **(kJ/mol)**	***a*-axis** ***c*-axis**	136.34 138.78	71.24 70.53	62.57 63.43	

The integrated interdiffusion coefficients were calculated for the intermediate phases using the compositional boundaries determined by EPMA for ε-$Mg_{24}Y_5$ and δ-Mg_2Y and the compositional boundaries from the phase diagram for MgY. The integrated interdiffusion coefficients are plotted as a function of inverse temperature in Figure 26. The temperature specific coefficients as well as the activation energy and pre-exponential factor for the observed intermediate phases are reported in Table 13.

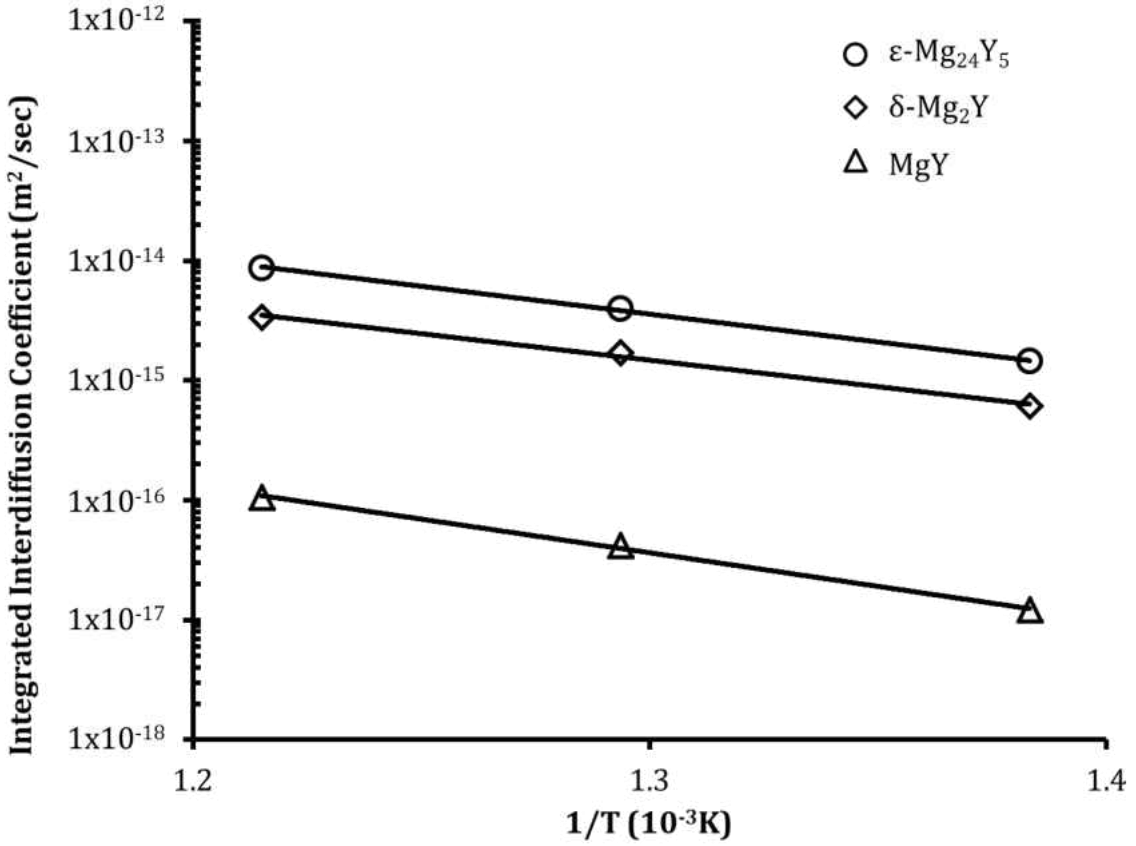

Figure 26: Integrated interdiffusion coefficients for δ-Mg_2Y, ε-$Mg_{24}Y_5$, and MgY phases as a function of temperature

Table 13: Integrated interdiffusion coefficients for intermediate phases in the Mg-Y system

		MgY	**δ-Mg_2Y**	**ε-$Mg_{24}Y_5$**
$\widetilde{D}^{int}$ **(m²/s)**	450°C	1.21x10^{-17}	6.11x10^{-16}	1.44x10^{-15}
$\widetilde{D}^{int}$ **(m²/s)**	500°C	4.17x10^{-17}	1.70x10^{-15}	4.00x10^{-15}
$\widetilde{D}^{int}$ **(m²/s)**	550°C	1.06x10^{-16}	3.37x10^{-15}	8.70x10^{-15}
$\widetilde{D}_o^{int}$ **(m²/s)**		7.30x10^{-10}	8.36x10^{-10}	4.03x10^{-9}
Q **(kJ/mol)**		107.5	84.7	89.19

As was seen for growth, the integrated interdiffusion activation energy for δ-Mg_2Y is slightly lower than the energy for ε-$Mg_{24}Y_5$, and the activation energy for MgY is larger. The implication of this consistency is that growth of an intermediate phase is not dependent on the growth of other phases. On the other hand, an order of magnitude difference is found between the parabolic growth constants and integrated interdiffusion coefficients for ε-$Mg_{24}Y_5$ and MgY. The integrated interdiffusion coefficient for ε-$Mg_{24}Y_5$ is an order of magnitude smaller than its parabolic growth constant. Conversely, the integrated interdiffusion coefficient for MgY is an order of magnitude larger than the parabolic growth constant. Because growth constants have a complex meaning dependent on the diffusion coefficients of all phases as well as the solubility limits of the phases, these differences may indicate a dominance of thermodynamic influences of ordering or kinetic influences of mechanism on the diffusion kinetics. The atom-vacancy exchange probability and frequency, the configuration entropy, and the correlation factor are all influenced by the degree of ordering [126-128]. When grain size is sufficiently small, as in the case of very thin layers, the measured interdiffusion coefficient includes both bulk and grain boundary diffusivities [62, 129].

The concentration dependent interdiffusion coefficient was calculated according to the Boltzmann-Matano method, presented in Figure 27. Because a concentration profile could not be measured across the small thickness of the MgY phase, concentration dependent interdiffusion coefficients could not be determined for this phase. Similarly, because no measureable concentration gradient was observed in the Y solid solution, interdiffusion coefficients could not be determined for this phase either. Interdiffusion in

the Mg solid solution, ε-$Mg_{24}Y_5$, and δ-Mg_2Y phases is composition dependent. The interdiffusion coefficient increases with Y content in the ε-$Mg_{24}Y_5$ phase, but it decreases with increasing Y concentration in δ-Mg_2Y and, to a greater extent, in Mg solid solution. From Figure 27, it is easy to see that interdiffusion occurs more readily in ε-$Mg_{24}Y_5$ than it does in δ-Mg_2Y and Mg solid solution.

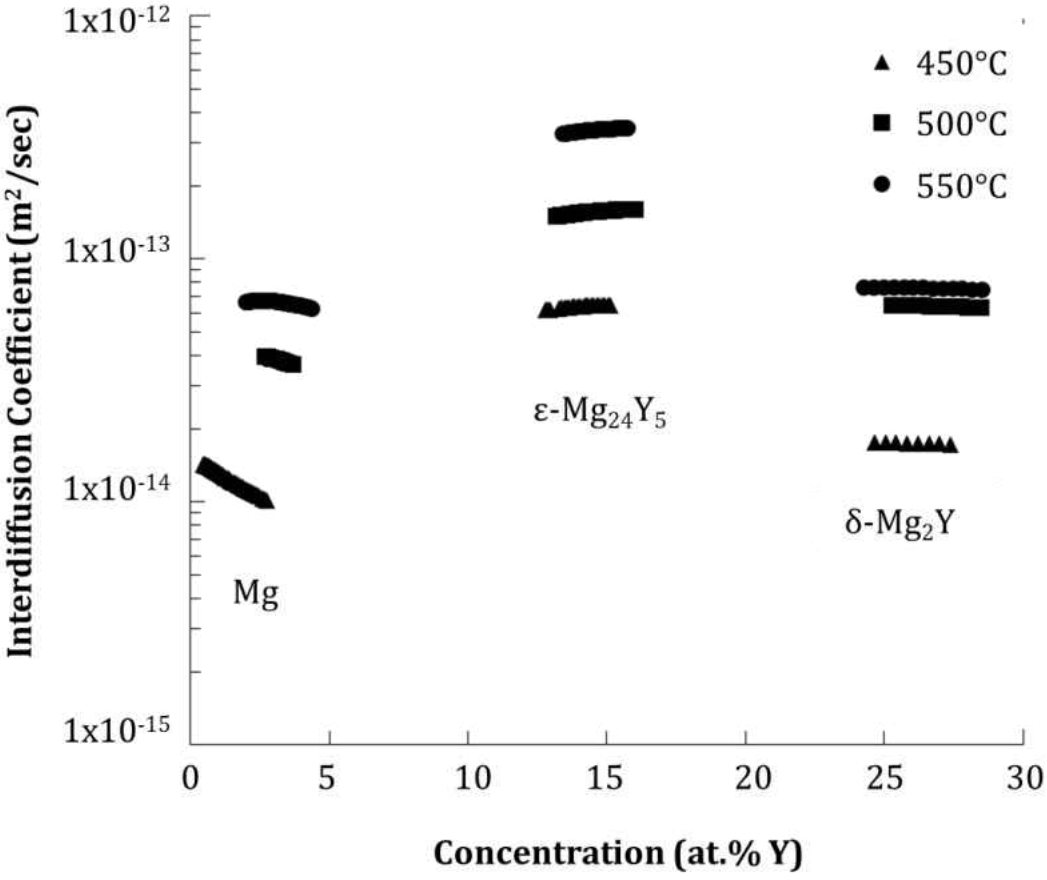

Figure 27: Interdiffusion coefficient for Mg solid solution, δ-Mg_2Y, and ε-$Mg_{24}Y_5$ phases as function of Y concentration

The effective interdiffusion coefficients were calculated using Equation 8. The temperature dependence of the coefficients is examined in Figure 28, from which the pre-

exponential factor and activation energy are determined. These effective interdiffusion coefficients, pre-exponential factors, and activation energies for the intermediate phases, along with similar data determined by the Heumann-Matano Method and reported by Das *et al*. [81], are reported in Table 14. It is important to note, literature values represent a numerical average over a composition range. Nonetheless, there is generally good agreement between the interdiffusion coefficients, pre-exponential factors, and activation energies found in this study with those previously reported by Das *et al*. [81].

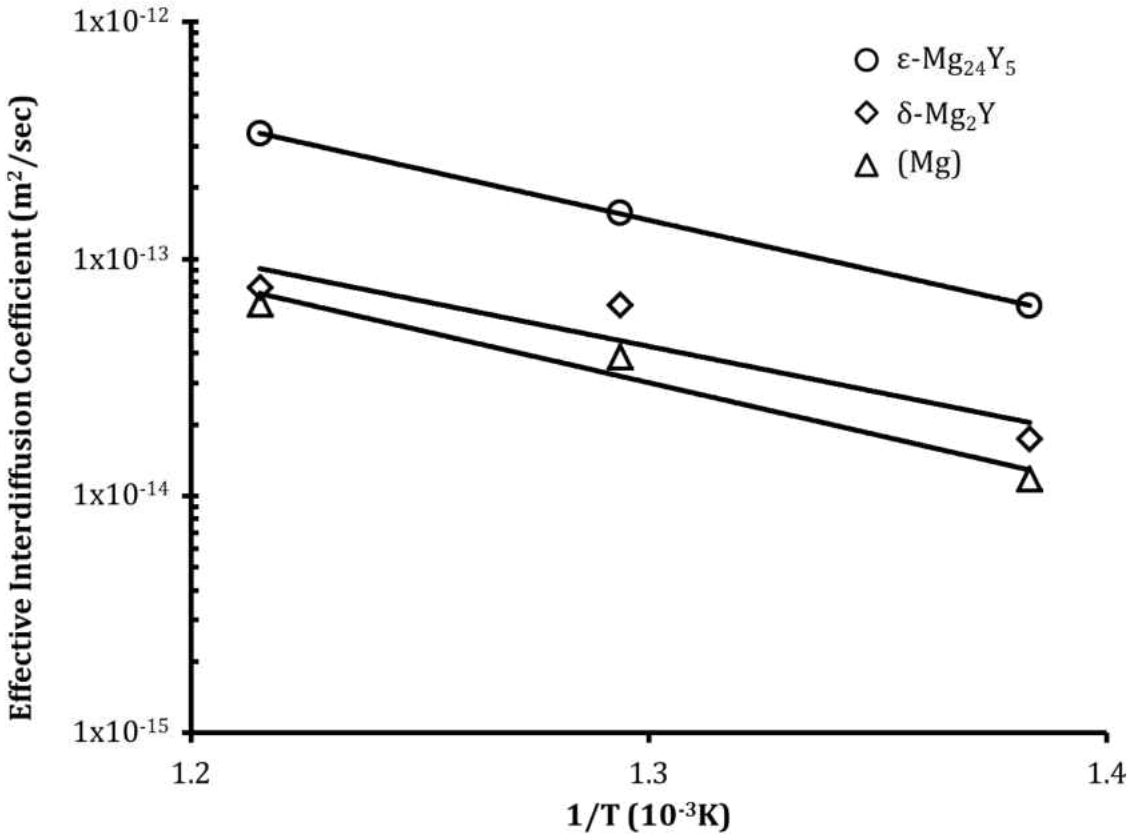

Figure 28: Effective interdiffusion coefficients for δ-Mg_2Y and ε-$Mg_{24}Y_5$ as a function of temperature

Table 14: Effective interdiffusion coefficients for intermediate phases in the Mg-Y system

		MgY	δ-Mg_2Y	ε-$Mg_{24}Y_5$	Mg(Y)	Source
$\widetilde{D}^{eff}$ (m²/s)	450°C	--	$1.74x10^{-14}$	$6.37x10^{-14}$	$1.18x10^{-14}$	This Study
$\widetilde{D}^{eff}$ (m²/s)	500°C	--	$6.38x10^{-14}$	$1.56x10^{-13}$	$3.87x10^{-14}$	
$\widetilde{D}^{eff}$ (m²/s)	550°C	--	$7.60x10^{-14}$	$3.39x10^{-13}$	$6.47x10^{-14}$	
$\widetilde{D}_o^{eff}$ (m²/s)		--	$4.56x10^{-9}$	$6.04x10^{-8}$	$1.72x10^{-8}$	
Q (kJ/mol)		--	74.0	82.7	84.8	
$\widetilde{D}_o$ (m²/s)	***a*-axis** ***c*-axis**	$5.38x10^{-7}$ $4.96x10^{-7}$	$3.23x10^{-8}$ $3.81x10^{-8}$	$5.43x10^{-8}$ $6.48x10^{-8}$	-- --	[81]
Q (kJ/mol)	***a*-axis** ***c*-axis**	109.67 108.53	85.96 87.28	78.50 80.67	-- --	

7.3.3 Y Impurity Diffusion in Mg Solid Solution

Using the Hall interdiffusion coefficient the impurity diffusion coefficients at the infinitely dilute composition were extracted from the concentration profiles for each diffusion couple. Implementation of the Hall method was carried out by performing a linear regression of the concentration distribution versus Boltzmann parameter over the composition range of 0.05–0.5 at.%Y. The impurity diffusion coefficient is extrapolated from the interdiffusion coefficients at concentrations less than 0.3 at.%Y as shown in Figure 29.

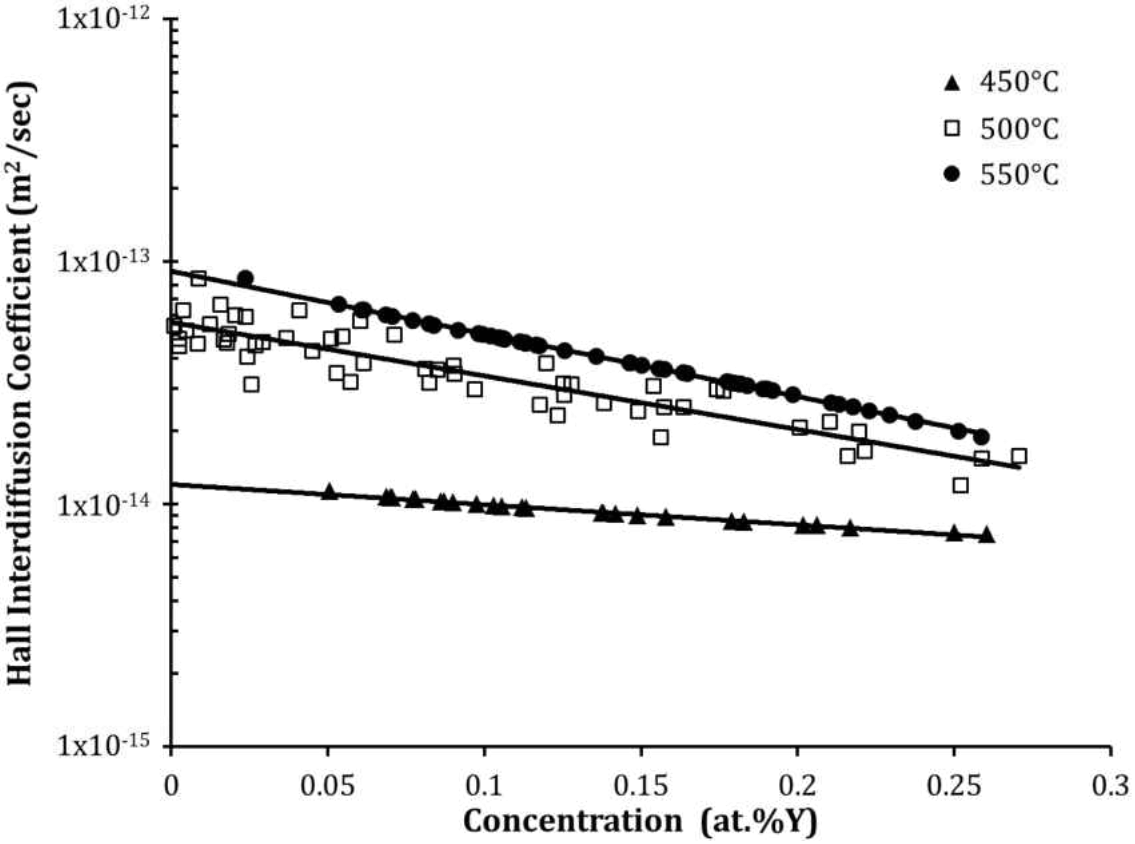

Figure 29: Hall interdiffusion coefficients in dilute Mg solid solution

Table 15 reports the findings of this study as well as literature values. There is exceptional agreement on the activation energy for Y impurity diffusion, however the pre-exponential factor found in literature is an order of magnitude lower than found in this study. Prior to this study, Y impurity diffusion coefficients were computed using a multiphase diffusion simulation approach and extrapolated from single-crystal, semi-infinite experimental data by fitting the data to the Gaussian, or thin film, solution of Fick's diffusion equation [81]. This difference can be attributed to the assumptions made in the simulation and experimental solutions. While the impurity diffusion coefficients and the

interdiffusion coefficients in Mg solid solution are fairly consistent with each other, the activation energy for Y impurity diffusion is greater than the activation energy for interdiffusion in Mg solid solution. Conversely, the pre-exponential factor for impurity diffusion is an order of magnitude larger than that for interdiffusion in Mg solid solution.

Table 15: Impurity diffusion coefficients in Mg solid solution

		Mg(Y)	**Source**
D_Y^{Mg} **(m²/s)**	450°C	1.20x10^{-14}	This Study
D_Y^{Mg} **(m²/s)**	500°C	2.34x10^{-14}	
D_Y^{Mg} **(m²/s)**	550°C	9.12x10^{-14}	
D_o^{imp} **(m²/s)**		1.62x10^{-7}	
Q **(kJ/mol)**		99.5	
D_o^{imp} **(m²/s)**	***a*-axis** ***c*-axis**	3.21x10^{-8} 2.79x10^{-8}	[81]
Q **(kJ/mol)**	***a*-axis** ***c*-axis**	99.13 97.85	

7.4 Mg-Gd System

7.4.1 Phase Diagram Examination

The Mg-Gd phase diagram, presented in Figure 30, is based on the thermodynamic modeling and optimization of available experimental data by means of the CALPHAD technique by Guo, *et al.* [130]. Most experimental studies of the binary Mg-Gd phase diagram have exploited the use of equilibrated alloys and thermal analysis techniques. Microstructural evaluation and X-ray diffraction studies on equilibrated alloys have shown that four intermetallic phases, Mg_5Gd, Mg_3Gd, Mg_2Gd, and MgGd, exist in the system; heating and cooling experiments at fixed compositions have allowed for determination of the phase diagram, revealing invariant reaction temperatures, solvus, and liquidus projections [13, 131-134]. Equilibrium can be approached with slow heating/cooling or very long isothermal treatments, however true equilibrium is difficult to achieve. The diffusion couple technique offers versatile alternative for phase diagram determination [29]. While the driving force for interdiffusion is the gradient of chemical potential across the diffusion reaction zone, local equilibrium exists in the interphase between each evolved layer [23, 30]. Recently, Das *et al.* [81] performed an interdiffusion study on the Mg-Gd system. They observed the nucleation and growth of a previously unidentified phase, reportedly Gd-rich. Though the phase was too thin to determine the exact composition using EPMA, Das *et al.* deduced that it was close to Mg_4Gd_6 [81].

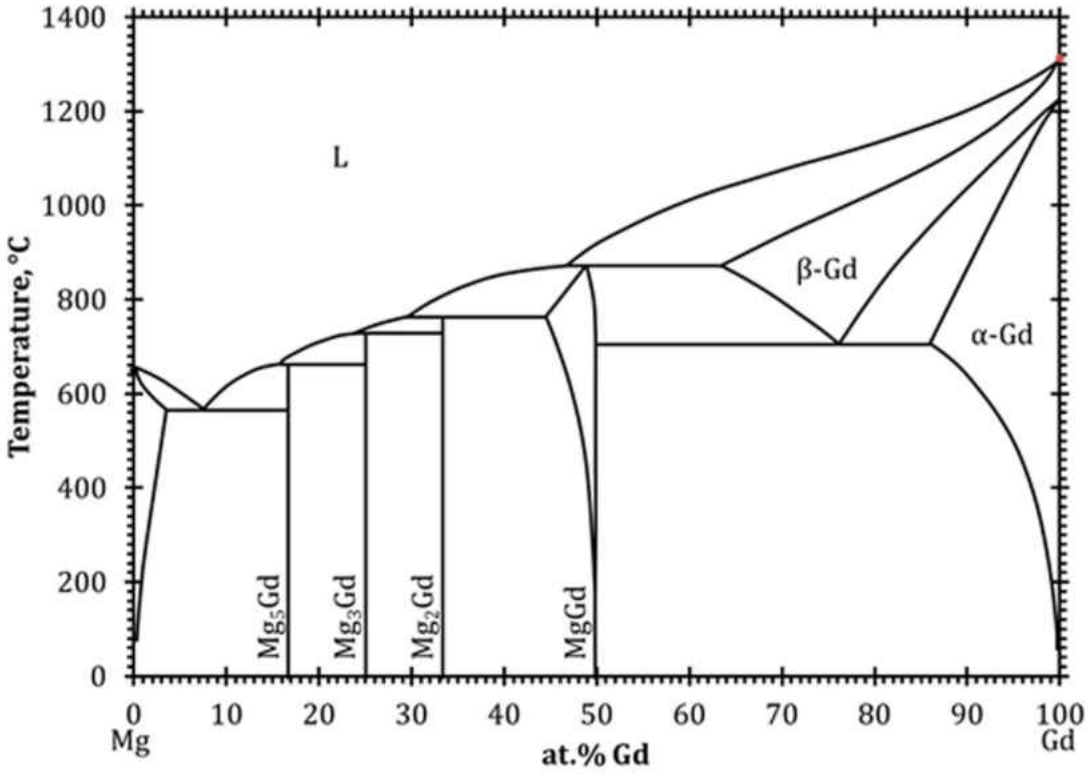

Figure 30: Equilibrium phase diagram for the Mg-Gd system

The solid-to-solid diffusion couple technique was used to horizontally assess the Mg-Gd phase diagram in the temperature range of 385°C to 500°C. Seven couples were assembled using discs of pure, polycrystalline Mg and Gd. The assembled couples were encapsulated in an inerted quartz ampoule, and heat treated according to the diffusion anneal parameters listed in Table 10. Heat treatment concluded with a cold water quench. The interdiffusion zone was exposed, and metallographically prepared to 1μm. A field emission-SEM (Zeiss Ultra55™) equipped with an angular selective backscattered electron detection system for maximum compositional contrast was utilized to image the layers of diffusion reaction products. Four layers formed in the diffusion couples annealed at

temperatures greater than 475°C while five layers formed in the couples annealed at temperatures less than 475°C. At 475°C, the fifth layer formed when the couple was subjected to an anneal of longer duration. Backscatter electron micrograph of the interdiffusion reaction zone in diffusion couples annealed at 490°C for 72 hours and 385°C for 192 hours is presented in Figure 31; high magnification image of the region at the Gd interface is inlaid to show the presence of two thin layers.

The composition of each layer of substantial thickness (> 5μm) was determined with standardless x-ray energy dispersive spectroscopy (XEDS) in the SEM. The accuracy of this technique is ±2% [135]. Based on the nominal compositions, the newly identified phase was assigned the Mg_6Gd formula. XEDS line scans indicated a range of homogeneity for the thick intermediate phases. Compositional boundaries were determined for the couples annealed at 385°C for 192 hours, 425°C for 166.5 hours, 450°C for 90 hours, and 500°C for 66 hours by collecting the spectral counts at three points approximately 5 μm from each interphase to avoid interaction volume effects. The Mg solid solution phase boundaries were obtained from XEDS line scans of couples annealed at 385°C for 192 hours, 425°C for 166.5 hours, 475°C for 96.5 hours, and 490°C for 72 hours. The electron beam accelerating voltage was maintained at 15keV for all points. The K shell x-rays for Mg and L shell x-rays for Gd were used for quantification. Additionally, a phi-rho-z curve was used to correct for matrix effects. The results of the compositional boundary assessment are reported in Table 16 and are plotted on the partial phase diagram in Figure 32. Light gray markers are used to denote the Mg_6Gd phase boundaries.

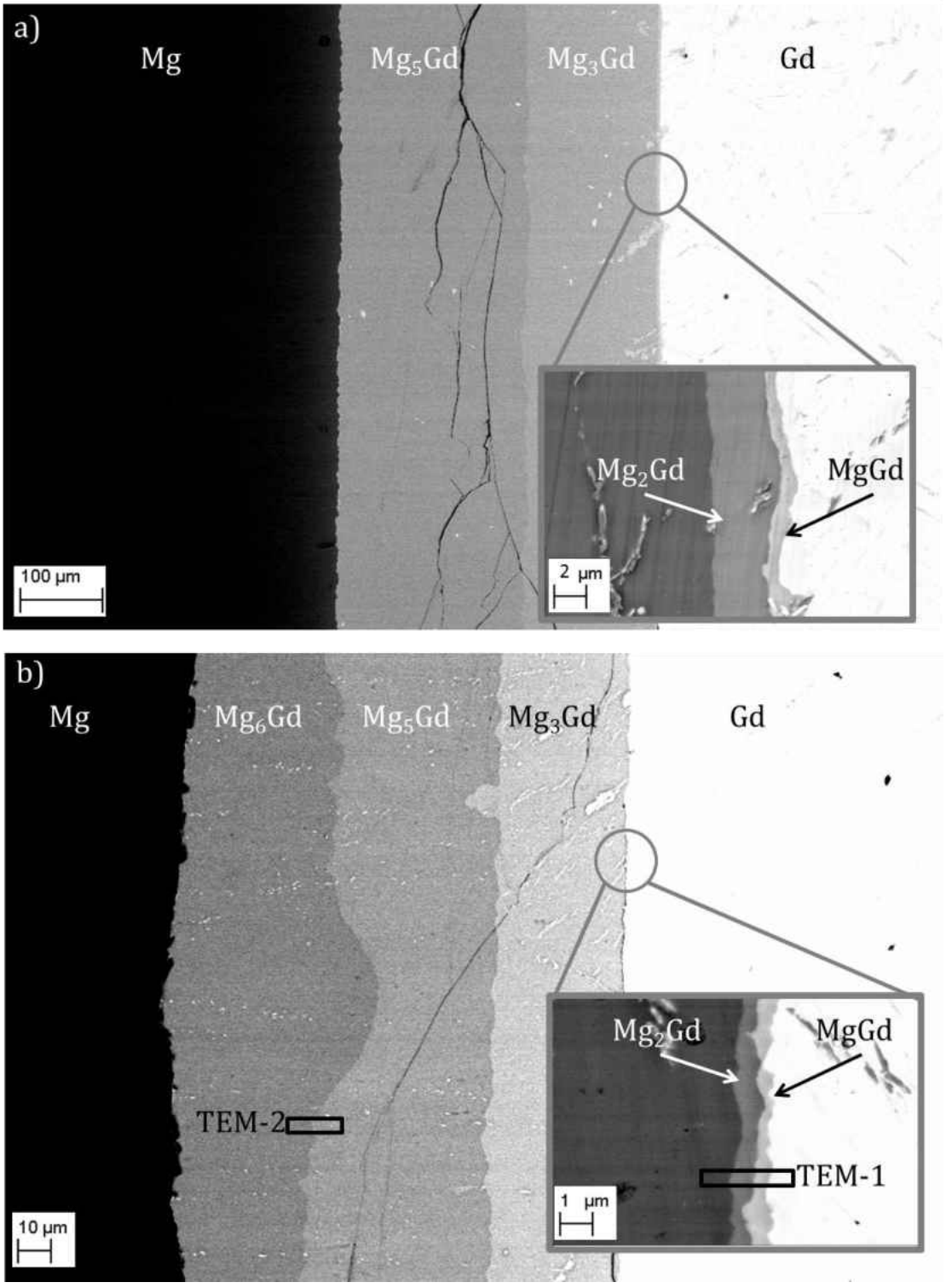

Figure 31: Backscatter electron micrograph of interdiffusion zone from diffusion couples annealed at a) 490°C for 72 hours, and b) 385°C for 192 hours

Table 16: Phase boundary compositions in at.%Gd (± 1σ) for Mg(Gd), Mg_6Gd, Mg_5Gd, and Mg_3Gd phases as determined by x-ray energy dispersive spectroscopy

Temperature (°C)	Time (Hr)	Mg(Gd)		Mg_6Gd		Mg_5Gd		Mg_3Gd	
385	192	0	1.3	13.79 (±0.18)	15.06 (±0.13)	16.81 (±0.11)	18.10 (±0.13)	23.37 (±0.15)	26.55 (±0.12)
425	166.5	0	2.2	14.24 (±0.05)	14.82 (±0.21)	16.63 (±0.14)	17.52 (±0.07)	22.28 (±0.25)	25.93 (±0.32)
450	90	0 @ 475°C/96.5Hr	3.5	15.08 (±0.45)	14.58 (±0.27)	16.28 (±0.12)	17.74 (±0.62)	21.25 (±0.63)	25.53 (±0.58)
500	66	0 @ 490°C/72Hr	4.0	N/A		15.12 (±0.34)	16.86 (±0.20)	20.72 (±0.71)	24.49 (±0.06)

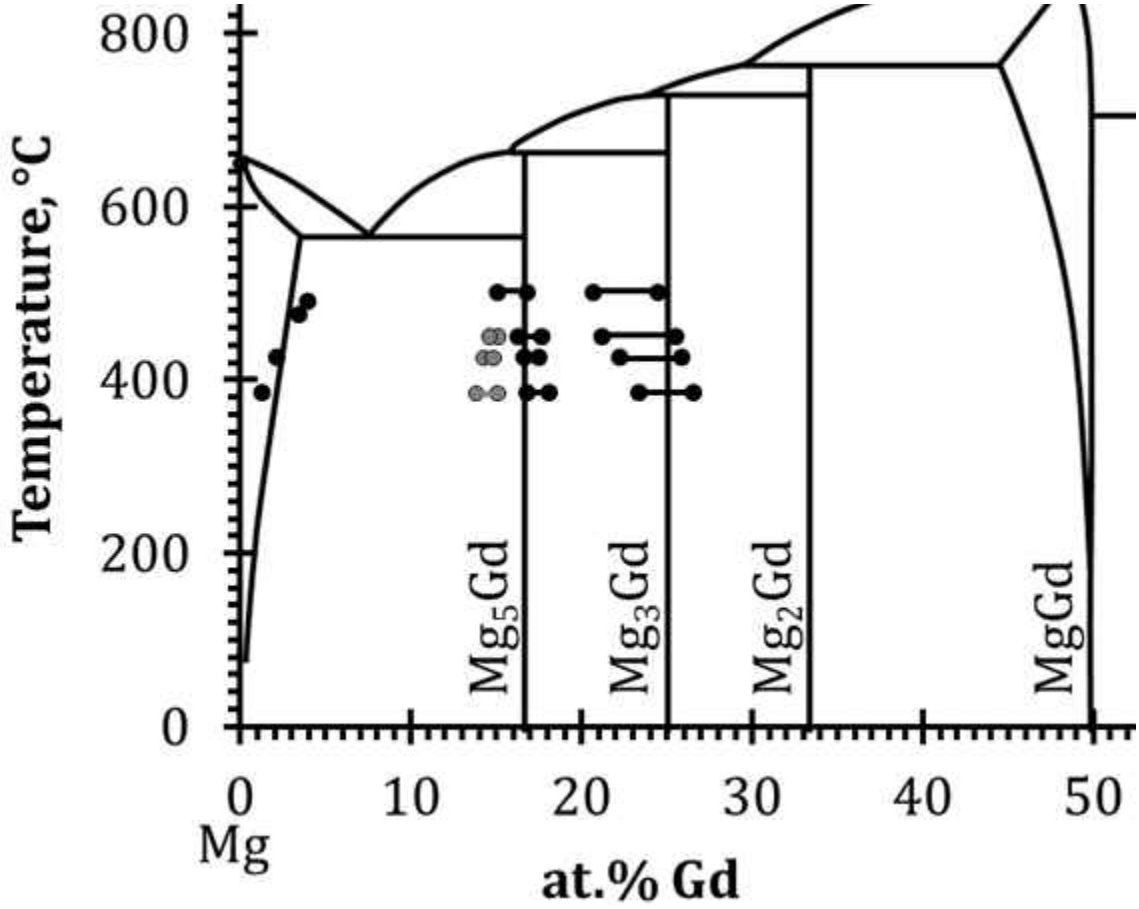

Figure 32: Mg-rich side of Mg-Gd phase diagram showing phase boundary compositions; light gray markers denote Mg_6Gd phase boundaries

7.4.2 Crystal Structure

To examine the crystal structure of the intermetallic compounds in the Mg-Gd system, the diffusion couple annealed at 385°C for 192 hours was subjected to transmission electron microscopy (TEM). Two specimens were extracted as shown in Figure 31b, identified as TEM-1 and TEM2. Figure 33 presents a High Angle Annular Dark-Field (HAADF) image and a corresponding bright-field micrograph from TEM-1. The Mg_3Gd, Mg_2Gd, and MgGd phases as well as the Gd solid solution are present in this specimen. Tilting series SAED was performed to determine the lattice parameters of each phase. Representative tilting series SAED patterns from TEM-1 are presented in Figure 34. Hexagonal Gd was found to have lattice parameters of a = 3.632Å and c = 5.747Å. The lattice parameters are in exceptional agreement with the published parameters for Gd solid solution (a = 3.6338Å, c = 5.7814Å) [136]. The thin MgGd, and Mg_2Gd phases were confirmed as such by comparison of the lattice parameters determined in this study with those found in literature. Through SAED, MgGd was found to have cubic symmetry with a = 3.772Å; MgGd has been shown to have bcc structure consistent with the CsCl prototype and a = 3.818Å [137]. The Mg_2Gd phase was found to have cubic symmetry with a = 8.657Å, and the lattice parameter for the cubic Mg_3Gd was determined to be 7.353Å. Again, these results are consistent with findings of Manfrinetti *et al.* in which the Mg_2Gd lattice parameter was reported to be a = 8.575Å while the Mg_3Gd parameter was given as 7.324Å [132]. Therefore, despite the lack of compositional data for the two thin layers, crystallography supports the specified formula designation.

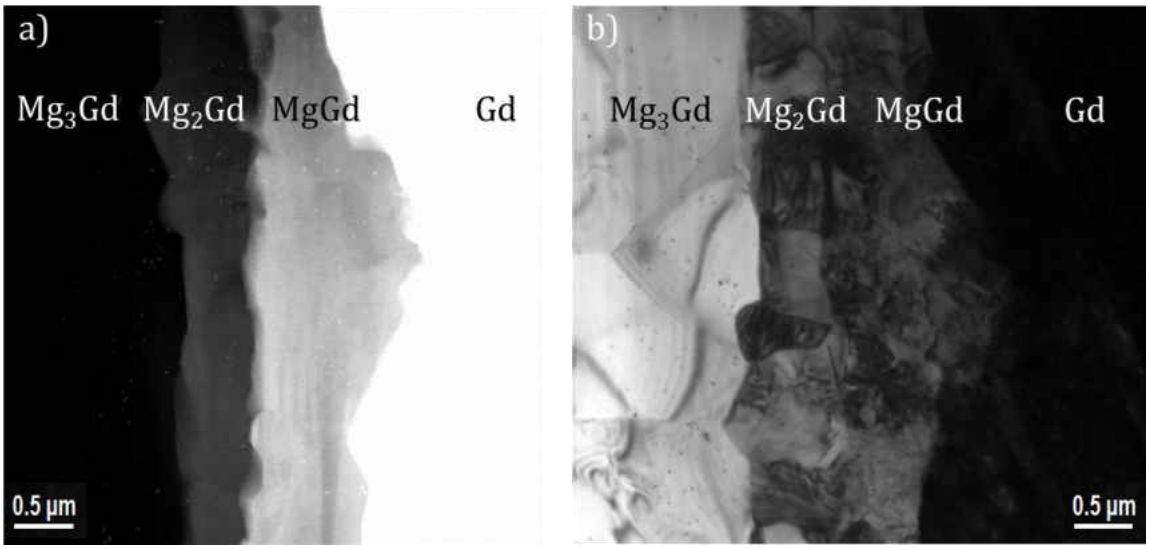

Figure 33: Transmission electron microscopy of TEM-1 in a) High Angle Annular Dark-Field imaging mode and b) bright field imaging mode

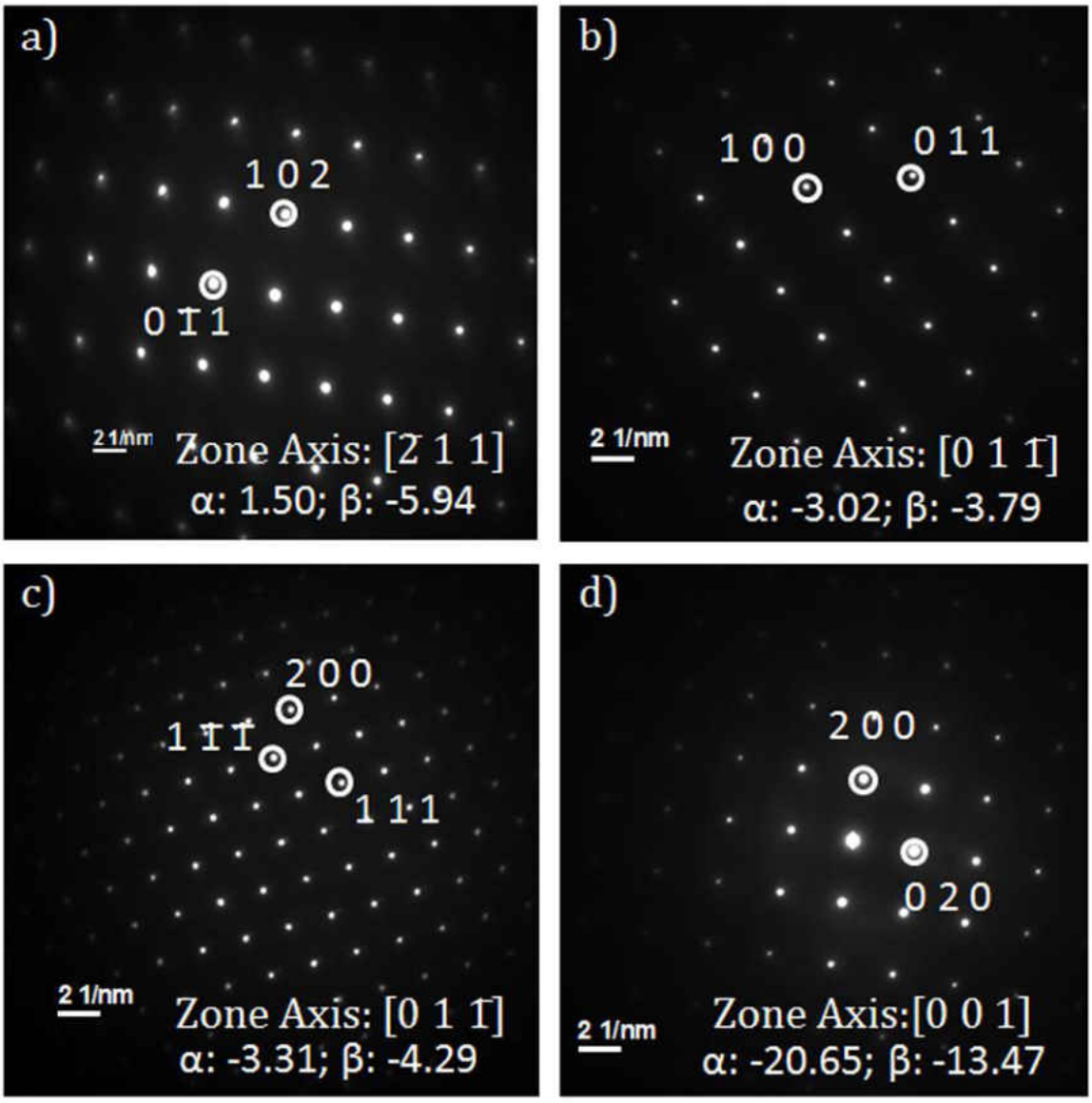

Figure 34: Representative tilting series SAED patterns from TEM-1 for a) zone axis $[\bar{2}11]$ hexagonal (space group $P6_3/mmc$) Gd with lattice parameters of a = 3.632Å, c = 5.747Å; b) zone axis $[01\bar{1}]$ cubic (space group $Pm\bar{3}m$) MgGd with lattice parameter of a = 3.772Å;c) zone axis $[01\bar{1}]$ cubic (space group $Fd\bar{3}m$) Mg_2Gd with lattice parameter of a = 8.657Å; d) zone axis $[001]$ cubic (space group $Fm\bar{3}m$) Mg_3Gd with lattice parameter of a = 7.353Å

Tilting series electron diffraction was also used to determine the structure and lattice parameters of the Mg_5Gd and Mg_6Gd phase. TEM-2, annotated on Figure 31b, was extracted from the couple and examined with the transmission electron microscope. Figure 35 presents a High Angle Annular Dark-Field (HAADF) image and a corresponding bright-field micrograph from TEM-2. An SAED pattern for Mg_5Gd with a zone axis of $[01\bar{1}]$ is presented in Figure 36a. It can be seen that the intermetallic phase has cubic symmetry. The calculated lattice parameter is 22.23Å. The Mg_5Gd phase was characterized by Fornasini *et al.* as a complex structure with a large cubic cell (i.e. a = 22.344Å) [138]. From the SAED in Figure 36b, the Mg_6Gd phase can be seen to have hexagonal symmetry.

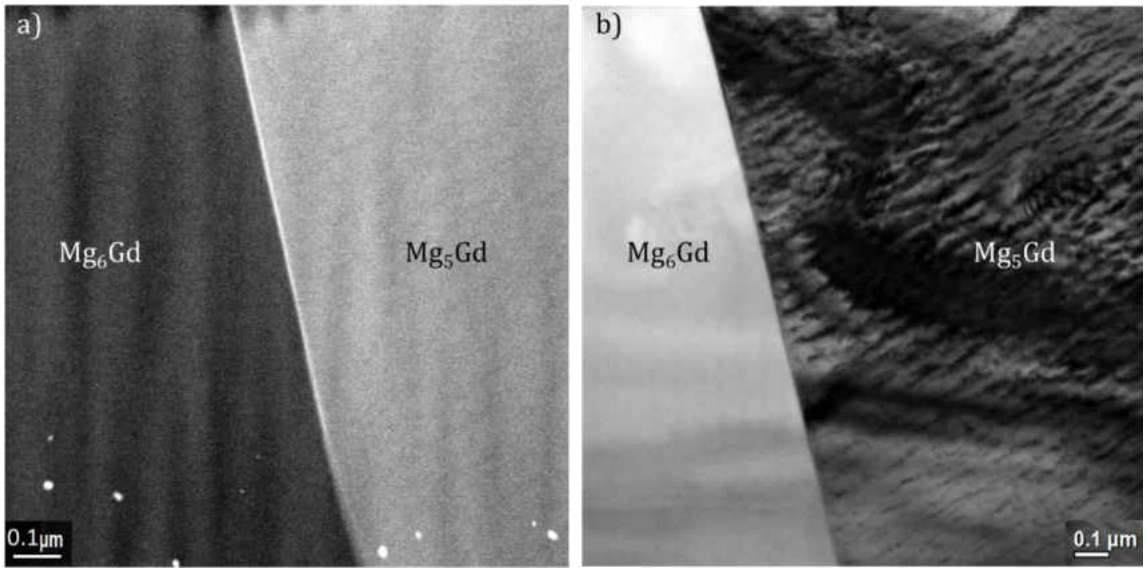

Figure 35: Transmission electron microscopy of TEM-2 in a) High Angle Annular Dark-Field imaging mode and b) bright field imaging mode

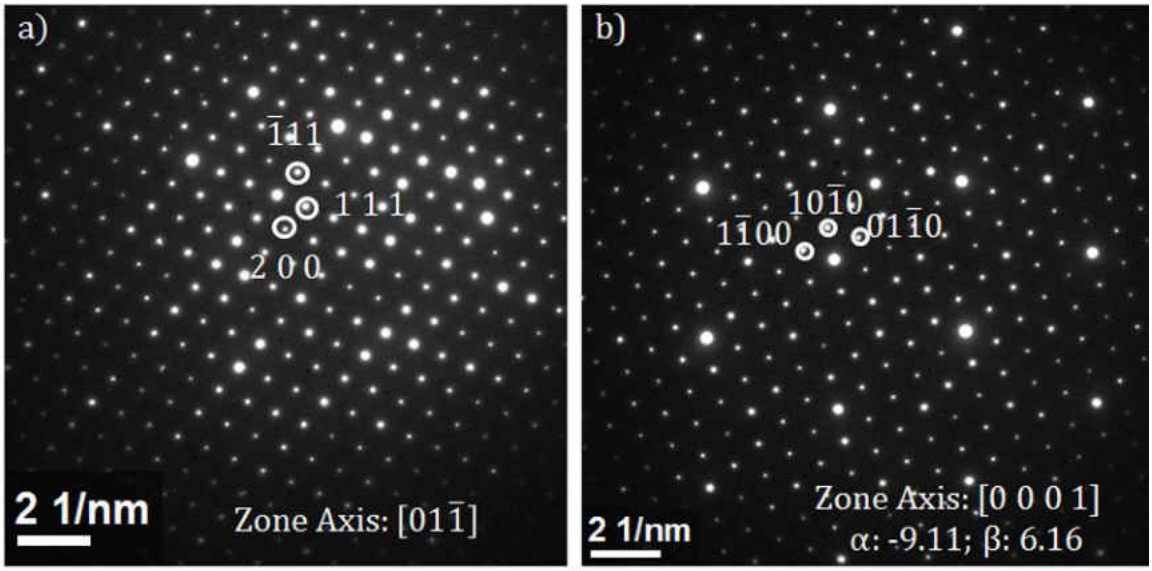

Figure 36: Representative tilting series SAED patterns from TEM-2 for a) zone axis [01$\bar{1}$] cubic (space group $F\bar{4}3m$) Mg_5Gd with lattice parameter of a = 22.23Å; b) complex hexagonal symmetry in Mg_6Gd with lattice parameter of a = 13.42Å and c = 9.77Å, zone axis [0001]

High Resolution Transmission Electron Microscopy (HRTEM) was also used to further characterize Mg_6Gd. Figure 37 presents a HRTEM image of Mg_6Gd. The HRTEM image shown in Figure 37a was Fourier filtered to suppress the high frequency noise; doing so highlights the atomic column periodicities present within the ordered inter-metallic. In frequency space, all spatial frequencies that did not correspond to the periodic atomic structure were masked before the image was transformed back into the spatial domain. It is not possible from the HRTEM image to discern Gd atoms from Mg atoms. Due to the nature of HRTEM images direct interpretation of atomic species and locations is not possible without HRTEM simulation and images captured under carefully controlled conditions. However, it is possible that the brighter dots present in Figure 37c could be

representative of the Gd atoms as they are present in approximately the correct proportion based on the composition of this ordered phase. In this lattice image, the bright dots appear to have a parallel alignment with periodic steps as indicated by the arrows in Figure 37c. Combining the SAED pattern and the HRTEM image, Mg_6Gd appears to be a modulated hexagonal superlattice with lattice parameters of a = 13.42Å and c = 9.77Å. Table 17 summarizes the crystallographic results of this study.

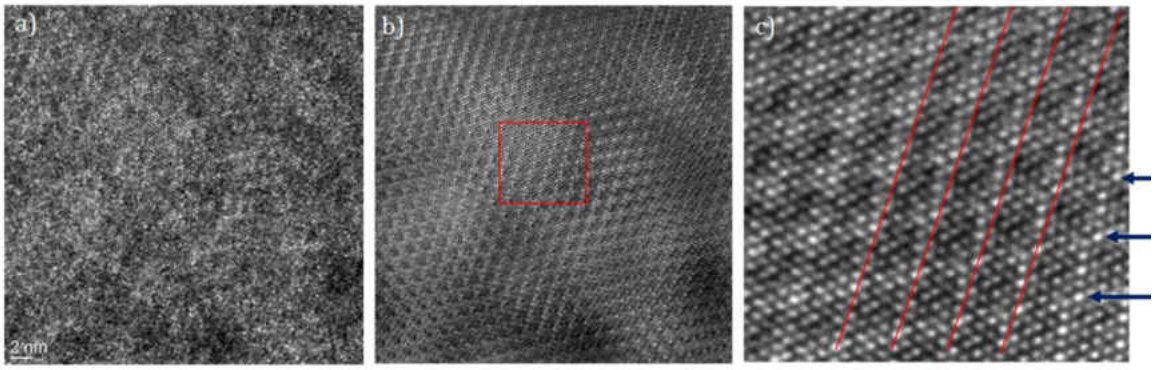

Figure 37: HRTEM image of Mg_6Gd showing the periodicity of atomic steps in the lattice: a) unprocessed HRTEM image; b) same image transformed to frequency domain with mask applied; c) masked image transformed back to spatial domain.

Table 17: Crystallographic parameters for intermetallic compounds in Mg-Gd system

	Structure, Prototype	**Pearson Symbol**	***a* (Å)**	***b* (Å)**	***c* (Å)**	***α***	***β***	***γ***	**Molar Volume (cm^3/mol)**
MgGd	Cubic, CsCl	cP2	3.773			90°			16.17
Mg_2Gd	C15 Laves	cF24	8.657			90°			16.27
Mg_3Gd	Cubic, BiF_3	cF16	7.353			90°			14.96
Mg_5Gd	Cubic	cF439.84	22.23			90°			15.04
Mg_6Gd	Hexagonal	TBD	13.42		9.77	90°		120°	TBD

7.4.3 Diffusion Kinetics

The thickness, *x*, of each layer was measured from multiple SEM fields of view using ImageJ™ image processing and analysis software. Table 18 presents the diffusion anneal parameters, layers evolved, and layer thicknesses. Parabolic growth constants were calculated according to Equation 1, and are reported in Table 18. The Mg_3Gd phase grows slightly slower than the Mg_5Gd phase, but both phases grow substantially faster than Mg_2Gd and MgGd. The Mg_6Gd phase grows comparably as fast as Mg_5Gd and Mg_3Gd. However, as temperature increases, the layer growth rate does not increase. Thermally activated processes can be represented as a function of temperature using the Arrhenius Relationship, as shown in Figure 38. The pre-exponential factor and activation energy of parabolic growth are calculated on the basis of this relationship. As reported in Table 18 and displayed by Figure 38, the activation energy and pre-exponential factor of Mg_5Gd and Mg_3Gd are similar as would be expected by the observed layer thicknesses. On the other hand, the thinnest layer, MgGd, has the smallest activation energy while the second thinnest layer has the largest activation energy. In addition, it is evident from Figure 38 that Mg_6Gd is not exclusively thermally activated. It is possible the growth constant for Mg_6Gd is time-dependent, meaning local equilibrium has not been achieved or maintained [139, 140].

Table 18: Layer thicknesses and parabolic growth constants for intermetallic compounds in Mg-Gd system

Anneal Parameters		**Mg_6Gd**	**Mg_5Gd**	**Mg_3Gd**	**Mg_2Gd**	**MgGd**
500°C/66hr	Thickness (μm)	--	256.50 (±4.54)	252.84 (±4.39)	5.19 (±0.82)	1.28 (±0.33)
	k_p (m^2/sec)	--	$1.38x10^{-13}$	$1.34x10^{-13}$	$5.66x10^{-17}$	$3.44x10^{-18}$
490°C/72hr	Thickness (μm)	--	227.19 (±2.76)	159.37 (±3.06)	3.58 (±0.44)	1.37 (±0.81)
	k_p (m^2/sec)	--	$9.95x10^{-14}$	$4.90x10^{-14}$	$2.48x10^{-17}$	$3.60x10^{-18}$
475°C/75hr	Thickness (μm)	--	246.92 (±3.41)	170.92 (±3.29)	4.65 (±0.72)	1.00 (±0.35)
	k_p (m^2/sec)	--	$1.13x10^{-13}$	$5.41x10^{-14}$	$4.01x10^{-17}$	$1.86x10^{-18}$
475°C/96.5hr	Thickness (μm)	22.44 (±7.02)	203.96 (±6.66)	134.88 (±2.25)	2.95 (±0.38)	1.17 (±0.42)
	k_p (m^2/sec)	$7.25x10^{-16}$	$5.99x10^{-14}$	$2.62x10^{-14}$	$1.26x10^{-17}$	$1.98x10^{-18}$
450°C/90hr	Thickness (μm)	39.91 (±21.63)	164.45 (±13.85)	97.74 (±4.20)	2.92 (±0.38)	0.91 (±0.29)
	k_p (m^2/sec)	$2.46x10^{-15}$	$4.17x10^{-14}$	$1.47x10^{-14}$	$1.32x10^{-17}$	$1.29x10^{-18}$
425°C/166.5hr	Thickness (μm)	58.56 (±12.33)	83.95 (±7.25)	53.11 (±1.38)	1.26 (±0.31)	0.63 (±0.20)
	k_p (m^2/sec)	$2.86x10^{-15}$	$5.88x10^{-15}$	$2.35x10^{-15}$	$1.32x10^{-18}$	$3.36x10^{-19}$
385°C/192hr	Thickness (μm)	43.96 (±9.56)	50.60 (±6.18)	40.56 (±2.01)	0.53 (±0.14)	0.42 (±0.15)
	k_p (m^2/sec)	$1.40x10^{-15}$	$1.85x10^{-15}$	$1.19x10^{-15}$	$2.05x10^{-19}$	$1.29x10^{-19}$
k_o (m^2/sec)		--	$4.31x10^{-2}$	$5.51x10^{-2}$	$4.77x10^{-3}$	$1.98x10^{-9}$
Q (kJ/mol)		--	168.89	174.45	205.80	128.79

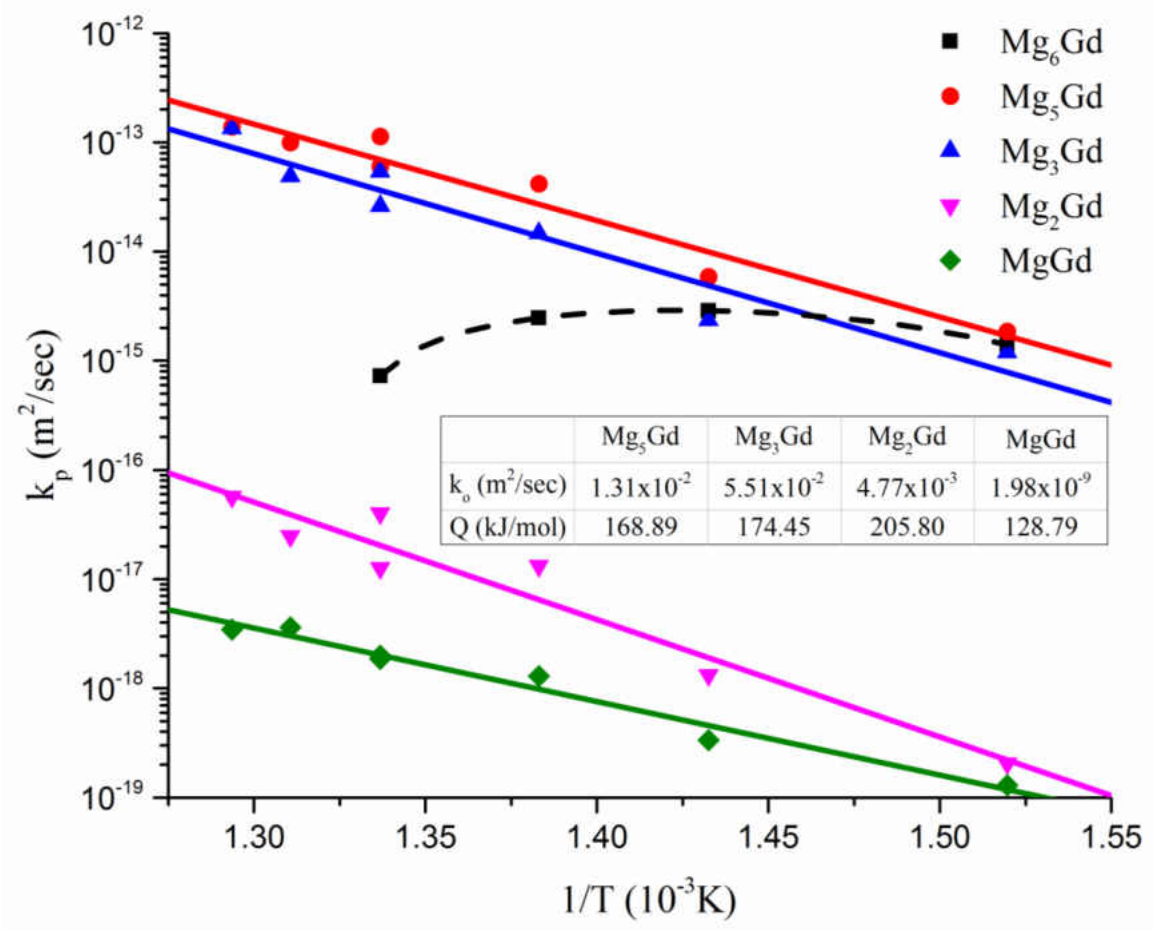

Figure 38: Parabolic growth constants plotted as a function of temperature

The integrated interdiffusion coefficients were calculated from Equation 2 for the intermediate phases using the phase diagram compositions for Mg solid solution, Mg_5Gd, Mg_3Gd, Mg_2Gd, and MgGd; the nominal XEDS composition of Mg_6Gd was used to calculate its integrated interdiffusion coefficient. Solubility of Mg in Gd was not observed, and therefore is not used in calculations of integrated interdiffusion coefficients. In addition, because Mg_6Gd did not exhibit parabolic growth, its integrated interdiffusion coefficients were not calculated. The integrated interdiffusion coefficients are plotted as a function of

inverse temperature in Figure 39. The temperature specific coefficients as well as the activation energy and pre-exponential factor for the observed intermediate phases are reported in Table 13.

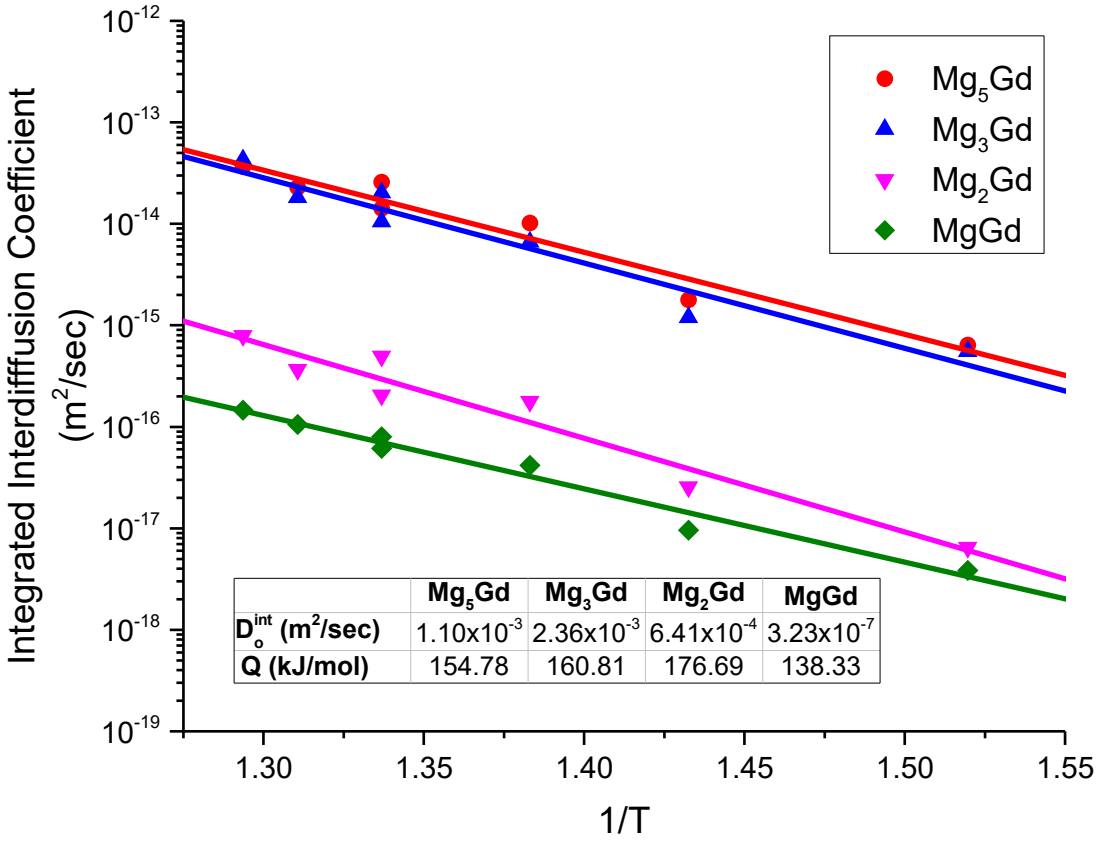

	Mg_5Gd	Mg_3Gd	Mg_2Gd	MgGd
D_o^{int} (m^2/sec)	1.10×10^{-3}	2.36×10^{-3}	6.41×10^{-4}	3.23×10^{-7}
Q (kJ/mol)	154.78	160.81	176.69	138.33

Figure 39: Integrated interdiffusion coefficient for Mg_5Gd, Mg_3Gd, Mg_2Gd, and MgGd phases

Similar trends seen in the activation energy for growth are seen in the activation energy for integrated interdiffusion. Mg_2Gd has the largest activation energy while MgGd has the smallest activation energy. The activation energy for Mg_3Gd is slightly larger than that for Mg_5Gd. The similarity in the activation energy for growth and integrated

interdiffusion imply that the growth of each intermetallic phase is not influenced by the growth of other phases. A substantial difference in magnitude between the parabolic growth constants and integrated interdiffusion coefficients for Mg_2Gd and MgGd is observed. The integrated interdiffusion coefficient for Mg_2Gd is an order of magnitude larger than its parabolic growth constant; the integrated interdiffusion coefficient for MgGd is nearly two orders of magnitude large than the parabolic growth constant. Because growth constants have a complex meaning dependent on the diffusion coefficients of all phases as well as the solubility limits of the phases, these differences may indicate a dominance of thermodynamic influences of ordering or kinetic influences of mechanism on the diffusion kinetics. The atom-vacancy exchange probability and frequency, the configuration entropy, and the correlation factor are all influenced by the degree of ordering [126-128]. When grain size is sufficiently small, as in the case of very thin layers, the measured interdiffusion coefficient includes both bulk and grain boundary diffusivities [62, 129].

Table 19: Integrated interdiffusion coefficients for intermediate phases in the Mg-Y system

		Mg_5Gd	**Mg_3Gd**	**Mg_2Gd**	**MgGd**
$\widetilde{D}^{int}$ **(m²/s)**	385°C	6.38×10^{-16}	5.51×10^{-16}	6.42×10^{-18}	3.89×10^{-18}
$\widetilde{D}^{int}$ **(m²/s)**	425°C	1.78×10^{-15}	1.20×10^{-15}	2.54×10^{-17}	9.70×10^{-18}
$\widetilde{D}^{int}$ **(m²/s)**	450°C	1.02×10^{-14}	6.60×10^{-15}	1.76×10^{-16}	4.20×10^{-17}
$\widetilde{D}^{int}$ **(m²/s)**	475°C	1.42×10^{-14}	1.04×10^{-14}	2.04×10^{-16}	6.19×10^{-17}
$\widetilde{D}^{int}$ **(m²/s)**	475°C	2.57×10^{-14}	2.02×10^{-14}	4.92×10^{-16}	8.08×10^{-17}
$\widetilde{D}^{int}$ **(m²/s)**	490°C	2.28×10^{-14}	1.82×10^{-14}	3.65×10^{-16}	1.07×10^{-16}
$\widetilde{D}^{int}$ **(m²/s)**	500°C	3.67×10^{-14}	4.28×10^{-14}	7.86×10^{-16}	1.48×10^{-16}
$\widetilde{D}_o^{int}$ **(m²/s)**		1.10×10^{-3}	2.36×10^{-3}	6.41×10^{-4}	3.23×10^{-7}
Q **(kJ/mol)**		154.79	160.81	176.69	138.33

The diffusion couples annealed at 385°C for 192 hours, 475°C for 96.5 hours, and 490°C for 72 hours were subjected to EPMA in order to establish precise compositional profiles. The concentration dependent interdiffusion coefficient was calculated according to the Boltzmann-Matano method, presented in Figure 40. Because a concentration profile could not be measured across the small thicknesses of the Mg_2Gd and MgGd phases, concentration dependent interdiffusion coefficients could not be determined for these phases. Similarly, because no measureable concentration gradient was observed in the Gd solid solution, interdiffusion coefficients could not be determined for this phase either. Interdiffusion in the intermetallic phases of the Mg-Gd system is not strongly composition dependent. Interdiffusion in Mg_3Gd is concentration independent, whereas the interdiffusion coefficient increases with increasing Gd content in Mg_6Gd and Mg_5Gd while it

decreases with increasing Gd content in the Mg solid solution. Interdiffusion occurs most readily in Mg_5Gd.

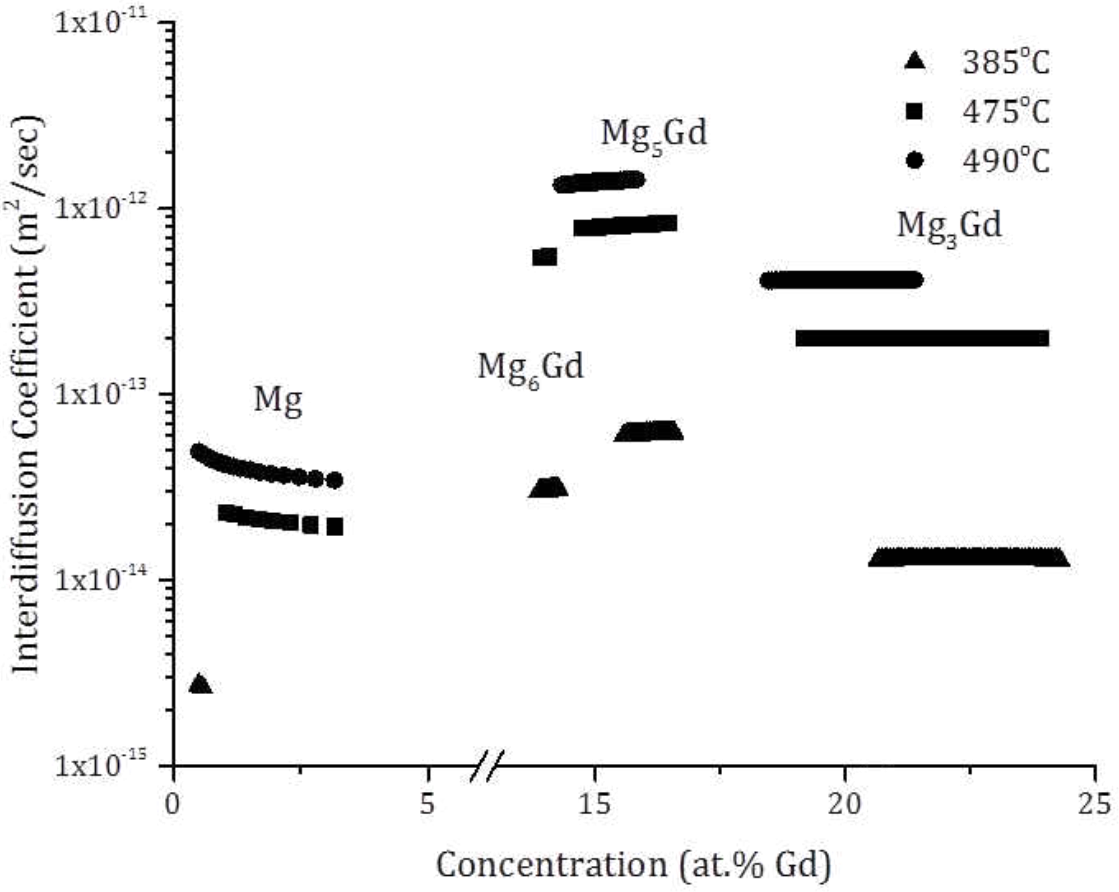

Figure 40: Concentration dependent interdiffusion coefficients for Mg solid solution, Mg_6Gd, Mg_5Gd, and Mg_3Gd

The effective interdiffusion coefficients were calculated using Equation 8. The temperature dependence of the coefficients is examined in Figure 41, from which the pre-exponential factor and activation energy are determined. These effective interdiffusion coefficients, pre-exponential factors, and activation energies for the intermediate phases

and Mg solid solution are reported in Table 20. The activation energy for interdiffusion in Mg_5Gd is smallest while that for Mg solid solution is largest.

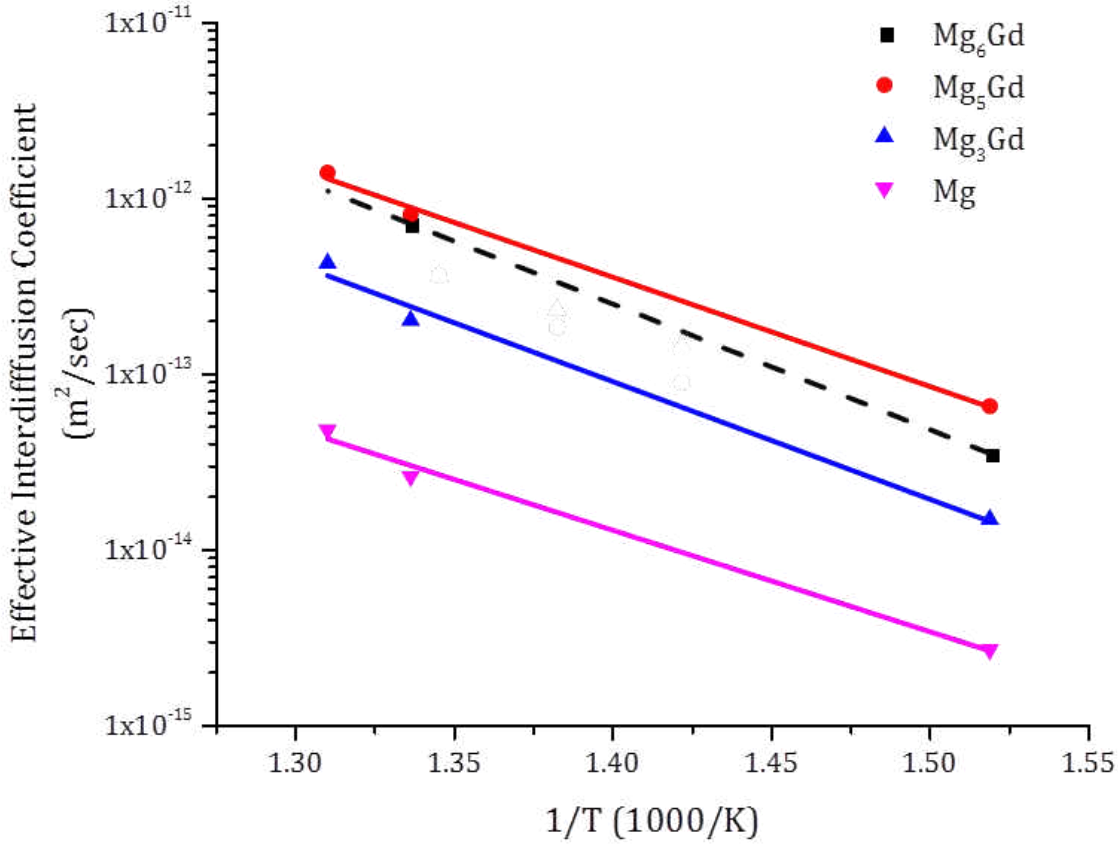

Figure 41: Effective interdiffusion coefficients for Mg, Mg_3Gd, Mg_5Gd, and Mg_6Gd as a function of temperature

Table 20: Effective interdiffusion coefficients for intermediate phases in the Mg-Gd system

		Mg(Gd)	**Mg_6Gd**	**Mg_5Gd**	**Mg_3Gd**
$\widetilde{D}^{eff}$ **(m²/s)**	385°C	2.62×10^{-15}	3.43×10^{-14}	6.39×10^{-14}	1.44×10^{-14}
$\widetilde{D}^{eff}$ **(m²/s)**	475°C	2.54×10^{-14}	6.98×10^{-13}	7.91×10^{-13}	1.97×10^{-13}
$\widetilde{D}^{eff}$ **(m²/s)**	490°C	4.68×10^{-14}	--	1.37×10^{-12}	4.16×10^{-13}
$\widetilde{D}_o^{eff}$ **(m²/s)**		1.51×10^{-6}	2.58×10^{-3}	1.80×10^{-4}	2.15×10^{-4}
Q **(kJ/mol)**		110.44	137.00	119.11	128.29

Using the Hall interdiffusion coefficient at the infinitely dilute composition, the impurity diffusion coefficients were extracted from the EPMA concentration profiles. Implementation of the Hall method was carried out by performing a linear regression of the concentration distribution versus Boltzmann parameter over the composition range of 0.02–0.5 at.%Gd. The impurity diffusion coefficient is extrapolated from the interdiffusion coefficients at concentrations less than 0.2 at.%Gd as shown in Figure 42.

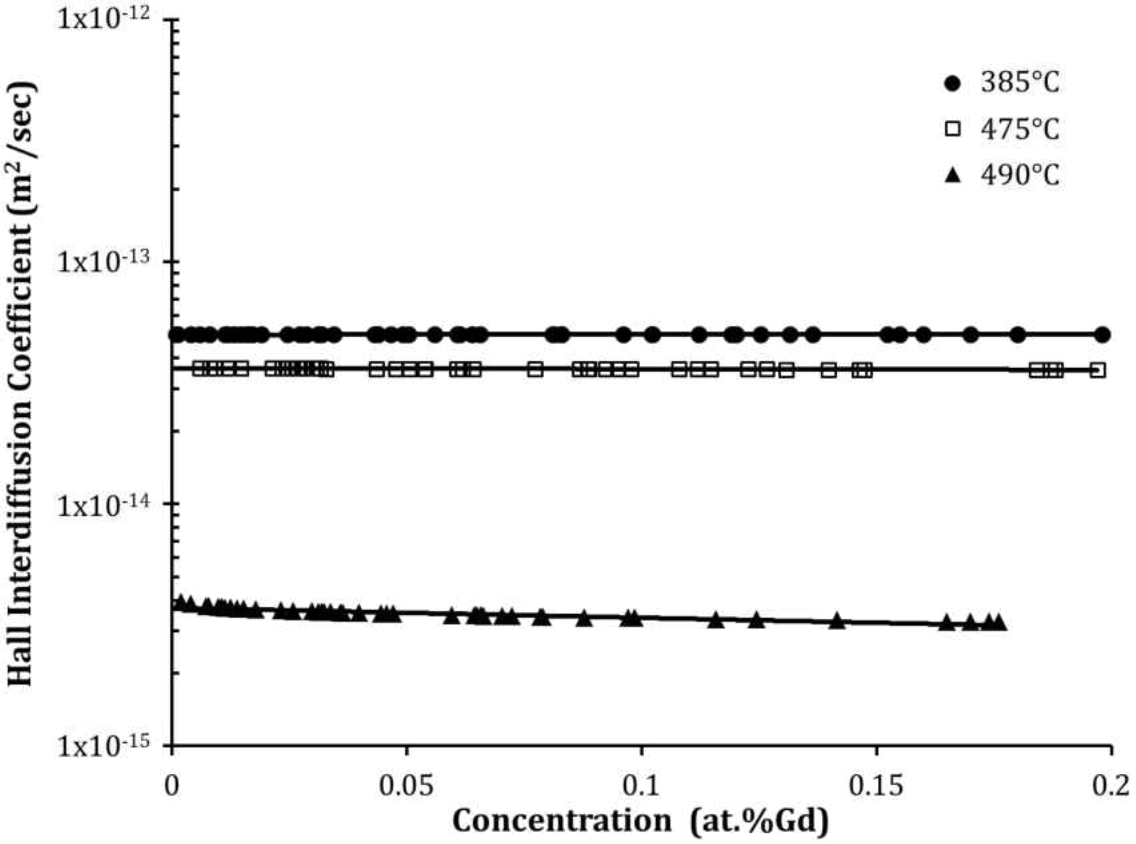

Figure 42: Hall interdiffusion coefficients in dilute Mg solid solution

Table 21 reports the findings of this study as well as literature values. The values reported in literature do not agree well with the values found in this study. There is an order of magnitude difference in the impurity diffusion coefficients. Prior to this study, Gd impurity diffusion coefficients were computed using a multiphase diffusion simulation approach and extrapolated from single-crystal experimental data by fitting the data to the Gaussian, or thin film, solution of Fick's diffusion equation [81]. The difference in reported impurity diffusion coefficients can be attributed to the assumptions made in the simulation and experimental solutions. Given this study demonstrated that the interdiffusion

coefficient decreases with increasing solute concentration in Mg solid solution, it is understandable [81] approximated the impurity diffusion to be lower than presently determined.

While the impurity diffusion coefficients and the interdiffusion coefficients in Mg solid solution are fairly consistent with each other, the activation energy for Gd impurity diffusion is lower than the activation energy for interdiffusion in Mg solid solution. The pre-exponential factor for impurity diffusion is an order of magnitude smaller than that for interdiffusion in Mg solid solution.

Table 21: Gd Impurity diffusion coefficients in Mg solid solution

		Mg(Gd)	**Source**
D_{Gd}^{Mg} **(m²/s)**	385°C	3.72×10^{-15}	This Study
D_{Gd}^{Mg} **(m²/s)**	475°C	3.64×10^{-14}	
D_{Gd}^{Mg} **(m²/s)**	490°C	5.00×10^{-14}	
D_o^{imp} **(m²/s)**		2.21×10^{-7}	
Q **(kJ/mol)**		97.83	
D_o^{imp} **(m²/s)**	***a*-axis** ***c*-axis**	1.27×10^{-9} 1.79×10^{-9}	[81]
Q **(kJ/mol)**	***a*-axis** ***c*-axis**	79.27 81.69	

7.5 Discussion

The intermediate phases in the Mg-Y and Mg-Gd systems are found to have a range of solubility, meaning they are not strict line compounds. Diffusion in the intermediate phases occurs more readily at elevated temperatures in the Mg-Gd system than in the Mg-Y system; at lower temperatures, because of their relatively small activation energy, intermetallic compounds from the Mg-Y phase interdiffuse more freely.

The similarity in the impurity diffusion coefficients for Y and Gd is interesting. Figure 43 plots the results from this study along with the impurity of other elements (i.e. Al, Zn, Ce, La) and the Mg self-diffusion coefficients as a function of temperature [65, 89, 141]. From this figure it is clear that Gd and Y impurity diffusion is intermediate to Al and Zn impurity diffusion over the temperature ranges studied.

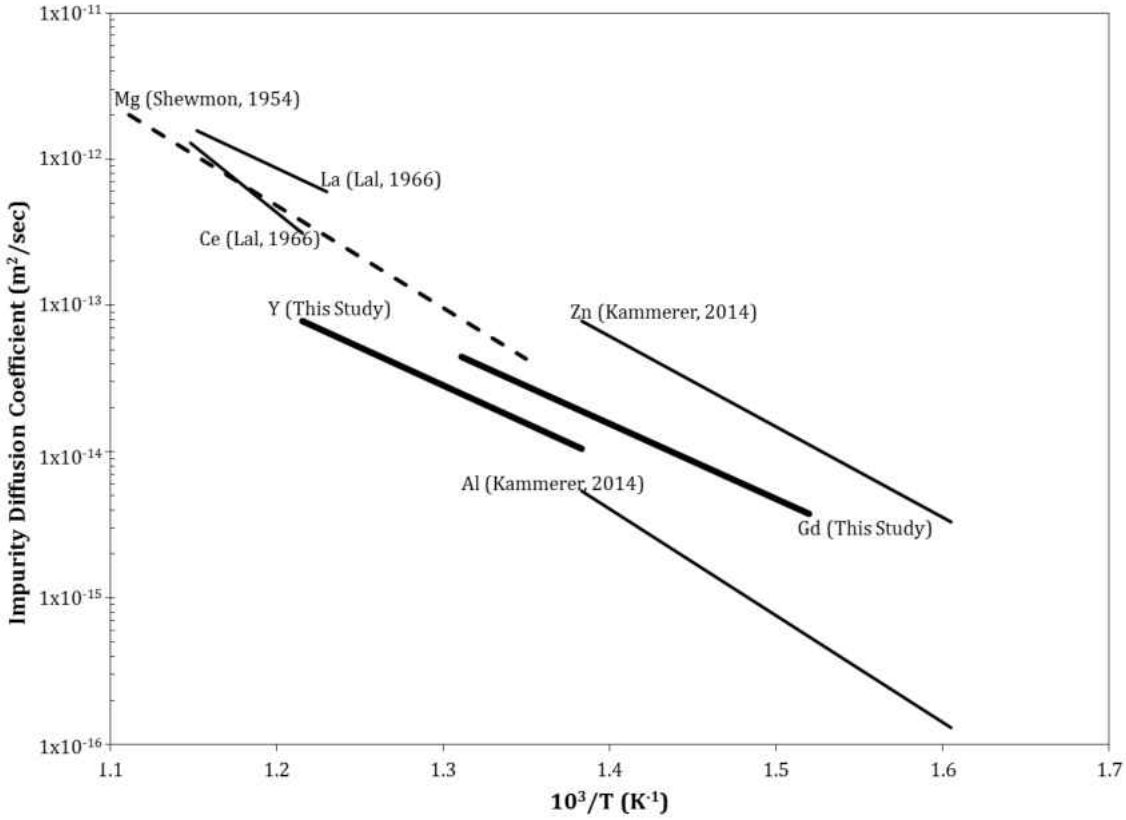

Figure 43: Impurity diffusion as a function of inverse temperature [65, 89, 141]

The RE elements have a larger atomic radius than Mg while Al and Zn are smaller than Mg. Additions of Al or Zn will put the lattice in tension; additions of Y or Gd will compressively strain the lattice. In consideration of elastic strain, where large solutes bind to vacancies as a means of relieving strain on the solvent matrix, one may expect, as suggested by Das [81], the oversized RE solutes will hinder impurity diffusion in Mg. Lal examined this relationship and found no correlation [89]. In further consideration of the impurity diffusion behavior, with the exception of Ce, the activation energy for the Gd, Y, and La impurities is smaller than those of Al and Zn. To better understand the underlying

reasons for these seemingly conflicting observations, the components of the activation must be more closely examined. Using Density Field Theory, Huber *et al*. performed calculations of solute-vacancy binding energies E_B, exchange energies E_X, and other migration barriers (i.e. correlation energies) for vacancy jumps around Al, Ca, and several RE impurities in Mg to obtain activation energies for diffusion [86]. Solute-vacancy binding and exchange barriers relate strongly with the solute size, displaying increasing E_B and decreasing E_X with increasing solute size (i.e. decreasing the activation energy). However, in the same study, correlation energies were found to increase with solute size, providing a compensating effect for the activation energy. All of the lanthanides investigated as well as Ca were found to have lower activation energies than Mg self-diffusion [86].

Interdiffusion in Mg(Gd) and Mg(Y) is strongly concentration dependent, decreasing with increasing solute concentration. This trend is unique in comparison with interdiffusion in Mg(Al) or Mg(Zn). Kammerer *et al.* [65] reported the magnitude of Mg(Al) interdiffusion coefficient increases as Al concentration increases while interdiffusion in Mg(Zn) was only slightly concentration dependent. In fact, the activation energy for interdiffusion in Mg(Al) and Mg(Zn) is reported as 186.8 kJ/mol and 139.5 kJ/mol, respectively [65]. An interdiffusion activation energy of 110.4 kJ/mol and 84.4 kJ/mol is found in this study for Mg(Y) and Mg(Gd), respectively. It is evident that the solute size may play a role on the concentration dependent interdiffusion coefficient in solid solution.

7.6 Summary

Solid-to-solid couples of pure polycrystalline Mg versus Gd and Mg versus Y were diffusion bonded. Evolved phases were characterized in terms of homogeneity ranges and crystal structures. Parabolic growth constants, interdiffusion coefficients, and impurity diffusion coefficients were calculated.

Based on the diffusion reaction zone morphology and the presence of Kirkendall voids, Mg was qualitatively found to diffuse faster than Y. The fastest growing phase in the Mg-Y system is ε-$Mg_{24}Y_5$; the slowest growing phase is MgY. The growth of each equilibrium phase is independent of the growth of other equilibrium phases in the Mg-Y system. However, ordering influence the diffusion in ε-$Mg_{24}Y_5$. Interdiffusion is concentration dependent in the Mg-Y system. The activation energy for Y impurity diffusion in Mg solid solution is smaller than the activation energy for interdiffusion in Mg solid solution; on the other hand, the pre-exponential factor for impurity diffusion is greater than that for interdiffusion.

The intermediate phases in the Mg-Gd system were found to have a range of homogeneity rather than maintaining the composition of the line compounds as shown in the equilibrium phase diagram. Additionally, a previously unidentified phase, Mg_6Gd, with an apparent modulated hexagonal superlattice (a = 13.42Å, c = 9.78Å) was found to be in equilibrium with Mg solid solution. The growth of this phase is not Arrhenius and may be time dependent. Mg_5Gd is the fastest growing phase while MgGd is the slowest. As was observed in the Mg-Y system, layer growth does not appear to be affected by the growth of other phases. Similarly, interdiffusion in Mg_2Gd and MgGd may be dominated by

thermodynamic factors or diffusion mechanisms. Unlike the Mg-Y system, interdiffusion in the intermetallic phases is not strongly concentration dependent. The activation energy and pre-exponential factor for Gd impurity diffusion in Mg solid solution is smaller than the pre-exponential factor and activation for interdiffusion.

CHAPTER 8: MECHANICAL PROPERTIES OF BINARY MAGNESIUM BASED INTERMETALLIC COMPOUNDS AND MAGNESIUM SOLID SOLUTIONS

8.1 Introduction

Mg–based alloys can exhibit both solution strengthening and precipitation hardening effects during decomposition of their supersaturated solid solutions. The connection of the mechanical property enhancements is the solubility of alloying elements in Mg and distribution of the second phase precipitates. In general, the Mg rich end of the binary phase diagrams reveals a eutectic reaction with varying degrees of solubility. Solute atoms with radii similar to Mg have greater solubility. Two of the most common alloying elements in magnesium alloys are aluminum and zinc. Aluminum (fcc) and zinc (hcp) are relatively soluble in magnesium (hcp) at high temperatures, and their solubility decreases at low temperatures. The substitutional solubility of Al in Mg is 11.6 at.% at 437°C and 2.7 at.% at 93°C; the substitutional solubility of Zn in Mg is 2.4 at.% at 340°C and 1.06 at.% at 204°C. Aluminum additions improve the strength and increase the solidification time. Mg alloys containing 5.4 at.%Al have a good balance between strength and ductility while those that have more than 5.4 at.%Al are age hardenable with the precipitation of $Mg_{17}Al_{12}$. Similarly, zinc is added, often times with aluminum, to magnesium in order to improve room temperature properties and corrosion resistance. Magnesium alloyed with Zn can be heat treated to form $Mg_{21}Zn_{25}$ precipitates [9]. Significant improvements to the properties can be achieved through alloying with rare earth (RE) elements. Mg–RE-based alloys exhibit both solution strengthening and precipitation hardening effects during

decomposition of their supersaturated solid solutions thus promoting unique mechanical behavior [118].

To generalize, the properties of the precipitate strengthened system increases linearly with increasing solute content and can be estimated by the composite rule of mixture model [11]. Therefore, to predict the mechanical properties of Mg alloys, the variation in mechanical properties as a function of solute concentration and those of the second phase precipitates must be known.

Solid solution strengthening manifests because solutes diffuse to dislocations in order to minimize the energy caused by the lattice strain. In order for the dislocation to move, it must either break away from the solute atmosphere (i.e. Cottrell atmosphere) or drag it along. The symmetry of the lattice distortion affects which types of dislocations are mired by the solute. Symmetric stress fields can only interact with hydrostatic stress fields of edge dislocations, whereas asymmetric stress fields can interact with the hydrostatic stress field of edge dislocations and the translational stress field of screw dislocations. [20]. The symmetry of lattice distortion can be inferred from the change in flow stress as a function of concentration. Symmetric distortion results in a linear concentration dependence, while flow stress in the presence of asymmetric lattice distortion is a function of the square root of solute concentration[142]. Hardness is the localized resistance to yielding and can be considered analogous to the flow stress [143]. An examination of the relationship between hardness and concentration can provide insight into the symmetry of the lattice distortion and the nature of the strengthening mechanism. On the other hand, the reduced modulus is proportional to elastic modulus, which is fundamentally related to

the interatomic bonding and binding energy. An increase in the modulus implicitly equates to an increase the attractive forces. That is, the derivative of the potential energy is the net force acting on two members; the slope of the force-displacement profile at equilibrium separation is proportional to the modulus of elasticity. Therefore, the modulus determined from indentation testing provides some insight into the general nature of bonding.

The elastic and plastic properties for each phase are determined through analysis of the load-displacement profiles by the Oliver-Pharr method. This study is the first measurement of mechanical properties (i.e. hardness, reduced modulus, creep, inhomogeneous yielding) of intermetallic compounds and solid solutions relevant to Mg alloys.

8.2 Hardness and Reduced Modulus in Mg-X (X = Al, Gd, Nd, Y, Zn) Intermetallic Compounds

The mechanical properties of binary Mg intermetallic compounds were measured by nanomechanical indentation testing. The reduced modulus and hardness were calculated from the multiple load-displacement curves. For comparison and validation, the mechanical properties of the pure elements were also measured. Figure 44, Figure 45, Figure 46, Figure 47, and Figure 48 show the typical nanoindentation load-displacement curves for the intermetallic phases in Mg-Al, Mg-Gd, Mg-Nd, Mg-Y and Mg-Zn binary systems, respectively.

Several qualitative observations can be made based on the load-displacement curves. Specifically, during the three-second holding segment of the nanoindentation

loading profile, the pure metals show significant creep whereas the intermetallic compounds tend to have negligible creep.

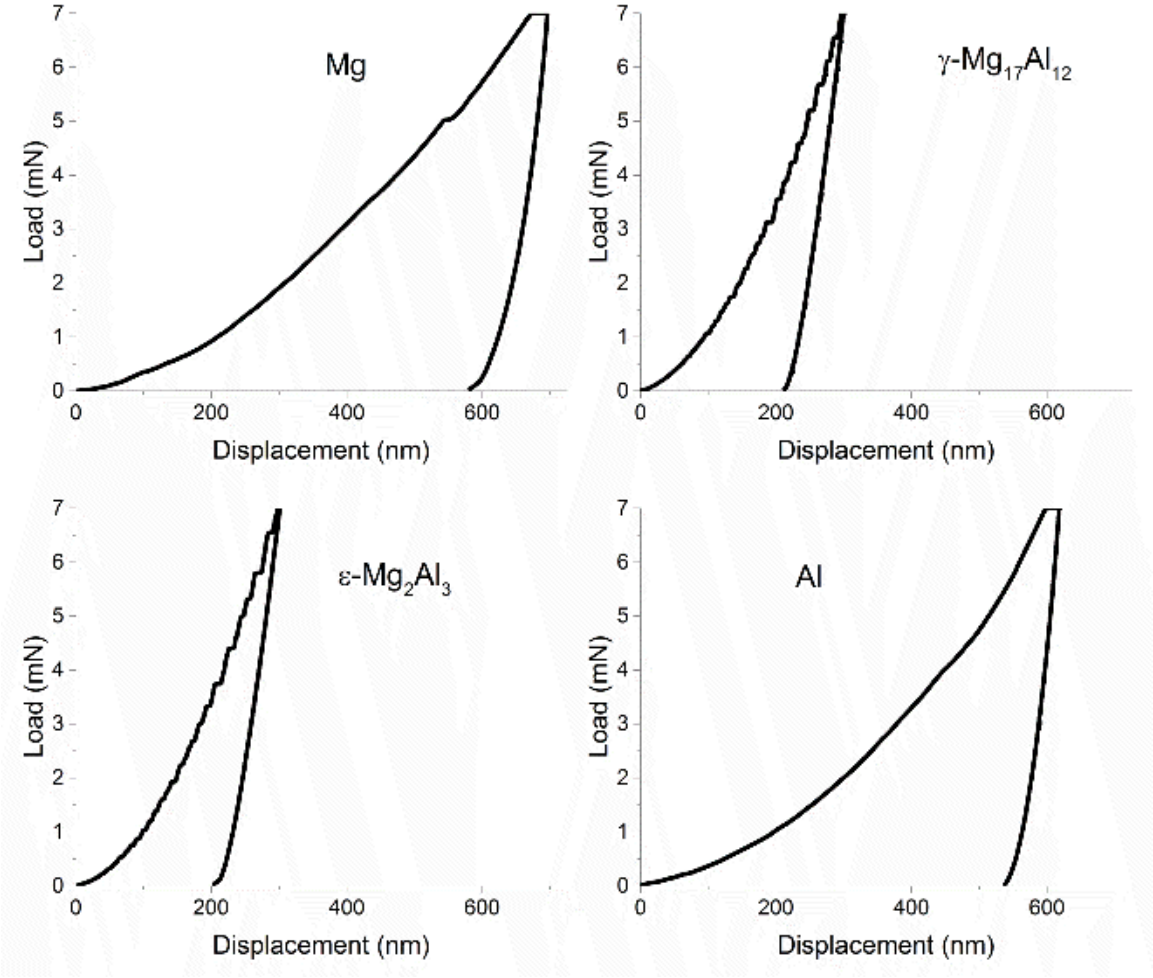

Figure 44: Typical load-displacement curves for the intermetallic compounds in the Mg-Al system including pure Mg and pure Al

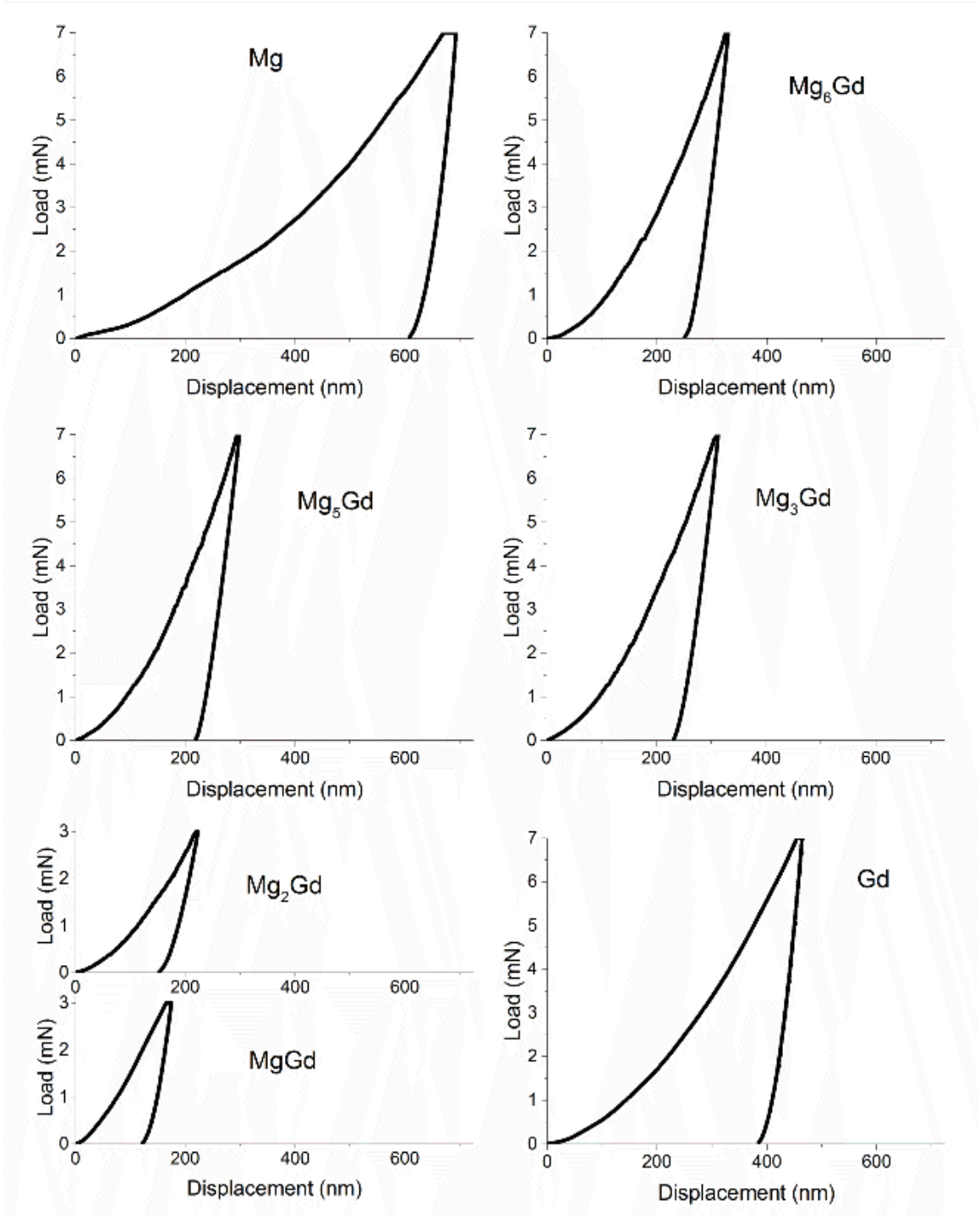

Figure 45: Typical load-displacement curves for the intermetallic compounds in the Mg-Gd system including pure Mg and pure Gd

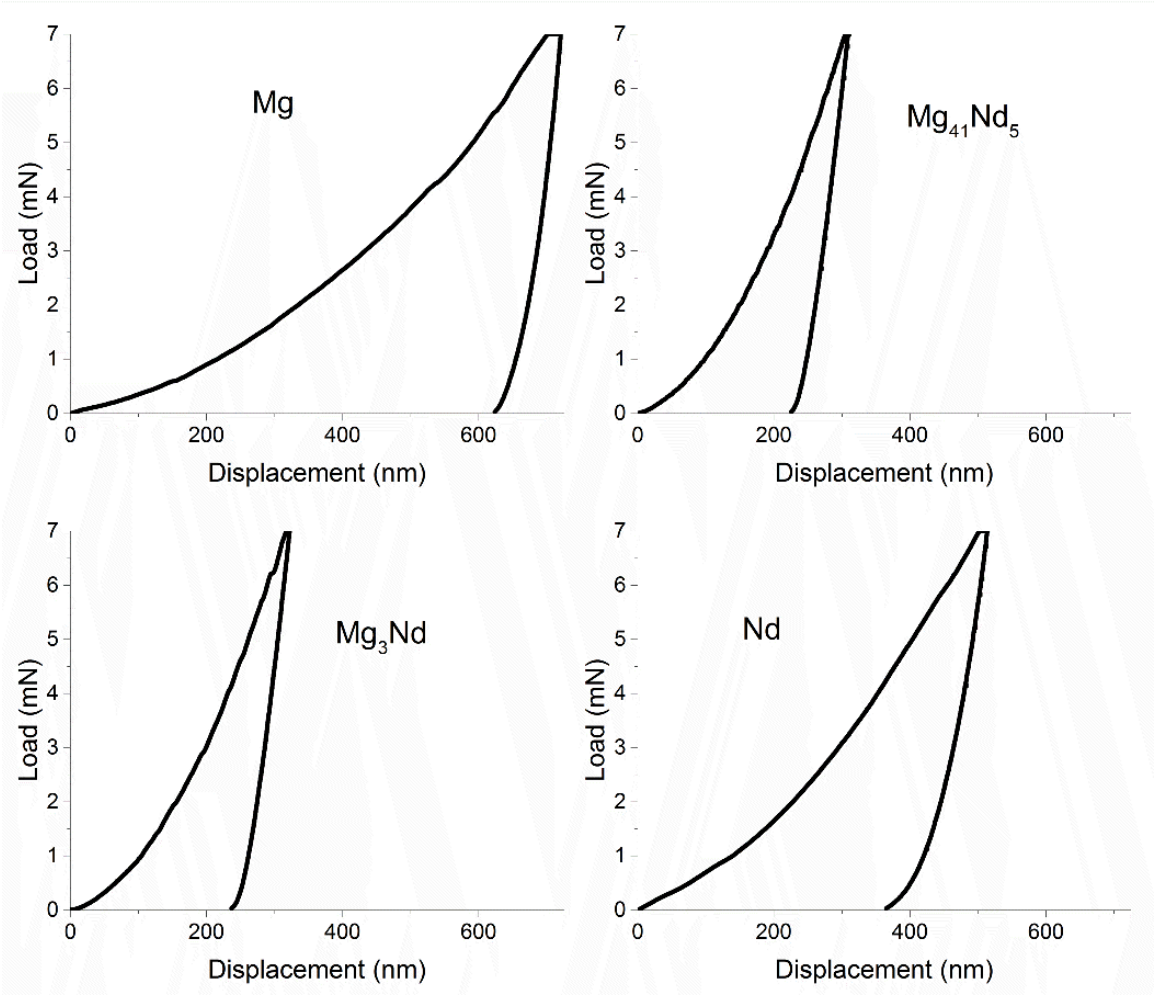

Figure 46: Typical load-displacement curves for the intermetallic compounds in the Mg-Nd system including pure Mg and pure Nd

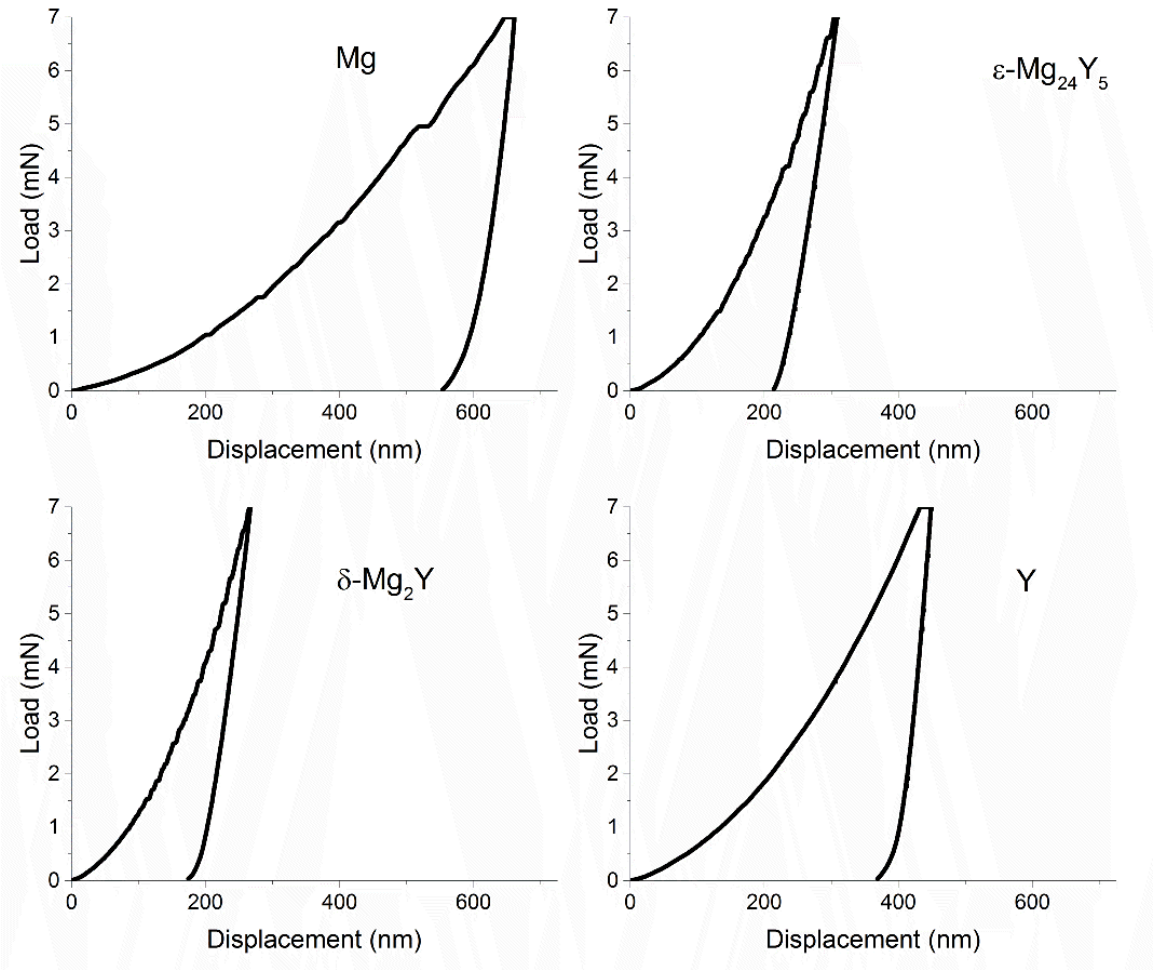

Figure 47: Typical load-displacement curves for the intermetallic compounds in the Mg-Y system including pure Mg and pure Y

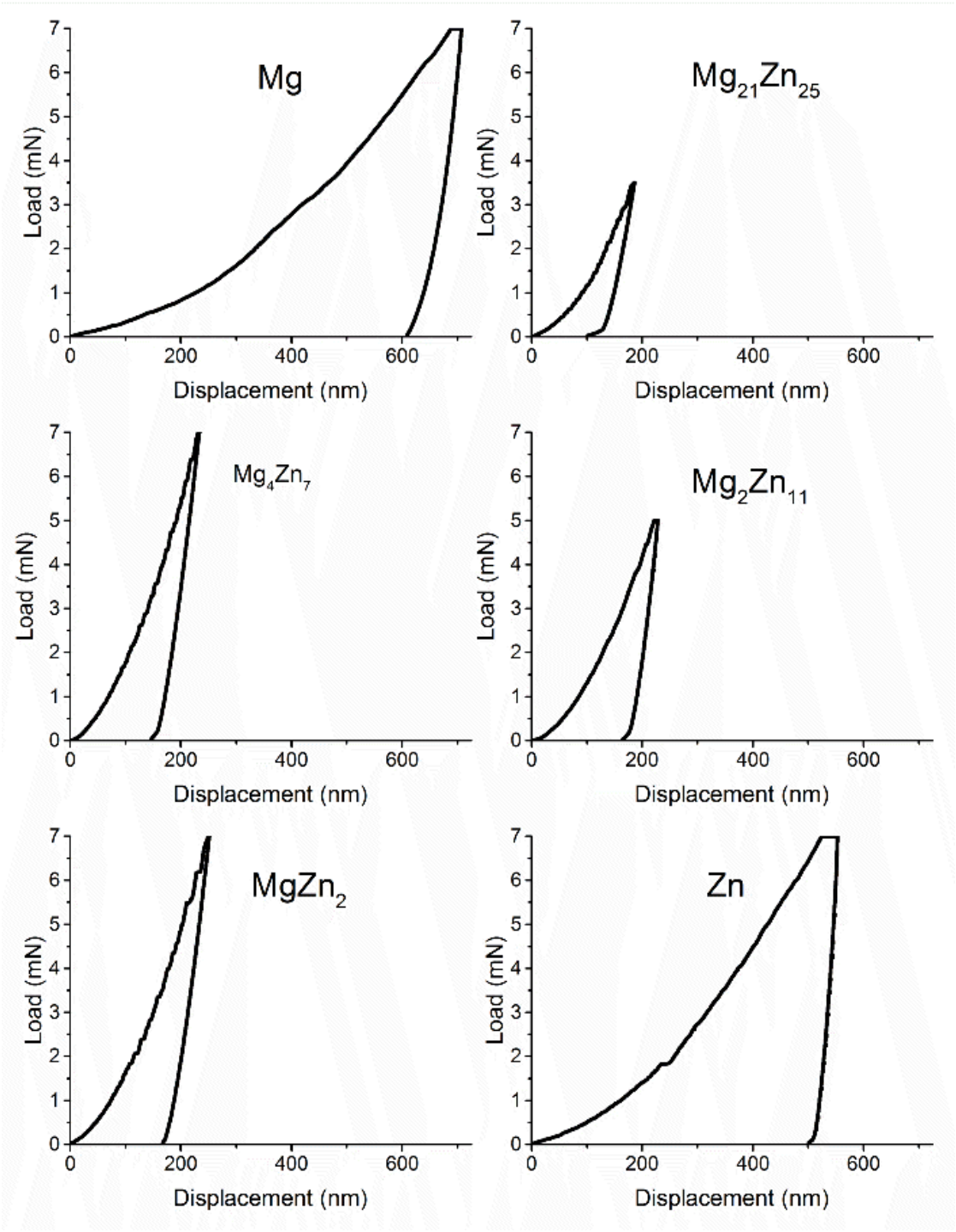

Figure 48: Typical load-displacement curves for the intermetallic compounds in the Mg-Zn system including pure Mg and pure Zn

Additionally, serrations seen in the loading profile are formed because of discontinuous yielding during plastic deformation. These serrations are termed pop-ins. This phenomenon is most commonly attributed to dynamic strain aging, often called Portevin – Le Chatelier (PLC) effect, and is due to interactions between moving dislocations and diffusing solute atoms, which leads to instantaneous negative strain rate sensitivity and localization of flow [144, 145]. The solute atoms catch and pin the dislocations. When the dislocations are torn away from the solute atoms, a jump in displacement is observed. The PLC effect has been well studied in Al-Mg alloys and is associated with free flight of mobile dislocations between subsequent blockings at obstacles [146-148]. However, dynamic strain aging is not the only phenomenon that can cause serrated load-displacement curves. Order-disorder transformations and mechanical twinning during deformation as well as work hardening sensitivity can also produce the same effect [20, 149]. In fact, it is understood that the PLC effect occurs within specific limits of temperature, strain, strain rate, and impurity concentration [145, 148].

Based on the load-displacement curves in Figure 44, the studied intermetallic compounds in the Mg-Al system are subject to significant inhomogeneous yielding. Similarly, from Figure 47 and Figure 48, the intermetallic compounds tested in the Mg-Y and Mg-Zn systems, respectively, exhibited sudden bursts of strain during loading. On the other hand, deformation of the Mg-Gd and Mg-Nd intermetallic compounds was stable throughout the loading cycle as evident in Figure 45 and Figure 46. Very few discontinuities are seen in the loading segment of the load-displacement curves for the pure metals.

The calculated hardness and reduced modulus along with their standard deviations of the pure metals are presented in Table 22, while those for the intermetallic phases are reported in Table 23. All tests were performed under load controlled feedback with a 10-3-10 load-hold-unload cycle. Peak loading was 7mN unless otherwise specified. Table 22 also includes literature values for Young's Modulus, Poisson ratio, and reduced modulus converted with Equation 19. Table 23 is organized is such a way that the first phase listed for each system is the phase in thermodynamic equilibrium with Mg solid solution.

Quantitatively, indentation creep, C_{IT}, can be measured as the change in displacement during the three-second hold segment. Under the designated test conditions (i.e. 10-3-10 at 7mN peak load unless otherwise specified), the primary strengthening phases undergo only 20 – 30% of the creep exhibited by the unalloyed elements. The indentation creep for the pure and primary strengthening phases is reported in Table 24. Likewise, the mechanical instabilities manifested as serrations in the load-displacement curves are quantified for the pure metals and the primary strengthening phases in Table 24. The average number of serrations was obtained by counting each step that was present in a sampling of load-displacement curves at loads greater than 1mN. The strain burst is the average displacement of a single step. The plastic instability is the percentage of total displacement during loading that can be attributed to pop-ins occurring at loads greater than 1mN.

Table 22: Hardness and reduced modulus (± 1σ) of pure metals determined from load-displacement curves by the Oliver-Pharr method

Metal	Pearson Symbol	Hardness (GPa)	Reduced Modulus (GPa)	From Wolfram ElementData [150]		
				Young's Modulus (GPa)	Poisson Ration	Reduced Modulus (GPa)
Mg	hP2	0.5 (±0.0)	35.0 (±1.7)	45	0.29	47
Al	cF4	0.6 (±0.0)	41.9 (±1.6)	70	0.35	75
Gd	hP2	1.5 (±0.2)	64.6 (±3.3)	55	0.26	56
Nd	hP4	1.1 (±0.1)	35.1 (±3.5)	41	0.28	43
Y	hP2	1.5 (±0.1)	70.9 (±2.7)	64	0.24	64
Zn	hP2	0.8 (±0.0)	76.4 (±3.7)	108	0.25	105

Table 23: Hardness and reduced modulus (± 1σ) of Mg-based intermetallic compounds determined from load-displacement curves by the Oliver-Parr method

System	Phase	Pearson Symbol	Hardness (GPa)	Reduced Modulus (GPa)
Mg-Al	γ-$Mg_{17}Al_{12}$	cI58	3.4 (±0.3)	69.8 (±6.1)
	β-Mg_2Al_3	cF1168	3.5 (±0.3)	65.0 (±3.0)
Mg-Gd	Mg_6Gd	TBD	3.1 (±0.1)	68.7 (±4.5)
	Mg_5Gd	cF440	4.0 (±0.1)	74.8 (±1.4)
	Mg_3Gd	cF16	3.2 (±0.1)	74.3 (±4.7)
	Mg_2Gd	cF24	2.9[(1)]	57.6[(1)]
	MgGd	cP2	4.2 (±0.5) [(1)]	97.9 (±2.8) [(1)]
Mg-Nd	$Mg_{41}Nd_5$	tI92	3.1 (0.0)	70.4 (1.0)
			3.0 (±0.1) [(3)]	75.1 (±1.6) [(3)]
	Mg_3Nd	cF16	2.8 (0.2)	69.1(.9)
			3.5 (±0.2) [(3)]	77.1 (±2.0) [(3)]
	MgNd	cP2	Not Tested	
Mg-Y	ε-$Mg_{24}Y_5$	cI58	3.7 (±0.1)	63.3 (±1.5)
	δ-Mg_2Y	hP12	5.0 (±0.2)	82.7 (4.7)
	MgY	cP2	Not Tested	
Mg-Zn	$Mg_{21}Zn_{25}$	hR276	4.7 (±0.9) [(2)]	83.2 (±9.2) [(2)]
	Mg_4Zn_7	mC110	5.1 (±0.5)	94.1 (±3.6)
	$MgZn_2$	hP12	5.1 (±0.3)	87.3 (±3.1)
	Mg_2Zn_{11}	cP39	3.8 (±0.4)	108.9 (±6.4)

[(1)] 3mN peak load
[(2)] 3.5mN peak load
[(3)] 5mN peak load

Table 24: Indentation creep and plastic instability (±1σ) of pure metals and Mg-based intermetallic compounds determined from load-displacement curves

System	Phase	Indentation Creep (%)	Serration Steps	Strain Burst (nm)	Plastic Instability (%)
Pure Metals	Mg	2.4 (±0.1)	1.5 (±1.0)	4.5 (±1.2)	1.3 (±1.0)
	Al	3.3 (±0.3)	2.8 (±1.5)	6.2 (±2.7)	3.1 (±1.7)
	Gd	2.2 (±0.4)	0.5 (±1.0)	1.2 (±0.4)	0.5 (±1.0)
	Nd	2.2 (±0.4)	0.0 (±0.0)	0.0 (±0.0)	0 (±0.0)
	Y	3.2 (±1.4)	0.0 (±0.0)	0.0 (±0.0)	0 (±0.0)
	Zn	4.3 (±0.5)	2.2 (±2.1)	7.8 (±2.4)	2.6 (±2.1)
Mg-Al	γ-$Mg_{17}Al_{12}$	0.8 (±0.4)	19.8 (±3.0)	5.0 (±2.6)	26.4 (±11.7)
Mg-Gd	Mg_5Gd	1.3 (±0.4)	7.0 (±2.2)	2.1 (±1.3)	4.9 (±1.2)
	Mg_3Gd	1.3 (±0.3)	10.2 (±1.9)	1.9 (±1.0)	6.4 (±1.8)
Mg-Nd	$Mg_{41}Nd_5$	1.3 (±0.3)	9.8 (1.5)	1.7 (0.8)	5.4 (±1.3)
	Mg_3Nd	1.6 (±0.2)	6.5 (1.3)	2.5 (1.9)	5.0 (±0.8)
Mg-Y	ε-$Mg_{24}Y_5$	0.6 (±0.5)	13.0 (±1.4)	10.3 (±2.0)	12.4 (±1.3)
Mg-Zn	$Mg_{21}Zn_{25}$	1.7 (±0.7) (1)	12.5 (±3.0) (1)	2.3 (±1.1) (1)	16.0 (±4.8) (1)
	Mg_4Zn_7	1.0 (±0.3)	17.2 (±2.2)	3.1 (±1.4)	22.2 (±1.5)
	$MgZn_2$	1.4 (±0.6)	15.5 (±1.3)	2.67 (±1.0)	16.8 (±1.4)

(1) 3.5mN peak load

All intermetallic compounds exhibited higher hardness with respect to their pure constituents; the increase in reduced modules is less significant. It can be seen from Table 23 that the phase in thermodynamic equilibrium with Mg solid solution is not always the highest strength phase. For example, precipitates of Mg_4Zn_7 and $MgZn_2$ will form before $Mg_{21}Zn_{25}$ precipitates in equilibrium with Mg solid solution; both Mg_4Zn_7 and $MgZn_2$ have higher mechanical properties than $Mg_{21}Zn_{25}$. Similarly, precipitation of Mg_3Nd will precede transformation to $Mg_{41}Nd_5$ in equilibrium with Mg solid solution. In all studied systems where an equilibrium phase forms as a transition phase in a precipitation sequence, the precursor phase is found to have higher mechanical properties than the phase in thermodynamic equilibrium with Mg solid solution.

The Mg-Zn intermetallic compounds exhibit the highest hardness and reduced modulus. The primary strengthening phases in the Mg-Zn system all have similar hardness and reduced moduli. The primary strengthening phase in the Mg-Y system, ε-$Mg_{24}Y_5$, has a lower hardness and reduced modulus than the non-strengthening phase, δ-Mg_2Y. It is interesting to note that phases with like structures have similar mechanical properties. Both γ-$Mg_{17}Al_{12}$ and ε-$Mg_{24}Y_5$ share the prototypical α-Mn structure (Pearson Symbol cI58) and their mechanical properties (i.e. reduced modulus and hardness) are nearly identical, despite significant differences in the properties of the pure constituents. Similarly, the C14 Laves phase common to $MgZn_2$ and δ-Mg_2Y (Pearson Symbol hP12) as well as the prototypic Fe_3Al DO_3 structure of the Mg_3Gd and Mg_3Nd phases have mechanical properties that are consistent to the structure.

In terms of indentation creep, pure Zn undergoes the most significant creep, followed by Al then Y. The intermetallic compounds are less prone to creep with ε-$Mg_{24}Y_5$ showing the least static indentation deformation. $Mg_{21}Zn_{25}$ followed by Mg_3Nd and then $MgZn_2$ had the largest indentation creep of the intermetallic compounds tested. The load-displacement curves for γ-$Mg_{17}Al_{12}$ phase reflect the discontinuous plastic deformation flow. In fact, deformation in γ-$Mg_{17}Al_{12}$ is dominated by plastic instability (i.e. 26.4%). Similarly, the strengthening phases in the Mg-Zn and Mg-Y systems are subject to significant instability. The plastic instability during yielding and creep behavior can be examined as a function of crystal structure. The Mg_3Gd and Mg_3Nd phases behave alike. The atomic coordinates of these phases are essentially identical with the RE element occupying alternating center positions of the 8 body-centered cubic subcells. On the other hand, the mechanical response under the given test conditions is substantially different for $Mg_{41}Nd_5$ and γ-$Mg_{17}Al_{12}$. While $Mg_{41}Nd_5$ and γ-$Mg_{17}Al_{12}$ share a common structure, the atomic coordinates and nearest-neighbor types differ significantly.

Nanoindentation studies have been carried out on AZ91 alloys, which show that the intermetallic precipitates (e.g. $Mg_{17}Al_{12}$) have hardness and modulus of 3.8 ± 0.3 and 71.3 ±6.6 GPa, respectively, compared to the hardness and modulus of surrounding matrix measured as 1.4 ± 0.1 and 51.7 ± 7.7 GPa, respectively [151]. Similar studies have evaluated the mechanical properties of the Mg solid solution in the Mg-Zn binary system, and the hardness and modulus was found to be 0.99 ± 0.03 and 43.5 ± 2.5 GPa, respectively [152]. Few studies have examined the Mg-RE systems [153], and mechanical properties for the

intermetallic and solid solution phases are not available in literature. Thus, prediction of mechanical properties in new alloy systems is limited to first-principles computations.

Surprisingly very few experiment investigations on the mechanical properties of intermetallic compounds in Mg alloys exist in the literature. Xie *et al*. [68] used first-principle calculations and Voigt–Reuss–Hill approximation to calculate upper and lower bounds of elastic properties of polycrystalline $MgZn_2$ and Mg_4Zn_7. Wu *et al*. [154] estimated elastic constants of $MgZn_2$ by first-principle calculations and predicted elastic modulus and Poisson's ratio of $MgZn_2$. Both papers compared their predictions of elastic constants with Seidenkranz's measurement of elastic constants of single crystalline $MgZn_2$ [155]. Similarly Tang *et al*. [156] calculated the Young's Modulus from first-principles calculation within the generalized gradient approximation by the Voigt–Reuss–Hill (VRH) approximation to investigate the Mg_3Gd intermetallic precipitate while Liu *et al*. [157] used a local spin density approximation. Zhang *et al*. estimated the elastic constants of the Mg-Y intermetallic compounds from first-principles calculations based on density functional theory, and the polycrystalline modulus were estimated by the Voigt method [158].

The results are shown in Table 25. For ease of comparison, reduced modulus, E_r, was calculated based on given values for elastic modulus and Poisson's ratio in the references using Equation 19. As can be seen, first principle calculations are comparable with nanoindentation results for the $MgZn_2$, Mg_4Zn_7, and Mg_3Gd.

Table 25: Calculated and measured elastic moduli and Poisson's ratio of intermetallic compounds

	Reference	E (GPa)	ν	E_r (GPa)
$MgZn_2$	**This work**	--	--	87.3 ± 3.10
	First-principle calc. [68]	60.53	0.34	64.58
	First-principle calc. [154]	85.91	0.28	86.20
Mg_4Zn_7	**This work**	--	--	94.09 ± 3.64
	First-principle calc. [68]	82.06	0.27	82.16
Mg_3Gd	**This work**	--	--	74.3 ± 4.7
	First-principle calc. [156]	46.09	0.30	48.50
	First-principle calc.	70.34	0.23	69.81
$Mg_{24}Y_5$	**This work**	--	--	63.3 ±1.5
	First-principle calc. [158]	38.28	0.34	41.81
Mg_2Y	**This work**	--	--	82.7 ±4.7
	First-principle calc. [158]	43.95	0.34	47.54

8.2.1 Composition Dependence of Mechanical Properties in Mg-X Intermetallic Compounds (X = Gd, Nd, Y, Zn)

Several Mg-based intermetallic compounds were observed to have a range of homogeneity. For example, as shown in Figure 21 and Figure 32, intermetallic phases in Mg-Y and Mg-Gd, respectively, have a degree of solid solubility. In addition, through solid-to-solid diffusion couple studies, Brennan *et al.* [36] reported that Mg_3Nd at 500°C contained 19.8 – 23.3 at.%Nd. Similar results were reported by [159]. Mechanical properties are strongly dependent on the crystal structure of a material. For highly ordered intermetallic compounds, the structure (i.e. defect structure) is dependent on the composition. Mechanical properties may also show concentration dependence in intermetallic compounds. In fact, the deformation properties of the Laves phase $MgZn_2$

have been reported to be strongly dependent on the compositions within the range of solubility [160].

The reduced modulus and hardness as a function of composition in several intermetallic compounds examined in this study are presented in Figure 49. The reduced modulus and hardness increase with increasing solute concentration in Mg_6Gd, Mg_5Gd, ε-$Mg_{24}Y_5$, δ-Mg_2Y, Mg_4Zn_7, and $MgZn_2$. The reduced modulus and hardness decrease with increasing Zn concentration in Mg_2Zn_{11}.The reduced modulus and hardness is essentially unaffected by compositional variation in Mg_3Gd and Mg_3Nd. Though the $Mg_{41}Nd_5$ layer thickness was substantial in the Mg-Nd combinatorial sample, no concentration gradient was observed; likewise, no variation in mechanical properties was observed. It is also worth noting, as demonstrated by comparing Figure 49c and Figure 49d, there is a slight load dependence on the reported hardness and modulus.

Another interesting observation can be made by comparing the concentration dependence of mechanical properties with that of interdiffusion in the intermetallic compounds. Comparison of Figure 49a and Figure 49b with Figure 40 reveals that the trends in mechanical properties are consistent with the trend of interdiffusion in the intermetallic compounds of the Mg-Gd system. Assessment of Figure 49e against Figure 27 indicates a consistency in response to increasing concentration in ε-$Mg_{24}Y_5$, but interdiffusion in δ-Mg_2Y Laves phase is unchanged while the reduced modulus and hardness slightly increase with increasing Y concentration. A similar but more significant response is seen in the Mg-Zn intermetallic compounds. From Figure 49f and Figure 20, it is

evident that hardness, reduced modulus, and interdiffusion all trend together in Mg_4Zn_7 and Mg_2Zn_{11}, but the trend conflicts in the $MgZn_2$ Laves phase.

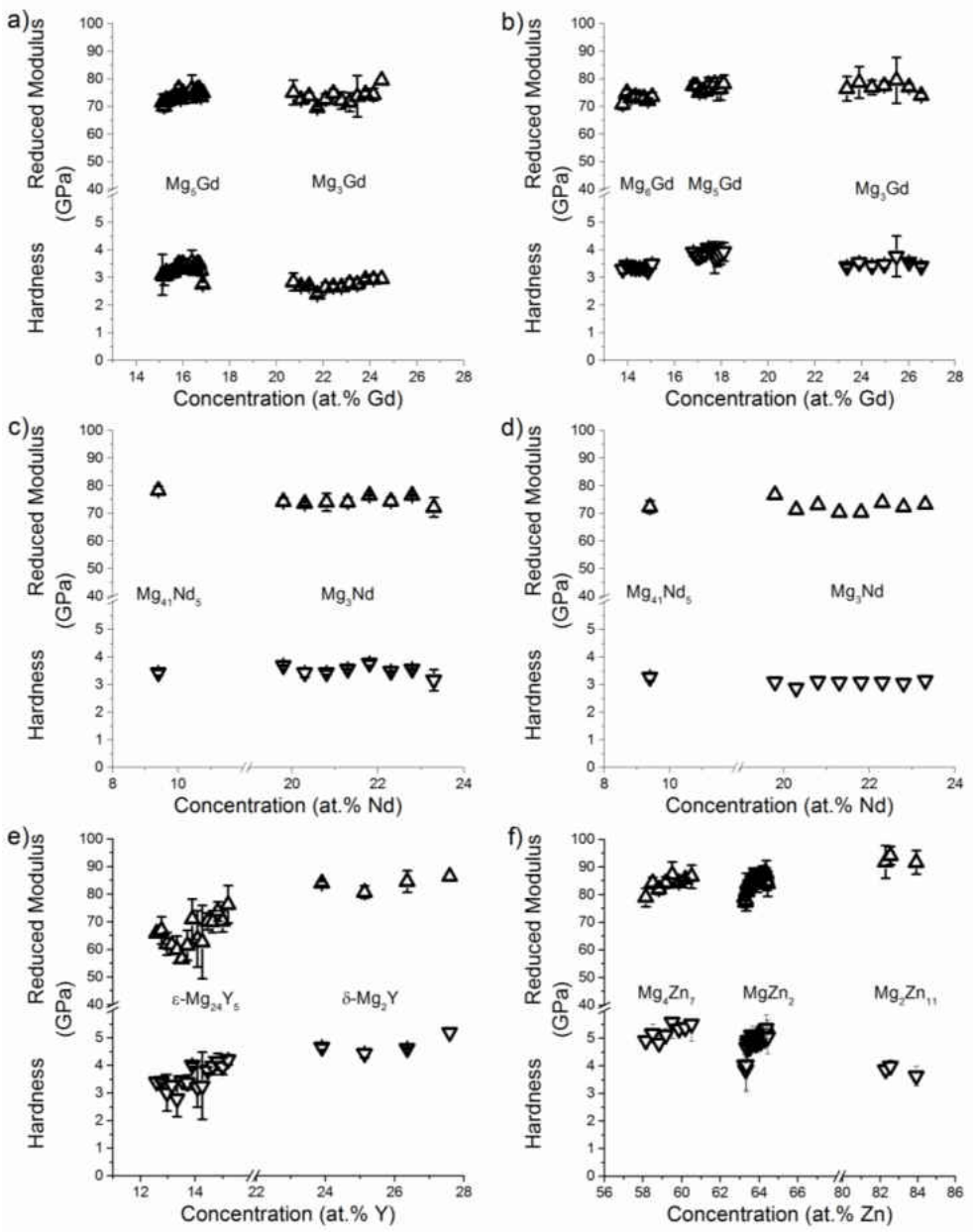

Figure 49: Reduced Modulus and Hardness of intermetallic compounds as a function of composition, tested under a 7mN peak load unless otherwise noted: a) Mg-Gd annealed at 490°C for 72 hours; b) Mg-Gd annealed at 385°C for 192 hours; c) Mg-Nd annealed at 500°C for 240 hours tested at 5mN peak load; d) Mg-Nd annealed at 500°C for 240 hours; e) Mg-Y annealed at 450°C for 360 hours; f) Mg-Zn annealed at 315°C for 168 hours

8.3 Solid Solution Strengthening in Mg(X) (X = Al, Gd, Y, Zn)

All solid solution line scans were performed under a 5mN peak load. As exercised in all other mechanical testing, indentation cycles consisted of a 10-second load segment, 3-second hold segment, and a 10-second unload segment with load controlled feedback. The combinatorial samples used for this study are detailed in Table 26.

Table 26: Combinatorial samples for solid solution study

Diffusion Couple	Anneal Temperature (˚C)	Anneal Time (Hours)
Mg vs. Mg-9at.%Al	450	24
Mg vs. Mg-3at.%Zn	450	24
Mg vs. Gd	490	72
Mg vs. Y	450	360
	550	120

In Mg solid solutions containing less than 8 at.%Al, the hardness and modulus are not appreciably increased with increasing solute concentration. As the concentration of Al approaches its solubility limit in Mg, notable strengthening is observed. This can be seen in Figure 50. The hardness is observed to generally increase linearly with concentration implying symmetric lattice distortion.

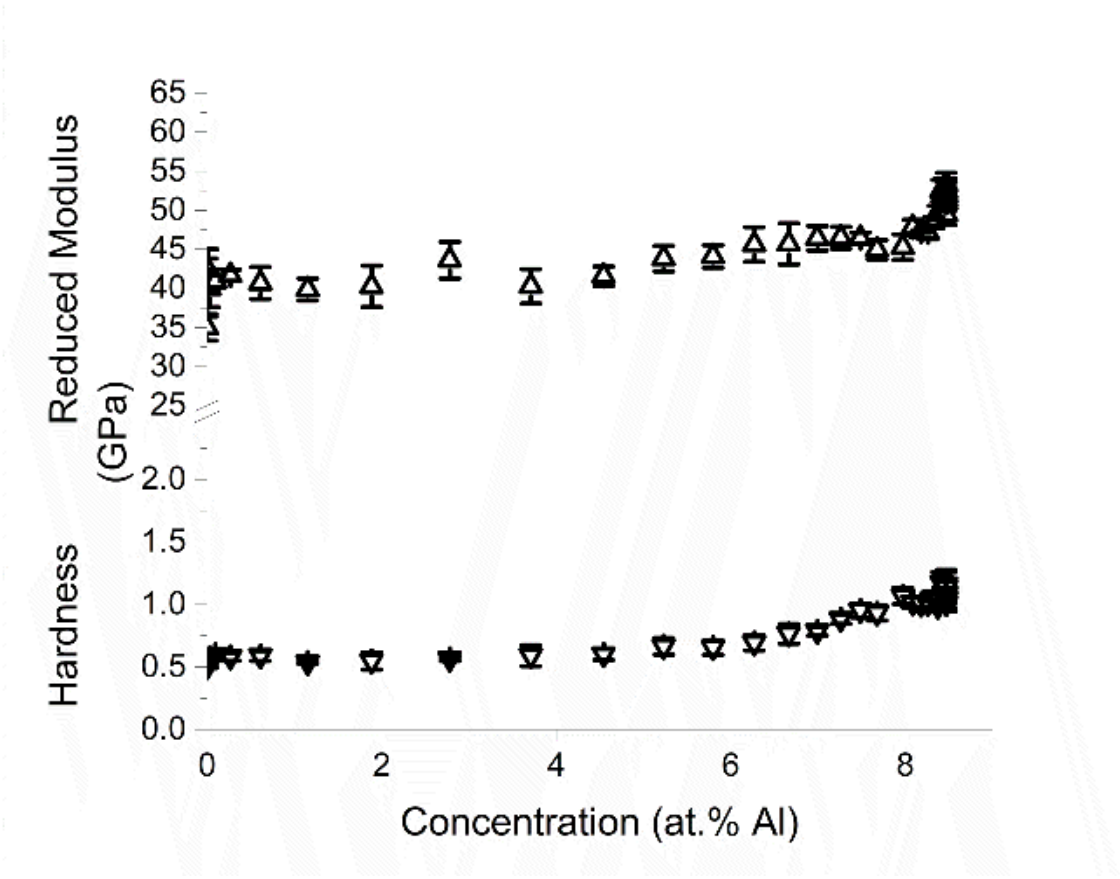

Figure 50: Reduced modulus and hardness of Mg solid solution as a function of composition, tested under a 5mN peak load

Figure 51 demonstrates the influence of solute concentration on the strengthening power, creep behavior, and plastic instability. Qualitatively, the extent of creep is reduced when solute concentration is greater than 4 at.%Al. Conversely, the degree of mechanical instability as evident through serrations in the loading segment increases with increasing Al concentration. From these curves, the contact depth substantially decreases as the Al solute concentration approaches the solubility limit.

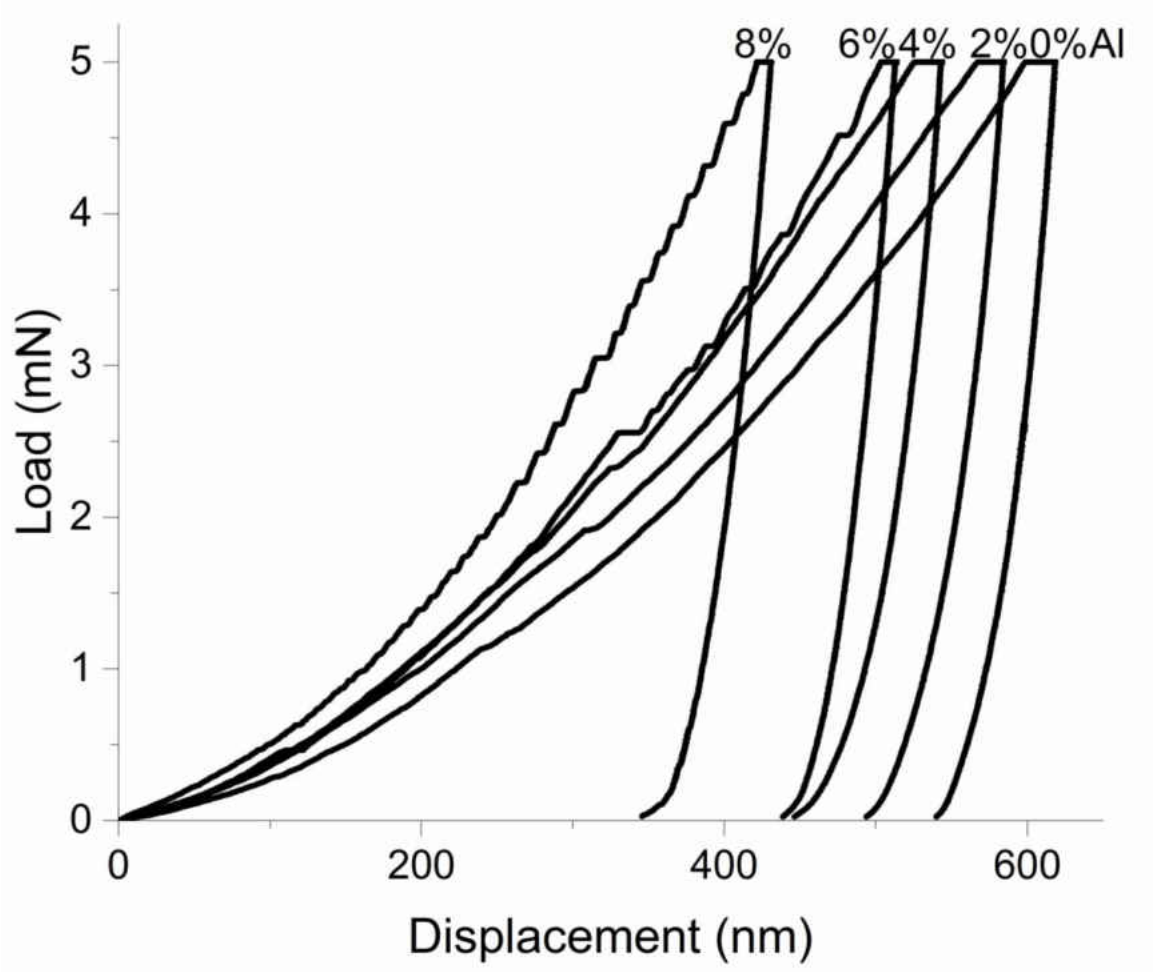

Figure 51: Influence of Al concentration on load-displacement curves, tested under a 5mN peak load

A similar assessment of the reduced modulus and hardness as a function of Zn concentration was performed. Figure 52 quantitatively reports the change in mechanical properties of Mg solid solution with increasing solute concentration. It is evident that Zn is an effective solid solution strengthener for Mg solid solution. Overall, the hardness increases linearly with concentration suggesting symmetric lattice distortion.

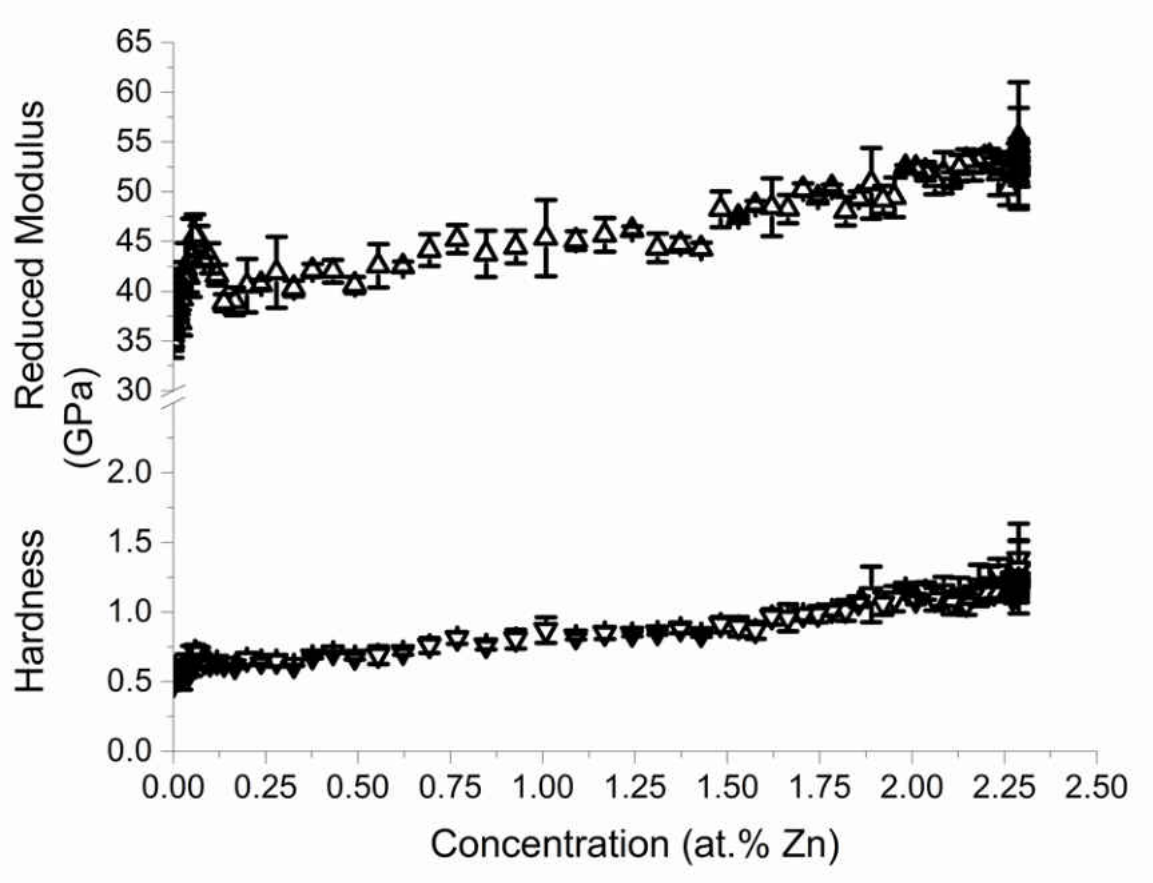

Figure 52: Influence of Zn concentration on reduced modulus and hardness of Mg solid solution, tested under a 5mN peak load

The reduced modulus and hardness sharply increase with increasing Zn concentration in dilute Mg solid solutions, but there is an apparent softening effect between 0.1 – 0.25 at.%Zn. Plastic deformation in Mg alloys is anisotropic as slip most readily occurs on the basal planes followed by the prismatic planes. Zn has been shown to harden basal planes , but soften prismatic planes at concentrations up to 0.6 at.% leading to an initial increase followed by a decrease in yield strength [161].

Figure 53 allows for a qualitative assessment of mechanical behavior by presenting a series of load-displacement cures showing the influence of alloying on strengthening, creep, and discontinuous yielding. The creep displacement decreases with increasing concentration whereas the number and magnitude of strain bursts increase. Additionally, a noticeable decrease in contact depth (i.e. displacement) is observed with small additions of Zn.

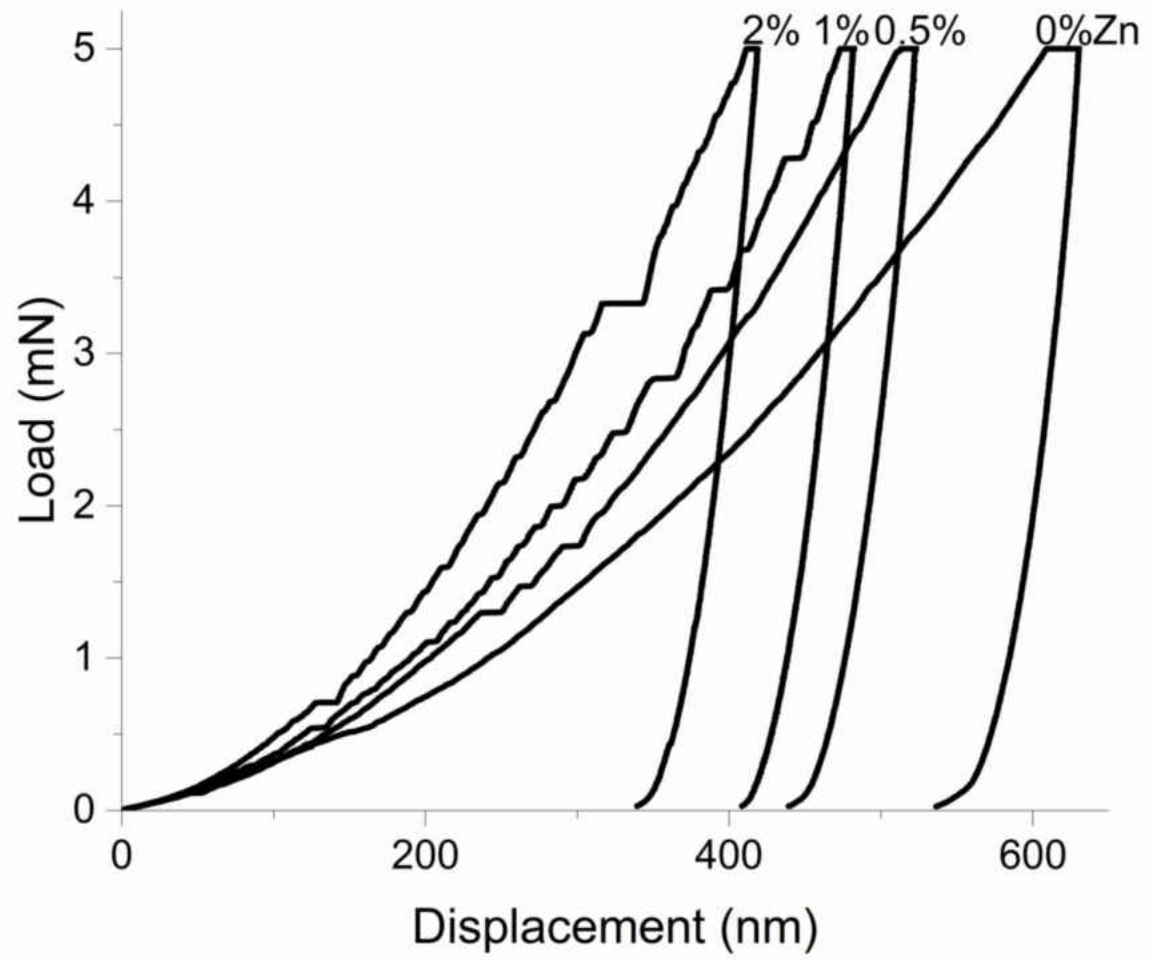

Figure 53: Representative load-displacement curves demonstrating the influence of Zn solute concentration has on the mechanical behavior of Mg solid solution

Concentration dependent mechanical properties of Mg solid solutions containing Y are presented in Figure 54. A dashed line is used to connect the reduced modulus and hardness of pure Mg to the assessed properties at solute concentrations greater than 1 at.%Y. It is important to note that the line serves only as a visual guide and does not imply actual properties. There is a notable increase in the reduced modulus of the Mg(Y) solid solution compared to that of pure Mg, but there is no appreciable change in the modulus at concentrations greater than 1.5 at.%Y. The hardness increases monotonically with solute concentration. In the evaluated compositional range, the relationship between hardness and concentration is linear. An assessment of the lattice distortion symmetry cannot be made.

A series of load-displacement curves representative of Mg solid solutions containing 1 – 4 at.%Y is presented in Figure 55. As noted for both Mg(Al) and Mg(Zn), the creep is reduced with increasing solute concentration, however Mg(Y) has few pop-ins or discontinuous yielding.

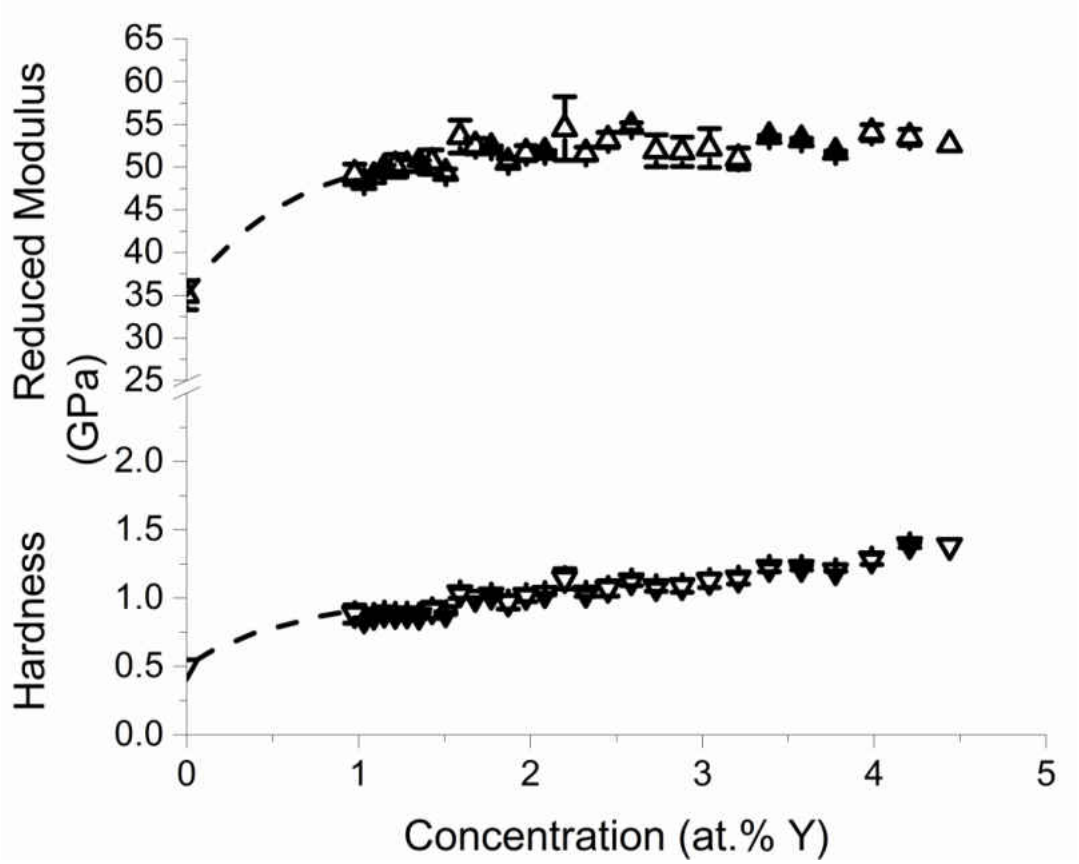

Figure 54: Influence of Y concentration on reduced modulus and hardness of Mg solid solution, tested under a 5mN peak load

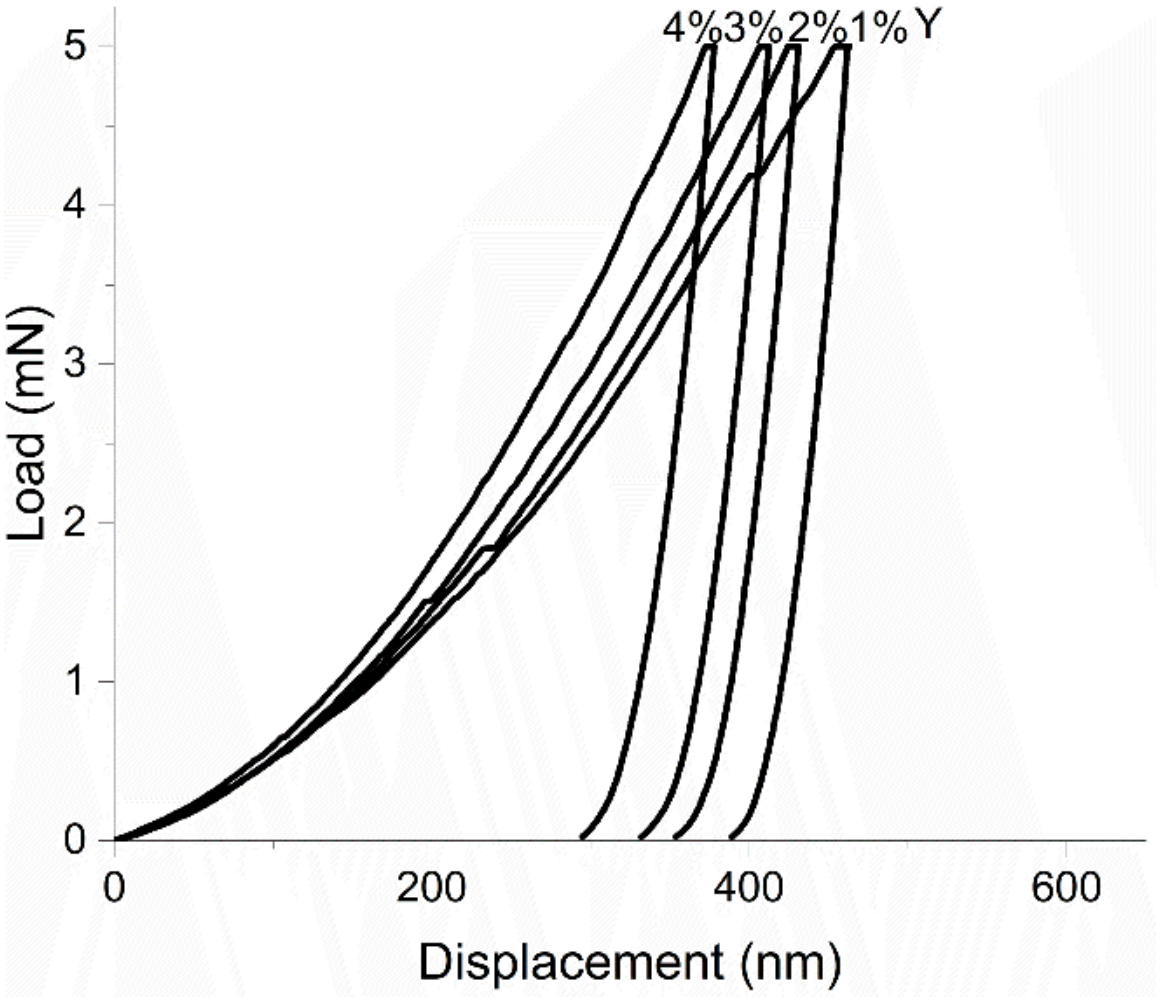

Figure 55: Representative load-displacement curves demonstrating the influence of Y solute concentration has on the mechanical behavior of Mg solid solution

The reduced modulus and hardness in Mg(Gd) was determined across the full solubility limit. As presented in Figure 56 the reduced modulus is significantly increased with even small amounts of Gd substitution (<0.5 at.%Gd), and continues to increase with increasing solute concentration up to about 1.5 at.%Gd. Moreover, the hardness increases continuously across the compositional spectrum. Gd substitution induces symmetric lattice distortion.

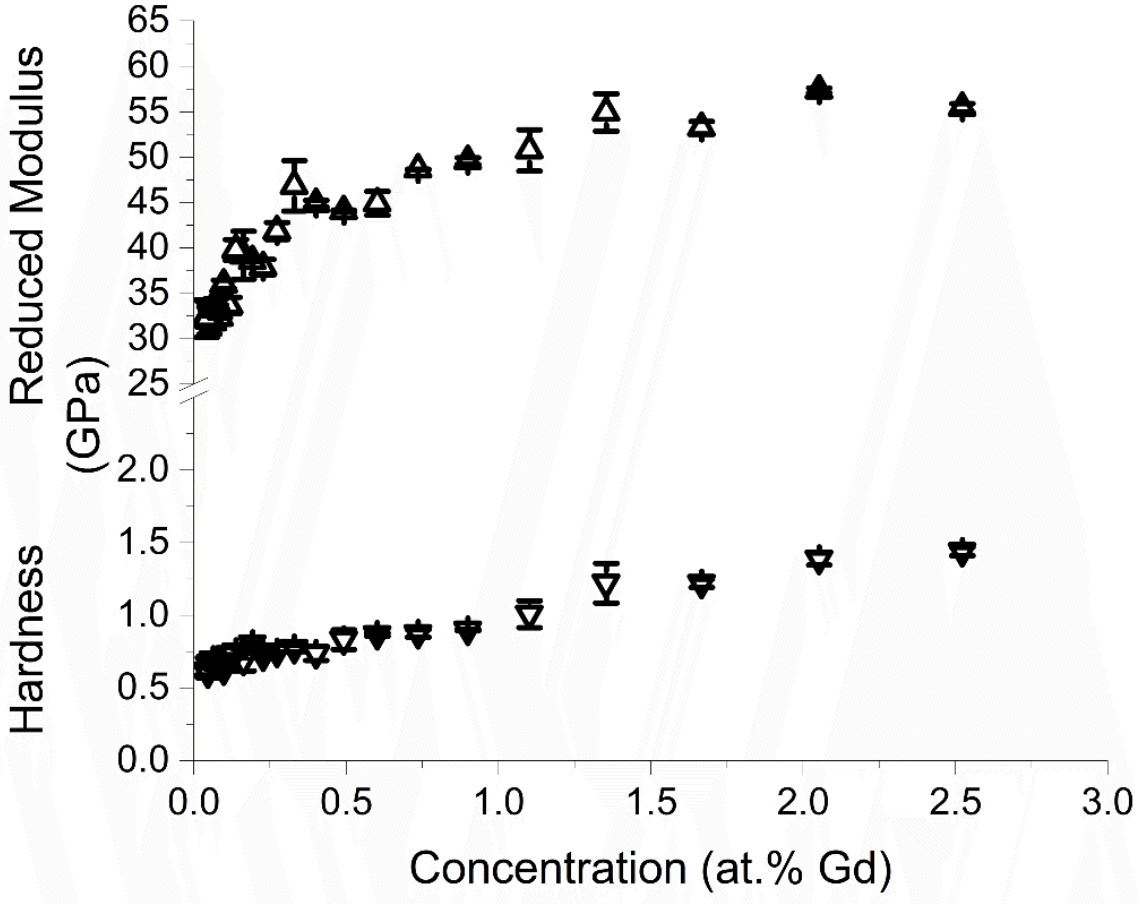

Figure 56: Influence of Gd concentration on reduced modulus and hardness of Mg solid solution, tested under a 5mN peak load

The substantial strengthening effect in dilute Mg solutions containing Gd can be observed in the series of load-displacement curves presented in Figure 57. There is large shift in contact depth with small additions of Gd. This behavior is similar to that which was seen in Mg(Zn). Like all other studied solid solutions, the creep behavior is restrained with increasing solute concentration. Though there is evidence of plastic instability, the number and magnitude of the serration steps are notably less than seen in Mg(Al) and Mg(Zn).

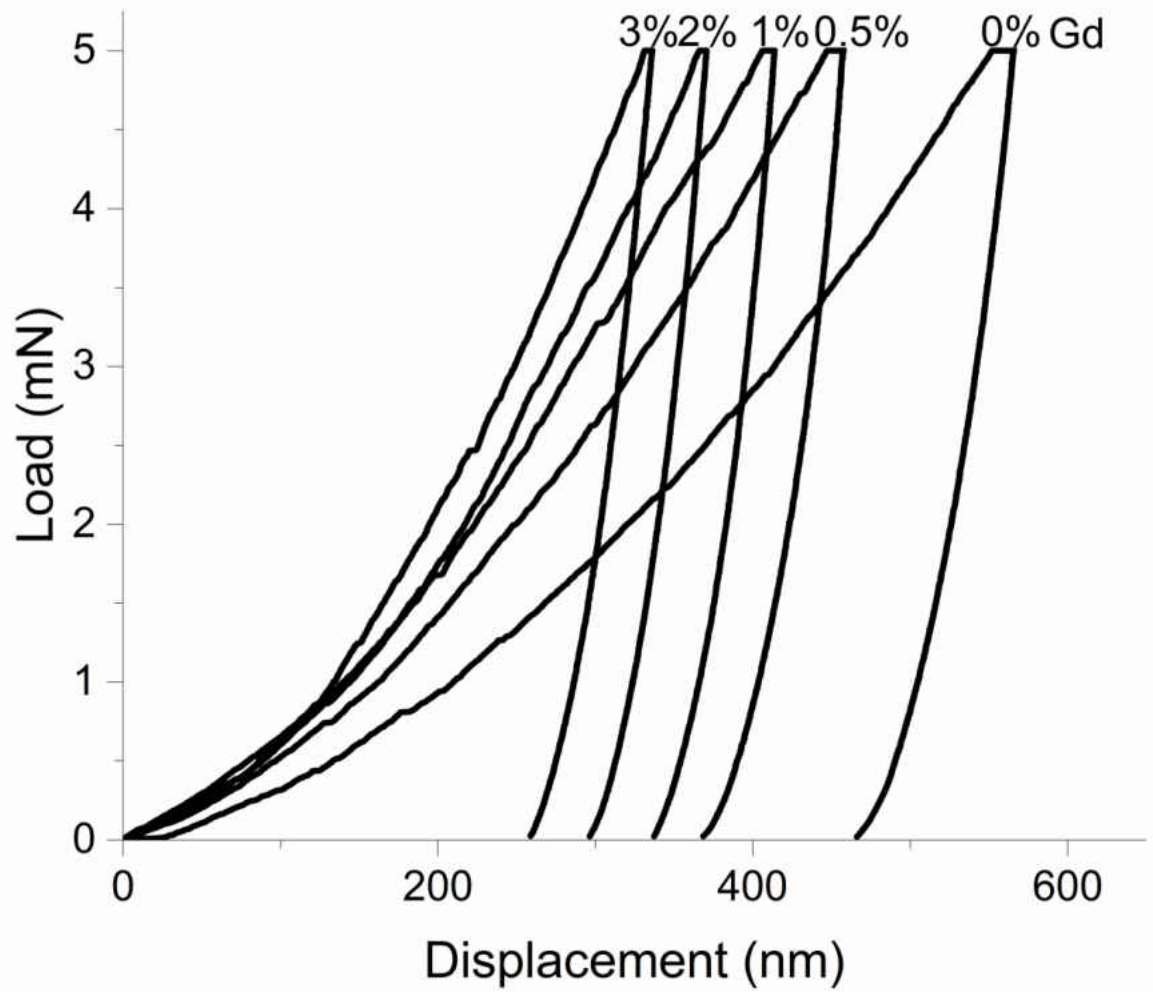

Figure 57: Representative load-displacement curves demonstrating the influence of Gd solute concentration has on the mechanical behavior of Mg solid solution

An interesting connection can be made between the nature of plastic deformation (i.e. plastic instability) and the activation energy for interdiffusion in Mg solid solution. In all solid solutions examined, the instability increases with increasing solute concentration with Mg(Al) being most sensitive and Mg(Y) being least sensitive. The trend in susceptibility to inhomogeneous yielding with increasing solute concentration is analogous to the trend in activation energy of interdiffusion in Mg solid solution. That is to say, the sensitivity to pop-ins (PI) is parallel to the activation energy for interdiffusion in Mg solid solution wherein $\left(PI_{Mg(Al)} > PI_{Mg(Zn)} > PI_{Mg(Gd)} > PI_{Mg(Y)}\right) \approx \left(\widetilde{Q}_{Mg(Al)} > \widetilde{Q}_{Mg(Zn)} > \widetilde{Q}_{Mg(Gd)} > \widetilde{Q}_{Mg(Y)}\right)$.

The change in the hardness as a result of alloying with Al, Zn, Y, and Gd is directly proportional to the solute content (i.e. linear function). This implies that the solid solution strengthening mechanism is dominated by the elastic interaction between substituted solute atoms and dislocations [20]. Both Al (143 pm) and Zn (134 pm) have smaller atomic radii than Mg (160 pm). As a result, substitution of either Al or Zn into Mg will distort the Mg lattice and generate internal tensile lattice strain and will hinder dislocation motion (i.e. increase strength). Conversely, Y (180 pm) and Gd (180pm) have large atomic radii than Mg. Substitution of Mg with either Y or Gd will cause a compressive strain field to form around the solute atom and will obstruct dislocation motion.

A lattice misfit factor can be quantified as $\varepsilon_V = 1/V_M \left(\partial V_M / \partial C\right)$ where V_M is the molar volume and C is the atomic concentration of the solute. Figure 58 presents the hardness as a function of the lattice misfit factor. The molar volume was calculated from a least squares linear regression of the experimentally determined lattice spacing for Mg(Al), Mg(Zn), and

Mg(Y) solid solutions [12, 67, 76, 162]. The molar volume for Mg(Gd) was determined by assuming adherence to Vegard's law. The sign of the misfit factor denotes the compressive (+) or tensile (-) stress field caused by the solute. Additions of Al or Zn will put the lattice in tension; additions of Y or Gd will compressively strain the lattice. The largest magnitude of misfit is caused by additions of Zn, whereas the smallest lattice misfit results from alloying with Al. The lattice misfit factor for Mg(Y) and Mg(Gd) are similar to each other and intermediate to that for Mg(Al) and Mg(Zn). In fact, between 430°C to 515°C the impurity diffusion coefficient trends with this misfit factor wherein $D_{Zn}^{Mg} > D_{Gd}^{Mg} \approx D_{Y}^{Mg} > D_{Al}^{Mg}$. Not surprisingly, additions of Zn into solution more effectively strengthen Mg than additions of Al. However, though Mg(Zn) has the largest misfit strain, the difference in hardness from peak strengthening to that of pure Mg is equivalent to Mg(Y) and smaller than Mg(Gd).

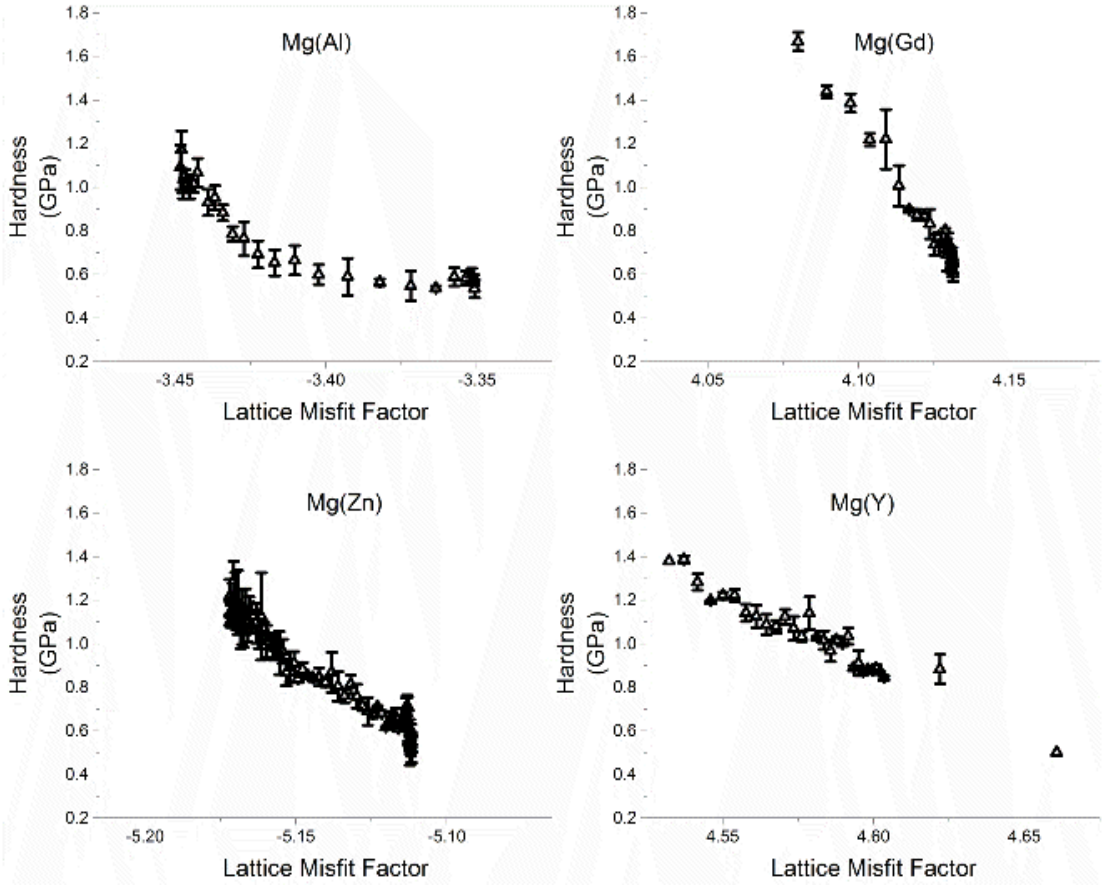

Figure 58: Hardness as a function of the lattice misfit factor

Indeed, both Y and Gd appear to provide unusual strengthening efficiency compared to their lattice misfit factors. Since atomic structure is fundamental to mechanical properties, the electron configuration of the solute elements is considered. Electrical interactions, associated with the solute atoms of dissimilar valence, also contribute to solid solution strengthening [20]. It is interesting to note that the valence of Zn and Y, like Mg, is 2 while the valence for Al and Gd is 3. Despite the similarities in valence, a closer examination of the quantum numbers reveals significant differences between the conventional alloying elements of Al and Zn and the rare earth alloying elements of Y and

Gd in this study. The rare earth elements have multiple partially filled shells. Zn, like Mg, has one partially filled shell containing an opposing spin pair of electrons filling the s-orbital. Al also has one unfilled shell containing an opposing spin pair of electrons filling the s-orbital as well as an unpaired electron the p-subshell. According to the Aufbau principle [163, 164], the N-shell of Y contains 4 pairs of electrons filling the s- and p-orbitals and 1 unpaired electron in the d-subshell while the O-shell of Y contains a pair of electrons filling the s-orbital. Therefore, while Y has only two electrons in its outermost shell, it has 11 electrons, with one being unpaired, in two partially filed shells available for bonding interactions. Similarly, under the same principle and in consideration of Hund's rule [163, 164], Gd has three partially filled shells (N, O, P) with 17 electrons, 8 of which are unpaired, available for interaction. Because these partially filled shells can participate in interatomic bonding, they too must be considered as factors in solid solution strengthening.

Gao, *et al*. [165, 166], Miura *et al*. [167], and Ninomiya *et al.* [168] have observed similar anomalous strengthening effects in Mg solid solution. Each has demonstrated the significance of the electronic structure of rare earth elements on its strengthening efficiency. Hybridization of Mg's p-orbitals with the d-orbitals of Gd or Y, leading to covalent bonding characteristics, have been demonstrated through partial density of state calculations [166].

8.4 Summary

The elastic and plastic properties of the intermetallic compounds and Mg solid solutions were determined through analysis of the load-displacement profiles of nanoindentation by the Oliver-Pharr method. Intermetallic compounds of the Mg-Al, Mg-Gd, Mg-Nd, Mg-Y, and Mg-Zn binary systems were examined. Few experimental data exists in literature, but first principles computations have yielded comparable mechanical property data when available.

The Mg-Zn intermetallic compounds exhibited the highest hardness and reduced modulus. The phase in thermodynamic equilibrium with Mg solid solution is not always the highest strength phase. In all studied systems where an equilibrium phase forms as a transition phase in a precipitation sequence, the precursor phase is found to have higher mechanical properties than the phase in thermodynamic equilibrium with Mg solid solution.

Pure Zn undergoes the most significant creep, followed by Al then Y and Gd. Conversely, the primary strengthening phases undergo only 20 – 30% of the creep exhibited by the unalloyed elements. The intermetallic compounds are less prone to creep with ε-$Mg_{24}Y_5$ showing the least static indentation deformation. $Mg_{21}Zn_{25}$ followed by Mg_3Nd and then $MgZn_2$ had the largest indentation creep of the intermetallic compounds tested.

Pop-ins or serrations in the loading profile of the intermetallic compounds were evidence of the PLC effect, mechanical twinning, or work hardening sensitivity. Plastic deformation in γ-$Mg_{17}Al_{12}$ is dominated by plastic instability (i.e. 26.4%). Similarly, the

strengthening phases in the Mg-Zn and Mg-Y systems are subject to significant instability. Mg_2Zn_{11}, though not a primary strengthening phase, was less susceptible to this discontinuous yielding during plastic deformation than the other intermetallic phases.

The reduced modulus and hardness increase with increasing solute concentration in Mg_6Gd, Mg_5Gd, ε-$Mg_{24}Y_5$, Mg_4Zn_7, $MgZn_2$, and to a lesser extent δ-Mg_2Y. The mechanical properties seem to decrease with increasing Zn concentration in Mg_2Zn_{11}. The reduced modulus and hardness are essentially unaffected by compositional variation in Mg_3Gd and Mg_3Nd. Though the $Mg_{41}Nd_5$ layer thickness was substantial in the Mg-Nd combinatorial sample, no concentration gradient was observed; likewise, no variation in mechanical properties was observed. Interestingly, the influence of alloying element concentration on reduced modulus and hardness trends with the influence of the same on interdiffusion except in the case of the C14 Laves phases (i.e. $MgZn_2$ and δ-Mg_2Y).

Phases with like structures have similar mechanical properties. The mechanical properties (i.e. hardness and reduced modulus) of the C14 Laves phase are nearly identical despite significant differences in the properties of the pure constituents. Similarly, the complex cubic structure common to γ-$Mg_{17}Al_{12}$ and ε-$Mg_{24}Y_5$ (i.e. cI58), as well as the prototypic Fe_3Al DO_3 structure of the Mg_3Gd and Mg_3Nd phases, have mechanical properties that are consistent to the structure. Mg_3Gd and Mg_3Nd phases behave alike in terms of discontinuous yielding and creep behavior due to the near identical atomic configuration. On the other hand, while ε-$Mg_{24}Y_5$ and γ-$Mg_{17}Al_{12}$ share a common structure, the atomic coordinates and nearest-neighbor types differ significantly, therefore the mechanical response during loading (i.e plastic instability) differ substantially.

Mg solid solutions of the Mg-Al, Mg-Gd, Mg-Y, and Mg-Zn binary systems were examined. The change in the hardness as a result of alloying with Al, Zn, Y, and Gd is directly proportional to the solute content (i.e. linear function). This implies that the solid solution strengthening mechanism is dominated by the elastic interaction between substituted solute atoms and dislocations. However, the strengthening efficacy of alloying elements does not trend with elastic interaction parameters (i.e. lattice parameter, c/a ratio, volumetric misfit factor). The largest magnitude of misfit is caused by additions of Zn, whereas the smallest lattice misfit results from alloying with Al; the lattice misfit factor for Mg(Y) and Mg(Gd) are equivalent and intermediate to that for Mg(Al) and Mg(Zn). It is interesting to note, between 430°C to 515°C the impurity diffusion coefficient trends with this misfit factor wherein $\left(\varepsilon_V^{Mg(Zn)} > \varepsilon_V^{Mg(Gd)} \cong \varepsilon_V^{Mg(Y)} > \varepsilon_V^{Mg(Al)}\right) \approx \left(D_{Zn}^{Mg} > D_{Gd}^{Mg} \cong D_Y^{Mg} > D_{Al}^{Mg}\right)$.

Electronic interactions, associated with the solute atoms of dissimilar valence, also contribute to solid solution strengthening. The rare earth elements have multiple partially filled shells which can take place in interatomic bonding. Orbital p-d hybridization in Mg solid solutions of RE elements leads to covalent characteristics of bonding and may account for the anomalous strengthening efficiency of Gd and Y.

Finally, given that the inhomogeneous yielding is associated with free flight of mobile dislocations between subsequent blockings at obstacles, it is easy to understand that the effect is magnified as solute concentration increases. Interestingly the sensitivity to the solute pinning is parallel to the activation energy for interdiffusion in Mg solid solution wherein $\left(PI_{Mg(Al)} > PI_{Mg(Zn)} > PI_{Mg(Gd)} > PI_{Mg(Y)}\right) \approx \left(\widetilde{Q}_{Mg(Al)} > \widetilde{Q}_{Mg(Zn)} > \widetilde{Q}_{Mg(Gd)} > \widetilde{Q}_{Mg(Y)}\right)$.

CHAPTER 9: COMPREHENSIVE SUMMARY

Magnesium is the lightest structural metal currently available for industrial applications in which reduced weight equates to enhanced operating efficiency and reduced greenhouse gas emissions (e.g. automotive and aerospace applications). Magnesium is one-quarter the density of steel; even aluminum is 50% heavier than magnesium. Unfortunately, due to its structure, magnesium must be cast to near-net shapes or processed at elevated temperatures, adding increased costs which have constrained its more expansive integration into "green" design. To fully capitalize on the opportunities offered by magnesium, improvements to its room-temperature formability are mandatory, and can be achieved without significantly affecting density by alloying with other elements. Essential to alloy development, inclusive of processing parameters, is the knowledge of thermodynamic, kinetic, and mechanical behavior. Through an aggregate of studies, the relationships between diffusion behavior, crystal structure, and mechanical properties of phases in binary and ternary Mg alloys have been collected, providing original, fundamental data for the purpose of wrought magnesium alloy development.

Solid-to-solid diffusion bonding technique was used to fabricate combinatorial samples of magnesium alloys. Conventional (i.e. Al, Zn) and rare earth (i.e. Gd, Nd, Y) alloying elements were employed. The resultant interdiffusion zone and reaction products were interrogated with an electron beam to ascertain structural and compositional information, as well as kinetic behavior. The samples were also subjected to

nanomechanical indentation testing to determine mechanical behavior of pure metals, solid solutions, and intermetallic compounds in binary and ternary systems.

Impurity diffusion coefficients for Zn in Mg(Al) solid solution and Al in Mg(Zn) solid solution were calculated by the Hall Method. The diffusion coefficients for Zn impurity Mg(Al) solid solutions determined in this study were consistent with those found in literature. The Zn impurity diffusion coefficient is only slightly affected by the presence of Al in Mg(Al) solid solution. The pre-exponential factor for Zn impurity diffusion is concentration dependent while the activation energy is independent of concentration of Al in solution with Mg. This study was the first report of the Al impurity diffusion coefficient in Mg(Zn) solid solutions. Al impurity diffusion in Mg(Zn) solid solution is strongly influenced by the Zn concentration. Both the pre-exponential factor and energy of activation for Al impurity diffusion are dependent on the concentration of Zn in solution with Mg. It was demonstrated that Zn in solid solution promotes Al impurity diffusion at higher temperatures.

Interdiffusion coefficients in the ternary Mg(Al,Zn) solid solution phase at 400° and 450°C were reported for the first time. On the basis of Kirkaldy's extension of Fick's law constructed on Onsager's formalism, the relationship of the components and their influence on the diffusion kinetics was revealed. Zn diffuses faster than Al in Mg solid solution. The magnitude of $\widetilde{D}^{Mg}_{ZnZn}$ ternary interdiffusion coefficients were approximately 3 to 5 times larger than that of $\tilde{D}^{Mg}_{AlAl}$. The magnitude of $\tilde{D}^{Zn}_{MgMg}$ was greater than that of $\tilde{D}^{Zn}_{AlAl}$, and magnitude of $\tilde{D}^{Al}_{MgMg}$ was less than that of $\tilde{D}^{Al}_{ZnZn}$. Diffusional interactions, in particular those

involving Zn, were shown to be appreciable. The $\tilde{D}^{Mg}_{AlZn}$ cross interdiffusion coefficients were negative and significant in magnitude comparable to $\tilde{D}^{Mg}_{AlAl}$. The $\tilde{D}^{Al}_{MgZn}$ cross interdiffusion coefficients are negative, and significant in magnitude, 5 to 10 times larger than $\tilde{D}^{Al}_{MgMg}$. This influence of Zn on Mg interdiffusion leads to observations of uphill diffusion and zero-flux planes in concentration profiles of Mg.

Structural characterization of the phases in binary Mg-Zn and Mg-Gd systems was performed. Within the Mg-Zn system, the crystallographic parameters of the equilibrium phases were characterized by TEM and SAED. $Mg_{21}Zn_{25}$ with trigonal, Mg_4Zn_7 with monoclinic, and Mg_2Zn_{11} with cubic structures were found and their lattice parameters were reported. Just as was done for the Mg-Zn system, the crystal structure and lattice parameters of the equilibrium phases of the Mg-Gd were determined through electron diffraction. A previously unidentified phase, Mg_6Gd, with an apparent modulated hexagonal superlattice (a = 134.2Å, c = 97.8Å) was found to be in equilibrium with Mg solid solution. Additional analysis is needed to fully characterize this phase.

The compositional boundaries of the equilibrium phases were determined and compared to the most current, accepted binary phase diagram for the Mg-Zn, Mg-Gd, and Mg-Y systems. Mg_4Zn_7 and Mg_2Zn_{11}, line compounds according to the phase diagram, were observed to have a range of solubility of approximately 2.4 at.% and 1.6 at.% at 315°C, respectively. Similarly, the new Mg_6Gd phase and Mg_5Gd and Mg_3Gd line compounds were also found to have a range of homogeneity. Mg_3Gd was found to have significant solubility range of 4.28 at.%Gd at 450°C. Consistent with the binary phase diagram, the intermetallic

phases in the Mg-Y system were also found to have a range of solubility. However, in conflict with the phase diagram, no solubility of Mg was observed in Y. A similar observation was made in Gd (i.e. no apparent solid solubility of Mg in Gd).

Within the intermetallic compounds of the Mg-Zn system, interdiffusion in $MgZn_2$ occurred most rapidly, was an order of magnitude slower in Mg_4Zn_7 and Mg_2Zn_{11}, and was the slowest in $Mg_{21}Zn_{25}$. Composition-dependence of interdiffusion within each intermetallic phase was negligible. The interdiffusion coefficients within the ε-$Mg_{24}Y_5$ phase were about three times greater than in the δ-Mg_2Y phase and nearly two orders of magnitude greater larger than the equiatomic MgY phase. Interdiffusion in ε-$Mg_{24}Y_5$, and δ-Mg_2Y phases found to be composition dependent. Additionally, ordering in ε-$Mg_{24}Y_5$ affects the diffusion kinetics. Growth and interdiffusion in MgGd and Mg_2Gd intermetallic compounds in the Mg-Gd system are also affected by ordering. The interdiffusion coefficients for MgGd were determined to be nearly an order of magnitude smaller than those established for Mg_2Gd. Mg_5Gd was found to have the largest interdiffusion coefficients, larger than Mg_3Gd which was determined to be two orders of magnitude greater than Mg_2Gd. Interdiffusion in the intermetallic phases of the Mg-Gd system is not strongly composition dependent, though a slight dependence was seen in Mg_5Gd.

Interdiffusion in Mg(Gd) and Mg(Y) is strongly concentration dependent decreasing with increasing solute concentration. This trend is unique in comparison with interdiffusion in Mg(Al) or Mg(Zn). An interdiffusion activation energy of 110.4 kJ/mol and 84.4 kJ/mol is found in this study for Mg(Y) and Mg(Gd), respectively. These activation energies are much lower than those for interdiffusion in Mg(Al) or Mg(Zn). A similar

relationship between conventional alloying elements (i.e. Al, Zn) and RE alloying element (i.e. Gd, Y) in Mg can be seen from the impurity diffusion coefficients.

Impurity diffusion coefficients for Gd and Y in Mg were determined and compared to those for Al and Zn. The Gd and Y impurity diffusion coefficients are quite similar to each other, but Gd and Y impurity diffusion is intermediate to Al and Zn impurity diffusion over the temperature ranges studied. The pre-exponential factor and activation energy for Gd impurity was found to be 2.21×10^{-7} m^2/sec and 97.8kJ/mol, respectively. The Y impurity pre-exponential factor and activation energy was found to be 1.62×10^{-7} m^2/sec and 99.5kJ/mol, respectively. The activation energy for impurity diffusion of the large RE elements is lower than that of the small conventional impurities. This is understood in consideration of solute size dependence on the solute-vacancy binding and exchange energies.

The influence of conventional (i.e. Al and Zn) and RE (i.e. Gd, Nd, and Y) alloying elements on the mechanical properties and behavior was studied. In terms of mechanical properties (i.e. hardness and reduced modulus) of the intermetallic compounds, the phase in thermodynamic equilibrium with Mg solid solution is not always the highest strength phase. In all studied systems where an equilibrium phase forms as a transition phase in a precipitation sequence, the precursor phase is found to have higher mechanical properties than the phase in thermodynamic equilibrium with Mg solid solution. Intermetallic compounds in the Mg-Zn system have higher hardness and reduced modulus than intermetallic compound in any other system studied. Several phases with a range of homogeneity were found to display concentration dependence in mechanical properties.

The influence of alloying element concentration on reduced modulus and hardness trends with the influence of the same on interdiffusion except in the case of the C14 Laves phases (i.e. $MgZn_2$ and δ-Mg_2Y). Additionally, it was found that phases with like structures have similar mechanical properties.

In addition to the connection between crystal structure and mechanical properties, a relationship between atomic configuration within the crystal structure and mechanical behavior (i.e. creep, discontinuous yielding) was shown to exist. ε-$Mg_{24}Y_5$ and γ-$Mg_{17}Al_{12}$ share a common structure (i.e. cI58), but the atomic coordinates and nearest-neighbor types differ significantly. Their mechanical properties are similar, but their mechanical responses to indentation loads differ substantially with ε-$Mg_{24}Y_5$ showing less mechanical instability during loading load than γ-$Mg_{17}Al_{12}$.

The mechanism of solid solution strengthening in Mg alloyed with conventional (i.e. Al, Zn) and RE (i.e. Gd, Y) elemental additions was found to be predominantly due to elastic interactions between solute atoms and dislocations. The volumetric misfit factor was found to trend with the impurity diffusion coefficient. However, anomalous strengthening efficacy of the RE elements was observed. It was demonstrated that electrical interactions due to dissimilar valence and multiple partially filled quantum shells also contribute to solid solution strengthening. Further indicting the electronic contributions to the mechanical behavior, the sensitivity to solute pinning and release (i.e. discontinuous yielding) trends with the activation energy for interdiffusion in Mg solid solution.

The goal of this research was to advance the metallurgical understanding of Mg systems. To that end, two deliverables were defined for the doctoral study. First, the

relationships between diffusion behavior, crystal structure, and mechanical properties in Mg and Mg alloys would be collected; second, fundamental datasets for the purpose of wrought Mg alloy development would be provided. Several relationships and dependencies were identified in this study, and are generalized as follows.

- Crystal structure and atomic configuration have significant impact on mechanical behavior and properties.
- Composition dependence of mechanical properties is mirrored in the interdiffusion coefficients of intermetallic compounds.
- Pop-in susceptibility and sensitivity correlates to the activation energy for effective interdiffusion in Mg solid solutions.
- Activation energy for impurity diffusion is dominated by elastic interactions.
- Solid solution strengthening is influenced by elastic interactions and electron configuration.

The datasets collected, analyzed, and described within this manuscript are presented in Appendix B for integration into the materials genome.

Fundamental relationships between diffusion behavior, crystal structure, and mechanical properties of phases in binary and ternary Mg alloys have been exposed through this collection of objective studies. Solid-to-solid diffusion bonding technique was used to fabricate combinatorial samples of magnesium alloys which were subjected to interrogation with an electron beam to establish structural and compositional characteristics, and expose the kinetic behavior. Samples were also physically prodded to determine mechanical behavior of the components and phases in binary and ternary

magnesium alloys. The original data and findings reported herein are constituents for the development and implementation of lower-cost wrought Mg alloys for structural applications.

APPENDIX A: RECOMMENDED FUTURE STUDIES

The goals and objectives of this doctoral study are broad-reaching. Through the course of this research, fundamental data and interdependencies were examined. However, this research has also revealed some aspects of magnesium alloy metallurgy which are deserving of additional investigation.

1. An extensive investigation into the crystal structure, thermodynamic stability, and diffusion kinetics of Mg_6Gd is warranted. As noted in this work, impurities may stabilize a non-equilibrium phase in the diffusion couple technique. The pure Gd used in this study contained as much as 0.46 wt.% O impurities. Both Gd and Mg have a high affinity for O, and quickly oxidize in standard atmosphere. Therefore, elemental analysis by XEDS and EPMA cannot reliably differentiate between surface oxides and bulk O. X-ray Diffraction and solid-state Nuclear Magnetic Resonance studies were not performed in this study but may reveal additional insight into the nature of the crystal structure and its constituents. Furthermore, incremental diffusion couples of pure Mg vs Mg_5Gd may provide insight into the thermodynamic stability of Mg_6Gd. This study showed that the phase does not immediately form at 475°C. Additional time-dependent diffusion studies may reveal insight into the kinetic nature of the phase.
2. Throughout this study, parabolic growth of interdiffusion reaction products is implicitly assumed. The assumption is substantiated by adherence to the Arrhenius relationship with temperature. However, order-of-magnitude differences between the parabolic growth rate and integrated interdiffusion

coefficient for Mg_2Gd, MgGd, MgY, and ε-$Mg_{24}Y_5$ suggest a strong influence of ordering or grain boundary diffusion on the growth of those phases. Additional study into the time-dependent growth in Mg-Gd and Mg-Y systems is warranted.

3. The pop-in phenomena was observed in the majority of Mg solid solutions and Mg based intermetallic compounds from this study. This behavior is often attributed to dynamic strain aging, the PLC effect, wherein the solute atoms pin the dislocation. When the dislocation is torn away from the atom, a jump in displacement is observed. However, the pop-in behavior can also be attributed to order-disorder transformations, mechanical twinning, and work hardening sensitivity. In this study, a correlation between pop-in severity and activation energy of interdiffusion in the Mg solid solutions was observed and lends credence to dynamic strain aging. Nonetheless, this is not sufficient evidence to definitively conclude the underlying mechanism. The PLC effect occurs within specific limits of temperature, strain, and strain rate [169]. As such, strain rate studied in Mg solid solutions in Mg based intermetallic strengthening phases should be investigated to narrow in on the mechanism of the pop-in behavior.
4. The influence of alloying element concentration on reduced modulus and hardness trends with the influence of the composition dependence of interdiffusion except in the case of the C14 Laves phases (i.e. $MgZn_2$ and δ-Mg_2Y). It would be interesting and original to further investigate the

principal mechanisms which lead to inverse correlation between reduced modulus and interdiffusion with respect to concentration in the hexagonal C14 Laves phases.

5. Zn is a dominant alloying element in Mg(Al,Zn) solid solution; Zn interdiffuses the fastest, and its presence influences both the pre-exponential factor and activation energy of Al impurity diffusion. The influence of Zn as a ternary alloying element in Mg(RE,Zn) solid solutions on the diffusional kinetics and mechanical properties would be interesting.
6. Small additions of neodymium to Mg alloys has been reported to be an effective texture modifier making it particularly interesting for wrought applications [170]. Small addition of scandium to Mg alloys has been reported to effectively increase the room temperature properties, creep resistance, and corrosion resistance [171, 172]. Similarly, small additions of zirconium are often used to refine the grain structure of Mg alloys [2]. Virtually no diffusion data, in particular impurity diffusion data, is available for these binary systems of technological importance. A thorough investigation into the impurity diffusion, interdiffusion, and mechanical properties of Mg-Zr, Mg-Sc, and Mg-Nd systems is warranted.
7. The experimental datasets obtained in this doctoral study, along with first principles studies thermodynamics, kinetics, and defect structures may provide insight into previously unexamined mechanisms. For example, Monte Carlo simulations of defect structure in cI58 may be useful explore

diffusion mechanism. Computational thermodynamic investigations should evaluate the stability of the Mg_6Gd phase and its influence on the phase diagram. Phase field modeling of Mg-Y and Mg-Gd may be useful to assess nucleation and growth dynamics.

APPENDIX B: FUNDAMENTAL DATASETS

B.1 Mg-Al Binary System

Table 27: Hall Interdiffusion coefficients in Mg solid solution as a function of composition obtained from 350°C diffusion anneal of Mg vs. Mg-9at.%Al after 96 hours; Matano plane, $x_o = 0$

Phase	Position (μm)	at.%Zn	EPMA Line Scan	Hall Interdiffusion Coefficient (m^2/sec)
Mg(Al)	-23.0	0.01	LS1	8.89×10^{-17}
Mg(Al)	-21.0	0.03	LS1	8.94×10^{-17}
Mg(Al)	-19.0	0.08	LS1	8.99×10^{-17}
Mg(Al)	-17.0	0.17	LS1	9.04×10^{-17}
Mg(Al)	-15.0	0.31	LS1	9.1×10^{-17}
Mg(Al)	-13.0	0.52	LS1	9.17×10^{-17}
Mg(Al)	-11.0	0.85	LS1	9.25×10^{-17}
Mg(Al)	-25.3	0.00	LS2	1.59×10^{-16}
Mg(Al)	-23.3	0.01	LS2	1.57×10^{-16}
Mg(Al)	-21.3	0.02	LS2	1.56×10^{-16}
Mg(Al)	-19.3	0.04	LS2	1.55×10^{-16}
Mg(Al)	-17.2	0.05	LS2	1.54×10^{-16}
Mg(Al)	-15.2	0.08	LS2	1.52×10^{-16}
Mg(Al)	-13.2	0.12	LS2	1.51×10^{-16}
Mg(Al)	-11.2	0.18	LS2	1.49×10^{-16}
Mg(Al)	-9.2	0.27	LS2	1.47×10^{-16}
Mg(Al)	-7.1	0.41	LS2	1.44×10^{-16}
Mg(Al)	-5.1	0.60	LS2	1.41×10^{-16}
Mg(Al)	-3.1	0.85	LS2	1.37×10^{-16}
Mg(Al)	-25.3	0.01	LS3	1.54×10^{-16}
Mg(Al)	-23.2	0.02	LS3	1.52×10^{-16}
Mg(Al)	-21.2	0.03	LS3	1.5×10^{-16}
Mg(Al)	-19.2	0.05	LS3	1.49×10^{-16}
Mg(Al)	-17.2	0.07	LS3	1.47×10^{-16}
Mg(Al)	-15.1	0.09	LS3	1.46×10^{-16}
Mg(Al)	-13.1	0.12	LS3	1.45×10^{-16}
Mg(Al)	-11.1	0.17	LS3	1.43×10^{-16}
Mg(Al)	-9.1	0.26	LS3	1.4×10^{-16}
Mg(Al)	-7.1	0.43	LS3	1.36×10^{-16}
Mg(Al)	-5.0	0.69	LS3	1.31×10^{-16}

Table 28: Hall Interdiffusion coefficients in Mg solid solution as a function of composition obtained from 400°C diffusion anneal of Mg vs. Mg-9at.%Al after 17 hours; Matano plane, $x_o = 0$

Phase	Position (μm)	at.%Zn	EPMA Line Scan	Hall Interdiffusion Coefficient (m^2/sec)
Mg(Al)	123.1	0.00	LS2	1.00×10^{-15}
Mg(Al)	121.7	0.01	LS2	1.01×10^{-15}
Mg(Al)	120.3	0.01	LS2	1.01×10^{-15}
Mg(Al)	118.9	0.01	LS2	1.01×10^{-15}
Mg(Al)	117.5	0.01	LS2	1.01×10^{-15}
Mg(Al)	116.0	0.01	LS2	1.01×10^{-15}
Mg(Al)	114.6	0.01	LS2	1.01×10^{-15}
Mg(Al)	113.2	0.01	LS2	1.02×10^{-15}
Mg(Al)	111.8	0.02	LS2	1.02×10^{-15}
Mg(Al)	110.4	0.02	LS2	1.03×10^{-15}
Mg(Al)	109.0	0.04	LS2	1.03×10^{-15}
Mg(Al)	107.6	0.05	LS2	1.04×10^{-15}
Mg(Al)	106.1	0.07	LS2	1.04×10^{-15}
Mg(Al)	104.7	0.09	LS2	1.05×10^{-15}
Mg(Al)	103.3	0.12	LS2	1.06×10^{-15}
Mg(Al)	101.9	0.17	LS2	1.07×10^{-15}
Mg(Al)	100.5	0.23	LS2	1.08×10^{-15}
Mg(Al)	99.1	0.32	LS2	1.09×10^{-15}
Mg(Al)	97.7	0.45	LS2	1.10×10^{-15}
Mg(Al)	96.2	0.60	LS2	1.12×10^{-15}
Mg(Al)	94.8	0.79	LS2	1.13×10^{-15}
Mg(Al)	114.6	0.00	LS3	8.47×10^{-16}
Mg(Al)	113.2	0.02	LS3	8.72×10^{-16}
Mg(Al)	111.8	0.03	LS3	8.82×10^{-16}
Mg(Al)	110.4	0.05	LS3	8.92×10^{-16}
Mg(Al)	109.0	0.07	LS3	9.04×10^{-16}
Mg(Al)	107.6	0.11	LS3	9.17×10^{-16}
Mg(Al)	106.1	0.16	LS3	9.31×10^{-16}
Mg(Al)	104.7	0.24	LS3	9.48×10^{-16}
Mg(Al)	103.3	0.34	LS3	9.67×10^{-16}
Mg(Al)	101.9	0.47	LS3	9.87×10^{-16}
Mg(Al)	100.5	0.63	LS3	1.01×10^{-15}
Mg(Al)	99.1	0.83	LS3	1.03×10^{-15}

Table 29: Hall Interdiffusion coefficients in Mg solid solution as a function of composition obtained from 450°C diffusion anneal of Mg vs. Mg-9at.%Al after 24 hours; Matano plane, $x_o = 0$

Phase	Position (μm)	at.%Zn	EPMA Line Scan	Hall Interdiffusion Coefficient (m^2/sec)
Mg(Al)	95.0	0.00	LS1	4.72×10^{-15}
Mg(Al)	99.5	0.01	LS1	4.77×10^{-15}
Mg(Al)	104.0	0.02	LS1	4.84×10^{-15}
Mg(Al)	108.6	0.03	LS1	4.88×10^{-15}
Mg(Al)	113.1	0.05	LS1	4.94×10^{-15}
Mg(Al)	117.7	0.09	LS1	5.01×10^{-15}
Mg(Al)	122.2	0.14	LS1	5.09×10^{-15}
Mg(Al)	126.7	0.22	LS1	5.18×10^{-15}
Mg(Al)	131.3	0.32	LS1	5.28×10^{-15}
Mg(Al)	135.8	0.47	LS1	5.39×10^{-15}
Mg(Al)	140.3	0.65	LS1	5.50×10^{-15}
Mg(Al)	144.9	0.87	LS1	5.63×10^{-15}
Mg(Al)	104.0	0.01	LS2	5.73×10^{-15}
Mg(Al)	108.6	0.02	LS2	5.82×10^{-15}
Mg(Al)	113.1	0.05	LS2	5.91×10^{-15}
Mg(Al)	117.7	0.09	LS2	5.99×10^{-15}
Mg(Al)	122.2	0.14	LS2	6.07×10^{-15}
Mg(Al)	126.7	0.22	LS2	6.16×10^{-15}
Mg(Al)	131.3	0.31	LS2	6.26×10^{-15}
Mg(Al)	135.8	0.45	LS2	6.36×10^{-15}
Mg(Al)	140.3	0.61	LS2	6.48×10^{-15}
Mg(Al)	144.9	0.82	LS2	6.61×10^{-15}
Mg(Al)	58.6	0.00	LS3	5.49×10^{-15}
Mg(Al)	63.1	0.00	LS3	5.49×10^{-15}
Mg(Al)	67.7	0.00	LS3	5.49×10^{-15}
Mg(Al)	72.2	0.00	LS3	5.49×10^{-15}
Mg(Al)	76.8	0.01	LS3	5.55×10^{-15}
Mg(Al)	81.3	0.01	LS3	5.55×10^{-15}
Mg(Al)	85.8	0.01	LS3	5.59×10^{-15}
Mg(Al)	90.4	0.01	LS3	5.59×10^{-15}
Mg(Al)	94.9	0.02	LS3	5.62×10^{-15}
Mg(Al)	99.4	0.02	LS3	5.64×10^{-15}
Mg(Al)	104.0	0.04	LS3	5.68×10^{-15}

Phase	Position (μm)	at.%Zn	EPMA Line Scan	Hall Interdiffusion Coefficient (m^2/sec)
Mg(Al)	108.5	0.05	LS3	$5.72x10^{-15}$
Mg(Al)	113.1	0.07	LS3	$5.77x10^{-15}$
Mg(Al)	117.6	0.10	LS3	$5.82x10^{-15}$
Mg(Al)	122.1	0.15	LS3	$5.89x10^{-15}$
Mg(Al)	126.7	0.22	LS3	$5.97x10^{-15}$
Mg(Al)	131.2	0.32	LS3	$6.06x10^{-15}$
Mg(Al)	135.7	0.47	LS3	$6.17x10^{-15}$
Mg(Al)	140.3	0.66	LS3	$6.30x10^{-15}$
Mg(Al)	144.8	0.89	LS3	$6.44x10^{-15}$

Table 30: Reduced modulus and hardness of Mg solid solution as a function of composition obtained from 450°C diffusion anneal of Mg vs. Mg-9at.%Al after 24 hours; Peak Load 5mN

Phase	at.%Al	Reduced Modulus (GPa)		Hardness (GPa)	
		Avg.	Std. Dev.	Avg.	Std. Dev.
Mg(Al)	0.00	35.00	1.70	0.50	0.00
Mg(Al)	0.00	40.13	3.72	0.55	0.06
Mg(Al)	0.01	42.33	2.66	0.53	0.04
Mg(Al)	0.03	40.02	2.43	0.57	0.03
Mg(Al)	0.10	40.88	0.79	0.60	0.03
Mg(Al)	0.27	41.67	0.70	0.58	0.03
Mg(Al)	0.61	40.68	2.04	0.59	0.04
Mg(Al)	1.15	39.87	1.42	0.54	0.01
Mg(Al)	1.89	40.27	2.65	0.55	0.07
Mg(Al)	2.78	43.63	2.35	0.56	0.02
Mg(Al)	3.71	40.28	2.19	0.59	0.09
Mg(Al)	4.55	41.56	1.24	0.60	0.05
Mg(Al)	5.23	43.81	1.62	0.66	0.07
Mg(Al)	5.80	44.10	1.45	0.65	0.06
Mg(Al)	6.27	45.62	2.21	0.69	0.06
Mg(Al)	6.67	45.69	2.62	0.76	0.08
Mg(Al)	6.99	46.42	1.57	0.78	0.03
Mg(Al)	7.26	46.47	1.40	0.88	0.04
Mg(Al)	7.49	46.42	0.73	0.95	0.06
Mg(Al)	7.68	44.94	1.23	0.93	0.06
Mg(Al)	7.98	45.28	1.63	1.07	0.07
Mg(Al)	8.09	47.80	1.00	1.01	0.04
Mg(Al)	8.18	47.28	0.12	1.00	0.05
Mg(Al)	8.26	47.16	0.85	1.01	0.03
Mg(Al)	8.33	48.48	0.65	1.05	0.03
Mg(Al)	8.38	49.65	0.91	0.99	0.04
Mg(Al)	8.42	52.50	1.37	1.17	0.09

Phase	at.%Al	Reduced Modulus (GPa)		Hardness (GPa)	
		Avg.	Std. Dev.	Avg.	Std. Dev.
Mg(Al)	0.00	35.00	1.70	0.50	0.00
Mg(Al)	0.00	40.13	3.72	0.55	0.06
Mg(Al)	0.01	42.33	2.66	0.53	0.04
Mg(Al)	0.03	40.02	2.43	0.57	0.03
Mg(Al)	0.10	40.88	0.79	0.60	0.03
Mg(Al)	0.27	41.67	0.70	0.58	0.03
Mg(Al)	0.61	40.68	2.04	0.59	0.04
Mg(Al)	8.45	51.93	2.10	1.09	0.10
Mg(Al)	8.47	51.78	1.78	1.09	0.05
Mg(Al)	8.47	52.43	1.62	1.16	0.12
Mg(Al)	8.47	51.33	0.96	1.08	0.05
Mg(Al)	8.47	53.26	1.53	1.13	0.13
Mg(Al)	8.47	49.45	1.33	1.01	0.06
Mg(Al)	8.47	51.95	0.88	1.04	0.03
Mg(Al)	8.47	50.95	0.17	1.05	0.08

B.2 Mg-Gd Binary System

Table 31: Hall Interdiffusion coefficients in Mg solid solution as a function of composition obtained from 385°C diffusion anneal of Mg vs. Gd after 192 hours; Matano plane, $x_o = 0$

Phase	Position (μm)	at.%Gd	Hall Interdiffusion Coefficient (m^2/sec)
Mg(Gd)	220.7	0.00	3.92×10^{-15}
Mg(Gd)	218.7	0.01	3.77×10^{-15}
Mg(Gd)	215.7	0.01	3.76×10^{-15}
Mg(Gd)	213.7	0.00	3.92×10^{-15}
Mg(Gd)	211.7	0.00	3.84×10^{-15}
Mg(Gd)	210.7	0.01	3.73×10^{-15}
Mg(Gd)	208.7	0.01	3.70×10^{-15}
Mg(Gd)	206.7	0.01	3.72×10^{-15}
Mg(Gd)	204.7	0.01	3.73×10^{-15}
Mg(Gd)	201.7	0.01	3.70×10^{-15}
Mg(Gd)	199.7	0.02	3.66×10^{-15}
Mg(Gd)	197.7	0.02	3.68×10^{-15}
Mg(Gd)	196.7	0.01	3.73×10^{-15}
Mg(Gd)	194.7	0.03	3.57×10^{-15}
Mg(Gd)	192.7	0.04	3.55×10^{-15}
Mg(Gd)	189.7	0.01	3.69×10^{-15}
Mg(Gd)	187.7	0.02	3.62×10^{-15}
Mg(Gd)	185.7	0.03	3.56×10^{-15}
Mg(Gd)	183.7	0.03	3.60×10^{-15}
Mg(Gd)	182.7	0.03	3.57×10^{-15}
Mg(Gd)	180.7	0.03	3.58×10^{-15}
Mg(Gd)	178.7	0.04	3.53×10^{-15}
Mg(Gd)	175.7	0.03	3.56×10^{-15}
Mg(Gd)	173.7	0.04	3.55×10^{-15}
Mg(Gd)	171.7	0.06	3.46×10^{-15}
Mg(Gd)	169.7	0.04	3.51×10^{-15}
Mg(Gd)	168.7	0.05	3.50×10^{-15}
Mg(Gd)	166.7	0.05	3.51×10^{-15}
Mg(Gd)	163.7	0.07	3.44×10^{-15}
Mg(Gd)	161.7	0.07	3.43×10^{-15}
Mg(Gd)	159.7	0.06	3.45×10^{-15}
Mg(Gd)	157.7	0.07	3.44×10^{-15}

Phase	Position (μm)	at.%Gd	Hall Interdiffusion Coefficient (m^2/sec)
Mg(Gd)	155.7	0.07	$3.44x10^{-15}$
Mg(Gd)	153.7	0.07	$3.42x10^{-15}$
Mg(Gd)	151.7	0.08	$3.41x10^{-15}$
Mg(Gd)	149.7	0.08	$3.41x10^{-15}$
Mg(Gd)	147.7	0.09	$3.39x10^{-15}$
Mg(Gd)	145.7	0.10	$3.37x10^{-15}$
Mg(Gd)	143.7	0.10	$3.36x10^{-15}$
Mg(Gd)	141.7	0.12	$3.33x10^{-15}$
Mg(Gd)	139.7	0.12	$3.31x10^{-15}$
Mg(Gd)	137.7	0.14	$3.29x10^{-15}$
Mg(Gd)	135.7	0.17	$3.24x10^{-15}$
Mg(Gd)	133.7	0.18	$3.24x10^{-15}$
Mg(Gd)	131.7	0.17	$3.24x10^{-15}$
Mg(Gd)	129.7	0.17	$3.25x10^{-15}$

Table 32: Hall Interdiffusion coefficients in Mg solid solution as a function of composition obtained from 475°C diffusion anneal of Mg vs. Gd after 96.5 hours; Matano plane, $x_o = 0$

Phase	Position (μm)	at.%Gd	Hall Interdiffusion Coefficient (m^2/sec)
Mg(Gd)	571	0.00	3.65×10^{-14}
Mg(Gd)	568	0.01	3.65×10^{-14}
Mg(Gd)	564	0.01	3.65×10^{-14}
Mg(Gd)	561	0.03	3.63×10^{-14}
Mg(Gd)	559	0.01	3.64×10^{-14}
Mg(Gd)	556	0.02	3.63×10^{-14}
Mg(Gd)	553	0.01	3.64×10^{-14}
Mg(Gd)	549	0.03	3.63×10^{-14}
Mg(Gd)	546	0.03	3.63×10^{-14}
Mg(Gd)	544	0.01	3.64×10^{-14}
Mg(Gd)	541	0.02	3.63×10^{-14}
Mg(Gd)	537	0.01	3.64×10^{-14}
Mg(Gd)	534	0.03	3.63×10^{-14}
Mg(Gd)	531	0.03	3.63×10^{-14}
Mg(Gd)	529	0.01	3.65×10^{-14}
Mg(Gd)	526	0.03	3.63×10^{-14}
Mg(Gd)	522	0.02	3.64×10^{-14}
Mg(Gd)	519	0.03	3.63×10^{-14}
Mg(Gd)	517	0.03	3.63×10^{-14}
Mg(Gd)	514	0.05	3.62×10^{-14}
Mg(Gd)	511	0.05	3.62×10^{-14}
Mg(Gd)	507	0.04	3.62×10^{-14}
Mg(Gd)	504	0.05	3.62×10^{-14}
Mg(Gd)	502	0.06	3.62×10^{-14}
Mg(Gd)	499	0.11	3.60×10^{-14}
Mg(Gd)	495	0.08	3.61×10^{-14}
Mg(Gd)	492	0.06	3.62×10^{-14}
Mg(Gd)	489	0.05	3.62×10^{-14}
Mg(Gd)	487	0.06	3.62×10^{-14}
Mg(Gd)	484	0.10	3.61×10^{-14}
Mg(Gd)	480	0.09	3.61×10^{-14}
Mg(Gd)	477	0.09	3.61×10^{-14}
Mg(Gd)	475	0.09	3.61×10^{-14}
Mg(Gd)	472	0.09	3.61×10^{-14}

Phase	Position (μm)	at.%Gd	Hall Interdiffusion Coefficient (m^2/sec)
Mg(Gd)	469	0.11	$3.61x10^{-14}$
Mg(Gd)	465	0.09	$3.61x10^{-14}$
Mg(Gd)	462	0.11	$3.60x10^{-14}$
Mg(Gd)	460	0.12	$3.60x10^{-14}$
Mg(Gd)	457	0.13	$3.60x10^{-14}$
Mg(Gd)	453	0.13	$3.60x10^{-14}$
Mg(Gd)	450	0.15	$3.60x10^{-14}$
Mg(Gd)	447	0.14	$3.60x10^{-14}$
Mg(Gd)	445	0.15	$3.60x10^{-14}$
Mg(Gd)	442	0.18	$3.59x10^{-14}$
Mg(Gd)	438	0.19	$3.59x10^{-14}$
Mg(Gd)	435	0.20	$3.59x10^{-14}$
Mg(Gd)	433	0.19	$3.59x10^{-14}$

Table 33: Hall Interdiffusion coefficients in Mg solid solution as a function of composition obtained from 490°C diffusion anneal of Mg vs. Gd after 72 hours; Matano plane, $x_o = 0$

Phase	Position (μm)	at.%Gd	Hall Interdiffusion Coefficient (m^2/sec)
Mg(Gd)	616	0.00	5.00×10^{-14}
Mg(Gd)	613	0.01	5.00×10^{-14}
Mg(Gd)	610	0.01	5.00×10^{-14}
Mg(Gd)	607	0.01	5.00×10^{-14}
Mg(Gd)	604	0.02	5.01×10^{-14}
Mg(Gd)	601	0.00	5.00×10^{-14}
Mg(Gd)	598	0.00	5.00×10^{-14}
Mg(Gd)	595	0.00	5.00×10^{-14}
Mg(Gd)	592	0.01	5.01×10^{-14}
Mg(Gd)	589	0.01	5.00×10^{-14}
Mg(Gd)	586	0.02	5.01×10^{-14}
Mg(Gd)	583	0.03	5.01×10^{-14}
Mg(Gd)	580	0.02	5.01×10^{-14}
Mg(Gd)	577	0.02	5.01×10^{-14}
Mg(Gd)	574	0.02	5.01×10^{-14}
Mg(Gd)	571	0.03	5.01×10^{-14}
Mg(Gd)	568	0.03	5.01×10^{-14}
Mg(Gd)	565	0.03	5.01×10^{-14}
Mg(Gd)	562	0.03	5.01×10^{-14}
Mg(Gd)	559	0.04	5.01×10^{-14}
Mg(Gd)	556	0.04	5.01×10^{-14}
Mg(Gd)	553	0.05	5.01×10^{-14}
Mg(Gd)	550	0.03	5.01×10^{-14}
Mg(Gd)	547	0.04	5.01×10^{-14}
Mg(Gd)	544	0.06	5.01×10^{-14}
Mg(Gd)	541	0.05	5.01×10^{-14}
Mg(Gd)	538	0.05	5.01×10^{-14}
Mg(Gd)	535	0.06	5.01×10^{-14}
Mg(Gd)	532	0.06	5.01×10^{-14}
Mg(Gd)	529	0.06	5.01×10^{-14}
Mg(Gd)	526	0.08	5.01×10^{-14}
Mg(Gd)	523	0.06	5.01×10^{-14}
Mg(Gd)	520	0.08	5.01×10^{-14}
Mg(Gd)	516	0.08	5.01×10^{-14}

Phase	Position (μm)	at.%Gd	Hall Interdiffusion Coefficient (m^2/sec)
Mg(Gd)	513	0.10	$5.01x10^{-14}$
Mg(Gd)	511	0.08	$5.01x10^{-14}$
Mg(Gd)	508	0.07	$5.01x10^{-14}$
Mg(Gd)	504	0.11	$5.01x10^{-14}$
Mg(Gd)	501	0.12	$5.01x10^{-14}$
Mg(Gd)	498	0.10	$5.01x10^{-14}$
Mg(Gd)	496	0.10	$5.01x10^{-14}$
Mg(Gd)	493	0.12	$5.01x10^{-14}$
Mg(Gd)	489	0.13	$5.01x10^{-14}$
Mg(Gd)	486	0.13	$5.01x10^{-14}$
Mg(Gd)	484	0.15	$5.01x10^{-14}$
Mg(Gd)	481	0.16	$5.01x10^{-14}$
Mg(Gd)	477	0.17	$5.01x10^{-14}$
Mg(Gd)	474	0.14	$5.01x10^{-14}$
Mg(Gd)	471	0.16	$5.01x10^{-14}$
Mg(Gd)	469	0.21	$5.02x10^{-14}$
Mg(Gd)	466	0.20	$5.02x10^{-14}$
Mg(Gd)	462	0.18	$5.01x10^{-14}$

Table 34: Interdiffusion flux and interdiffusion coefficients as a function of composition in intermetallic compounds formed during 385°C diffusion anneal of Mg vs. Gd after 192 hours; Matano plane, $x_o = 0$

Phase	Position (μm)	at.%Gd	Flux $\left(\frac{\mu m \cdot at.frac.}{sec}\right)$	Boltzmann-Matano Interdiffusion Coefficient (m^2/sec)
Mg(Gd)	106.9	0.46	4.62×10^{-7}	2.78×10^{-15}
Mg(Gd)	105.1	0.49	4.85×10^{-7}	2.73×10^{-15}
Mg(Gd)	103.3	0.53	5.10×10^{-7}	2.68×10^{-15}
Mg(Gd)	101.5	0.57	5.36×10^{-7}	2.64×10^{-15}
Mg(Gd)	99.7	0.60	5.63×10^{-7}	2.59×10^{-15}
Mg_6Gd	95.6	13.88	9.97×10^{-6}	3.01×10^{-14}
Mg_6Gd	95.5	13.88	9.97×10^{-6}	3.01×10^{-14}
Mg_6Gd	95.3	13.89	9.97×10^{-6}	3.01×10^{-14}
Mg_6Gd	95.2	13.89	9.98×10^{-6}	3.02×10^{-14}
Mg_6Gd	95.1	13.89	9.98×10^{-6}	3.01×10^{-14}
Mg_6Gd	95.0	13.90	9.98×10^{-6}	3.02×10^{-14}
Mg_6Gd	94.9	13.90	9.99×10^{-6}	3.01×10^{-14}
Mg_6Gd	94.7	13.91	9.99×10^{-6}	3.02×10^{-14}
Mg_6Gd	94.6	13.91	9.99×10^{-6}	3.01×10^{-14}
Mg_6Gd	94.5	13.91	9.99×10^{-6}	3.02×10^{-14}
Mg_6Gd	94.4	13.92	1.00×10^{-5}	3.01×10^{-14}
Mg_6Gd	94.2	13.92	1.00×10^{-5}	3.02×10^{-14}
Mg_6Gd	94.1	13.93	1.00×10^{-5}	3.02×10^{-14}
Mg_6Gd	94.0	13.93	1.00×10^{-5}	3.02×10^{-14}
Mg_6Gd	93.9	13.93	1.00×10^{-5}	3.02×10^{-14}
Mg_6Gd	93.8	13.94	1.00×10^{-5}	3.02×10^{-14}
Mg_6Gd	93.6	13.94	1.00×10^{-5}	3.03×10^{-14}
Mg_6Gd	93.5	13.95	1.00×10^{-5}	3.02×10^{-14}
Mg_6Gd	93.4	13.95	1.00×10^{-5}	3.03×10^{-14}
Mg_6Gd	93.3	13.95	1.00×10^{-5}	3.02×10^{-14}
Mg_6Gd	93.2	13.96	1.00×10^{-5}	3.03×10^{-14}
Mg_6Gd	93.0	13.96	1.00×10^{-5}	3.02×10^{-14}
Mg_6Gd	92.9	13.97	1.00×10^{-5}	3.03×10^{-14}
Mg_6Gd	92.8	13.97	1.00×10^{-5}	3.02×10^{-14}
Mg_6Gd	92.7	13.97	1.00×10^{-5}	3.03×10^{-14}
Mg_6Gd	92.5	13.98	1.00×10^{-5}	3.03×10^{-14}
Mg_6Gd	92.4	13.98	1.00×10^{-5}	3.03×10^{-14}

Phase	Position (μm)	at.%Gd	Flux $\left(\frac{\mu m \cdot at.frac.}{sec}\right)$	Boltzmann-Matano Interdiffusion Coefficient (m^2/sec)
Mg_6Gd	92.3	13.99	$1.00x10^{-5}$	$3.03x10^{-14}$
Mg_6Gd	92.2	13.99	$1.00x10^{-5}$	$3.04x10^{-14}$
Mg_6Gd	92.1	13.99	$1.00x10^{-5}$	$3.03x10^{-14}$
Mg_6Gd	91.9	14.00	$1.01x10^{-5}$	$3.04x10^{-14}$
Mg_6Gd	91.8	14.00	$1.01x10^{-5}$	$3.03x10^{-14}$
Mg_6Gd	91.7	14.01	$1.01x10^{-5}$	$3.04x10^{-14}$
Mg_6Gd	91.6	14.01	$1.01x10^{-5}$	$3.03x10^{-14}$
Mg_6Gd	91.5	14.01	$1.01x10^{-5}$	$3.04x10^{-14}$
Mg_6Gd	91.3	14.02	$1.01x10^{-5}$	$3.03x10^{-14}$
Mg_6Gd	91.2	14.02	$1.01x10^{-5}$	$3.04x10^{-14}$
Mg_6Gd	91.1	14.03	$1.01x10^{-5}$	$3.04x10^{-14}$
Mg_6Gd	91.0	14.03	$1.01x10^{-5}$	$3.04x10^{-14}$
Mg_6Gd	90.9	14.03	$1.01x10^{-5}$	$3.04x10^{-14}$
Mg_6Gd	90.7	14.04	$1.01x10^{-5}$	$3.05x10^{-14}$
Mg_6Gd	90.6	14.04	$1.01x10^{-5}$	$3.04x10^{-14}$
Mg_6Gd	90.5	14.05	$1.01x10^{-5}$	$3.05x10^{-14}$
Mg_6Gd	90.4	14.05	$1.01x10^{-5}$	$3.04x10^{-14}$
Mg_6Gd	90.2	14.05	$1.01x10^{-5}$	$3.05x10^{-14}$
Mg_6Gd	90.1	14.06	$1.01x10^{-5}$	$3.04x10^{-14}$
Mg_6Gd	90.0	14.06	$1.01x10^{-5}$	$3.05x10^{-14}$
Mg_6Gd	89.9	14.07	$1.01x10^{-5}$	$3.04x10^{-14}$
Mg_6Gd	89.8	14.07	$1.01x10^{-5}$	$3.04x10^{-14}$
Mg_6Gd	89.6	14.07	$1.01x10^{-5}$	$3.05x10^{-14}$
Mg_6Gd	89.5	14.08	$1.01x10^{-5}$	$3.05x10^{-14}$
Mg_6Gd	89.4	14.08	$1.01x10^{-5}$	$3.05x10^{-14}$
Mg_6Gd	89.3	14.09	$1.01x10^{-5}$	$3.05x10^{-14}$
Mg_6Gd	89.2	14.09	$1.01x10^{-5}$	$3.06x10^{-14}$
Mg_6Gd	89.0	14.09	$1.01x10^{-5}$	$3.05x10^{-14}$
Mg_6Gd	88.9	14.10	$1.01x10^{-5}$	$3.06x10^{-14}$
Mg_6Gd	88.8	14.10	$1.01x10^{-5}$	$3.05x10^{-14}$
Mg_6Gd	88.7	14.11	$1.01x10^{-5}$	$3.06x10^{-14}$
Mg_6Gd	88.5	14.11	$1.01x10^{-5}$	$3.05x10^{-14}$
Mg_6Gd	88.4	14.11	$1.01x10^{-5}$	$3.06x10^{-14}$
Mg_6Gd	88.3	14.12	$1.01x10^{-5}$	$3.05x10^{-14}$
Mg_6Gd	88.2	14.12	$1.01x10^{-5}$	$3.06x10^{-14}$

Phase	Position (μm)	at.%Gd	Flux $\left(\frac{\mu m \cdot at.frac.}{sec}\right)$	Boltzmann-Matano Interdiffusion Coefficient (m^2/sec)
Mg_6Gd	88.1	14.13	$1.01x10^{-5}$	$3.06x10^{-14}$
Mg_6Gd	87.9	14.13	$1.01x10^{-5}$	$3.06x10^{-14}$
Mg_6Gd	87.8	14.13	$1.01x10^{-5}$	$3.06x10^{-14}$
Mg_6Gd	87.7	14.14	$1.01x10^{-5}$	$3.07x10^{-14}$
Mg_6Gd	87.6	14.14	$1.01x10^{-5}$	$3.06x10^{-14}$
Mg_6Gd	87.5	14.15	$1.01x10^{-5}$	$3.07x10^{-14}$
Mg_6Gd	87.3	14.15	$1.02x10^{-5}$	$3.06x10^{-14}$
Mg_6Gd	87.2	14.15	$1.02x10^{-5}$	$3.07x10^{-14}$
Mg_6Gd	87.1	14.16	$1.02x10^{-5}$	$3.06x10^{-14}$
Mg_6Gd	87.0	14.16	$1.02x10^{-5}$	$3.07x10^{-14}$
Mg_6Gd	86.9	14.17	$1.02x10^{-5}$	$3.06x10^{-14}$
Mg_6Gd	86.7	14.17	$1.02x10^{-5}$	$3.07x10^{-14}$
Mg_6Gd	86.6	14.17	$1.02x10^{-5}$	$3.07x10^{-14}$
Mg_6Gd	86.5	14.18	$1.02x10^{-5}$	$3.07x10^{-14}$
Mg_6Gd	86.4	14.18	$1.02x10^{-5}$	$3.07x10^{-14}$
Mg_6Gd	86.2	14.19	$1.02x10^{-5}$	$3.08x10^{-14}$
Mg_6Gd	86.1	14.19	$1.02x10^{-5}$	$3.07x10^{-14}$
Mg_6Gd	86.0	14.19	$1.02x10^{-5}$	$3.08x10^{-14}$
Mg_6Gd	85.9	14.20	$1.02x10^{-5}$	$3.07x10^{-14}$
Mg_6Gd	85.8	14.20	$1.02x10^{-5}$	$3.07x10^{-14}$
Mg_6Gd	85.6	14.21	$1.02x10^{-5}$	$3.08x10^{-14}$
Mg_6Gd	85.5	14.21	$1.02x10^{-5}$	$3.07x10^{-14}$
Mg_6Gd	85.4	14.21	$1.02x10^{-5}$	$3.08x10^{-14}$
Mg_6Gd	85.3	14.22	$1.02x10^{-5}$	$3.07x10^{-14}$
Mg_6Gd	85.2	14.22	$1.02x10^{-5}$	$3.08x10^{-14}$
Mg_6Gd	85.0	14.23	$1.02x10^{-5}$	$3.08x10^{-14}$
Mg_6Gd	84.9	14.23	$1.02x10^{-5}$	$3.08x10^{-14}$
Mg_6Gd	84.8	14.23	$1.02x10^{-5}$	$3.08x10^{-14}$
Mg_6Gd	84.7	14.24	$1.02x10^{-5}$	$3.08x10^{-14}$
Mg_6Gd	84.5	14.24	$1.02x10^{-5}$	$3.08x10^{-14}$
Mg_6Gd	84.4	14.25	$1.02x10^{-5}$	$3.09x10^{-14}$
Mg_6Gd	84.3	14.25	$1.02x10^{-5}$	$3.08x10^{-14}$
Mg_6Gd	84.2	14.25	$1.02x10^{-5}$	$3.09x10^{-14}$
Mg_6Gd	84.1	14.26	$1.02x10^{-5}$	$3.08x10^{-14}$
Mg_6Gd	83.9	14.26	$1.02x10^{-5}$	$3.09x10^{-14}$

Phase	Position (μm)	at.%Gd	Flux $\left(\frac{\mu m \cdot at.frac.}{sec}\right)$	Boltzmann-Matano Interdiffusion Coefficient (m^2/sec)
Mg_6Gd	83.8	14.27	$1.02x10^{-5}$	$3.08x10^{-14}$
Mg_6Gd	83.7	14.27	$1.02x10^{-5}$	$3.09x10^{-14}$
Mg_5Gd	79.1	15.56	$1.10x10^{-5}$	$6.01x10^{-14}$
Mg_5Gd	78.6	15.57	$1.10x10^{-5}$	$6.01x10^{-14}$
Mg_5Gd	78.0	15.59	$1.10x10^{-5}$	$6.02x10^{-14}$
Mg_5Gd	77.4	15.60	$1.10x10^{-5}$	$6.01x10^{-14}$
Mg_5Gd	76.9	15.61	$1.10x10^{-5}$	$6.02x10^{-14}$
Mg_5Gd	76.3	15.62	$1.10x10^{-5}$	$6.02x10^{-14}$
Mg_5Gd	75.7	15.63	$1.10x10^{-5}$	$6.03x10^{-14}$
Mg_5Gd	75.2	15.64	$1.10x10^{-5}$	$6.03x10^{-14}$
Mg_5Gd	74.6	15.65	$1.10x10^{-5}$	$6.04x10^{-14}$
Mg_5Gd	74.0	15.66	$1.10x10^{-5}$	$6.03x10^{-14}$
Mg_5Gd	73.5	15.67	$1.10x10^{-5}$	$6.04x10^{-14}$
Mg_5Gd	72.9	15.68	$1.10x10^{-5}$	$6.04x10^{-14}$
Mg_5Gd	72.3	15.69	$1.11x10^{-5}$	$6.04x10^{-14}$
Mg_5Gd	71.8	15.70	$1.11x10^{-5}$	$6.05x10^{-14}$
Mg_5Gd	71.2	15.71	$1.11x10^{-5}$	$6.05x10^{-14}$
Mg_5Gd	70.6	15.72	$1.11x10^{-5}$	$6.06x10^{-14}$
Mg_5Gd	70.1	15.73	$1.11x10^{-5}$	$6.05x10^{-14}$
Mg_5Gd	69.5	15.74	$1.11x10^{-5}$	$6.06x10^{-14}$
Mg_5Gd	69.0	15.75	$1.11x10^{-5}$	$6.06x10^{-14}$
Mg_5Gd	68.4	15.76	$1.11x10^{-5}$	$6.07x10^{-14}$
Mg_5Gd	67.8	15.77	$1.11x10^{-5}$	$6.06x10^{-14}$
Mg_5Gd	67.3	15.78	$1.11x10^{-5}$	$6.07x10^{-14}$
Mg_5Gd	66.7	15.79	$1.11x10^{-5}$	$6.07x10^{-14}$
Mg_5Gd	66.1	15.80	$1.11x10^{-5}$	$6.08x10^{-14}$
Mg_5Gd	65.6	15.81	$1.11x10^{-5}$	$6.08x10^{-14}$
Mg_5Gd	65.0	15.82	$1.11x10^{-5}$	$6.08x10^{-14}$
Mg_5Gd	64.4	15.83	$1.11x10^{-5}$	$6.09x10^{-14}$
Mg_5Gd	63.9	15.84	$1.11x10^{-5}$	$6.08x10^{-14}$
Mg_5Gd	63.3	15.85	$1.11x10^{-5}$	$6.09x10^{-14}$
Mg_5Gd	62.7	15.86	$1.11x10^{-5}$	$6.09x10^{-14}$
Mg_5Gd	62.2	15.87	$1.11x10^{-5}$	$6.10x10^{-14}$
Mg_5Gd	61.6	15.89	$1.12x10^{-5}$	$6.09x10^{-14}$
Mg_5Gd	61.0	15.90	$1.12x10^{-5}$	$6.10x10^{-14}$

Phase	Position (μm)	at.%Gd	Flux $\left(\frac{\mu m \cdot at.frac.}{sec}\right)$	Boltzmann-Matano Interdiffusion Coefficient (m^2/sec)
Mg_5Gd	60.5	15.91	$1.12x10^{-5}$	$6.10x10^{-14}$
Mg_5Gd	59.9	15.92	$1.12x10^{-5}$	$6.11x10^{-14}$
Mg_5Gd	59.3	15.93	$1.12x10^{-5}$	$6.10x10^{-14}$
Mg_5Gd	58.8	15.94	$1.12x10^{-5}$	$6.11x10^{-14}$
Mg_5Gd	58.2	15.95	$1.12x10^{-5}$	$6.11x10^{-14}$
Mg_5Gd	57.6	15.96	$1.12x10^{-5}$	$6.12x10^{-14}$
Mg_5Gd	57.1	15.97	$1.12x10^{-5}$	$6.11x10^{-14}$
Mg_5Gd	56.5	15.98	$1.12x10^{-5}$	$6.12x10^{-14}$
Mg_5Gd	55.9	15.99	$1.12x10^{-5}$	$6.12x10^{-14}$
Mg_5Gd	55.4	16.00	$1.12x10^{-5}$	$6.13x10^{-14}$
Mg_5Gd	54.8	16.01	$1.12x10^{-5}$	$6.13x10^{-14}$
Mg_5Gd	54.2	16.02	$1.12x10^{-5}$	$6.13x10^{-14}$
Mg_5Gd	53.7	16.03	$1.12x10^{-5}$	$6.13x10^{-14}$
Mg_5Gd	53.1	16.04	$1.12x10^{-5}$	$6.13x10^{-14}$
Mg_5Gd	52.5	16.05	$1.12x10^{-5}$	$6.14x10^{-14}$
Mg_5Gd	52.0	16.06	$1.12x10^{-5}$	$6.13x10^{-14}$
Mg_5Gd	51.4	16.07	$1.12x10^{-5}$	$6.14x10^{-14}$
Mg_5Gd	50.9	16.08	$1.12x10^{-5}$	$6.14x10^{-14}$
Mg_5Gd	50.3	16.09	$1.12x10^{-5}$	$6.15x10^{-14}$
Mg_5Gd	49.7	16.10	$1.12x10^{-5}$	$6.14x10^{-14}$
Mg_5Gd	49.2	16.11	$1.12x10^{-5}$	$6.15x10^{-14}$
Mg_5Gd	48.6	16.12	$1.12x10^{-5}$	$6.15x10^{-14}$
Mg_5Gd	48.0	16.13	$1.12x10^{-5}$	$6.15x10^{-14}$
Mg_5Gd	47.5	16.14	$1.13x10^{-5}$	$6.15x10^{-14}$
Mg_5Gd	46.9	16.15	$1.13x10^{-5}$	$6.16x10^{-14}$
Mg_5Gd	46.3	16.16	$1.13x10^{-5}$	$6.16x10^{-14}$
Mg_5Gd	45.8	16.17	$1.13x10^{-5}$	$6.16x10^{-14}$
Mg_5Gd	45.2	16.19	$1.13x10^{-5}$	$6.16x10^{-14}$
Mg_5Gd	44.6	16.20	$1.13x10^{-5}$	$6.16x10^{-14}$
Mg_5Gd	44.1	16.21	$1.13x10^{-5}$	$6.17x10^{-14}$
Mg_5Gd	43.5	16.22	$1.13x10^{-5}$	$6.16x10^{-14}$
Mg_5Gd	42.9	16.23	$1.13x10^{-5}$	$6.17x10^{-14}$
Mg_5Gd	42.4	16.24	$1.13x10^{-5}$	$6.17x10^{-14}$
Mg_5Gd	41.8	16.25	$1.13x10^{-5}$	$6.17x10^{-14}$
Mg_5Gd	41.2	16.26	$1.13x10^{-5}$	$6.17x10^{-14}$

Phase	Position (μm)	at.%Gd	Flux $\left(\frac{\mu m \cdot at.frac.}{sec}\right)$	Boltzmann-Matano Interdiffusion Coefficient (m^2/sec)
Mg_5Gd	40.7	16.27	$1.13x10^{-5}$	$6.18x10^{-14}$
Mg_5Gd	40.1	16.28	$1.13x10^{-5}$	$6.17x10^{-14}$
Mg_5Gd	39.5	16.29	$1.13x10^{-5}$	$6.18x10^{-14}$
Mg_5Gd	39.0	16.30	$1.13x10^{-5}$	$6.18x10^{-14}$
Mg_5Gd	38.4	16.31	$1.13x10^{-5}$	$6.18x10^{-14}$
Mg_5Gd	37.8	16.32	$1.13x10^{-5}$	$6.18x10^{-14}$
Mg_5Gd	37.3	16.33	$1.13x10^{-5}$	$6.19x10^{-14}$
Mg_5Gd	36.7	16.34	$1.13x10^{-5}$	$6.19x10^{-14}$
Mg_5Gd	36.1	16.35	$1.13x10^{-5}$	$6.18x10^{-14}$
Mg_5Gd	35.6	16.36	$1.13x10^{-5}$	$6.19x10^{-14}$
Mg_5Gd	35.0	16.37	$1.13x10^{-5}$	$6.19x10^{-14}$
Mg_5Gd	34.4	16.38	$1.13x10^{-5}$	$6.20x10^{-14}$
Mg_5Gd	33.9	16.39	$1.13x10^{-5}$	$6.19x10^{-14}$
Mg_5Gd	33.3	16.40	$1.13x10^{-5}$	$6.20x10^{-14}$
Mg_5Gd	32.8	16.41	$1.13x10^{-5}$	$6.19x10^{-14}$
Mg_5Gd	32.2	16.42	$1.13x10^{-5}$	$6.20x10^{-14}$
Mg_5Gd	31.6	16.43	$1.13x10^{-5}$	$6.20x10^{-14}$
Mg_5Gd	31.1	16.44	$1.13x10^{-5}$	$6.20x10^{-14}$
Mg_5Gd	30.5	16.45	$1.13x10^{-5}$	$6.20x10^{-14}$
Mg_5Gd	29.9	16.46	$1.13x10^{-5}$	$6.21x10^{-14}$
Mg_5Gd	29.4	16.47	$1.13x10^{-5}$	$6.20x10^{-14}$
Mg_5Gd	28.8	16.49	$1.13x10^{-5}$	$6.21x10^{-14}$
Mg_5Gd	28.2	16.50	$1.14x10^{-5}$	$6.21x10^{-14}$
Mg_5Gd	27.7	16.51	$1.14x10^{-5}$	$6.20x10^{-14}$
Mg_5Gd	27.1	16.52	$1.14x10^{-5}$	$6.21x10^{-14}$
Mg_5Gd	26.5	16.53	$1.14x10^{-5}$	$6.21x10^{-14}$
Mg_5Gd	26.0	16.54	$1.14x10^{-5}$	$6.21x10^{-14}$
Mg_5Gd	25.4	16.55	$1.14x10^{-5}$	$6.21x10^{-14}$
Mg_5Gd	24.8	16.56	$1.14x10^{-5}$	$6.22x10^{-14}$
Mg_5Gd	24.3	16.57	$1.14x10^{-5}$	$6.21x10^{-14}$
Mg_5Gd	23.7	16.58	$1.14x10^{-5}$	$6.22x10^{-14}$
Mg_3Gd	19.3	20.63	$1.20x10^{-5}$	$1.29x10^{-14}$
Mg_3Gd	18.9	20.66	$1.20x10^{-5}$	$1.29x10^{-14}$
Mg_3Gd	18.5	20.70	$1.20x10^{-5}$	$1.29x10^{-14}$
Mg_3Gd	18.1	20.74	$1.20x10^{-5}$	$1.29x10^{-14}$

Phase	Position (μm)	at.%Gd	Flux $\left(\frac{\mu m \cdot at.frac.}{sec}\right)$	Boltzmann-Matano Interdiffusion Coefficient (m^2/sec)
Mg_3Gd	17.7	20.78	$1.20x10^{-5}$	$1.29x10^{-14}$
Mg_3Gd	17.3	20.81	$1.20x10^{-5}$	$1.29x10^{-14}$
Mg_3Gd	16.9	20.85	$1.20x10^{-5}$	$1.29x10^{-14}$
Mg_3Gd	16.5	20.89	$1.20x10^{-5}$	$1.29x10^{-14}$
Mg_3Gd	16.1	20.93	$1.20x10^{-5}$	$1.29x10^{-14}$
Mg_3Gd	15.7	20.96	$1.20x10^{-5}$	$1.29x10^{-14}$
Mg_3Gd	15.3	21.00	$1.20x10^{-5}$	$1.29x10^{-14}$
Mg_3Gd	14.9	21.04	$1.21x10^{-5}$	$1.29x10^{-14}$
Mg_3Gd	14.4	21.08	$1.21x10^{-5}$	$1.29x10^{-14}$
Mg_3Gd	14.0	21.12	$1.21x10^{-5}$	$1.29x10^{-14}$
Mg_3Gd	13.6	21.15	$1.21x10^{-5}$	$1.29x10^{-14}$
Mg_3Gd	13.2	21.19	$1.21x10^{-5}$	$1.29x10^{-14}$
Mg_3Gd	12.8	21.23	$1.21x10^{-5}$	$1.30x10^{-14}$
Mg_3Gd	12.4	21.27	$1.21x10^{-5}$	$1.30x10^{-14}$
Mg_3Gd	12.0	21.30	$1.21x10^{-5}$	$1.30x10^{-14}$
Mg_3Gd	11.6	21.34	$1.21x10^{-5}$	$1.30x10^{-14}$
Mg_3Gd	11.2	21.38	$1.21x10^{-5}$	$1.30x10^{-14}$
Mg_3Gd	10.8	21.42	$1.21x10^{-5}$	$1.30x10^{-14}$
Mg_3Gd	10.4	21.45	$1.21x10^{-5}$	$1.30x10^{-14}$
Mg_3Gd	10.0	21.49	$1.21x10^{-5}$	$1.30x10^{-14}$
Mg_3Gd	9.6	21.53	$1.21x10^{-5}$	$1.30x10^{-14}$
Mg_3Gd	9.2	21.57	$1.21x10^{-5}$	$1.30x10^{-14}$
Mg_3Gd	8.8	21.60	$1.21x10^{-5}$	$1.30x10^{-14}$
Mg_3Gd	8.4	21.64	$1.21x10^{-5}$	$1.30x10^{-14}$
Mg_3Gd	8.0	21.68	$1.21x10^{-5}$	$1.30x10^{-14}$
Mg_3Gd	7.6	21.72	$1.21x10^{-5}$	$1.30x10^{-14}$
Mg_3Gd	7.2	21.76	$1.21x10^{-5}$	$1.30x10^{-14}$
Mg_3Gd	6.8	21.79	$1.21x10^{-5}$	$1.30x10^{-14}$
Mg_3Gd	6.4	21.83	$1.21x10^{-5}$	$1.30x10^{-14}$
Mg_3Gd	6.0	21.87	$1.21x10^{-5}$	$1.30x10^{-14}$
Mg_3Gd	5.6	21.91	$1.21x10^{-5}$	$1.30x10^{-14}$
Mg_3Gd	5.2	21.94	$1.21x10^{-5}$	$1.30x10^{-14}$
Mg_3Gd	4.8	21.98	$1.21x10^{-5}$	$1.30x10^{-14}$
Mg_3Gd	4.3	22.02	$1.21x10^{-5}$	$1.30x10^{-14}$
Mg_3Gd	3.9	22.06	$1.21x10^{-5}$	$1.30x10^{-14}$

Phase	Position (μm)	at.%Gd	Flux $\left(\frac{\mu m \cdot at.frac.}{sec}\right)$	Boltzmann-Matano Interdiffusion Coefficient (m^2/sec)
Mg_3Gd	3.5	22.09	$1.21x10^{-5}$	$1.30x10^{-14}$
Mg_3Gd	3.1	22.13	$1.21x10^{-5}$	$1.30x10^{-14}$
Mg_3Gd	2.7	22.17	$1.21x10^{-5}$	$1.30x10^{-14}$
Mg_3Gd	2.3	22.21	$1.21x10^{-5}$	$1.30x10^{-14}$
Mg_3Gd	1.9	22.24	$1.21x10^{-5}$	$1.30x10^{-14}$
Mg_3Gd	1.5	22.28	$1.21x10^{-5}$	$1.30x10^{-14}$
Mg_3Gd	1.1	22.32	$1.21x10^{-5}$	$1.30x10^{-14}$
Mg_3Gd	0.7	22.36	$1.21x10^{-5}$	$1.30x10^{-14}$
Mg_3Gd	0.3	22.40	$1.21x10^{-5}$	$1.30x10^{-14}$
Mg_3Gd	-0.1	22.43	$1.21x10^{-5}$	$1.30x10^{-14}$
Mg_3Gd	-0.5	22.47	$1.21x10^{-5}$	$1.30x10^{-14}$
Mg_3Gd	-0.9	22.51	$1.21x10^{-5}$	$1.30x10^{-14}$
Mg_3Gd	-1.3	22.55	$1.21x10^{-5}$	$1.30x10^{-14}$
Mg_3Gd	-1.7	22.58	$1.21x10^{-5}$	$1.30x10^{-14}$
Mg_3Gd	-2.1	22.62	$1.21x10^{-5}$	$1.30x10^{-14}$
Mg_3Gd	-2.5	22.66	$1.21x10^{-5}$	$1.30x10^{-14}$
Mg_3Gd	-2.9	22.70	$1.21x10^{-5}$	$1.30x10^{-14}$
Mg_3Gd	-3.3	22.73	$1.21x10^{-5}$	$1.30x10^{-14}$
Mg_3Gd	-3.7	22.77	$1.21x10^{-5}$	$1.30x10^{-14}$
Mg_3Gd	-4.1	22.81	$1.21x10^{-5}$	$1.30x10^{-14}$
Mg_3Gd	-4.5	22.85	$1.21x10^{-5}$	$1.30x10^{-14}$
Mg_3Gd	-4.9	22.88	$1.21x10^{-5}$	$1.30x10^{-14}$
Mg_3Gd	-5.4	22.92	$1.21x10^{-5}$	$1.30x10^{-14}$
Mg_3Gd	-5.8	22.96	$1.21x10^{-5}$	$1.30x10^{-14}$
Mg_3Gd	-6.2	23.00	$1.21x10^{-5}$	$1.30x10^{-14}$
Mg_3Gd	-6.6	23.04	$1.21x10^{-5}$	$1.30x10^{-14}$
Mg_3Gd	-7.0	23.07	$1.21x10^{-5}$	$1.30x10^{-14}$
Mg_3Gd	-7.4	23.11	$1.21x10^{-5}$	$1.30x10^{-14}$
Mg_3Gd	-7.8	23.15	$1.21x10^{-5}$	$1.30x10^{-14}$
Mg_3Gd	-8.2	23.19	$1.21x10^{-5}$	$1.30x10^{-14}$
Mg_3Gd	-8.6	23.22	$1.21x10^{-5}$	$1.30x10^{-14}$
Mg_3Gd	-9.0	23.26	$1.21x10^{-5}$	$1.30x10^{-14}$
Mg_3Gd	-9.4	23.30	$1.21x10^{-5}$	$1.30x10^{-14}$
Mg_3Gd	-9.8	23.34	$1.21x10^{-5}$	$1.30x10^{-14}$
Mg_3Gd	-10.2	23.37	$1.21x10^{-5}$	$1.30x10^{-14}$

Phase	Position (μm)	at.%Gd	Flux $\left(\frac{\mu m \cdot at.frac.}{sec}\right)$	Boltzmann-Matano Interdiffusion Coefficient (m^2/sec)
Mg_3Gd	-10.6	23.41	$1.21x10^{-5}$	$1.30x10^{-14}$
Mg_3Gd	-11.0	23.45	$1.21x10^{-5}$	$1.30x10^{-14}$
Mg_3Gd	-11.4	23.49	$1.21x10^{-5}$	$1.30x10^{-14}$
Mg_3Gd	-11.8	23.52	$1.21x10^{-5}$	$1.30x10^{-14}$
Mg_3Gd	-12.2	23.56	$1.21x10^{-5}$	$1.30x10^{-14}$
Mg_3Gd	-12.6	23.60	$1.21x10^{-5}$	$1.30x10^{-14}$
Mg_3Gd	-13.0	23.64	$1.21x10^{-5}$	$1.30x10^{-14}$
Mg_3Gd	-13.4	23.68	$1.21x10^{-5}$	$1.30x10^{-14}$
Mg_3Gd	-13.8	23.71	$1.21x10^{-5}$	$1.30x10^{-14}$
Mg_3Gd	-14.2	23.75	$1.21x10^{-5}$	$1.29x10^{-14}$
Mg_3Gd	-14.6	23.79	$1.21x10^{-5}$	$1.29x10^{-14}$
Mg_3Gd	-15.0	23.83	$1.21x10^{-5}$	$1.29x10^{-14}$
Mg_3Gd	-15.5	23.86	$1.21x10^{-5}$	$1.29x10^{-14}$
Mg_3Gd	-15.9	23.90	$1.20x10^{-5}$	$1.29x10^{-14}$
Mg_3Gd	-16.3	23.94	$1.20x10^{-5}$	$1.29x10^{-14}$
Mg_3Gd	-16.7	23.98	$1.20x10^{-5}$	$1.29x10^{-14}$
Mg_3Gd	-17.1	24.01	$1.20x10^{-5}$	$1.29x10^{-14}$
Mg_3Gd	-17.5	24.05	$1.20x10^{-5}$	$1.29x10^{-14}$
Mg_3Gd	-17.9	24.09	$1.20x10^{-5}$	$1.29x10^{-14}$
Mg_3Gd	-18.3	24.13	$1.20x10^{-5}$	$1.29x10^{-14}$
Mg_3Gd	-18.7	24.16	$1.20x10^{-5}$	$1.29x10^{-14}$
Mg_3Gd	-19.1	24.20	$1.20x10^{-5}$	$1.29x10^{-14}$
Mg_3Gd	-19.5	24.24	$1.20x10^{-5}$	$1.29x10^{-14}$
Mg_3Gd	-19.9	24.28	$1.20x10^{-5}$	$1.29x10^{-14}$
Mg_3Gd	-20.3	24.32	$1.20x10^{-5}$	$1.29x10^{-14}$

Table 35: Interdiffusion flux and interdiffusion coefficients as a function of composition in intermetallic compounds formed during 475°C diffusion anneal of Mg vs. Gd after 96.5 hours; Matano plane, $x_o = 0$

Phase	Position (μm)	at.%Gd	Flux $\left(\frac{\mu m \cdot at.frac.}{sec}\right)$	Boltzmann-Matano Interdiffusion Coefficient (m^2/sec)
Mg(Gd)	206.5	1.04	5.61E-6	2.31E-14
Mg(Gd)	203.3	1.12	6.00E-6	2.27E-14
Mg(Gd)	200.1	1.21	6.42E-6	2.24E-14
Mg(Gd)	196.8	1.31	6.88E-6	2.21E-14
Mg(Gd)	193.6	1.42	7.37E-6	2.18E-14
Mg(Gd)	190.4	1.54	7.89E-6	2.16E-14
Mg(Gd)	187.2	1.67	8.46E-6	2.13E-14
Mg(Gd)	184.0	1.81	9.07E-6	2.10E-14
Mg(Gd)	180.8	1.96	9.72E-6	2.08E-14
Mg(Gd)	177.6	2.12	1.04E-5	2.05E-14
Mg(Gd)	174.4	2.30	1.12E-5	2.03E-14
Mg(Gd)	171.1	2.49	1.20E-5	2.00E-14
Mg(Gd)	167.9	2.70	1.29E-5	1.98E-14
Mg(Gd)	164.7	2.92	1.38E-5	1.96E-14
Mg(Gd)	161.5	3.17	1.48E-5	1.93E-14
Mg(Gd)	158.3	3.44	1.59E-5	1.91E-14
Mg_6Gd	155.1	13.91	6.20E-5	5.40E-13
Mg_6Gd	155.0	13.91	6.20E-5	5.43E-13
Mg_6Gd	154.8	13.92	6.20x10-5	5.40x10-13
Mg_6Gd	154.7	13.92	6.20x10-5	5.43x10-13
Mg_6Gd	154.5	13.92	6.21x10-5	5.40x10-13
Mg_6Gd	154.4	13.92	6.21x10-5	5.44x10-13
Mg_6Gd	154.2	13.92	6.21x10-5	5.40x10-13
Mg_6Gd	154.1	13.92	6.21x10-5	5.41x10-13
Mg_6Gd	153.9	13.93	6.21x10-5	5.44x10-13
Mg_6Gd	153.8	13.93	6.21x10-5	5.41x10-13
Mg_6Gd	153.6	13.93	6.21x10-5	5.44x10-13
Mg_6Gd	153.5	13.93	6.21x10-5	5.41x10-13
Mg_6Gd	153.3	13.93	6.21x10-5	5.44x10-13
Mg_6Gd	153.2	13.93	6.21x10-5	5.41x10-13
Mg_6Gd	153.0	13.94	6.21x10-5	5.44x10-13
Mg_6Gd	152.9	13.94	6.21x10-5	5.41x10-13

Phase	Position (μm)	at.%Gd	Flux $\left(\frac{\mu m \cdot at.frac.}{sec}\right)$	Boltzmann-Matano Interdiffusion Coefficient (m^2/sec)
Mg_6Gd	152.7	13.94	$6.21x10^{-5}$	$5.44x10^{-13}$
Mg_6Gd	152.6	13.94	$6.21x10^{-5}$	$5.41x10^{-13}$
Mg_6Gd	152.4	13.94	$6.22x10^{-5}$	$5.44x10^{-13}$
Mg_6Gd	152.3	13.95	$6.22x10^{-5}$	$5.41x10^{-13}$
Mg_6Gd	152.1	13.95	$6.22x10^{-5}$	$5.45x10^{-13}$
Mg_6Gd	152.0	13.95	$6.22x10^{-5}$	$5.41x10^{-13}$
Mg_6Gd	151.8	13.95	$6.22x10^{-5}$	$5.45x10^{-13}$
Mg_6Gd	151.7	13.95	$6.22x10^{-5}$	$5.42x10^{-13}$
Mg_6Gd	151.5	13.95	$6.22x10^{-5}$	$5.45x10^{-13}$
Mg_6Gd	151.4	13.96	$6.22x10^{-5}$	$5.42x10^{-13}$
Mg_6Gd	151.2	13.96	$6.22x10^{-5}$	$5.45x10^{-13}$
Mg_6Gd	151.1	13.96	$6.22x10^{-5}$	$5.42x10^{-13}$
Mg_6Gd	150.9	13.96	$6.22x10^{-5}$	$5.45x10^{-13}$
Mg_6Gd	150.8	13.96	$6.22x10^{-5}$	$5.42x10^{-13}$
Mg_6Gd	150.6	13.96	$6.22x10^{-5}$	$5.45x10^{-13}$
Mg_6Gd	150.5	13.97	$6.23x10^{-5}$	$5.42x10^{-13}$
Mg_6Gd	150.3	13.97	$6.23x10^{-5}$	$5.42x10^{-13}$
Mg_6Gd	150.1	13.97	$6.23x10^{-5}$	$5.45x10^{-13}$
Mg_6Gd	150.0	13.97	$6.23x10^{-5}$	$5.42x10^{-13}$
Mg_6Gd	149.8	13.97	$6.23x10^{-5}$	$5.45x10^{-13}$
Mg_6Gd	149.7	13.97	$6.23x10^{-5}$	$5.42x10^{-13}$
Mg_6Gd	149.5	13.98	$6.23x10^{-5}$	$5.46x10^{-13}$
Mg_6Gd	149.4	13.98	$6.23x10^{-5}$	$5.43x10^{-13}$
Mg_6Gd	149.2	13.98	$6.23x10^{-5}$	$5.46x10^{-13}$
Mg_6Gd	149.1	13.98	$6.23x10^{-5}$	$5.43x10^{-13}$
Mg_6Gd	148.9	13.98	$6.23x10^{-5}$	$5.46x10^{-13}$
Mg_6Gd	148.8	13.98	$6.23x10^{-5}$	$5.43x10^{-13}$
Mg_6Gd	148.6	13.99	$6.23x10^{-5}$	$5.46x10^{-13}$
Mg_6Gd	148.5	13.99	$6.23x10^{-5}$	$5.43x10^{-13}$
Mg_6Gd	148.3	13.99	$6.24x10^{-5}$	$5.46x10^{-13}$
Mg_6Gd	148.2	13.99	$6.24x10^{-5}$	$5.43x10^{-13}$
Mg_6Gd	148.0	13.99	$6.24x10^{-5}$	$5.46x10^{-13}$
Mg_6Gd	147.9	14.00	$6.24x10^{-5}$	$5.43x10^{-13}$
Mg_6Gd	147.7	14.00	$6.24x10^{-5}$	$5.46x10^{-13}$
Mg_6Gd	147.6	14.00	$6.24x10^{-5}$	$5.43x10^{-13}$

Phase	Position (μm)	at.%Gd	Flux $\left(\frac{\mu m \cdot at.frac.}{sec}\right)$	Boltzmann-Matano Interdiffusion Coefficient (m^2/sec)
Mg_6Gd	147.4	14.00	$6.24x10^{-5}$	$5.47x10^{-13}$
Mg_6Gd	147.3	14.00	$6.24x10^{-5}$	$5.43x10^{-13}$
Mg_6Gd	147.1	14.00	$6.24x10^{-5}$	$5.47x10^{-13}$
Mg_6Gd	147.0	14.01	$6.24x10^{-5}$	$5.44x10^{-13}$
Mg_6Gd	146.8	14.01	$6.24x10^{-5}$	$5.44x10^{-13}$
Mg_6Gd	146.7	14.01	$6.24x10^{-5}$	$5.47x10^{-13}$
Mg_6Gd	146.5	14.01	$6.24x10^{-5}$	$5.44x10^{-13}$
Mg_6Gd	146.4	14.01	$6.24x10^{-5}$	$5.47x10^{-13}$
Mg_6Gd	146.2	14.01	$6.25x10^{-5}$	$5.44x10^{-13}$
Mg_6Gd	146.1	14.02	$6.25x10^{-5}$	$5.47x10^{-13}$
Mg_6Gd	145.9	14.02	$6.25x10^{-5}$	$5.44x10^{-13}$
Mg_6Gd	145.8	14.02	$6.25x10^{-5}$	$5.47x10^{-13}$
Mg_6Gd	145.6	14.02	$6.25x10^{-5}$	$5.44x10^{-13}$
Mg_6Gd	145.5	14.02	$6.25x10^{-5}$	$5.47x10^{-13}$
Mg_6Gd	145.3	14.02	$6.25x10^{-5}$	$5.44x10^{-13}$
Mg_6Gd	145.1	14.03	$6.25x10^{-5}$	$5.47x10^{-13}$
Mg_6Gd	145.0	14.03	$6.25x10^{-5}$	$5.44x10^{-13}$
Mg_6Gd	144.8	14.03	$6.25x10^{-5}$	$5.48x10^{-13}$
Mg_6Gd	144.7	14.03	$6.25x10^{-5}$	$5.44x10^{-13}$
Mg_6Gd	144.5	14.03	$6.25x10^{-5}$	$5.48x10^{-13}$
Mg_6Gd	144.4	14.04	$6.25x10^{-5}$	$5.45x10^{-13}$
Mg_6Gd	144.2	14.04	$6.25x10^{-5}$	$5.48x10^{-13}$
Mg_6Gd	144.1	14.04	$6.26x10^{-5}$	$5.45x10^{-13}$
Mg_6Gd	143.9	14.04	$6.26x10^{-5}$	$5.48x10^{-13}$
Mg_6Gd	143.8	14.04	$6.26x10^{-5}$	$5.45x10^{-13}$
Mg_6Gd	143.6	14.04	$6.26x10^{-5}$	$5.48x10^{-13}$
Mg_6Gd	143.5	14.05	$6.26x10^{-5}$	$5.45x10^{-13}$
Mg_6Gd	143.3	14.05	$6.26x10^{-5}$	$5.48x10^{-13}$
Mg_6Gd	143.2	14.05	$6.26x10^{-5}$	$5.45x10^{-13}$
Mg_6Gd	143.0	14.05	$6.26x10^{-5}$	$5.45x10^{-13}$
Mg_6Gd	142.9	14.05	$6.26x10^{-5}$	$5.48x10^{-13}$
Mg_6Gd	142.7	14.05	$6.26x10^{-5}$	$5.45x10^{-13}$
Mg_6Gd	142.6	14.06	$6.26x10^{-5}$	$5.48x10^{-13}$
Mg_6Gd	142.4	14.06	$6.26x10^{-5}$	$5.45x10^{-13}$
Mg_6Gd	142.3	14.06	$6.26x10^{-5}$	$5.49x10^{-13}$

Phase	Position (μm)	at.%Gd	Flux $\left(\frac{\mu m \cdot at.frac.}{sec}\right)$	Boltzmann-Matano Interdiffusion Coefficient (m^2/sec)
Mg_6Gd	142.1	14.06	$6.26x10^{-5}$	$5.46x10^{-13}$
Mg_6Gd	142.0	14.06	$6.27x10^{-5}$	$5.49x10^{-13}$
Mg_6Gd	141.8	14.06	$6.27x10^{-5}$	$5.46x10^{-13}$
Mg_6Gd	141.7	14.07	$6.27x10^{-5}$	$5.49x10^{-13}$
Mg_6Gd	141.5	14.07	$6.27x10^{-5}$	$5.46x10^{-13}$
Mg_6Gd	141.4	14.07	$6.27x10^{-5}$	$5.49x10^{-13}$
Mg_6Gd	141.2	14.07	$6.27x10^{-5}$	$5.46x10^{-13}$
Mg_6Gd	141.1	14.07	$6.27x10^{-5}$	$5.49x10^{-13}$
Mg_6Gd	140.9	14.08	$6.27x10^{-5}$	$5.46x10^{-13}$
Mg_6Gd	140.8	14.08	$6.27x10^{-5}$	$5.49x10^{-13}$
Mg_6Gd	140.6	14.08	$6.27x10^{-5}$	$5.46x10^{-13}$
Mg_6Gd	140.5	14.08	$6.27x10^{-5}$	$5.49x10^{-13}$
Mg_6Gd	140.3	14.08	$6.27x10^{-5}$	$5.46x10^{-13}$
Mg_5Gd	136.1	14.72	$6.52x10^{-5}$	$7.77x10^{-13}$
Mg_5Gd	134.0	14.73	$6.53x10^{-5}$	$7.78x10^{-13}$
Mg_5Gd	131.8	14.75	$6.54x10^{-5}$	$7.79x10^{-13}$
Mg_5Gd	129.7	14.77	$6.54x10^{-5}$	$7.80x10^{-13}$
Mg_5Gd	127.5	14.79	$6.55x10^{-5}$	$7.81x10^{-13}$
Mg_5Gd	125.3	14.81	$6.56x10^{-5}$	$7.82x10^{-13}$
Mg_5Gd	123.2	14.83	$6.57x10^{-5}$	$7.82x10^{-13}$
Mg_5Gd	121.0	14.84	$6.57x10^{-5}$	$7.83x10^{-13}$
Mg_5Gd	118.8	14.86	$6.58x10^{-5}$	$7.84x10^{-13}$
Mg_5Gd	116.7	14.88	$6.59x10^{-5}$	$7.85x10^{-13}$
Mg_5Gd	114.5	14.90	$6.59x10^{-5}$	$7.86x10^{-13}$
Mg_5Gd	112.4	14.92	$6.60x10^{-5}$	$7.86x10^{-13}$
Mg_5Gd	110.2	14.93	$6.61x10^{-5}$	$7.87x10^{-13}$
Mg_5Gd	108.0	14.95	$6.61x10^{-5}$	$7.88x10^{-13}$
Mg_5Gd	105.9	14.97	$6.62x10^{-5}$	$7.89x10^{-13}$
Mg_5Gd	103.7	14.99	$6.63x10^{-5}$	$7.90x10^{-13}$
Mg_5Gd	101.6	15.01	$6.63x10^{-5}$	$7.90x10^{-13}$
Mg_5Gd	99.4	15.02	$6.64x10^{-5}$	$7.91x10^{-13}$
Mg_5Gd	97.2	15.04	$6.65x10^{-5}$	$7.92x10^{-13}$
Mg_5Gd	95.1	15.06	$6.65x10^{-5}$	$7.93x10^{-13}$
Mg_5Gd	92.9	15.08	$6.66x10^{-5}$	$7.93x10^{-13}$
Mg_5Gd	90.7	15.10	$6.66x10^{-5}$	$7.94x10^{-13}$

Phase	Position (μm)	at.%Gd	Flux $\left(\frac{\mu m \cdot at.frac.}{sec}\right)$	Boltzmann-Matano Interdiffusion Coefficient (m^2/sec)
Mg_5Gd	88.6	15.12	$6.67x10^{-5}$	$7.95x10^{-13}$
Mg_5Gd	86.4	15.13	$6.68x10^{-5}$	$7.96x10^{-13}$
Mg_5Gd	84.3	15.15	$6.68x10^{-5}$	$7.96x10^{-13}$
Mg_5Gd	82.1	15.17	$6.69x10^{-5}$	$7.97x10^{-13}$
Mg_5Gd	79.9	15.19	$6.69x10^{-5}$	$7.98x10^{-13}$
Mg_5Gd	77.8	15.21	$6.70x10^{-5}$	$7.98x10^{-13}$
Mg_5Gd	75.6	15.22	$6.71x10^{-5}$	$7.99x10^{-13}$
Mg_5Gd	73.5	15.24	$6.71x10^{-5}$	$8.00x10^{-13}$
Mg_5Gd	71.3	15.26	$6.72x10^{-5}$	$8.00x10^{-13}$
Mg_5Gd	69.1	15.28	$6.72x10^{-5}$	$8.01x10^{-13}$
Mg_5Gd	67.0	15.30	$6.73x10^{-5}$	$8.02x10^{-13}$
Mg_5Gd	64.8	15.32	$6.73x10^{-5}$	$8.02x10^{-13}$
Mg_5Gd	62.6	15.33	$6.74x10^{-5}$	$8.03x10^{-13}$
Mg_5Gd	60.5	15.35	$6.74x10^{-5}$	$8.04x10^{-13}$
Mg_5Gd	58.3	15.37	$6.75x10^{-5}$	$8.05x10^{-13}$
Mg_5Gd	56.2	15.39	$6.76x10^{-5}$	$8.05x10^{-13}$
Mg_5Gd	54.0	15.41	$6.76x10^{-5}$	$8.06x10^{-13}$
Mg_5Gd	51.8	15.42	$6.77x10^{-5}$	$8.06x10^{-13}$
Mg_5Gd	49.7	15.44	$6.77x10^{-5}$	$8.07x10^{-13}$
Mg_5Gd	47.5	15.46	$6.78x10^{-5}$	$8.07x10^{-13}$
Mg_5Gd	45.4	15.48	$6.78x10^{-5}$	$8.08x10^{-13}$
Mg_5Gd	43.2	15.50	$6.79x10^{-5}$	$8.09x10^{-13}$
Mg_5Gd	41.0	15.51	$6.79x10^{-5}$	$8.09x10^{-13}$
Mg_5Gd	38.9	15.53	$6.80x10^{-5}$	$8.10x10^{-13}$
Mg_5Gd	36.7	15.55	$6.80x10^{-5}$	$8.10x10^{-13}$
Mg_5Gd	34.5	15.57	$6.80x10^{-5}$	$8.11x10^{-13}$
Mg_5Gd	32.4	15.59	$6.81x10^{-5}$	$8.11x10^{-13}$
Mg_5Gd	30.2	15.61	$6.81x10^{-5}$	$8.12x10^{-13}$
Mg_5Gd	28.1	15.62	$6.82x10^{-5}$	$8.12x10^{-13}$
Mg_5Gd	25.9	15.64	$6.82x10^{-5}$	$8.13x10^{-13}$
Mg_5Gd	23.7	15.66	$6.83x10^{-5}$	$8.14x10^{-13}$
Mg_5Gd	21.6	15.68	$6.83x10^{-5}$	$8.14x10^{-13}$
Mg_5Gd	19.4	15.70	$6.84x10^{-5}$	$8.15x10^{-13}$
Mg_5Gd	17.2	15.71	$6.84x10^{-5}$	$8.15x10^{-13}$
Mg_5Gd	15.1	15.73	$6.84x10^{-5}$	$8.16x10^{-13}$

Phase	Position (μm)	at.%Gd	Flux $\left(\frac{\mu m \cdot at.frac.}{sec}\right)$	Boltzmann-Matano Interdiffusion Coefficient (m^2/sec)
Mg_5Gd	12.9	15.75	$6.85x10^{-5}$	$8.16x10^{-13}$
Mg_5Gd	10.8	15.77	$6.85x10^{-5}$	$8.17x10^{-13}$
Mg_5Gd	8.6	15.79	$6.86x10^{-5}$	$8.17x10^{-13}$
Mg_5Gd	6.4	15.80	$6.86x10^{-5}$	$8.17x10^{-13}$
Mg_5Gd	4.3	15.82	$6.86x10^{-5}$	$8.18x10^{-13}$
Mg_5Gd	2.1	15.84	$6.87x10^{-5}$	$8.18x10^{-13}$
Mg_5Gd	0.0	15.86	$6.87x10^{-5}$	$8.19x10^{-13}$
Mg_5Gd	-2.2	15.88	$6.88x10^{-5}$	$8.19x10^{-13}$
Mg_5Gd	-4.4	15.90	$6.88x10^{-5}$	$8.20x10^{-13}$
Mg_5Gd	-6.5	15.91	$6.88x10^{-5}$	$8.20x10^{-13}$
Mg_5Gd	-8.7	15.93	$6.89x10^{-5}$	$8.21x10^{-13}$
Mg_5Gd	-10.9	15.95	$6.89x10^{-5}$	$8.21x10^{-13}$
Mg_5Gd	-13.0	15.97	$6.89x10^{-5}$	$8.21x10^{-13}$
Mg_5Gd	-15.2	15.99	$6.90x10^{-5}$	$8.22x10^{-13}$
Mg_5Gd	-17.3	16.00	$6.90x10^{-5}$	$8.22x10^{-13}$
Mg_5Gd	-19.5	16.02	$6.90x10^{-5}$	$8.23x10^{-13}$
Mg_5Gd	-21.7	16.04	$6.91x10^{-5}$	$8.23x10^{-13}$
Mg_5Gd	-23.8	16.06	$6.91x10^{-5}$	$8.23x10^{-13}$
Mg_5Gd	-26.0	16.08	$6.91x10^{-5}$	$8.24x10^{-13}$
Mg_5Gd	-28.1	16.10	$6.92x10^{-5}$	$8.24x10^{-13}$
Mg_5Gd	-30.3	16.11	$6.92x10^{-5}$	$8.24x10^{-13}$
Mg_5Gd	-32.5	16.13	$6.92x10^{-5}$	$8.25x10^{-13}$
Mg_5Gd	-34.6	16.15	$6.92x10^{-5}$	$8.25x10^{-13}$
Mg_5Gd	-36.8	16.17	$6.93x10^{-5}$	$8.25x10^{-13}$
Mg_5Gd	-39.0	16.19	$6.93x10^{-5}$	$8.26x10^{-13}$
Mg_5Gd	-41.1	16.20	$6.93x10^{-5}$	$8.26x10^{-13}$
Mg_5Gd	-43.3	16.22	$6.94x10^{-5}$	$8.26x10^{-13}$
Mg_5Gd	-45.4	16.24	$6.94x10^{-5}$	$8.27x10^{-13}$
Mg_5Gd	-47.6	16.26	$6.94x10^{-5}$	$8.27x10^{-13}$
Mg_5Gd	-49.8	16.28	$6.94x10^{-5}$	$8.27x10^{-13}$
Mg_5Gd	-51.9	16.29	$6.95x10^{-5}$	$8.28x10^{-13}$
Mg_5Gd	-54.1	16.31	$6.95x10^{-5}$	$8.28x10^{-13}$
Mg_5Gd	-56.2	16.33	$6.95x10^{-5}$	$8.28x10^{-13}$
Mg_5Gd	-58.4	16.35	$6.95x10^{-5}$	$8.28x10^{-13}$
Mg_5Gd	-60.6	16.37	$6.95x10^{-5}$	$8.29x10^{-13}$

Phase	Position (μm)	at.%Gd	Flux $\left(\frac{\mu m \cdot at.frac.}{sec}\right)$	Boltzmann-Matano Interdiffusion Coefficient (m^2/sec)
Mg_5Gd	-62.7	16.39	$6.96x10^{-5}$	$8.29x10^{-13}$
Mg_5Gd	-64.9	16.40	$6.96x10^{-5}$	$8.29x10^{-13}$
Mg_5Gd	-67.1	16.42	$6.96x10^{-5}$	$8.29x10^{-13}$
Mg_5Gd	-69.2	16.44	$6.96x10^{-5}$	$8.30x10^{-13}$
Mg_5Gd	-71.4	16.46	$6.96x10^{-5}$	$8.30x10^{-13}$
Mg_5Gd	-73.5	16.48	$6.97x10^{-5}$	$8.30x10^{-13}$
Mg_5Gd	-75.6	16.49	$6.97x10^{-5}$	$7.92x10^{-13}$
Mg_3Gd	-72.7	19.07	$6.96x10^{-5}$	-7.82x10-15
Mg_3Gd	-74.1	19.12	$7.21x10^{-5}$	$1.99x10^{-13}$
Mg_3Gd	-75.4	19.17	$7.21x10^{-5}$	$1.99x10^{-13}$
Mg_3Gd	-76.8	19.22	$7.22x10^{-5}$	$1.99x10^{-13}$
Mg_3Gd	-78.2	19.27	$7.22x10^{-5}$	$1.99x10^{-13}$
Mg_3Gd	-79.5	19.32	$7.22x10^{-5}$	$1.99x10^{-13}$
Mg_3Gd	-80.9	19.37	$7.23x10^{-5}$	$1.99x10^{-13}$
Mg_3Gd	-82.2	19.42	$7.23x10^{-5}$	$1.99x10^{-13}$
Mg_3Gd	-83.6	19.47	$7.24x10^{-5}$	$1.99x10^{-13}$
Mg_3Gd	-85.0	19.52	$7.24x10^{-5}$	$2.00x10^{-13}$
Mg_3Gd	-86.3	19.57	$7.25x10^{-5}$	$2.00x10^{-13}$
Mg_3Gd	-87.7	19.62	$7.25x10^{-5}$	$2.00x10^{-13}$
Mg_3Gd	-89.1	19.67	$7.25x10^{-5}$	$2.00x10^{-13}$
Mg_3Gd	-90.4	19.72	$7.26x10^{-5}$	$2.00x10^{-13}$
Mg_3Gd	-91.8	19.77	$7.26x10^{-5}$	$2.00x10^{-13}$
Mg_3Gd	-93.2	19.81	$7.27x10^{-5}$	$2.00x10^{-13}$
Mg_3Gd	-94.5	19.86	$7.27x10^{-5}$	$2.00x10^{-13}$
Mg_3Gd	-95.9	19.91	$7.27x10^{-5}$	$2.00x10^{-13}$
Mg_3Gd	-97.2	19.96	$7.28x10^{-5}$	$2.00x10^{-13}$
Mg_3Gd	-98.6	20.01	$7.28x10^{-5}$	$2.01x10^{-13}$
Mg_3Gd	-100.0	20.06	$7.28x10^{-5}$	$2.01x10^{-13}$
Mg_3Gd	-101.3	20.11	$7.28x10^{-5}$	$2.01x10^{-13}$
Mg_3Gd	-102.7	20.16	$7.29x10^{-5}$	$2.01x10^{-13}$
Mg_3Gd	-104.1	20.21	$7.29x10^{-5}$	$2.01x10^{-13}$
Mg_3Gd	-105.4	20.26	$7.29x10^{-5}$	$2.01x10^{-13}$
Mg_3Gd	-106.8	20.31	$7.30x10^{-5}$	$2.01x10^{-13}$
Mg_3Gd	-108.2	20.36	$7.30x10^{-5}$	$2.01x10^{-13}$
Mg_3Gd	-109.5	20.41	$7.30x10^{-5}$	$2.01x10^{-13}$

Phase	Position (μm)	at.%Gd	Flux $\left(\frac{\mu m \cdot at.frac.}{sec}\right)$	Boltzmann-Matano Interdiffusion Coefficient (m^2/sec)
Mg_3Gd	-110.9	20.46	$7.30x10^{-5}$	$2.01x10^{-13}$
Mg_3Gd	-112.2	20.51	$7.31x10^{-5}$	$2.01x10^{-13}$
Mg_3Gd	-113.6	20.56	$7.31x10^{-5}$	$2.01x10^{-13}$
Mg_3Gd	-115.0	20.61	$7.31x10^{-5}$	$2.01x10^{-13}$
Mg_3Gd	-116.3	20.66	$7.31x10^{-5}$	$2.01x10^{-13}$
Mg_3Gd	-117.7	20.71	$7.31x10^{-5}$	$2.02x10^{-13}$
Mg_3Gd	-119.1	20.76	$7.32x10^{-5}$	$2.02x10^{-13}$
Mg_3Gd	-120.4	20.80	$7.32x10^{-5}$	$2.02x10^{-13}$
Mg_3Gd	-121.8	20.85	$7.32x10^{-5}$	$2.02x10^{-13}$
Mg_3Gd	-123.2	20.90	$7.32x10^{-5}$	$2.02x10^{-13}$
Mg_3Gd	-124.5	20.95	$7.32x10^{-5}$	$2.02x10^{-13}$
Mg_3Gd	-125.9	21.00	$7.32x10^{-5}$	$2.02x10^{-13}$
Mg_3Gd	-127.2	21.05	$7.32x10^{-5}$	$2.02x10^{-13}$
Mg_3Gd	-128.6	21.10	$7.32x10^{-5}$	$2.02x10^{-13}$
Mg_3Gd	-130.0	21.15	$7.33x10^{-5}$	$2.02x10^{-13}$
Mg_3Gd	-131.3	21.20	$7.33x10^{-5}$	$2.02x10^{-13}$
Mg_3Gd	-132.7	21.25	$7.33x10^{-5}$	$2.02x10^{-13}$
Mg_3Gd	-134.1	21.30	$7.33x10^{-5}$	$2.02x10^{-13}$
Mg_3Gd	-135.4	21.35	$7.33x10^{-5}$	$2.02x10^{-13}$
Mg_3Gd	-136.8	21.40	$7.33x10^{-5}$	$2.02x10^{-13}$
Mg_3Gd	-138.2	21.45	$7.33x10^{-5}$	$2.02x10^{-13}$
Mg_3Gd	-139.5	21.50	$7.33x10^{-5}$	$2.02x10^{-13}$
Mg_3Gd	-140.9	21.55	$7.33x10^{-5}$	$2.02x10^{-13}$
Mg_3Gd	-142.2	21.60	$7.33x10^{-5}$	$2.02x10^{-13}$
Mg_3Gd	-143.6	21.65	$7.33x10^{-5}$	$2.02x10^{-13}$
Mg_3Gd	-145.0	21.70	$7.33x10^{-5}$	$2.02x10^{-13}$
Mg_3Gd	-146.3	21.74	$7.33x10^{-5}$	$2.02x10^{-13}$
Mg_3Gd	-147.7	21.79	$7.33x10^{-5}$	$2.02x10^{-13}$
Mg_3Gd	-149.1	21.84	$7.33x10^{-5}$	$2.02x10^{-13}$
Mg_3Gd	-150.4	21.89	$7.33x10^{-5}$	$2.02x10^{-13}$
Mg_3Gd	-151.8	21.94	$7.33x10^{-5}$	$2.02x10^{-13}$
Mg_3Gd	-153.2	21.99	$7.33x10^{-5}$	$2.02x10^{-13}$
Mg_3Gd	-154.5	22.04	$7.33x10^{-5}$	$2.02x10^{-13}$
Mg_3Gd	-155.9	22.09	$7.33x10^{-5}$	$2.02x10^{-13}$
Mg_3Gd	-157.2	22.14	$7.33x10^{-5}$	$2.02x10^{-13}$

Phase	Position (μm)	at.%Gd	Flux $\left(\frac{\mu m \cdot at.frac.}{sec}\right)$	Boltzmann-Matano Interdiffusion Coefficient (m^2/sec)
Mg_3Gd	-158.6	22.19	$7.32x10^{-5}$	$2.02x10^{-13}$
Mg_3Gd	-160.0	22.24	$7.32x10^{-5}$	$2.02x10^{-13}$
Mg_3Gd	-161.3	22.29	$7.32x10^{-5}$	$2.02x10^{-13}$
Mg_3Gd	-162.7	22.34	$7.32x10^{-5}$	$2.02x10^{-13}$
Mg_3Gd	-164.1	22.39	$7.32x10^{-5}$	$2.02x10^{-13}$
Mg_3Gd	-165.4	22.44	$7.32x10^{-5}$	$2.02x10^{-13}$
Mg_3Gd	-166.8	22.49	$7.32x10^{-5}$	$2.02x10^{-13}$
Mg_3Gd	-168.2	22.54	$7.31x10^{-5}$	$2.02x10^{-13}$
Mg_3Gd	-169.5	22.59	$7.31x10^{-5}$	$2.01x10^{-13}$
Mg_3Gd	-170.9	22.64	$7.31x10^{-5}$	$2.01x10^{-13}$
Mg_3Gd	-172.2	22.69	$7.31x10^{-5}$	$2.01x10^{-13}$
Mg_3Gd	-173.6	22.73	$7.31x10^{-5}$	$2.01x10^{-13}$
Mg_3Gd	-175.0	22.78	$7.30x10^{-5}$	$2.01x10^{-13}$
Mg_3Gd	-176.3	22.83	$7.30x10^{-5}$	$2.01x10^{-13}$
Mg_3Gd	-177.7	22.88	$7.30x10^{-5}$	$2.01x10^{-13}$
Mg_3Gd	-179.1	22.93	$7.30x10^{-5}$	$2.01x10^{-13}$
Mg_3Gd	-180.4	22.98	$7.29x10^{-5}$	$2.01x10^{-13}$
Mg_3Gd	-181.8	23.03	$7.29x10^{-5}$	$2.01x10^{-13}$
Mg_3Gd	-183.2	23.08	$7.29x10^{-5}$	$2.01x10^{-13}$
Mg_3Gd	-184.5	23.13	$7.29x10^{-5}$	$2.01x10^{-13}$
Mg_3Gd	-185.9	23.18	$7.28x10^{-5}$	$2.01x10^{-13}$
Mg_3Gd	-187.2	23.23	$7.28x10^{-5}$	$2.01x10^{-13}$
Mg_3Gd	-188.6	23.28	$7.28x10^{-5}$	$2.01x10^{-13}$
Mg_3Gd	-190.0	23.33	$7.27x10^{-5}$	$2.00x10^{-13}$
Mg_3Gd	-191.3	23.38	$7.27x10^{-5}$	$2.00x10^{-13}$
Mg_3Gd	-192.7	23.43	$7.27x10^{-5}$	$2.00x10^{-13}$
Mg_3Gd	-194.1	23.48	$7.26x10^{-5}$	$2.00x10^{-13}$
Mg_3Gd	-195.4	23.53	$7.26x10^{-5}$	$2.00x10^{-13}$
Mg_3Gd	-196.8	23.58	$7.25x10^{-5}$	$2.00x10^{-13}$
Mg_3Gd	-198.2	23.63	$7.25x10^{-5}$	$2.00x10^{-13}$
Mg_3Gd	-199.5	23.67	$7.25x10^{-5}$	$2.00x10^{-13}$
Mg_3Gd	-200.9	23.72	$7.24x10^{-5}$	$2.00x10^{-13}$
Mg_3Gd	-202.2	23.77	$7.24x10^{-5}$	$1.99x10^{-13}$
Mg_3Gd	-203.6	23.82	$7.23x10^{-5}$	$1.99x10^{-13}$
Mg_3Gd	-205.0	23.87	$7.23x10^{-5}$	$1.99x10^{-13}$

Phase	Position (μm)	at.%Gd	Flux $\left(\frac{\mu m \cdot at.frac.}{sec}\right)$	Boltzmann-Matano Interdiffusion Coefficient (m^2/sec)
Mg_3Gd	-206.3	23.92	7.23×10^{-5}	1.99×10^{-13}
Mg_3Gd	-207.6	23.97	7.22×10^{-5}	1.99×10^{-13}

Table 36: Interdiffusion flux and interdiffusion coefficients as a function of composition in intermetallic compounds formed during 490°C diffusion anneal of Mg vs. Gd after 72 hours; Matano plane, $x_o = 0$

Phase	Position (μm)	at.%Gd	Flux $\left(\frac{\mu m \cdot at.frac.}{sec}\right)$	Boltzmann-Matano Interdiffusion Coefficient (m^2/sec)
Mg(Gd)	414.3	0.47	4.50×10^{-6}	5.00×10^{-14}
Mg(Gd)	411.3	0.50	4.72×10^{-6}	4.92×10^{-14}
Mg(Gd)	408.3	0.53	4.95×10^{-6}	4.84×10^{-14}
Mg(Gd)	405.3	0.56	5.20×10^{-6}	4.77×10^{-14}
Mg(Gd)	402.3	0.60	5.45×10^{-6}	4.70×10^{-14}
Mg(Gd)	399.3	0.64	5.72×10^{-6}	4.63×10^{-14}
Mg(Gd)	396.3	0.68	6.01×10^{-6}	4.57×10^{-14}
Mg(Gd)	393.3	0.72	6.32×10^{-6}	4.51×10^{-14}
Mg(Gd)	390.2	0.76	6.64×10^{-6}	4.45×10^{-14}
Mg(Gd)	387.2	0.81	6.98×10^{-6}	4.39×10^{-14}
Mg(Gd)	384.2	0.86	7.34×10^{-6}	4.33×10^{-14}
Mg(Gd)	381.2	0.92	7.71×10^{-6}	4.28×10^{-14}
Mg(Gd)	378.2	0.97	8.12×10^{-6}	4.23×10^{-14}
Mg(Gd)	375.2	1.04	8.54×10^{-6}	4.18×10^{-14}
Mg(Gd)	372.2	1.10	8.99×10^{-6}	4.13×10^{-14}
Mg(Gd)	369.2	1.17	9.46×10^{-6}	4.08×10^{-14}
Mg(Gd)	366.2	1.24	9.96×10^{-6}	4.03×10^{-14}
Mg(Gd)	363.2	1.32	1.05×10^{-5}	3.99×10^{-14}
Mg(Gd)	360.1	1.41	1.10×10^{-5}	3.94×10^{-14}
Mg(Gd)	357.1	1.50	1.16×10^{-5}	3.90×10^{-14}
Mg(Gd)	354.1	1.59	1.23×10^{-5}	3.86×10^{-14}
Mg(Gd)	351.1	1.70	1.29×10^{-5}	3.81×10^{-14}
Mg(Gd)	348.1	1.80	1.36×10^{-5}	3.77×10^{-14}
Mg(Gd)	345.1	1.92	1.43×10^{-5}	3.73×10^{-14}
Mg(Gd)	342.1	2.04	1.51×10^{-5}	3.69×10^{-14}
Mg(Gd)	339.1	2.17	1.59×10^{-5}	3.66×10^{-14}
Mg(Gd)	336.1	2.31	1.68×10^{-5}	3.62×10^{-14}
Mg(Gd)	333.1	2.46	1.77×10^{-5}	3.58×10^{-14}
Mg(Gd)	330.0	2.62	1.87×10^{-5}	3.55×10^{-14}
Mg(Gd)	327.0	2.79	1.97×10^{-5}	3.51×10^{-14}
Mg(Gd)	324.0	2.97	2.07×10^{-5}	3.47×10^{-14}
Mg(Gd)	321.0	3.16	2.19×10^{-5}	3.44×10^{-14}

Phase	Position (μm)	at.%Gd	Flux $\left(\frac{\mu m \cdot at.frac.}{sec}\right)$	Boltzmann-Matano Interdiffusion Coefficient (m^2/sec)
Mg(Gd)	318.0	3.36	2.30×10^{-5}	3.41×10^{-14}
Mg_5Gd	309.7	14.31	9.07×10^{-5}	1.34×10^{-12}
Mg_5Gd	307.4	14.33	9.08×10^{-5}	1.34×10^{-12}
Mg_5Gd	305.1	14.34	9.09×10^{-5}	1.34×10^{-12}
Mg_5Gd	302.7	14.36	9.10×10^{-5}	1.35×10^{-12}
Mg_5Gd	300.4	14.37	9.11×10^{-5}	1.35×10^{-12}
Mg_5Gd	298.1	14.39	9.12×10^{-5}	1.35×10^{-12}
Mg_5Gd	295.8	14.40	9.13×10^{-5}	1.35×10^{-12}
Mg_5Gd	293.5	14.42	9.14×10^{-5}	1.35×10^{-12}
Mg_5Gd	291.2	14.44	9.15×10^{-5}	1.35×10^{-12}
Mg_5Gd	288.9	14.45	9.15×10^{-5}	1.35×10^{-12}
Mg_5Gd	286.6	14.47	9.16×10^{-5}	1.35×10^{-12}
Mg_5Gd	284.2	14.48	9.17×10^{-5}	1.36×10^{-12}
Mg_5Gd	281.9	14.50	9.18×10^{-5}	1.36×10^{-12}
Mg_5Gd	279.6	14.51	9.19×10^{-5}	1.36×10^{-12}
Mg_5Gd	277.3	14.53	9.20×10^{-5}	1.36×10^{-12}
Mg_5Gd	275.0	14.54	9.21×10^{-5}	1.36×10^{-12}
Mg_5Gd	272.7	14.56	9.21×10^{-5}	1.36×10^{-12}
Mg_5Gd	270.4	14.58	9.22×10^{-5}	1.36×10^{-12}
Mg_5Gd	268.1	14.59	9.23×10^{-5}	1.36×10^{-12}
Mg_5Gd	265.7	14.61	9.24×10^{-5}	1.37×10^{-12}
Mg_5Gd	263.4	14.62	9.25×10^{-5}	1.37×10^{-12}
Mg_5Gd	261.1	14.64	9.25×10^{-5}	1.37×10^{-12}
Mg_5Gd	258.8	14.65	9.26×10^{-5}	1.37×10^{-12}
Mg_5Gd	256.5	14.67	9.27×10^{-5}	1.37×10^{-12}
Mg_5Gd	254.2	14.69	9.28×10^{-5}	1.37×10^{-12}
Mg_5Gd	251.9	14.70	9.29×10^{-5}	1.37×10^{-12}
Mg_5Gd	249.5	14.72	9.29×10^{-5}	1.37×10^{-12}
Mg_5Gd	247.2	14.73	9.30×10^{-5}	1.38×10^{-12}
Mg_5Gd	244.9	14.75	9.31×10^{-5}	1.38×10^{-12}
Mg_5Gd	242.6	14.76	9.32×10^{-5}	1.38×10^{-12}
Mg_5Gd	240.3	14.78	9.32×10^{-5}	1.38×10^{-12}
Mg_5Gd	238.0	14.79	9.33×10^{-5}	1.38×10^{-12}
Mg_5Gd	235.7	14.81	9.34×10^{-5}	1.38×10^{-12}
Mg_5Gd	233.4	14.83	9.34×10^{-5}	1.38×10^{-12}

Phase	Position (μm)	at.%Gd	Flux $\left(\frac{\mu m \cdot at.frac.}{sec}\right)$	Boltzmann-Matano Interdiffusion Coefficient (m^2/sec)
Mg_5Gd	231.0	14.84	$9.35x10^{-5}$	$1.38x10^{-12}$
Mg_5Gd	228.7	14.86	$9.36x10^{-5}$	$1.38x10^{-12}$
Mg_5Gd	226.4	14.87	$9.37x10^{-5}$	$1.39x10^{-12}$
Mg_5Gd	224.1	14.89	$9.37x10^{-5}$	$1.39x10^{-12}$
Mg_5Gd	221.8	14.90	$9.38x10^{-5}$	$1.39x10^{-12}$
Mg_5Gd	219.5	14.92	$9.39x10^{-5}$	$1.39x10^{-12}$
Mg_5Gd	217.2	14.94	$9.39x10^{-5}$	$1.39x10^{-12}$
Mg_5Gd	214.8	14.95	$9.40x10^{-5}$	$1.39x10^{-12}$
Mg_5Gd	212.5	14.97	$9.41x10^{-5}$	$1.39x10^{-12}$
Mg_5Gd	210.2	14.98	$9.41x10^{-5}$	$1.39x10^{-12}$
Mg_5Gd	207.9	15.00	$9.42x10^{-5}$	$1.39x10^{-12}$
Mg_5Gd	205.6	15.01	$9.43x10^{-5}$	$1.39x10^{-12}$
Mg_5Gd	203.3	15.03	$9.43x10^{-5}$	$1.39x10^{-12}$
Mg_5Gd	201.0	15.05	$9.44x10^{-5}$	$1.40x10^{-12}$
Mg_5Gd	198.7	15.06	$9.44x10^{-5}$	$1.40x10^{-12}$
Mg_5Gd	196.3	15.08	$9.45x10^{-5}$	$1.40x10^{-12}$
Mg_5Gd	194.0	15.09	$9.46x10^{-5}$	$1.40x10^{-12}$
Mg_5Gd	191.7	15.11	$9.46x10^{-5}$	$1.40x10^{-12}$
Mg_5Gd	189.4	15.12	$9.47x10^{-5}$	$1.40x10^{-12}$
Mg_5Gd	187.1	15.14	$9.47x10^{-5}$	$1.40x10^{-12}$
Mg_5Gd	184.8	15.15	$9.48x10^{-5}$	$1.40x10^{-12}$
Mg_5Gd	182.5	15.17	$9.48x10^{-5}$	$1.40x10^{-12}$
Mg_5Gd	180.2	15.19	$9.49x10^{-5}$	$1.40x10^{-12}$
Mg_5Gd	177.8	15.20	$9.50x10^{-5}$	$1.40x10^{-12}$
Mg_5Gd	175.5	15.22	$9.50x10^{-5}$	$1.41x10^{-12}$
Mg_5Gd	173.2	15.23	$9.51x10^{-5}$	$1.41x10^{-12}$
Mg_5Gd	170.9	15.25	$9.51x10^{-5}$	$1.41x10^{-12}$
Mg_5Gd	168.6	15.26	$9.52x10^{-5}$	$1.41x10^{-12}$
Mg_5Gd	166.3	15.28	$9.52x10^{-5}$	$1.41x10^{-12}$
Mg_5Gd	164.0	15.30	$9.53x10^{-5}$	$1.41x10^{-12}$
Mg_5Gd	161.6	15.31	$9.53x10^{-5}$	$1.41x10^{-12}$
Mg_5Gd	159.3	15.33	$9.54x10^{-5}$	$1.41x10^{-12}$
Mg_5Gd	157.0	15.34	$9.54x10^{-5}$	$1.41x10^{-12}$
Mg_5Gd	154.7	15.36	$9.55x10^{-5}$	$1.41x10^{-12}$
Mg_5Gd	152.4	15.37	$9.55x10^{-5}$	$1.41x10^{-12}$

Phase	Position (μm)	at.%Gd	Flux $\left(\frac{\mu m \cdot at.frac.}{sec}\right)$	Boltzmann-Matano Interdiffusion Coefficient (m^2/sec)
Mg_5Gd	150.1	15.39	$9.56x10^{-5}$	$1.41x10^{-12}$
Mg_5Gd	147.8	15.40	$9.56x10^{-5}$	$1.41x10^{-12}$
Mg_5Gd	145.5	15.42	$9.56x10^{-5}$	$1.41x10^{-12}$
Mg_5Gd	143.1	15.44	$9.57x10^{-5}$	$1.42x10^{-12}$
Mg_5Gd	140.8	15.45	$9.57x10^{-5}$	$1.42x10^{-12}$
Mg_5Gd	138.5	15.47	$9.58x10^{-5}$	$1.42x10^{-12}$
Mg_5Gd	136.2	15.48	$9.58x10^{-5}$	$1.42x10^{-12}$
Mg_5Gd	133.9	15.50	$9.59x10^{-5}$	$1.42x10^{-12}$
Mg_5Gd	131.6	15.51	$9.59x10^{-5}$	$1.42x10^{-12}$
Mg_5Gd	129.3	15.53	$9.59x10^{-5}$	$1.42x10^{-12}$
Mg_5Gd	126.9	15.55	$9.60x10^{-5}$	$1.42x10^{-12}$
Mg_5Gd	124.6	15.56	$9.60x10^{-5}$	$1.42x10^{-12}$
Mg_5Gd	122.3	15.58	$9.61x10^{-5}$	$1.42x10^{-12}$
Mg_5Gd	120.0	15.59	$9.61x10^{-5}$	$1.42x10^{-12}$
Mg_5Gd	117.7	15.61	$9.61x10^{-5}$	$1.42x10^{-12}$
Mg_5Gd	115.4	15.62	$9.62x10^{-5}$	$1.42x10^{-12}$
Mg_5Gd	113.1	15.64	$9.62x10^{-5}$	$1.42x10^{-12}$
Mg_5Gd	110.8	15.66	$9.62x10^{-5}$	$1.42x10^{-12}$
Mg_5Gd	108.4	15.67	$9.63x10^{-5}$	$1.42x10^{-12}$
Mg_5Gd	106.1	15.69	$9.63x10^{-5}$	$1.42x10^{-12}$
Mg_5Gd	103.8	15.70	$9.63x10^{-5}$	$1.42x10^{-12}$
Mg_5Gd	101.5	15.72	$9.64x10^{-5}$	$1.42x10^{-12}$
Mg_5Gd	99.2	15.73	$9.64x10^{-5}$	$1.43x10^{-12}$
Mg_5Gd	96.9	15.75	$9.64x10^{-5}$	$1.43x10^{-12}$
Mg_5Gd	94.6	15.76	$9.65x10^{-5}$	$1.43x10^{-12}$
Mg_5Gd	92.3	15.78	$9.65x10^{-5}$	$1.43x10^{-12}$
Mg_5Gd	89.9	15.80	$9.65x10^{-5}$	$1.43x10^{-12}$
Mg_5Gd	87.6	15.81	$9.65x10^{-5}$	$1.43x10^{-12}$
Mg_5Gd	85.3	15.83	$9.66x10^{-5}$	$1.43x10^{-12}$
Mg_5Gd	83.0	15.84	$9.66x10^{-5}$	$1.43x10^{-12}$
Mg_3Gd	76.8	18.43	$1.01x10^{-4}$	$4.09x10^{-13}$
Mg_3Gd	75.5	18.46	$1.01x10^{-4}$	$4.09x10^{-13}$
Mg_3Gd	74.3	18.49	$1.01x10^{-4}$	$4.09x10^{-13}$
Mg_3Gd	73.0	18.52	$1.01x10^{-4}$	$4.10x10^{-13}$
Mg_3Gd	71.8	18.55	$1.01x10^{-4}$	$4.10x10^{-13}$

Phase	Position (μm)	at.%Gd	Flux $\left(\frac{\mu m \cdot at.frac.}{sec}\right)$	Boltzmann-Matano Interdiffusion Coefficient (m^2/sec)
Mg_3Gd	70.5	18.58	$1.01x10^{-4}$	$4.10x10^{-13}$
Mg_3Gd	69.3	18.61	$1.01x10^{-4}$	$4.10x10^{-13}$
Mg_3Gd	68.1	18.64	$1.01x10^{-4}$	$4.10x10^{-13}$
Mg_3Gd	66.8	18.67	$1.01x10^{-4}$	$4.10x10^{-13}$
Mg_3Gd	65.6	18.70	$1.01x10^{-4}$	$4.11x10^{-13}$
Mg_3Gd	64.3	18.73	$1.01x10^{-4}$	$4.11x10^{-13}$
Mg_3Gd	63.1	18.77	$1.01x10^{-4}$	$4.11x10^{-13}$
Mg_3Gd	61.8	18.80	$1.01x10^{-4}$	$4.11x10^{-13}$
Mg_3Gd	60.6	18.83	$1.01x10^{-4}$	$4.11x10^{-13}$
Mg_3Gd	59.4	18.86	$1.01x10^{-4}$	$4.11x10^{-13}$
Mg_3Gd	58.1	18.89	$1.01x10^{-4}$	$4.12x10^{-13}$
Mg_3Gd	56.9	18.92	$1.01x10^{-4}$	$4.12x10^{-13}$
Mg_3Gd	55.6	18.95	$1.01x10^{-4}$	$4.12x10^{-13}$
Mg_3Gd	54.4	18.98	$1.01x10^{-4}$	$4.12x10^{-13}$
Mg_3Gd	53.2	19.01	$1.01x10^{-4}$	$4.12x10^{-13}$
Mg_3Gd	51.9	19.04	$1.01x10^{-4}$	$4.12x10^{-13}$
Mg_3Gd	50.7	19.07	$1.01x10^{-4}$	$4.12x10^{-13}$
Mg_3Gd	49.4	19.10	$1.01x10^{-4}$	$4.12x10^{-13}$
Mg_3Gd	48.2	19.13	$1.01x10^{-4}$	$4.12x10^{-13}$
Mg_3Gd	46.9	19.16	$1.01x10^{-4}$	$4.13x10^{-13}$
Mg_3Gd	45.7	19.19	$1.02x10^{-4}$	$4.13x10^{-13}$
Mg_3Gd	44.5	19.22	$1.02x10^{-4}$	$4.13x10^{-13}$
Mg_3Gd	43.2	19.25	$1.02x10^{-4}$	$4.13x10^{-13}$
Mg_3Gd	42.0	19.28	$1.02x10^{-4}$	$4.13x10^{-13}$
Mg_3Gd	40.7	19.32	$1.02x10^{-4}$	$4.13x10^{-13}$
Mg_3Gd	39.5	19.35	$1.02x10^{-4}$	$4.13x10^{-13}$
Mg_3Gd	38.2	19.38	$1.02x10^{-4}$	$4.13x10^{-13}$
Mg_3Gd	37.0	19.41	$1.02x10^{-4}$	$4.13x10^{-13}$
Mg_3Gd	35.8	19.44	$1.02x10^{-4}$	$4.14x10^{-13}$
Mg_3Gd	34.5	19.47	$1.02x10^{-4}$	$4.14x10^{-13}$
Mg_3Gd	33.3	19.50	$1.02x10^{-4}$	$4.14x10^{-13}$
Mg_3Gd	32.0	19.53	$1.02x10^{-4}$	$4.14x10^{-13}$
Mg_3Gd	30.8	19.56	$1.02x10^{-4}$	$4.14x10^{-13}$
Mg_3Gd	29.5	19.59	$1.02x10^{-4}$	$4.14x10^{-13}$
Mg_3Gd	28.3	19.62	$1.02x10^{-4}$	$4.14x10^{-13}$

Phase	Position (μm)	at.%Gd	Flux $\left(\frac{\mu m \cdot at.frac.}{sec}\right)$	Boltzmann-Matano Interdiffusion Coefficient (m^2/sec)
Mg_3Gd	27.1	19.65	$1.02x10^{-4}$	$4.14x10^{-13}$
Mg_3Gd	25.8	19.68	$1.02x10^{-4}$	$4.14x10^{-13}$
Mg_3Gd	24.6	19.71	$1.02x10^{-4}$	$4.14x10^{-13}$
Mg_3Gd	23.3	19.74	$1.02x10^{-4}$	$4.14x10^{-13}$
Mg_3Gd	22.1	19.77	$1.02x10^{-4}$	$4.14x10^{-13}$
Mg_3Gd	20.8	19.80	$1.02x10^{-4}$	$4.14x10^{-13}$
Mg_3Gd	19.6	19.83	$1.02x10^{-4}$	$4.15x10^{-13}$
Mg_3Gd	18.4	19.87	$1.02x10^{-4}$	$4.14x10^{-13}$
Mg_3Gd	17.1	19.90	$1.02x10^{-4}$	$4.15x10^{-13}$
Mg_3Gd	15.9	19.93	$1.02x10^{-4}$	$4.15x10^{-13}$
Mg_3Gd	14.6	19.96	$1.02x10^{-4}$	$4.15x10^{-13}$
Mg_3Gd	13.4	19.99	$1.02x10^{-4}$	$4.15x10^{-13}$
Mg_3Gd	12.2	20.02	$1.02x10^{-4}$	$4.15x10^{-13}$
Mg_3Gd	10.9	20.05	$1.02x10^{-4}$	$4.15x10^{-13}$
Mg_3Gd	9.7	20.08	$1.02x10^{-4}$	$4.15x10^{-13}$
Mg_3Gd	8.4	20.11	$1.02x10^{-4}$	$4.15x10^{-13}$
Mg_3Gd	7.2	20.14	$1.02x10^{-4}$	$4.15x10^{-13}$
Mg_3Gd	5.9	20.17	$1.02x10^{-4}$	$4.15x10^{-13}$
Mg_3Gd	4.7	20.20	$1.02x10^{-4}$	$4.15x10^{-13}$
Mg_3Gd	3.5	20.23	$1.02x10^{-4}$	$4.15x10^{-13}$
Mg_3Gd	2.2	20.26	$1.02x10^{-4}$	$4.15x10^{-13}$
Mg_3Gd	1.0	20.29	$1.02x10^{-4}$	$4.15x10^{-13}$
Mg_3Gd	-0.3	20.32	$1.02x10^{-4}$	$4.15x10^{-13}$
Mg_3Gd	-1.5	20.35	$1.02x10^{-4}$	$4.15x10^{-13}$
Mg_3Gd	-2.8	20.38	$1.02x10^{-4}$	$4.15x10^{-13}$
Mg_3Gd	-4.0	20.42	$1.02x10^{-4}$	$4.15x10^{-13}$
Mg_3Gd	-5.2	20.45	$1.02x10^{-4}$	$4.15x10^{-13}$
Mg_3Gd	-6.5	20.48	$1.02x10^{-4}$	$4.15x10^{-13}$
Mg_3Gd	-7.7	20.51	$1.02x10^{-4}$	$4.15x10^{-13}$
Mg_3Gd	-9.0	20.54	$1.02x10^{-4}$	$4.15x10^{-13}$
Mg_3Gd	-10.2	20.57	$1.02x10^{-4}$	$4.15x10^{-13}$
Mg_3Gd	-11.5	20.60	$1.02x10^{-4}$	$4.15x10^{-13}$
Mg_3Gd	-12.7	20.63	$1.02x10^{-4}$	$4.15x10^{-13}$
Mg_3Gd	-13.9	20.66	$1.02x10^{-4}$	$4.15x10^{-13}$
Mg_3Gd	-15.2	20.69	$1.02x10^{-4}$	$4.15x10^{-13}$

Phase	Position (μm)	at.%Gd	Flux $\left(\frac{\mu m \cdot at.frac.}{sec}\right)$	Boltzmann-Matano Interdiffusion Coefficient (m^2/sec)
Mg_3Gd	-16.4	20.72	$1.02x10^{-4}$	$4.15x10^{-13}$
Mg_3Gd	-17.7	20.75	$1.02x10^{-4}$	$4.15x10^{-13}$
Mg_3Gd	-18.9	20.78	$1.02x10^{-4}$	$4.15x10^{-13}$
Mg_3Gd	-20.2	20.81	$1.02x10^{-4}$	$4.14x10^{-13}$
Mg_3Gd	-21.4	20.84	$1.02x10^{-4}$	$4.15x10^{-13}$
Mg_3Gd	-22.6	20.87	$1.02x10^{-4}$	$4.14x10^{-13}$
Mg_3Gd	-23.9	20.90	$1.02x10^{-4}$	$4.14x10^{-13}$
Mg_3Gd	-25.1	20.93	$1.02x10^{-4}$	$4.14x10^{-13}$
Mg_3Gd	-26.4	20.97	$1.02x10^{-4}$	$4.14x10^{-13}$
Mg_3Gd	-27.6	21.00	$1.02x10^{-4}$	$4.14x10^{-13}$
Mg_3Gd	-28.8	21.03	$1.02x10^{-4}$	$4.14x10^{-13}$
Mg_3Gd	-30.1	21.06	$1.02x10^{-4}$	$4.14x10^{-13}$
Mg_3Gd	-31.3	21.09	$1.02x10^{-4}$	$4.14x10^{-13}$
Mg_3Gd	-32.6	21.12	$1.02x10^{-4}$	$4.14x10^{-13}$
Mg_3Gd	-33.8	21.15	$1.02x10^{-4}$	$4.14x10^{-13}$
Mg_3Gd	-35.1	21.18	$1.02x10^{-4}$	$4.14x10^{-13}$
Mg_3Gd	-36.3	21.21	$1.02x10^{-4}$	$4.14x10^{-13}$
Mg_3Gd	-37.5	21.24	$1.02x10^{-4}$	$4.14x10^{-13}$
Mg_3Gd	-38.8	21.27	$1.02x10^{-4}$	$4.14x10^{-13}$
Mg_3Gd	-40.0	21.30	$1.02x10^{-4}$	$4.14x10^{-13}$
Mg_3Gd	-41.3	21.33	$1.02x10^{-4}$	$4.13x10^{-13}$
Mg_3Gd	-42.5	21.36	$1.02x10^{-4}$	$4.13x10^{-13}$
Mg_3Gd	-43.8	21.39	$1.02x10^{-4}$	$4.13x10^{-13}$
Mg_3Gd	-45.0	21.42	$1.02x10^{-4}$	$4.13x10^{-13}$

Table 37: Reduced modulus and hardness of Mg solid solution as a function of composition obtained from 490°C diffusion anneal of Mg vs. Gd after 72 hours; Peak Load 5mN

Phase	at.%Gd	Reduced Modulus (GPa)		Hardness (GPa)	
		Avg.	Std. Dev.	Avg.	Std. Dev.
Mg(Gd)	0.04	32.24	2.08	0.62	0.03
Mg(Gd)	0.05	32.66	1.40	0.60	0.03
Mg(Gd)	0.05	32.00	1.49	0.66	0.01
Mg(Gd)	0.06	32.20	0.91	0.67	0.00
Mg(Gd)	0.06	31.82	0.71	0.69	0.03
Mg(Gd)	0.07	34.08	0.34	0.67	0.04
Mg(Gd)	0.08	32.32	0.05	0.67	0.03
Mg(Gd)	0.10	35.98	0.47	0.62	0.00
Mg(Gd)	0.12	33.67	0.89	0.73	0.00
Mg(Gd)	0.14	39.78	1.15	0.75	0.04
Mg(Gd)	0.16	39.19	2.65	0.69	0.07
Mg(Gd)	0.19	38.57	0.03	0.80	0.01
Mg(Gd)	0.23	37.89	0.82	0.72	0.01
Mg(Gd)	0.27	41.86	0.94	0.75	0.00
Mg(Gd)	0.33	46.85	2.78	0.77	0.02
Mg(Gd)	0.40	44.87	0.35	0.74	0.05
Mg(Gd)	0.49	44.06	0.11	0.83	0.07
Mg(Gd)	0.60	44.91	1.31	0.87	0.01
Mg(Gd)	0.74	48.65	0.01	0.87	0.03
Mg(Gd)	0.90	49.56	0.36	0.90	0.01
Mg(Gd)	1.10	50.74	2.25	1.01	0.09
Mg(Gd)	1.35	54.91	2.04	1.22	0.14
Mg(Gd)	1.67	53.23	0.70	1.22	0.03
Mg(Gd)	2.05	57.34	0.26	1.39	0.04
Mg(Gd)	2.52	55.42	0.48	1.44	0.03
Mg(Gd)	3.09	58.16	0.95	1.67	0.04

Table 38: Reduced modulus and hardness of intermetallic compounds formed during 490°C diffusion anneal of Mg vs. Gd after 72 hours; Peak load 7mN

Phase	at.%Gd	Reduced Modulus (GPa)		Hardness (GPa)	
		Avg.	Std. Dev.	Avg.	Std. Dev.
Mg_5Gd	15.1	71.64	2.83	3.11	0.74
Mg_5Gd	15.2	69.96	1.94	3.05	0.32
Mg_5Gd	15.3	72.50	1.14	3.20	0.12
Mg_5Gd	15.4	71.90	1.63	3.16	0.12
Mg_5Gd	15.4	72.33	0.72	3.14	0.06
Mg_5Gd	15.5	72.80	0.52	3.19	0.10
Mg_5Gd	15.6	72.60	1.51	3.18	0.16
Mg_5Gd	15.7	73.55	2.02	3.32	0.18
Mg_5Gd	15.8	73.39	1.21	3.34	0.08
Mg_5Gd	15.8	76.51	1.41	3.51	0.17
Mg_5Gd	15.9	72.54	1.42	3.29	0.09
Mg_5Gd	16.0	75.13	1.19	3.51	0.08
Mg_5Gd	16.1	73.91	2.92	3.42	0.27
Mg_5Gd	16.4	76.31	4.99	3.54	0.45
Mg_5Gd	16.5	74.59	3.39	3.38	0.21
Mg_5Gd	16.5	74.75	0.51	3.34	0.11
Mg_5Gd	16.6	76.14	1.58	3.51	0.11
Mg_5Gd	16.7	76.29	0.86	3.50	0.08
Mg_5Gd	16.8	73.38	1.18	3.27	0.21
Mg_5Gd	16.9	74.91	0.55	2.76	0.08
Mg_3Gd	20.7	75.07	4.46	2.84	0.32
Mg_3Gd	21.1	72.39	1.14	2.69	0.03
Mg_3Gd	21.4	73.71	1.34	2.71	0.03
Mg_3Gd	21.7	69.50	0.49	2.40	0.06
Mg_3Gd	22.1	72.56	1.97	2.65	0.18
Mg_3Gd	22.4	74.78	1.42	2.67	0.11
Mg_3Gd	22.8	72.02	3.12	2.66	0.14
Mg_3Gd	23.1	71.49	3.40	2.79	0.19
Mg_3Gd	23.5	73.65	7.54	2.76	0.19
Mg_3Gd	23.8	74.55	0.98	2.93	0.08
Mg_3Gd	24.1	74.28	2.23	2.94	0.16
Mg_3Gd	24.5	79.47	--	2.96	--

Table 39: Reduced modulus and hardness of intermetallic compounds formed during 385°C diffusion anneal of Mg vs. Gd after 192 hours; Peak load 7mN

Phase	at.%Gd	Reduced Modulus (GPa)		Hardness (GPa)	
		Avg.	Std. Dev.	Avg.	Std. Dev.
Mg_6Gd	13.8	70.76	1.96	3.30	0.14
Mg_6Gd	14.0	75.05	0.98	3.44	0.03
Mg_6Gd	14.2	73.00	1.51	3.38	0.06
Mg_6Gd	14.3	73.51	1.06	3.37	0.02
Mg_6Gd	14.5	72.96	1.38	3.37	0.09
Mg_6Gd	14.7	73.10	0.93	3.39	0.08
Mg_6Gd	14.9	72.11	1.00	3.24	0.03
Mg_6Gd	15.1	73.61	1.46	3.50	0.16
Mg_5Gd	16.8	77.58	1.51	3.92	0.15
Mg_5Gd	16.9	77.36	1.00	3.77	0.14
Mg_5Gd	17.1	75.05	0.05	3.78	0.20
Mg_5Gd	17.2	75.56	0.65	3.84	0.06
Mg_5Gd	17.3	75.45	1.59	3.88	0.15
Mg_5Gd	17.5	77.88	2.52	4.08	0.04
Mg_5Gd	17.6	76.58	2.23	3.96	0.11
Mg_5Gd	17.7	78.24	2.00	3.72	0.58
Mg_5Gd	17.8	76.17	4.13	3.80	0.40
Mg_5Gd	18.0	76.32	4.11	3.88	0.41
Mg_5Gd	18.1	78.15	3.20	3.93	0.34
Mg_3Gd	23.4	76.29	4.43	3.40	0.06
Mg_3Gd	23.9	78.70	5.75	3.55	0.13
Mg_3Gd	24.4	76.91	2.63	3.43	0.11
Mg_3Gd	25.0	77.44	1.67	3.48	0.14
Mg_3Gd	25.5	79.42	8.34	3.78	0.75
Mg_3Gd	26.0	77.02	1.18	3.57	0.05
Mg_3Gd	26.6	73.83	1.11	3.42	0.07

B.3 Mg-Nd Binary System

Table 40: Reduced modulus and hardness of intermetallic compounds formed during 500°C diffusion anneal of Mg vs. Nd after 240 hours; Peak Load 7mN

Phase	at.%Nd	Reduced Modulus (GPa)	Hardness (GPa)
$Mg_{41}Nd_5$	9.4	72.28	3.26
$Mg_{41}Nd_5$	9.4	72.64	3.23
$Mg_{41}Nd_5$	9.4	71.62	3.13
$Mg_{41}Nd_5$	9.4	71.86	3.21
$Mg_{41}Nd_5$	9.4	70.74	3.08
$Mg_{41}Nd_5$	9.4	72.45	3.14
$Mg_{41}Nd_5$	9.4	72.60	3.12
$Mg_{41}Nd_5$	9.4	72.43	3.13
$Mg_{41}Nd_5$	9.4	70.15	3.20
$Mg_{41}Nd_5$	9.4	70.95	3.19
$Mg_{41}Nd_5$	9.4	70.97	3.18
$Mg_{41}Nd_5$	9.4	70.53	2.86
$Mg_{41}Nd_5$	9.4	67.50	2.74
$Mg_{41}Nd_5$	9.4	65.02	3.12
$Mg_{41}Nd_5$	9.4	65.86	2.95
$Mg_{41}Nd_5$	9.4	72.01	3.23
$Mg_{41}Nd_5$	9.4	68.97	3.01
$Mg_{41}Nd_5$	9.4	70.68	3.06
$Mg_{41}Nd_5$	9.4	70.04	3.13
$Mg_{41}Nd_5$	9.4	72.27	3.06
$Mg_{41}Nd_5$	9.4	72.85	3.21
$Mg_{41}Nd_5$	9.4	71.38	3.10
$Mg_{41}Nd_5$	9.4	71.83	3.09
$Mg_{41}Nd_5$	9.4	74.00	3.19
$Mg_{41}Nd_5$	9.4	73.44	3.25
$Mg_{41}Nd_5$	9.4	73.60	3.31
Mg_3Nd	23.3	73.30	3.16
Mg_3Nd	22.8	72.18	3.06
Mg_3Nd	22.3	73.97	3.08
Mg_3Nd	21.8	70.27	3.09
Mg_3Nd	21.3	70.28	3.08
Mg_3Nd	20.8	73.01	3.12
Mg_3Nd	20.3	71.23	2.87

Phase	at.%Nd	Reduced Modulus (GPa)	Hardness (GPa)
Mg_3Nd	19.8	76.66	3.11

Table 41: Reduced modulus and hardness of intermetallic compounds formed during 500°C diffusion anneal of Mg vs. Nd after 240 hours; Peak Load 5mN

Phase	at.%Nd	Reduced Modulus (GPa)		Hardness (GPa)	
		Avg.	Std. Dev.	Avg.	Std. Dev.
$Mg_{41}Nd_5$	9.4	78.28	1.50	3.43	0.09
$Mg_{41}Nd_5$	9.4	76.72	1.50	3.59	0.09
$Mg_{41}Nd_5$	9.4	76.58	1.50	3.42	0.09
$Mg_{41}Nd_5$	9.4	73.83	1.50	3.36	0.09
$Mg_{41}Nd_5$	9.4	73.76	1.50	3.32	0.09
$Mg_{41}Nd_5$	9.4	75.00	1.50	3.49	0.09
$Mg_{41}Nd_5$	9.4	72.70	1.50	3.24	0.09
$Mg_{41}Nd_5$	9.4	74.93	1.50	3.41	0.09
$Mg_{41}Nd_5$	9.4	70.75	1.50	3.20	0.09
$Mg_{41}Nd_5$	9.4	70.87	1.50	3.29	0.09
$Mg_{41}Nd_5$	9.4	69.34	1.50	3.15	0.09
$Mg_{41}Nd_5$	9.4	72.17	1.50	3.27	0.09
$Mg_{41}Nd_5$	9.4	72.43	1.50	3.30	0.09
$Mg_{41}Nd_5$	9.4	70.85	1.50	3.22	0.09
$Mg_{41}Nd_5$	9.4	70.68	1.50	3.24	0.09
$Mg_{41}Nd_5$	9.4	70.61	1.50	3.21	0.09
$Mg_{41}Nd_5$	9.4	70.66	1.50	3.26	0.09
$Mg_{41}Nd_5$	9.4	70.68	1.50	3.21	0.09
$Mg_{41}Nd_5$	9.4	70.41	1.50	3.21	0.09
$Mg_{41}Nd_5$	9.4	72.23	1.50	3.29	0.09
$Mg_{41}Nd_5$	9.4	75.57	1.50	3.38	0.09
$Mg_{41}Nd_5$	9.4	76.89	1.50	3.63	0.09
$Mg_{41}Nd_5$	9.4	76.11	1.50	3.54	0.09
$Mg_{41}Nd_5$	9.4	75.39	1.50	3.39	0.09
$Mg_{41}Nd_5$	9.4	75.74	1.50	3.41	0.09
$Mg_{41}Nd_5$	9.4	76.52	1.50	3.51	0.09
$Mg_{41}Nd_5$	9.4	75.18	1.50	3.65	0.09
Mg_3Nd	19.8	74.17	1.33	3.69	0.01
Mg_3Nd	20.3	73.64	0.48	3.43	0.15
Mg_3Nd	20.8	73.99	3.14	3.43	0.07
Mg_3Nd	21.3	74.09	1.80	3.56	0.02
Mg_3Nd	21.8	76.59	0.28	3.77	0.09
Mg_3Nd	22.3	74.43	1.52	3.48	0.02
Mg_3Nd	22.8	76.51	0.32	3.56	0.03

Phase	at.%Nd	Reduced Modulus (GPa)		Hardness (GPa)	
		Avg.	Std. Dev.	Avg.	Std. Dev.
Mg_3Nd	23.3	72.16	3.54	3.17	0.39

B.4 Mg-Y Binary System

Table 42: Hall Interdiffusion coefficients in Mg solid solution as a function of composition obtained from 450°C diffusion anneal of Mg vs. Y after 360 hours; Matano plane, $x_o = 0$

Phase	Position (μm)	at.%Y	Hall Interdiffusion Coefficient (m^2/sec)
Mg(Y)	-239.5	0.07	1.07×10^{-14}
Mg(Y)	-234.5	0.05	1.13×10^{-14}
Mg(Y)	-229.5	0.09	1.02×10^{-14}
Mg(Y)	-224.5	0.10	9.82×10^{-15}
Mg(Y)	-219.5	0.11	9.76×10^{-15}
Mg(Y)	-214.5	0.08	1.04×10^{-14}
Mg(Y)	-209.5	0.10	9.93×10^{-15}
Mg(Y)	-204.5	0.07	1.06×10^{-14}
Mg(Y)	-199.5	0.09	1.02×10^{-14}
Mg(Y)	-194.5	0.08	1.04×10^{-14}
Mg(Y)	-189.5	0.11	9.60×10^{-15}
Mg(Y)	-184.5	0.09	1.01×10^{-14}
Mg(Y)	-179.5	0.07	1.06×10^{-14}
Mg(Y)	-174.5	0.14	9.14×10^{-15}
Mg(Y)	-169.5	0.11	9.63×10^{-15}
Mg(Y)	-164.5	0.14	9.15×10^{-15}
Mg(Y)	-159.5	0.16	8.81×10^{-15}
Mg(Y)	-154.5	0.16	8.81×10^{-15}
Mg(Y)	-149.5	0.14	9.07×10^{-15}
Mg(Y)	-144.5	0.15	8.95×10^{-15}
Mg(Y)	-139.5	0.18	8.49×10^{-15}
Mg(Y)	-134.5	0.18	8.44×10^{-15}
Mg(Y)	-129.5	0.18	8.44×10^{-15}
Mg(Y)	-124.5	0.20	8.18×10^{-15}
Mg(Y)	-119.5	0.22	7.99×10^{-15}
Mg(Y)	-114.5	0.21	8.12×10^{-15}
Mg(Y)	-109.5	0.26	7.48×10^{-15}
Mg(Y)	-104.5	0.25	7.60×10^{-15}

Table 43: Hall Interdiffusion coefficients in Mg solid solution as a function of composition obtained from 500°C diffusion anneal of Mg vs. Y after 240 hours; Matano plane, $x_o = 0$

Phase	Position (μm)	at.%Y	Hall Interdiffusion Coefficient (m^2/sec)
Mg(Y)	-492.2	0.02	2.27×10^{-14}
Mg(Y)	-477.2	0.02	2.21×10^{-14}
Mg(Y)	-457.2	0.06	1.97×10^{-14}
Mg(Y)	-452.2	0.02	2.29×10^{-14}
Mg(Y)	-442.2	0.01	2.41×10^{-14}
Mg(Y)	-437.2	0.02	2.24×10^{-14}
Mg(Y)	-427.2	0.01	2.34×10^{-14}
Mg(Y)	-422.2	0.00	2.63×10^{-14}
Mg(Y)	-417.2	0.00	2.52×10^{-14}
Mg(Y)	-412.2	0.00	2.63×10^{-14}
Mg(Y)	-407.2	0.04	2.08×10^{-14}
Mg(Y)	-397.2	0.02	2.26×10^{-14}
Mg(Y)	-392.2	0.05	2.05×10^{-14}
Mg(Y)	-387.2	0.00	2.55×10^{-14}
Mg(Y)	-382.2	0.02	2.28×10^{-14}
Mg(Y)	-377.2	0.02	2.20×10^{-14}
Mg(Y)	-372.2	0.01	2.42×10^{-14}
Mg(Y)	-362.2	0.04	2.10×10^{-14}
Mg(Y)	-357.2	0.03	2.16×10^{-14}
Mg(Y)	-352.2	0.00	2.76×10^{-14}
Mg(Y)	-347.2	0.03	2.19×10^{-14}
Mg(Y)	-342.2	0.03	2.18×10^{-14}
Mg(Y)	-337.2	0.05	2.00×10^{-14}
Mg(Y)	-332.2	0.06	1.97×10^{-14}
Mg(Y)	-327.2	0.05	2.02×10^{-14}
Mg(Y)	-322.2	0.07	1.93×10^{-14}
Mg(Y)	-317.2	0.06	1.99×10^{-14}
Mg(Y)	-312.2	0.09	1.86×10^{-14}
Mg(Y)	-307.2	0.05	2.01×10^{-14}
Mg(Y)	-302.2	0.09	1.86×10^{-14}
Mg(Y)	-297.2	0.09	1.88×10^{-14}
Mg(Y)	-292.2	0.12	1.77×10^{-14}
Mg(Y)	-287.2	0.10	1.84×10^{-14}
Mg(Y)	-282.2	0.08	1.89×10^{-14}

Phase	Position (μm)	at.%Y	Hall Interdiffusion Coefficient (m^2/sec)
Mg(Y)	-277.2	0.12	$1.78x10^{-14}$
Mg(Y)	-272.2	0.08	$1.89x10^{-14}$
Mg(Y)	-267.2	0.13	$1.76x10^{-14}$
Mg(Y)	-262.2	0.13	$1.76x10^{-14}$
Mg(Y)	-257.2	0.12	$1.76x10^{-14}$
Mg(Y)	-252.2	0.13	$1.75x10^{-14}$
Mg(Y)	-247.2	0.14	$1.73x10^{-14}$
Mg(Y)	-242.2	0.15	$1.69x10^{-14}$
Mg(Y)	-237.2	0.18	$1.64x10^{-14}$
Mg(Y)	-232.2	0.17	$1.65x10^{-14}$
Mg(Y)	-227.2	0.16	$1.67x10^{-14}$
Mg(Y)	-222.2	0.16	$1.68x10^{-14}$
Mg(Y)	-217.2	0.16	$1.68x10^{-14}$
Mg(Y)	-212.2	0.15	$1.70x10^{-14}$
Mg(Y)	-207.2	0.21	$1.58x10^{-14}$
Mg(Y)	-202.2	0.22	$1.56x10^{-14}$
Mg(Y)	-197.2	0.22	$1.57x10^{-14}$
Mg(Y)	-192.2	0.20	$1.60x10^{-14}$
Mg(Y)	-187.2	0.22	$1.56x10^{-14}$
Mg(Y)	-182.2	0.27	$1.48x10^{-14}$
Mg(Y)	-177.2	0.26	$1.50x10^{-14}$
Mg(Y)	-172.2	0.25	$1.51x10^{-14}$

Table 44: Hall Interdiffusion coefficients in Mg solid solution as a function of composition obtained from 550°C diffusion anneal of Mg vs. Y after 120 hours; Matano plane, $x_o = 0$

Phase	Position (μm)	at.%Y	Hall Interdiffusion Coefficient (m^2/sec)
Mg(Y)	-156.6	0.11	4.63×10^{-14}
Mg(Y)	-156.6	0.07	5.94×10^{-14}
Mg(Y)	-156.6	0.08	5.70×10^{-14}
Mg(Y)	-156.6	0.05	6.65×10^{-14}
Mg(Y)	-156.7	0.02	8.52×10^{-14}
Mg(Y)	-156.6	0.07	6.02×10^{-14}
Mg(Y)	-156.6	0.08	5.53×10^{-14}
Mg(Y)	-156.6	0.11	4.82×10^{-14}
Mg(Y)	-156.6	0.09	5.22×10^{-14}
Mg(Y)	-156.6	0.12	4.50×10^{-14}
Mg(Y)	-156.6	0.06	6.30×10^{-14}
Mg(Y)	-156.6	0.10	5.04×10^{-14}
Mg(Y)	-156.6	0.13	4.30×10^{-14}
Mg(Y)	-156.6	0.06	6.33×10^{-14}
Mg(Y)	-156.6	0.11	4.80×10^{-14}
Mg(Y)	-156.6	0.14	4.07×10^{-14}
Mg(Y)	-156.6	0.11	4.62×10^{-14}
Mg(Y)	-156.6	0.10	4.85×10^{-14}
Mg(Y)	-156.6	0.11	4.67×10^{-14}
Mg(Y)	-156.6	0.08	5.47×10^{-14}
Mg(Y)	-156.5	0.18	3.12×10^{-14}
Mg(Y)	-156.6	0.12	4.53×10^{-14}
Mg(Y)	-156.6	0.10	4.92×10^{-14}
Mg(Y)	-156.6	0.15	3.83×10^{-14}
Mg(Y)	-156.6	0.11	4.81×10^{-14}
Mg(Y)	-156.6	0.10	4.99×10^{-14}
Mg(Y)	-156.5	0.18	3.20×10^{-14}
Mg(Y)	-156.5	0.15	3.75×10^{-14}
Mg(Y)	-156.5	0.16	3.48×10^{-14}
Mg(Y)	-156.5	0.16	3.45×10^{-14}
Mg(Y)	-156.5	0.16	3.59×10^{-14}
Mg(Y)	-156.6	0.15	3.83×10^{-14}
Mg(Y)	-156.5	0.19	2.98×10^{-14}
Mg(Y)	-156.5	0.16	3.63×10^{-14}

Phase	Position (μm)	at.%Y	Hall Interdiffusion Coefficient (m^2/sec)
Mg(Y)	-156.5	0.21	$2.58x10^{-14}$
Mg(Y)	-156.5	0.18	$3.19x10^{-14}$
Mg(Y)	-156.5	0.18	$3.16x10^{-14}$
Mg(Y)	-156.5	0.20	$2.83x10^{-14}$
Mg(Y)	-156.5	0.23	$2.33x10^{-14}$
Mg(Y)	-156.5	0.18	$3.14x10^{-14}$
Mg(Y)	-156.5	0.21	$2.62x10^{-14}$
Mg(Y)	-156.5	0.18	$3.09x10^{-14}$
Mg(Y)	-156.5	0.19	$2.94x10^{-14}$
Mg(Y)	-156.5	0.19	$3.00x10^{-14}$
Mg(Y)	-156.5	0.22	$2.51x10^{-14}$
Mg(Y)	-156.5	0.22	$2.51x10^{-14}$
Mg(Y)	-156.4	0.26	$1.89x10^{-14}$
Mg(Y)	-156.5	0.22	$2.43x10^{-14}$
Mg(Y)	-156.5	0.24	$2.20x10^{-14}$
Mg(Y)	-156.4	0.25	$2.00x10^{-14}$

Table 45: Reduced modulus and hardness of Mg solid solution as a function of composition obtained from 550°C diffusion anneal of Mg vs. Y after 120 hours; Peak Load 5mN

Phase	at.%Nd	Reduced Modulus (GPa)		Hardness (GPa)	
		Avg.	Std. Dev.	Avg.	Std. Dev.
Mg(Y)	0.00	35.00	--	0.50	--
Mg(Y)	0.98	49.14	1.19	0.88	0.07
Mg(Y)	1.03	48.19	0.25	0.85	0.01
Mg(Y)	1.09	48.88	0.08	0.87	0.00
Mg(Y)	1.15	49.90	0.33	0.89	0.02
Mg(Y)	1.21	50.14	1.33	0.88	0.00
Mg(Y)	1.28	50.20	0.69	0.88	0.01
Mg(Y)	1.35	50.50	0.31	0.87	0.01
Mg(Y)	1.43	50.57	1.42	0.91	0.06
Mg(Y)	1.51	49.27	0.51	0.89	0.01
Mg(Y)	1.59	53.56	1.93	1.03	0.04
Mg(Y)	1.68	52.45	0.90	1.00	0.00
Mg(Y)	1.77	52.27	0.19	1.02	0.01
Mg(Y)	1.87	50.55	0.42	0.97	0.05
Mg(Y)	1.98	51.64	0.87	1.02	0.04
Mg(Y)	2.08	51.76	0.17	1.03	0.01
Mg(Y)	2.20	54.50	3.72	1.14	0.07
Mg(Y)	2.32	51.57	0.77	1.03	0.02
Mg(Y)	2.45	53.16	0.89	1.07	0.06
Mg(Y)	2.59	54.75	0.42	1.12	0.03
Mg(Y)	2.73	51.90	1.87	1.08	0.03
Mg(Y)	2.88	51.79	1.73	1.09	0.05
Mg(Y)	3.04	52.22	2.26	1.13	0.05
Mg(Y)	3.21	51.00	1.23	1.14	0.04
Mg(Y)	3.39	53.56	0.18	1.22	0.03
Mg(Y)	3.58	53.19	0.21	1.22	0.02
Mg(Y)	3.78	51.74	0.18	1.20	0.00
Mg(Y)	3.99	54.02	0.93	1.28	0.04
Mg(Y)	4.21	53.48	0.94	1.39	0.02
Mg(Y)	4.44	52.64	--	1.38	--

Table 46: Reduced modulus and hardness of intermetallic compounds formed during 450°C diffusion anneal of Mg vs. Y after 360 hours; Peak Load 7mN

Phase	at.%Y	Reduced Modulus (GPa)		Hardness (GPa)	
		Avg.	Std. Dev.	Avg.	Std. Dev.
$Mg_{24}Y_5$	12.6	65.87	--	3.40	--
$Mg_{24}Y_5$	12.8	66.84	4.87	3.42	0.05
$Mg_{24}Y_5$	13.0	61.95	4.13	3.00	0.66
$Mg_{24}Y_5$	13.2	61.54	--	3.29	--
$Mg_{24}Y_5$	13.3	59.85	4.83	2.79	0.65
$Mg_{24}Y_5$	13.5	56.53	--	3.44	--
$Mg_{24}Y_5$	13.7	61.39	5.44	3.38	0.27
$Mg_{24}Y_5$	13.9	70.87	7.28	4.01	0.05
$Mg_{24}Y_5$	14.1	63.77	10.17	3.20	0.73
$Mg_{24}Y_5$	14.3	62.63	13.28	3.26	1.23
$Mg_{24}Y_5$	14.5	70.09	3.05	3.83	0.11
$Mg_{24}Y_5$	14.6	69.96	4.00	3.98	0.32
$Mg_{24}Y_5$	14.8	73.68	3.58	4.13	0.30
$Mg_{24}Y_5$	15.0	70.05	3.87	3.95	0.30
$Mg_{24}Y_5$	15.2	76.25	6.81	4.21	0.18
MgY_2	23.9	83.85	0.72	4.66	0.10
MgY_2	25.1	80.71	2.25	4.43	0.15
MgY_2	26.4	84.61	3.95	4.62	0.03
MgY_2	27.6	86.32	--	5.19	--

B.5 Mg-Zn Binary System

Table 47: Hall Interdiffusion coefficients in Mg solid solution as a function of composition obtained from 350°C diffusion anneal of Mg vs. Mg-3at.%Zn after 125 hours; Matano plane, $x_o = 0$

Phase	Position (μm)	at.%Zn	EPMA Line Scan	Hall Interdiffusion Coefficient (m^2/sec)
Mg(Zn)	157.8	0.00	LS1	$3.54x10^{-15}$
Mg(Zn)	154.6	0.01	LS1	$3.53x10^{-15}$
Mg(Zn)	151.5	0.01	LS1	$3.52x10^{-15}$
Mg(Zn)	148.4	0.02	LS1	$3.52x10^{-15}$
Mg(Zn)	145.2	0.02	LS1	$3.51x10^{-15}$
Mg(Zn)	142.1	0.02	LS1	$3.51x10^{-15}$
Mg(Zn)	139.0	0.03	LS1	$3.51x10^{-15}$
Mg(Zn)	135.8	0.03	LS1	$3.51x10^{-15}$
Mg(Zn)	132.7	0.03	LS1	$3.51x10^{-15}$
Mg(Zn)	129.6	0.03	LS1	$3.50x10^{-15}$
Mg(Zn)	126.5	0.04	LS1	$3.50x10^{-15}$
Mg(Zn)	123.3	0.04	LS1	$3.50x10^{-15}$
Mg(Zn)	120.2	0.05	LS1	$3.50x10^{-15}$
Mg(Zn)	117.1	0.05	LS1	$3.50x10^{-15}$
Mg(Zn)	113.9	0.05	LS1	$3.49x10^{-15}$
Mg(Zn)	110.8	0.06	LS1	$3.49x10^{-15}$
Mg(Zn)	107.7	0.07	LS1	$3.49x10^{-15}$
Mg(Zn)	104.5	0.07	LS1	$3.49x10^{-15}$
Mg(Zn)	101.4	0.08	LS1	$3.48x10^{-15}$
Mg(Zn)	98.3	0.09	LS1	$3.48x10^{-15}$
Mg(Zn)	95.1	0.10	LS1	$3.48x10^{-15}$
Mg(Zn)	92.0	0.11	LS1	$3.47x10^{-15}$
Mg(Zn)	88.9	0.13	LS1	$3.47x10^{-15}$
Mg(Zn)	85.7	0.14	LS1	$3.46x10^{-15}$
Mg(Zn)	82.6	0.16	LS1	$3.46x10^{-15}$
Mg(Zn)	79.5	0.17	LS1	$3.46x10^{-15}$
Mg(Zn)	76.4	0.19	LS1	$3.45x10^{-15}$
Mg(Zn)	73.2	0.21	LS1	$3.45x10^{-15}$
Mg(Zn)	70.1	0.24	LS1	$3.44x10^{-15}$
Mg(Zn)	67.0	0.26	LS1	$3.43x10^{-15}$
Mg(Zn)	63.8	0.29	LS1	$3.43x10^{-15}$

Phase	Position (μm)	at.%Zn	EPMA Line Scan	Hall Interdiffusion Coefficient (m^2/sec)
Mg(Zn)	60.7	0.32	LS1	$3.42x10^{-15}$
Mg(Zn)	57.6	0.35	LS1	$3.42x10^{-15}$
Mg(Zn)	54.4	0.38	LS1	$3.41x10^{-15}$
Mg(Zn)	51.3	0.41	LS1	$3.40x10^{-15}$
Mg(Zn)	48.2	0.45	LS1	$3.39x10^{-15}$
Mg(Zn)	45.0	0.49	LS1	$3.38x10^{-15}$
Mg(Zn)	119.9	0.00	LS2	$2.90x10^{-15}$
Mg(Zn)	116.9	0.01	LS2	$2.91x10^{-15}$
Mg(Zn)	113.9	0.02	LS2	$2.91x10^{-15}$
Mg(Zn)	110.9	0.03	LS2	$2.91x10^{-15}$
Mg(Zn)	107.8	0.04	LS2	$2.92x10^{-15}$
Mg(Zn)	104.8	0.05	LS2	$2.92x10^{-15}$
Mg(Zn)	101.8	0.06	LS2	$2.92x10^{-15}$
Mg(Zn)	98.8	0.07	LS2	$2.93x10^{-15}$
Mg(Zn)	95.8	0.09	LS2	$2.93x10^{-15}$
Mg(Zn)	92.8	0.10	LS2	$2.93x10^{-15}$
Mg(Zn)	89.8	0.12	LS2	$2.93x10^{-15}$
Mg(Zn)	86.8	0.13	LS2	$2.94x10^{-15}$
Mg(Zn)	83.8	0.15	LS2	$2.94x10^{-15}$
Mg(Zn)	80.8	0.17	LS2	$2.94x10^{-15}$
Mg(Zn)	77.7	0.19	LS2	$2.95x10^{-15}$
Mg(Zn)	74.7	0.22	LS2	$2.95x10^{-15}$
Mg(Zn)	71.7	0.24	LS2	$2.95x10^{-15}$
Mg(Zn)	68.7	0.27	LS2	$2.96x10^{-15}$
Mg(Zn)	65.7	0.30	LS2	$2.96x10^{-15}$
Mg(Zn)	62.7	0.33	LS2	$2.96x10^{-15}$
Mg(Zn)	59.7	0.36	LS2	$2.97x10^{-15}$
Mg(Zn)	56.7	0.39	LS2	$2.97x10^{-15}$
Mg(Zn)	53.7	0.43	LS2	$2.97x10^{-15}$
Mg(Zn)	50.7	0.46	LS2	$2.98x10^{-15}$
Mg(Zn)	47.6	0.50	LS2	$2.98x10^{-15}$
Mg(Zn)	113.5	0.01	LS3	$2.71x10^{-15}$
Mg(Zn)	111.0	0.02	LS3	$2.71x10^{-15}$
Mg(Zn)	108.5	0.02	LS3	$2.71x10^{-15}$
Mg(Zn)	106.0	0.03	LS3	$2.71x10^{-15}$
Mg(Zn)	103.4	0.04	LS3	$2.71x10^{-15}$

Phase	Position (μm)	at.%Zn	EPMA Line Scan	Hall Interdiffusion Coefficient (m^2/sec)
Mg(Zn)	100.9	0.04	LS3	$2.71x10^{-15}$
Mg(Zn)	98.4	0.05	LS3	$2.71x10^{-15}$
Mg(Zn)	95.9	0.06	LS3	$2.71x10^{-15}$
Mg(Zn)	93.3	0.07	LS3	$2.71x10^{-15}$
Mg(Zn)	90.8	0.08	LS3	$2.71x10^{-15}$
Mg(Zn)	88.3	0.09	LS3	$2.71x10^{-15}$
Mg(Zn)	85.8	0.11	LS3	$2.71x10^{-15}$
Mg(Zn)	83.2	0.12	LS3	$2.71x10^{-15}$
Mg(Zn)	80.7	0.14	LS3	$2.71x10^{-15}$
Mg(Zn)	78.2	0.15	LS3	$2.71x10^{-15}$
Mg(Zn)	75.7	0.17	LS3	$2.71x10^{-15}$
Mg(Zn)	73.1	0.18	LS3	$2.71x10^{-15}$
Mg(Zn)	70.6	0.20	LS3	$2.71x10^{-15}$
Mg(Zn)	68.1	0.22	LS3	$2.71x10^{-15}$
Mg(Zn)	65.6	0.24	LS3	$2.71x10^{-15}$
Mg(Zn)	63.0	0.26	LS3	$2.71x10^{-15}$
Mg(Zn)	60.5	0.28	LS3	$2.71x10^{-15}$
Mg(Zn)	58.0	0.31	LS3	$2.71x10^{-15}$
Mg(Zn)	55.5	0.33	LS3	$2.71x10^{-15}$
Mg(Zn)	52.9	0.36	LS3	$2.71x10^{-15}$
Mg(Zn)	50.4	0.38	LS3	$2.71x10^{-15}$
Mg(Zn)	47.9	0.41	LS3	$2.71x10^{-15}$
Mg(Zn)	45.4	0.45	LS3	$2.71x10^{-15}$
Mg(Zn)	42.8	0.48	LS3	$2.71x10^{-15}$
Mg(Zn)	40.3	0.51	LS3	$2.72x10^{-15}$

Table 48: Hall Interdiffusion coefficients in Mg solid solution as a function of composition obtained from 400°C diffusion anneal of Mg vs. Mg-3at.%Zn after 8 hours; Matano plane, $x_o = 0$

Phase	Position (μm)	at.%Zn	EPMA Line Scan	Hall Interdiffusion Coefficient (m^2/sec)
Mg(Zn)	150.4	0.01	LS1	$1.57x10^{-14}$
Mg(Zn)	147.3	0.01	LS1	$1.57x10^{-14}$
Mg(Zn)	144.3	0.01	LS1	$1.57x10^{-14}$
Mg(Zn)	141.3	0.01	LS1	$1.57x10^{-14}$
Mg(Zn)	138.2	0.01	LS1	$1.57x10^{-14}$
Mg(Zn)	135.2	0.01	LS1	$1.57x10^{-14}$
Mg(Zn)	132.2	0.01	LS1	$1.57x10^{-14}$
Mg(Zn)	129.1	0.01	LS1	$1.57x10^{-14}$
Mg(Zn)	126.1	0.01	LS1	$1.57x10^{-14}$
Mg(Zn)	123.1	0.01	LS1	$1.57x10^{-14}$
Mg(Zn)	120.0	0.01	LS1	$1.57x10^{-14}$
Mg(Zn)	117.0	0.02	LS1	$1.57x10^{-14}$
Mg(Zn)	114.0	0.02	LS1	$1.57x10^{-14}$
Mg(Zn)	110.9	0.02	LS1	$1.57x10^{-14}$
Mg(Zn)	107.9	0.02	LS1	$1.57x10^{-14}$
Mg(Zn)	104.9	0.02	LS1	$1.57x10^{-14}$
Mg(Zn)	101.8	0.02	LS1	$1.57x10^{-14}$
Mg(Zn)	98.8	0.03	LS1	$1.57x10^{-14}$
Mg(Zn)	95.8	0.03	LS1	$1.57x10^{-14}$
Mg(Zn)	92.7	0.03	LS1	$1.57x10^{-14}$
Mg(Zn)	89.7	0.03	LS1	$1.57x10^{-14}$
Mg(Zn)	86.7	0.03	LS1	$1.57x10^{-14}$
Mg(Zn)	83.6	0.04	LS1	$1.57x10^{-14}$
Mg(Zn)	80.6	0.04	LS1	$1.57x10^{-14}$
Mg(Zn)	77.6	0.04	LS1	$1.57x10^{-14}$
Mg(Zn)	74.5	0.04	LS1	$1.57x10^{-14}$
Mg(Zn)	71.5	0.04	LS1	$1.57x10^{-14}$
Mg(Zn)	68.5	0.04	LS1	$1.57x10^{-14}$
Mg(Zn)	65.4	0.05	LS1	$1.57x10^{-14}$
Mg(Zn)	62.4	0.05	LS1	$1.57x10^{-14}$
Mg(Zn)	59.4	0.06	LS1	$1.57x10^{-14}$
Mg(Zn)	56.3	0.07	LS1	$1.58x10^{-14}$
Mg(Zn)	53.3	0.08	LS1	$1.58x10^{-14}$

Phase	Position (μm)	at.%Zn	EPMA Line Scan	Hall Interdiffusion Coefficient (m^2/sec)
Mg(Zn)	50.3	0.09	LS1	$1.58x10^{-14}$
Mg(Zn)	47.2	0.11	LS1	$1.58x10^{-14}$
Mg(Zn)	44.2	0.13	LS1	$1.58x10^{-14}$
Mg(Zn)	41.2	0.15	LS1	$1.58x10^{-14}$
Mg(Zn)	38.1	0.19	LS1	$1.59x10^{-14}$
Mg(Zn)	35.1	0.22	LS1	$1.59x10^{-14}$
Mg(Zn)	32.1	0.26	LS1	$1.59x10^{-14}$
Mg(Zn)	29.0	0.31	LS1	$1.60x10^{-14}$
Mg(Zn)	26.0	0.37	LS1	$1.60x10^{-14}$
Mg(Zn)	23.0	0.43	LS1	$1.61x10^{-14}$
Mg(Zn)	19.9	0.50	LS1	$1.61x10^{-14}$
Mg(Zn)	153.2	0.02	LS2	$2.15x10^{-14}$
Mg(Zn)	150.2	0.02	LS2	$2.15x10^{-14}$
Mg(Zn)	147.3	0.02	LS2	$2.15x10^{-14}$
Mg(Zn)	144.3	0.02	LS2	$2.15x10^{-14}$
Mg(Zn)	141.4	0.02	LS2	$2.15x10^{-14}$
Mg(Zn)	138.4	0.02	LS2	$2.15x10^{-14}$
Mg(Zn)	135.4	0.02	LS2	$2.15x10^{-14}$
Mg(Zn)	132.5	0.02	LS2	$2.15x10^{-14}$
Mg(Zn)	129.5	0.02	LS2	$2.15x10^{-14}$
Mg(Zn)	126.6	0.02	LS2	$2.15x10^{-14}$
Mg(Zn)	123.6	0.02	LS2	$2.15x10^{-14}$
Mg(Zn)	120.7	0.02	LS2	$2.15x10^{-14}$
Mg(Zn)	117.7	0.02	LS2	$2.15x10^{-14}$
Mg(Zn)	114.8	0.02	LS2	$2.15x10^{-14}$
Mg(Zn)	111.8	0.02	LS2	$2.15x10^{-14}$
Mg(Zn)	108.9	0.02	LS2	$2.14x10^{-14}$
Mg(Zn)	105.9	0.02	LS2	$2.14x10^{-14}$
Mg(Zn)	103.0	0.03	LS2	$2.14x10^{-14}$
Mg(Zn)	100.0	0.03	LS2	$2.14x10^{-14}$
Mg(Zn)	97.1	0.03	LS2	$2.14x10^{-14}$
Mg(Zn)	94.1	0.03	LS2	$2.14x10^{-14}$
Mg(Zn)	91.1	0.03	LS2	$2.14x10^{-14}$
Mg(Zn)	88.2	0.03	LS2	$2.14x10^{-14}$
Mg(Zn)	85.2	0.04	LS2	$2.14x10^{-14}$
Mg(Zn)	82.3	0.04	LS2	$2.14x10^{-14}$

Phase	Position (μm)	at.%Zn	EPMA Line Scan	Hall Interdiffusion Coefficient (m^2/sec)
Mg(Zn)	79.3	0.04	LS2	$2.14x10^{-14}$
Mg(Zn)	76.4	0.04	LS2	$2.14x10^{-14}$
Mg(Zn)	73.4	0.05	LS2	$2.14x10^{-14}$
Mg(Zn)	70.5	0.05	LS2	$2.14x10^{-14}$
Mg(Zn)	67.5	0.06	LS2	$2.13x10^{-14}$
Mg(Zn)	64.6	0.06	LS2	$2.13x10^{-14}$
Mg(Zn)	61.6	0.07	LS2	$2.13x10^{-14}$
Mg(Zn)	58.7	0.08	LS2	$2.13x10^{-14}$
Mg(Zn)	55.7	0.09	LS2	$2.13x10^{-14}$
Mg(Zn)	52.8	0.10	LS2	$2.12x10^{-14}$
Mg(Zn)	49.8	0.12	LS2	$2.12x10^{-14}$
Mg(Zn)	46.8	0.14	LS2	$2.12x10^{-14}$
Mg(Zn)	43.9	0.16	LS2	$2.11x10^{-14}$
Mg(Zn)	40.9	0.18	LS2	$2.11x10^{-14}$
Mg(Zn)	38.0	0.21	LS2	$2.11x10^{-14}$
Mg(Zn)	35.0	0.25	LS2	$2.10x10^{-14}$
Mg(Zn)	32.1	0.28	LS2	$2.10x10^{-14}$
Mg(Zn)	29.1	0.33	LS2	$2.09x10^{-14}$
Mg(Zn)	26.2	0.37	LS2	$2.08x10^{-14}$
Mg(Zn)	23.2	0.43	LS2	$2.08x10^{-14}$
Mg(Zn)	20.3	0.49	LS2	$2.07x10^{-14}$
Mg(Zn)	149.9	0.01	LS3	$2.61x10^{-14}$
Mg(Zn)	146.9	0.01	LS3	$2.61x10^{-14}$
Mg(Zn)	143.9	0.01	LS3	$2.61x10^{-14}$
Mg(Zn)	140.9	0.01	LS3	$2.61x10^{-14}$
Mg(Zn)	137.9	0.01	LS3	$2.61x10^{-14}$
Mg(Zn)	134.9	0.02	LS3	$2.61x10^{-14}$
Mg(Zn)	132.0	0.02	LS3	$2.60x10^{-14}$
Mg(Zn)	129.0	0.02	LS3	$2.60x10^{-14}$
Mg(Zn)	126.0	0.02	LS3	$2.60x10^{-14}$
Mg(Zn)	123.0	0.02	LS3	$2.60x10^{-14}$
Mg(Zn)	120.0	0.02	LS3	$2.60x10^{-14}$
Mg(Zn)	117.0	0.02	LS3	$2.60x10^{-14}$
Mg(Zn)	114.0	0.02	LS3	$2.60x10^{-14}$
Mg(Zn)	111.0	0.02	LS3	$2.60x10^{-14}$
Mg(Zn)	108.0	0.02	LS3	$2.59x10^{-14}$

Phase	Position (μm)	at.%Zn	EPMA Line Scan	Hall Interdiffusion Coefficient (m^2/sec)
Mg(Zn)	105.0	0.02	LS3	$2.59x10^{-14}$
Mg(Zn)	102.0	0.03	LS3	$2.59x10^{-14}$
Mg(Zn)	99.1	0.03	LS3	$2.59x10^{-14}$
Mg(Zn)	96.1	0.03	LS3	$2.59x10^{-14}$
Mg(Zn)	93.1	0.03	LS3	$2.59x10^{-14}$
Mg(Zn)	90.1	0.04	LS3	$2.58x10^{-14}$
Mg(Zn)	87.1	0.04	LS3	$2.58x10^{-14}$
Mg(Zn)	84.1	0.04	LS3	$2.58x10^{-14}$
Mg(Zn)	81.1	0.04	LS3	$2.57x10^{-14}$
Mg(Zn)	78.1	0.05	LS3	$2.57x10^{-14}$
Mg(Zn)	75.1	0.05	LS3	$2.57x10^{-14}$
Mg(Zn)	72.1	0.06	LS3	$2.56x10^{-14}$
Mg(Zn)	69.1	0.06	LS3	$2.56x10^{-14}$
Mg(Zn)	66.2	0.07	LS3	$2.56x10^{-14}$
Mg(Zn)	63.2	0.08	LS3	$2.55x10^{-14}$
Mg(Zn)	60.2	0.08	LS3	$2.55x10^{-14}$
Mg(Zn)	57.2	0.09	LS3	$2.54x10^{-14}$
Mg(Zn)	54.2	0.11	LS3	$2.53x10^{-14}$
Mg(Zn)	51.2	0.12	LS3	$2.53x10^{-14}$
Mg(Zn)	48.2	0.13	LS3	$2.52x10^{-14}$
Mg(Zn)	45.2	0.15	LS3	$2.51x10^{-14}$
Mg(Zn)	42.2	0.17	LS3	$2.50x10^{-14}$
Mg(Zn)	39.2	0.19	LS3	$2.49x10^{-14}$
Mg(Zn)	36.2	0.22	LS3	$2.48x10^{-14}$
Mg(Zn)	33.3	0.25	LS3	$2.47x10^{-14}$
Mg(Zn)	30.3	0.28	LS3	$2.45x10^{-14}$
Mg(Zn)	27.3	0.32	LS3	$2.44x10^{-14}$
Mg(Zn)	24.3	0.37	LS3	$2.42x10^{-14}$
Mg(Zn)	21.3	0.43	LS3	$2.40x10^{-14}$
Mg(Zn)	18.3	0.49	LS3	$2.37x10^{-14}$

Table 49: Hall Interdiffusion coefficients in Mg solid solution as a function of composition obtained from 450°C diffusion anneal of Mg vs. Mg-3at.%Zn after 24 hours; Matano plane, $x_o = 0$

Phase	Position (μm)	at.%Zn	EPMA Line Scan	Hall Interdiffusion Coefficient (m^2/sec)
Mg(Zn)	395.7	0.00	LS1	7.21×10^{-14}
Mg(Zn)	386.7	0.01	LS1	7.23×10^{-14}
Mg(Zn)	377.8	0.01	LS1	7.25×10^{-14}
Mg(Zn)	368.8	0.01	LS1	7.26×10^{-14}
Mg(Zn)	359.9	0.01	LS1	7.26×10^{-14}
Mg(Zn)	350.9	0.01	LS1	7.26×10^{-14}
Mg(Zn)	342.0	0.01	LS1	7.26×10^{-14}
Mg(Zn)	333.0	0.01	LS1	7.26×10^{-14}
Mg(Zn)	324.1	0.01	LS1	7.26×10^{-14}
Mg(Zn)	315.1	0.01	LS1	7.26×10^{-14}
Mg(Zn)	306.1	0.01	LS1	7.27×10^{-14}
Mg(Zn)	297.2	0.01	LS1	7.27×10^{-14}
Mg(Zn)	288.2	0.02	LS1	7.28×10^{-14}
Mg(Zn)	279.3	0.02	LS1	7.30×10^{-14}
Mg(Zn)	270.3	0.02	LS1	7.31×10^{-14}
Mg(Zn)	261.4	0.03	LS1	7.33×10^{-14}
Mg(Zn)	252.4	0.04	LS1	7.34×10^{-14}
Mg(Zn)	243.5	0.05	LS1	7.36×10^{-14}
Mg(Zn)	234.5	0.06	LS1	7.38×10^{-14}
Mg(Zn)	225.6	0.07	LS1	7.40×10^{-14}
Mg(Zn)	216.6	0.08	LS1	7.43×10^{-14}
Mg(Zn)	207.6	0.10	LS1	7.45×10^{-14}
Mg(Zn)	198.7	0.12	LS1	7.48×10^{-14}
Mg(Zn)	189.7	0.15	LS1	7.50×10^{-14}
Mg(Zn)	180.8	0.17	LS1	7.53×10^{-14}
Mg(Zn)	171.8	0.20	LS1	7.56×10^{-14}
Mg(Zn)	162.9	0.23	LS1	7.59×10^{-14}
Mg(Zn)	153.9	0.27	LS1	7.62×10^{-14}
Mg(Zn)	145.0	0.31	LS1	7.66×10^{-14}
Mg(Zn)	136.0	0.35	LS1	7.70×10^{-14}
Mg(Zn)	127.1	0.39	LS1	7.74×10^{-14}
Mg(Zn)	118.1	0.44	LS1	7.78×10^{-14}
Mg(Zn)	109.1	0.49	LS1	7.83×10^{-14}

Phase	Position (μm)	at.%Zn	EPMA Line Scan	Hall Interdiffusion Coefficient (m^2/sec)
Mg(Zn)	364.8	0.00	LS2	$6.98x10^{-14}$
Mg(Zn)	356.1	0.01	LS2	$7.02x10^{-14}$
Mg(Zn)	347.5	0.01	LS2	$7.04x10^{-14}$
Mg(Zn)	338.8	0.01	LS2	$7.05x10^{-14}$
Mg(Zn)	330.1	0.01	LS2	$7.06x10^{-14}$
Mg(Zn)	321.4	0.01	LS2	$7.06x10^{-14}$
Mg(Zn)	312.8	0.02	LS2	$7.07x10^{-14}$
Mg(Zn)	304.1	0.02	LS2	$7.07x10^{-14}$
Mg(Zn)	295.4	0.02	LS2	$7.08x10^{-14}$
Mg(Zn)	286.7	0.02	LS2	$7.09x10^{-14}$
Mg(Zn)	278.1	0.02	LS2	$7.10x10^{-14}$
Mg(Zn)	269.4	0.03	LS2	$7.11x10^{-14}$
Mg(Zn)	260.7	0.03	LS2	$7.12x10^{-14}$
Mg(Zn)	252.0	0.04	LS2	$7.14x10^{-14}$
Mg(Zn)	243.4	0.05	LS2	$7.16x10^{-14}$
Mg(Zn)	234.7	0.06	LS2	$7.17x10^{-14}$
Mg(Zn)	226.0	0.07	LS2	$7.20x10^{-14}$
Mg(Zn)	217.3	0.08	LS2	$7.22x10^{-14}$
Mg(Zn)	208.7	0.10	LS2	$7.24x10^{-14}$
Mg(Zn)	200.0	0.12	LS2	$7.27x10^{-14}$
Mg(Zn)	191.3	0.14	LS2	$7.29x10^{-14}$
Mg(Zn)	182.6	0.16	LS2	$7.32x10^{-14}$
Mg(Zn)	174.0	0.19	LS2	$7.35x10^{-14}$
Mg(Zn)	165.3	0.22	LS2	$7.39x10^{-14}$
Mg(Zn)	156.6	0.25	LS2	$7.42x10^{-14}$
Mg(Zn)	147.9	0.29	LS2	$7.46x10^{-14}$
Mg(Zn)	139.3	0.33	LS2	$7.50x10^{-14}$
Mg(Zn)	130.6	0.38	LS2	$7.54x10^{-14}$
Mg(Zn)	121.9	0.43	LS2	$7.59x10^{-14}$
Mg(Zn)	113.2	0.48	LS2	$7.64x10^{-14}$
Mg(Zn)	366.2	0.00	LS3	$7.00x10^{-14}$
Mg(Zn)	357.5	0.01	LS3	$7.05x10^{-14}$
Mg(Zn)	348.9	0.01	LS3	$7.07x10^{-14}$
Mg(Zn)	340.2	0.01	LS3	$7.08x10^{-14}$
Mg(Zn)	331.5	0.01	LS3	$7.09x10^{-14}$
Mg(Zn)	322.8	0.01	LS3	$7.09x10^{-14}$

Phase	Position (μm)	at.%Zn	EPMA Line Scan	Hall Interdiffusion Coefficient (m^2/sec)
Mg(Zn)	314.2	0.02	LS3	$7.10x10^{-14}$
Mg(Zn)	305.5	0.02	LS3	$7.11x10^{-14}$
Mg(Zn)	296.8	0.02	LS3	$7.11x10^{-14}$
Mg(Zn)	288.1	0.02	LS3	$7.12x10^{-14}$
Mg(Zn)	279.5	0.02	LS3	$7.13x10^{-14}$
Mg(Zn)	270.8	0.03	LS3	$7.14x10^{-14}$
Mg(Zn)	262.1	0.03	LS3	$7.16x10^{-14}$
Mg(Zn)	253.4	0.04	LS3	$7.17x10^{-14}$
Mg(Zn)	244.8	0.05	LS3	$7.19x10^{-14}$
Mg(Zn)	236.1	0.06	LS3	$7.21x10^{-14}$
Mg(Zn)	227.4	0.07	LS3	$7.23x10^{-14}$
Mg(Zn)	218.7	0.08	LS3	$7.26x10^{-14}$
Mg(Zn)	210.1	0.10	LS3	$7.28x10^{-14}$
Mg(Zn)	201.4	0.12	LS3	$7.31x10^{-14}$
Mg(Zn)	192.7	0.14	LS3	$7.34x10^{-14}$
Mg(Zn)	184.0	0.16	LS3	$7.37x10^{-14}$
Mg(Zn)	175.4	0.19	LS3	$7.40x10^{-14}$
Mg(Zn)	166.7	0.22	LS3	$7.44x10^{-14}$
Mg(Zn)	158.0	0.25	LS3	$7.47x10^{-14}$
Mg(Zn)	149.3	0.29	LS3	$7.51x10^{-14}$
Mg(Zn)	140.7	0.33	LS3	$7.56x10^{-14}$
Mg(Zn)	132.0	0.38	LS3	$7.60x10^{-14}$
Mg(Zn)	123.3	0.43	LS3	$7.65x10^{-14}$
Mg(Zn)	114.6	0.48	LS3	$7.70x10^{-14}$

Table 50: Interdiffusion flux and interdiffusion coefficients as a function of composition in intermetallic compounds formed during 315°C diffusion anneal of Mg vs. Zn after 168 hours; Matano plane, $x_o = 0$

Phase	Position (μm)	at.%Zn	Flux $\left(\frac{\mu m \cdot at.frac.}{sec}\right)$	Interdiffusion Coefficient (m^2/sec)	
				Boltzmann-Matano	Sauer-Freise
Mg_4Zn_7	-108.2	58.19	-5.28×10^{-5}	8.94×10^{-14}	9.11×10^{-14}
Mg_4Zn_7	-107.8	58.21	-5.29×10^{-5}	8.94×10^{-14}	9.11×10^{-14}
Mg_4Zn_7	-107.4	58.23	-5.29×10^{-5}	8.95×10^{-14}	9.11×10^{-14}
Mg_4Zn_7	-107.0	58.26	-5.29×10^{-5}	8.95×10^{-14}	9.12×10^{-14}
Mg_4Zn_7	-106.6	58.28	-5.29×10^{-5}	8.96×10^{-14}	9.12×10^{-14}
Mg_4Zn_7	-106.2	58.31	-5.30×10^{-5}	8.96×10^{-14}	9.13×10^{-14}
Mg_4Zn_7	-105.8	58.33	-5.30×10^{-5}	8.96×10^{-14}	9.13×10^{-14}
Mg_4Zn_7	-105.4	58.35	-5.30×10^{-5}	8.97×10^{-14}	9.13×10^{-14}
Mg_4Zn_7	-105.0	58.38	-5.30×10^{-5}	8.97×10^{-14}	9.14×10^{-14}
Mg_4Zn_7	-104.6	58.40	-5.30×10^{-5}	8.97×10^{-14}	9.14×10^{-14}
Mg_4Zn_7	-104.2	58.42	-5.31×10^{-5}	8.97×10^{-14}	9.14×10^{-14}
Mg_4Zn_7	-103.8	58.45	-5.31×10^{-5}	8.98×10^{-14}	9.14×10^{-14}
Mg_4Zn_7	-103.3	58.47	-5.31×10^{-5}	8.98×10^{-14}	9.15×10^{-14}
Mg_4Zn_7	-102.9	58.50	-5.31×10^{-5}	8.98×10^{-14}	9.15×10^{-14}
Mg_4Zn_7	-102.5	58.52	-5.31×10^{-5}	8.99×10^{-14}	9.16×10^{-14}
Mg_4Zn_7	-102.1	58.54	-5.32×10^{-5}	8.99×10^{-14}	9.16×10^{-14}
Mg_4Zn_7	-101.7	58.57	-5.32×10^{-5}	8.99×10^{-14}	9.16×10^{-14}
Mg_4Zn_7	-101.3	58.59	-5.32×10^{-5}	9.00×10^{-14}	9.17×10^{-14}
Mg_4Zn_7	-100.9	58.62	-5.32×10^{-5}	9.00×10^{-14}	9.17×10^{-14}
Mg_4Zn_7	-100.5	58.64	-5.32×10^{-5}	9.01×10^{-14}	9.17×10^{-14}
Mg_4Zn_7	-100.1	58.66	-5.33×10^{-5}	9.01×10^{-14}	9.18×10^{-14}
Mg_4Zn_7	-99.7	58.69	-5.33×10^{-5}	9.01×10^{-14}	9.18×10^{-14}
Mg_4Zn_7	-99.3	58.71	-5.33×10^{-5}	9.02×10^{-14}	9.18×10^{-14}
Mg_4Zn_7	-98.9	58.73	-5.33×10^{-5}	9.02×10^{-14}	9.19×10^{-14}
Mg_4Zn_7	-98.5	58.76	-5.33×10^{-5}	9.02×10^{-14}	9.19×10^{-14}
Mg_4Zn_7	-98.1	58.78	-5.34×10^{-5}	9.02×10^{-14}	9.19×10^{-14}
Mg_4Zn_7	-97.7	58.81	-5.34×10^{-5}	9.03×10^{-14}	9.20×10^{-14}
Mg_4Zn_7	-97.3	58.83	-5.34×10^{-5}	9.03×10^{-14}	9.20×10^{-14}
Mg_4Zn_7	-96.9	58.85	-5.34×10^{-5}	9.03×10^{-14}	9.20×10^{-14}
Mg_4Zn_7	-96.5	58.88	-5.34×10^{-5}	9.04×10^{-14}	9.21×10^{-14}
Mg_4Zn_7	-96.1	58.90	-5.34×10^{-5}	9.04×10^{-14}	9.21×10^{-14}
Mg_4Zn_7	-95.7	58.93	-5.35×10^{-5}	9.04×10^{-14}	9.21×10^{-14}

Phase	Position (μm)	at.%Zn	Flux $\left(\frac{\mu m \cdot at.frac.}{sec}\right)$	Interdiffusion Coefficient (m^2/sec)	
				Boltzmann-Matano	Sauer-Freise
Mg_4Zn_7	-95.3	58.95	-5.35×10^{-5}	9.05×10^{-14}	9.22×10^{-14}
Mg_4Zn_7	-94.9	58.97	-5.35×10^{-5}	9.05×10^{-14}	9.22×10^{-14}
Mg_4Zn_7	-94.5	59.00	-5.35×10^{-5}	9.06×10^{-14}	9.22×10^{-14}
Mg_4Zn_7	-94.1	59.02	-5.35×10^{-5}	9.06×10^{-14}	9.23×10^{-14}
Mg_4Zn_7	-93.7	59.05	-5.36×10^{-5}	9.06×10^{-14}	9.23×10^{-14}
Mg_4Zn_7	-93.2	59.07	-5.36×10^{-5}	9.07×10^{-14}	9.23×10^{-14}
Mg_4Zn_7	-92.8	59.09	-5.36×10^{-5}	9.06×10^{-14}	9.24×10^{-14}
Mg_4Zn_7	-92.4	59.12	-5.36×10^{-5}	9.07×10^{-14}	9.24×10^{-14}
Mg_4Zn_7	-92.0	59.14	-5.36×10^{-5}	9.07×10^{-14}	9.24×10^{-14}
Mg_4Zn_7	-91.6	59.16	-5.37×10^{-5}	9.07×10^{-14}	9.24×10^{-14}
Mg_4Zn_7	-91.2	59.19	-5.37×10^{-5}	9.08×10^{-14}	9.25×10^{-14}
Mg_4Zn_7	-90.8	59.21	-5.37×10^{-5}	9.08×10^{-14}	9.25×10^{-14}
Mg_4Zn_7	-90.4	59.24	-5.37×10^{-5}	9.09×10^{-14}	9.26×10^{-14}
Mg_4Zn_7	-90.0	59.26	-5.37×10^{-5}	9.09×10^{-14}	9.26×10^{-14}
Mg_4Zn_7	-89.6	59.28	-5.37×10^{-5}	9.09×10^{-14}	9.26×10^{-14}
Mg_4Zn_7	-89.2	59.31	-5.38×10^{-5}	9.10×10^{-14}	9.27×10^{-14}
Mg_4Zn_7	-88.8	59.33	-5.38×10^{-5}	9.09×10^{-14}	9.27×10^{-14}
Mg_4Zn_7	-88.4	59.36	-5.38×10^{-5}	9.10×10^{-14}	9.27×10^{-14}
Mg_4Zn_7	-88.0	59.38	-5.38×10^{-5}	9.10×10^{-14}	9.27×10^{-14}
Mg_4Zn_7	-87.6	59.40	-5.38×10^{-5}	9.10×10^{-14}	9.28×10^{-14}
Mg_4Zn_7	-87.2	59.43	-5.38×10^{-5}	9.11×10^{-14}	9.28×10^{-14}
Mg_4Zn_7	-86.8	59.45	-5.39×10^{-5}	9.11×10^{-14}	9.28×10^{-14}
Mg_4Zn_7	-86.4	59.48	-5.39×10^{-5}	9.12×10^{-14}	9.29×10^{-14}
Mg_4Zn_7	-86.0	59.50	-5.39×10^{-5}	9.12×10^{-14}	9.29×10^{-14}
Mg_4Zn_7	-85.6	59.52	-5.39×10^{-5}	9.12×10^{-14}	9.29×10^{-14}
Mg_4Zn_7	-85.2	59.55	-5.39×10^{-5}	9.12×10^{-14}	9.30×10^{-14}
Mg_4Zn_7	-84.8	59.57	-5.39×10^{-5}	9.12×10^{-14}	9.30×10^{-14}
Mg_4Zn_7	-84.4	59.59	-5.40×10^{-5}	9.13×10^{-14}	9.30×10^{-14}
Mg_4Zn_7	-84.0	59.62	-5.40×10^{-5}	9.13×10^{-14}	9.30×10^{-14}
Mg_4Zn_7	-83.5	59.64	-5.40×10^{-5}	9.13×10^{-14}	9.30×10^{-14}
Mg_4Zn_7	-83.1	59.67	-5.40×10^{-5}	9.14×10^{-14}	9.31×10^{-14}
Mg_4Zn_7	-82.7	59.69	-5.40×10^{-5}	9.14×10^{-14}	9.31×10^{-14}
Mg_4Zn_7	-82.3	59.71	-5.40×10^{-5}	9.14×10^{-14}	9.32×10^{-14}
Mg_4Zn_7	-81.9	59.74	-5.41×10^{-5}	9.14×10^{-14}	9.32×10^{-14}
Mg_4Zn_7	-81.5	59.76	-5.41×10^{-5}	9.15×10^{-14}	9.32×10^{-14}

Phase	Position (μm)	at.%Zn	Flux $\left(\frac{\mu m \cdot at.frac.}{sec}\right)$	Interdiffusion Coefficient (m^2/sec)	
				Boltzmann-Matano	Sauer-Freise
Mg_4Zn_7	-81.1	59.79	-5.41×10^{-5}	9.15×10^{-14}	9.32×10^{-14}
Mg_4Zn_7	-80.7	59.81	-5.41×10^{-5}	9.15×10^{-14}	9.33×10^{-14}
Mg_4Zn_7	-80.3	59.83	-5.41×10^{-5}	9.16×10^{-14}	9.33×10^{-14}
Mg_4Zn_7	-79.9	59.86	-5.41×10^{-5}	9.16×10^{-14}	9.33×10^{-14}
Mg_4Zn_7	-79.5	59.88	-5.42×10^{-5}	9.16×10^{-14}	9.33×10^{-14}
Mg_4Zn_7	-79.1	59.91	-5.42×10^{-5}	9.17×10^{-14}	9.34×10^{-14}
Mg_4Zn_7	-78.7	59.93	-5.42×10^{-5}	9.16×10^{-14}	9.34×10^{-14}
Mg_4Zn_7	-78.3	59.95	-5.42×10^{-5}	9.17×10^{-14}	9.34×10^{-14}
Mg_4Zn_7	-77.9	59.98	-5.42×10^{-5}	9.17×10^{-14}	9.35×10^{-14}
Mg_4Zn_7	-77.5	60.00	-5.42×10^{-5}	9.17×10^{-14}	9.35×10^{-14}
Mg_4Zn_7	-77.1	60.02	-5.42×10^{-5}	9.18×10^{-14}	9.35×10^{-14}
Mg_4Zn_7	-76.7	60.05	-5.43×10^{-5}	9.18×10^{-14}	9.35×10^{-14}
Mg_4Zn_7	-76.3	60.07	-5.43×10^{-5}	9.18×10^{-14}	9.36×10^{-14}
Mg_4Zn_7	-75.9	60.10	-5.43×10^{-5}	9.18×10^{-14}	9.36×10^{-14}
Mg_4Zn_7	-75.5	60.12	-5.43×10^{-5}	9.18×10^{-14}	9.36×10^{-14}
Mg_4Zn_7	-75.1	60.14	-5.43×10^{-5}	9.19×10^{-14}	9.36×10^{-14}
Mg_4Zn_7	-74.7	60.17	-5.43×10^{-5}	9.19×10^{-14}	9.37×10^{-14}
Mg_4Zn_7	-74.3	60.19	-5.44×10^{-5}	9.20×10^{-14}	9.37×10^{-14}
Mg_4Zn_7	-73.9	60.22	-5.44×10^{-5}	9.19×10^{-14}	9.37×10^{-14}
Mg_4Zn_7	-73.4	60.24	-5.44×10^{-5}	9.20×10^{-14}	9.37×10^{-14}
Mg_4Zn_7	-73.0	60.26	-5.44×10^{-5}	9.20×10^{-14}	9.38×10^{-14}
Mg_4Zn_7	-72.6	60.29	-5.44×10^{-5}	9.20×10^{-14}	9.38×10^{-14}
Mg_4Zn_7	-72.2	60.31	-5.44×10^{-5}	9.21×10^{-14}	9.38×10^{-14}
Mg_4Zn_7	-71.8	60.34	-5.44×10^{-5}	9.21×10^{-14}	9.38×10^{-14}
Mg_4Zn_7	-71.4	60.36	-5.45×10^{-5}	9.21×10^{-14}	9.38×10^{-14}
Mg_4Zn_7	-71.0	60.38	-5.45×10^{-5}	9.22×10^{-14}	9.39×10^{-14}
Mg_4Zn_7	-70.6	60.41	-5.45×10^{-5}	9.21×10^{-14}	9.39×10^{-14}
Mg_4Zn_7	-70.2	60.43	-5.45×10^{-5}	9.22×10^{-14}	9.39×10^{-14}
Mg_4Zn_7	-69.8	60.45	-5.45×10^{-5}	9.22×10^{-14}	9.40×10^{-14}
Mg_4Zn_7	-69.4	60.48	-5.45×10^{-5}	9.22×10^{-14}	9.40×10^{-14}
Mg_4Zn_7	-69.0	60.50	-5.45×10^{-5}	9.23×10^{-14}	9.40×10^{-14}
$MgZn_2$	-64.2	63.28	-5.61×10^{-5}	1.13×10^{-12}	1.13×10^{-12}
$MgZn_2$	-61.8	63.29	-5.61×10^{-5}	1.13×10^{-12}	1.13×10^{-12}
$MgZn_2$	-59.3	63.31	-5.61×10^{-5}	1.13×10^{-12}	1.13×10^{-12}
$MgZn_2$	-56.9	63.32	-5.61×10^{-5}	1.13×10^{-12}	1.13×10^{-12}

Phase	Position (μm)	at.%Zn	Flux $\left(\frac{\mu m \cdot at.frac.}{sec}\right)$	Interdiffusion Coefficient (m^2/sec)	
				Boltzmann-Matano	Sauer-Freise
$MgZn_2$	-54.5	63.33	-5.61×10^{-5}	1.13×10^{-12}	1.13×10^{-12}
$MgZn_2$	-52.1	63.34	-5.61×10^{-5}	1.13×10^{-12}	1.13×10^{-12}
$MgZn_2$	-49.6	63.35	-5.61×10^{-5}	1.13×10^{-12}	1.13×10^{-12}
$MgZn_2$	-47.2	63.37	-5.61×10^{-5}	1.13×10^{-12}	1.13×10^{-12}
$MgZn_2$	-44.8	63.38	-5.61×10^{-5}	1.13×10^{-12}	1.13×10^{-12}
$MgZn_2$	-42.4	63.39	-5.61×10^{-5}	1.13×10^{-12}	1.13×10^{-12}
$MgZn_2$	-39.9	63.40	-5.61×10^{-5}	1.13×10^{-12}	1.13×10^{-12}
$MgZn_2$	-37.5	63.41	-5.61×10^{-5}	1.13×10^{-12}	1.13×10^{-12}
$MgZn_2$	-35.1	63.43	-5.61×10^{-5}	1.13×10^{-12}	1.13×10^{-12}
$MgZn_2$	-32.7	63.44	-5.61×10^{-5}	1.13×10^{-12}	1.13×10^{-12}
$MgZn_2$	-30.2	63.45	-5.61×10^{-5}	1.13×10^{-12}	1.13×10^{-12}
$MgZn_2$	-27.8	63.46	-5.61×10^{-5}	1.13×10^{-12}	1.13×10^{-12}
$MgZn_2$	-25.4	63.47	-5.61×10^{-5}	1.13×10^{-12}	1.13×10^{-12}
$MgZn_2$	-23.0	63.49	-5.61×10^{-5}	1.13×10^{-12}	1.13×10^{-12}
$MgZn_2$	-20.5	63.50	-5.62×10^{-5}	1.13×10^{-12}	1.13×10^{-12}
$MgZn_2$	-18.1	63.51	-5.62×10^{-5}	1.13×10^{-12}	1.13×10^{-12}
$MgZn_2$	-15.7	63.52	-5.62×10^{-5}	1.13×10^{-12}	1.13×10^{-12}
$MgZn_2$	-13.3	63.53	-5.62×10^{-5}	1.13×10^{-12}	1.13×10^{-12}
$MgZn_2$	-10.8	63.55	-5.62×10^{-5}	1.13×10^{-12}	1.13×10^{-12}
$MgZn_2$	-8.4	63.56	-5.62×10^{-5}	1.13×10^{-12}	1.13×10^{-12}
$MgZn_2$	-6.0	63.57	-5.62×10^{-5}	1.13×10^{-12}	1.13×10^{-12}
$MgZn_2$	-3.6	63.58	-5.62×10^{-5}	1.13×10^{-12}	1.13×10^{-12}
$MgZn_2$	-1.1	63.59	-5.62×10^{-5}	1.13×10^{-12}	1.13×10^{-12}
$MgZn_2$	1.3	63.61	-5.62×10^{-5}	1.13×10^{-12}	1.13×10^{-12}
$MgZn_2$	3.7	63.62	-5.62×10^{-5}	1.13×10^{-12}	1.13×10^{-12}
$MgZn_2$	6.1	63.63	-5.62×10^{-5}	1.13×10^{-12}	1.13×10^{-12}
$MgZn_2$	8.6	63.64	-5.62×10^{-5}	1.13×10^{-12}	1.13×10^{-12}
$MgZn_2$	11.0	63.65	-5.62×10^{-5}	1.13×10^{-12}	1.13×10^{-12}
$MgZn_2$	13.4	63.67	-5.62×10^{-5}	1.13×10^{-12}	1.13×10^{-12}
$MgZn_2$	15.8	63.68	-5.62×10^{-5}	1.13×10^{-12}	1.13×10^{-12}
$MgZn_2$	18.2	63.69	-5.61×10^{-5}	1.13×10^{-12}	1.13×10^{-12}
$MgZn_2$	20.7	63.70	-5.61×10^{-5}	1.13×10^{-12}	1.13×10^{-12}
$MgZn_2$	23.1	63.71	-5.61×10^{-5}	1.13×10^{-12}	1.13×10^{-12}
$MgZn_2$	25.5	63.73	-5.61×10^{-5}	1.13×10^{-12}	1.13×10^{-12}
$MgZn_2$	27.9	63.74	-5.61×10^{-5}	1.13×10^{-12}	1.13×10^{-12}

Phase	Position (μm)	at.%Zn	Flux $\left(\frac{\mu m \cdot at.frac.}{sec}\right)$	Interdiffusion Coefficient (m^2/sec)	
				Boltzmann-Matano	Sauer-Freise
$MgZn_2$	30.4	63.75	-5.61×10^{-5}	1.13×10^{-12}	1.13×10^{-12}
$MgZn_2$	32.8	63.76	-5.61×10^{-5}	1.13×10^{-12}	1.13×10^{-12}
$MgZn_2$	35.2	63.77	-5.61×10^{-5}	1.13×10^{-12}	1.13×10^{-12}
$MgZn_2$	37.6	63.79	-5.61×10^{-5}	1.13×10^{-12}	1.13×10^{-12}
$MgZn_2$	40.1	63.80	-5.61×10^{-5}	1.13×10^{-12}	1.13×10^{-12}
$MgZn_2$	42.5	63.81	-5.61×10^{-5}	1.13×10^{-12}	1.13×10^{-12}
$MgZn_2$	44.9	63.82	-5.61×10^{-5}	1.13×10^{-12}	1.13×10^{-12}
$MgZn_2$	47.3	63.83	-5.61×10^{-5}	1.13×10^{-12}	1.13×10^{-12}
$MgZn_2$	49.8	63.85	-5.61×10^{-5}	1.13×10^{-12}	1.13×10^{-12}
$MgZn_2$	52.2	63.86	-5.61×10^{-5}	1.13×10^{-12}	1.13×10^{-12}
$MgZn_2$	54.6	63.87	-5.61×10^{-5}	1.13×10^{-12}	1.13×10^{-12}
$MgZn_2$	57.0	63.88	-5.61×10^{-5}	1.13×10^{-12}	1.13×10^{-12}
$MgZn_2$	59.5	63.90	-5.61×10^{-5}	1.13×10^{-12}	1.13×10^{-12}
$MgZn_2$	61.9	63.91	-5.61×10^{-5}	1.13×10^{-12}	1.13×10^{-12}
$MgZn_2$	64.3	63.92	-5.61×10^{-5}	1.13×10^{-12}	1.13×10^{-12}
$MgZn_2$	66.7	63.93	-5.61×10^{-5}	1.13×10^{-12}	1.13×10^{-12}
$MgZn_2$	69.2	63.94	-5.61×10^{-5}	1.13×10^{-12}	1.13×10^{-12}
$MgZn_2$	71.6	63.96	-5.60×10^{-5}	1.13×10^{-12}	1.13×10^{-12}
$MgZn_2$	74.0	63.97	-5.60×10^{-5}	1.13×10^{-12}	1.13×10^{-12}
$MgZn_2$	76.4	63.98	-5.60×10^{-5}	1.13×10^{-12}	1.13×10^{-12}
$MgZn_2$	78.9	63.99	-5.60×10^{-5}	1.13×10^{-12}	1.13×10^{-12}
$MgZn_2$	81.3	64.00	-5.60×10^{-5}	1.13×10^{-12}	1.13×10^{-12}
$MgZn_2$	83.7	64.02	-5.60×10^{-5}	1.13×10^{-12}	1.13×10^{-12}
$MgZn_2$	86.1	64.03	-5.60×10^{-5}	1.13×10^{-12}	1.13×10^{-12}
$MgZn_2$	88.6	64.04	-5.60×10^{-5}	1.13×10^{-12}	1.13×10^{-12}
$MgZn_2$	91.0	64.05	-5.60×10^{-5}	1.13×10^{-12}	1.13×10^{-12}
$MgZn_2$	93.4	64.06	-5.60×10^{-5}	1.13×10^{-12}	1.13×10^{-12}
$MgZn_2$	95.8	64.08	-5.60×10^{-5}	1.13×10^{-12}	1.13×10^{-12}
$MgZn_2$	98.2	64.09	-5.59×10^{-5}	1.13×10^{-12}	1.13×10^{-12}
$MgZn_2$	100.7	64.10	-5.59×10^{-5}	1.13×10^{-12}	1.13×10^{-12}
$MgZn_2$	103.1	64.11	-5.59×10^{-5}	1.13×10^{-12}	1.13×10^{-12}
$MgZn_2$	105.5	64.12	-5.59×10^{-5}	1.12×10^{-12}	1.13×10^{-12}
$MgZn_2$	107.9	64.14	-5.59×10^{-5}	1.13×10^{-12}	1.13×10^{-12}
$MgZn_2$	110.4	64.15	-5.59×10^{-5}	1.12×10^{-12}	1.13×10^{-12}
$MgZn_2$	112.8	64.16	-5.59×10^{-5}	1.13×10^{-12}	1.13×10^{-12}

Phase	Position (μm)	at.%Zn	Flux $\left(\frac{\mu m \cdot at.frac.}{sec}\right)$	Interdiffusion Coefficient (m^2/sec)	
				Boltzmann-Matano	Sauer-Freise
$MgZn_2$	115.2	64.17	-5.59×10^{-5}	1.12×10^{-12}	1.13×10^{-12}
$MgZn_2$	117.6	64.18	-5.59×10^{-5}	1.12×10^{-12}	1.13×10^{-12}
$MgZn_2$	120.1	64.20	-5.58×10^{-5}	1.12×10^{-12}	1.13×10^{-12}
$MgZn_2$	122.5	64.21	-5.58×10^{-5}	1.12×10^{-12}	1.13×10^{-12}
$MgZn_2$	124.9	64.22	-5.58×10^{-5}	1.12×10^{-12}	1.13×10^{-12}
$MgZn_2$	127.3	64.23	-5.58×10^{-5}	1.12×10^{-12}	1.13×10^{-12}
$MgZn_2$	129.8	64.24	-5.58×10^{-5}	1.12×10^{-12}	1.13×10^{-12}
$MgZn_2$	132.2	64.26	-5.58×10^{-5}	1.12×10^{-12}	1.13×10^{-12}
$MgZn_2$	134.6	64.27	-5.58×10^{-5}	1.12×10^{-12}	1.13×10^{-12}
$MgZn_2$	137.0	64.28	-5.58×10^{-5}	1.12×10^{-12}	1.13×10^{-12}
$MgZn_2$	139.5	64.29	-5.57×10^{-5}	1.12×10^{-12}	1.13×10^{-12}
$MgZn_2$	141.9	64.30	-5.57×10^{-5}	1.12×10^{-12}	1.13×10^{-12}
$MgZn_2$	144.3	64.32	-5.57×10^{-5}	1.12×10^{-12}	1.13×10^{-12}
$MgZn_2$	146.7	64.33	-5.57×10^{-5}	1.12×10^{-12}	1.12×10^{-12}
$MgZn_2$	149.2	64.34	-5.57×10^{-5}	1.12×10^{-12}	1.12×10^{-12}
$MgZn_2$	151.6	64.35	-5.57×10^{-5}	1.12×10^{-12}	1.12×10^{-12}
$MgZn_2$	154.0	64.36	-5.57×10^{-5}	1.12×10^{-12}	1.12×10^{-12}
$MgZn_2$	156.4	64.38	-5.56×10^{-5}	1.12×10^{-12}	1.12×10^{-12}
$MgZn_2$	158.9	64.39	-5.56×10^{-5}	1.12×10^{-12}	1.12×10^{-12}
$MgZn_2$	161.3	64.40	-5.56×10^{-5}	1.12×10^{-12}	1.12×10^{-12}
$MgZn_2$	163.7	64.41	-5.56×10^{-5}	1.12×10^{-12}	1.12×10^{-12}
$MgZn_2$	166.1	64.43	-5.56×10^{-5}	1.12×10^{-12}	1.12×10^{-12}
$MgZn_2$	168.6	64.44	-5.56×10^{-5}	1.12×10^{-12}	1.12×10^{-12}
$MgZn_2$	171.0	64.45	-5.55×10^{-5}	1.12×10^{-12}	1.12×10^{-12}
Mg_2Zn_{11}	175.7	82.29	-2.98×10^{-5}	5.94×10^{-14}	5.45×10^{-14}
Mg_2Zn_{11}	176.1	82.31	-2.98×10^{-5}	5.93×10^{-14}	5.45×10^{-14}
Mg_2Zn_{11}	176.4	82.33	-2.98×10^{-5}	5.93×10^{-14}	5.44×10^{-14}
Mg_2Zn_{11}	176.7	82.34	-2.97×10^{-5}	5.92×10^{-14}	5.44×10^{-14}
Mg_2Zn_{11}	177.1	82.36	-2.97×10^{-5}	5.92×10^{-14}	5.44×10^{-14}
Mg_2Zn_{11}	177.4	82.38	-2.97×10^{-5}	5.91×10^{-14}	5.43×10^{-14}
Mg_2Zn_{11}	177.7	82.39	-2.97×10^{-5}	5.91×10^{-14}	5.43×10^{-14}
Mg_2Zn_{11}	178.1	82.41	-2.96×10^{-5}	5.90×10^{-14}	5.43×10^{-14}
Mg_2Zn_{11}	178.4	82.43	-2.96×10^{-5}	5.90×10^{-14}	5.42×10^{-14}
Mg_2Zn_{11}	178.7	82.44	-2.96×10^{-5}	5.89×10^{-14}	5.42×10^{-14}
Mg_2Zn_{11}	179.1	82.46	-2.96×10^{-5}	5.89×10^{-14}	5.42×10^{-14}

Phase	Position (μm)	at.%Zn	Flux $\left(\frac{\mu m \cdot at.frac.}{sec}\right)$	Interdiffusion Coefficient (m^2/sec)	
				Boltzmann-Matano	Sauer-Freise
Mg_2Zn_{11}	179.4	82.48	-2.95×10^{-5}	5.88×10^{-14}	5.41×10^{-14}
Mg_2Zn_{11}	179.7	82.49	-2.95×10^{-5}	5.88×10^{-14}	5.41×10^{-14}
Mg_2Zn_{11}	180.1	82.51	-2.95×10^{-5}	5.87×10^{-14}	5.41×10^{-14}
Mg_2Zn_{11}	180.4	82.53	-2.95×10^{-5}	5.87×10^{-14}	5.40×10^{-14}
Mg_2Zn_{11}	180.7	82.54	-2.94×10^{-5}	5.86×10^{-14}	5.40×10^{-14}
Mg_2Zn_{11}	181.1	82.56	-2.94×10^{-5}	5.86×10^{-14}	5.39×10^{-14}
Mg_2Zn_{11}	181.4	82.58	-2.94×10^{-5}	5.85×10^{-14}	5.39×10^{-14}
Mg_2Zn_{11}	181.7	82.59	-2.94×10^{-5}	5.85×10^{-14}	5.39×10^{-14}
Mg_2Zn_{11}	182.1	82.61	-2.93×10^{-5}	5.84×10^{-14}	5.38×10^{-14}
Mg_2Zn_{11}	182.4	82.63	-2.93×10^{-5}	5.84×10^{-14}	5.38×10^{-14}
Mg_2Zn_{11}	182.7	82.65	-2.93×10^{-5}	5.83×10^{-14}	5.38×10^{-14}
Mg_2Zn_{11}	183.1	82.66	-2.93×10^{-5}	5.83×10^{-14}	5.37×10^{-14}
Mg_2Zn_{11}	183.4	82.68	-2.92×10^{-5}	5.82×10^{-14}	5.37×10^{-14}
Mg_2Zn_{11}	183.7	82.70	-2.92×10^{-5}	5.82×10^{-14}	5.36×10^{-14}
Mg_2Zn_{11}	184.1	82.71	-2.92×10^{-5}	5.81×10^{-14}	5.36×10^{-14}
Mg_2Zn_{11}	184.4	82.73	-2.92×10^{-5}	5.81×10^{-14}	5.36×10^{-14}
Mg_2Zn_{11}	184.7	82.75	-2.91×10^{-5}	5.80×10^{-14}	5.35×10^{-14}
Mg_2Zn_{11}	185.1	82.76	-2.91×10^{-5}	5.80×10^{-14}	5.35×10^{-14}
Mg_2Zn_{11}	185.4	82.78	-2.91×10^{-5}	5.79×10^{-14}	5.35×10^{-14}
Mg_2Zn_{11}	185.7	82.80	-2.91×10^{-5}	5.79×10^{-14}	5.34×10^{-14}
Mg_2Zn_{11}	186.1	82.81	-2.90×10^{-5}	5.78×10^{-14}	5.34×10^{-14}
Mg_2Zn_{11}	186.4	82.83	-2.90×10^{-5}	5.78×10^{-14}	5.33×10^{-14}
Mg_2Zn_{11}	186.7	82.85	-2.90×10^{-5}	5.77×10^{-14}	5.33×10^{-14}
Mg_2Zn_{11}	187.1	82.86	-2.90×10^{-5}	5.77×10^{-14}	5.33×10^{-14}
Mg_2Zn_{11}	187.4	82.88	-2.89×10^{-5}	5.76×10^{-14}	5.32×10^{-14}
Mg_2Zn_{11}	187.7	82.90	-2.89×10^{-5}	5.76×10^{-14}	5.32×10^{-14}
Mg_2Zn_{11}	188.1	82.91	-2.89×10^{-5}	5.75×10^{-14}	5.32×10^{-14}
Mg_2Zn_{11}	188.4	82.93	-2.88×10^{-5}	5.75×10^{-14}	5.31×10^{-14}
Mg_2Zn_{11}	188.7	82.95	-2.88×10^{-5}	5.74×10^{-14}	5.31×10^{-14}
Mg_2Zn_{11}	189.1	82.96	-2.88×10^{-5}	5.74×10^{-14}	5.30×10^{-14}
Mg_2Zn_{11}	189.4	82.98	-2.88×10^{-5}	5.73×10^{-14}	5.30×10^{-14}
Mg_2Zn_{11}	189.7	83.00	-2.87×10^{-5}	5.73×10^{-14}	5.29×10^{-14}
Mg_2Zn_{11}	190.1	83.01	-2.87×10^{-5}	5.72×10^{-14}	5.29×10^{-14}
Mg_2Zn_{11}	190.4	83.03	-2.87×10^{-5}	5.72×10^{-14}	5.29×10^{-14}
Mg_2Zn_{11}	190.7	83.05	-2.87×10^{-5}	5.71×10^{-14}	5.28×10^{-14}

Phase	Position (μm)	at.%Zn	Flux $\left(\frac{\mu m \cdot at.frac.}{sec}\right)$	Interdiffusion Coefficient (m^2/sec)	
				Boltzmann-Matano	Sauer-Freise
Mg_2Zn_{11}	191.1	83.06	-2.86×10^{-5}	5.71×10^{-14}	5.28×10^{-14}
Mg_2Zn_{11}	191.4	83.08	-2.86×10^{-5}	5.70×10^{-14}	5.28×10^{-14}
Mg_2Zn_{11}	191.7	83.10	-2.86×10^{-5}	5.70×10^{-14}	5.27×10^{-14}
Mg_2Zn_{11}	192.1	83.11	-2.86×10^{-5}	5.69×10^{-14}	5.27×10^{-14}
Mg_2Zn_{11}	192.4	83.13	-2.85×10^{-5}	5.68×10^{-14}	5.26×10^{-14}
Mg_2Zn_{11}	192.7	83.15	-2.85×10^{-5}	5.68×10^{-14}	5.26×10^{-14}
Mg_2Zn_{11}	193.1	83.16	-2.85×10^{-5}	5.67×10^{-14}	5.26×10^{-14}
Mg_2Zn_{11}	193.4	83.18	-2.84×10^{-5}	5.67×10^{-14}	5.25×10^{-14}
Mg_2Zn_{11}	193.7	83.20	-2.84×10^{-5}	5.66×10^{-14}	5.25×10^{-14}
Mg_2Zn_{11}	194.1	83.21	-2.84×10^{-5}	5.66×10^{-14}	5.24×10^{-14}
Mg_2Zn_{11}	194.4	83.23	-2.84×10^{-5}	5.65×10^{-14}	5.24×10^{-14}
Mg_2Zn_{11}	194.7	83.25	-2.83×10^{-5}	5.65×10^{-14}	5.24×10^{-14}
Mg_2Zn_{11}	195.1	83.26	-2.83×10^{-5}	5.64×10^{-14}	5.23×10^{-14}
Mg_2Zn_{11}	195.4	83.28	-2.83×10^{-5}	5.63×10^{-14}	5.23×10^{-14}
Mg_2Zn_{11}	195.7	83.30	-2.83×10^{-5}	5.63×10^{-14}	5.22×10^{-14}
Mg_2Zn_{11}	196.1	83.31	-2.82×10^{-5}	5.63×10^{-14}	5.22×10^{-14}
Mg_2Zn_{11}	196.4	83.33	-2.82×10^{-5}	5.62×10^{-14}	5.22×10^{-14}
Mg_2Zn_{11}	196.7	83.35	-2.82×10^{-5}	5.61×10^{-14}	5.21×10^{-14}
Mg_2Zn_{11}	197.1	83.36	-2.82×10^{-5}	5.61×10^{-14}	5.21×10^{-14}
Mg_2Zn_{11}	197.4	83.38	-2.81×10^{-5}	5.60×10^{-14}	5.20×10^{-14}
Mg_2Zn_{11}	197.7	83.40	-2.81×10^{-5}	5.60×10^{-14}	5.20×10^{-14}
Mg_2Zn_{11}	198.1	83.41	-2.81×10^{-5}	5.59×10^{-14}	5.19×10^{-14}
Mg_2Zn_{11}	198.4	83.43	-2.80×10^{-5}	5.58×10^{-14}	5.19×10^{-14}
Mg_2Zn_{11}	198.7	83.45	-2.80×10^{-5}	5.58×10^{-14}	5.18×10^{-14}
Mg_2Zn_{11}	199.1	83.46	-2.80×10^{-5}	5.58×10^{-14}	5.18×10^{-14}
Mg_2Zn_{11}	199.4	83.48	-2.80×10^{-5}	5.57×10^{-14}	5.18×10^{-14}
Mg_2Zn_{11}	199.7	83.50	-2.79×10^{-5}	5.57×10^{-14}	5.17×10^{-14}
Mg_2Zn_{11}	200.1	83.52	-2.79×10^{-5}	5.56×10^{-14}	5.17×10^{-14}
Mg_2Zn_{11}	200.4	83.53	-2.79×10^{-5}	5.55×10^{-14}	5.16×10^{-14}
Mg_2Zn_{11}	200.7	83.55	-2.78×10^{-5}	5.55×10^{-14}	5.16×10^{-14}
Mg_2Zn_{11}	201.1	83.57	-2.78×10^{-5}	5.54×10^{-14}	5.16×10^{-14}
Mg_2Zn_{11}	201.4	83.58	-2.78×10^{-5}	5.53×10^{-14}	5.15×10^{-14}
Mg_2Zn_{11}	201.7	83.60	-2.78×10^{-5}	5.53×10^{-14}	5.15×10^{-14}
Mg_2Zn_{11}	202.1	83.62	-2.77×10^{-5}	5.53×10^{-14}	5.14×10^{-14}
Mg_2Zn_{11}	202.4	83.63	-2.77×10^{-5}	5.52×10^{-14}	5.14×10^{-14}

Phase	Position (μm)	at.%Zn	Flux $\left(\frac{\mu m \cdot at.frac.}{sec}\right)$	Interdiffusion Coefficient (m^2/sec)	
				Boltzmann-Matano	Sauer-Freise
Mg_2Zn_{11}	202.7	83.65	-2.77×10^{-5}	5.52×10^{-14}	5.13×10^{-14}
Mg_2Zn_{11}	203.1	83.67	-2.77×10^{-5}	5.51×10^{-14}	5.13×10^{-14}
Mg_2Zn_{11}	203.4	83.68	-2.76×10^{-5}	5.50×10^{-14}	5.13×10^{-14}
Mg_2Zn_{11}	203.7	83.70	-2.76×10^{-5}	5.50×10^{-14}	5.12×10^{-14}
Mg_2Zn_{11}	204.1	83.72	-2.76×10^{-5}	5.49×10^{-14}	5.12×10^{-14}
Mg_2Zn_{11}	204.4	83.73	-2.75×10^{-5}	5.48×10^{-14}	5.11×10^{-14}
Mg_2Zn_{11}	204.7	83.75	-2.75×10^{-5}	5.48×10^{-14}	5.11×10^{-14}
Mg_2Zn_{11}	205.1	83.77	-2.75×10^{-5}	5.48×10^{-14}	5.10×10^{-14}
Mg_2Zn_{11}	205.4	83.78	-2.75×10^{-5}	5.47×10^{-14}	5.10×10^{-14}
Mg_2Zn_{11}	205.7	83.80	-2.74×10^{-5}	5.46×10^{-14}	5.10×10^{-14}
Mg_2Zn_{11}	206.1	83.82	-2.74×10^{-5}	5.46×10^{-14}	5.09×10^{-14}
Mg_2Zn_{11}	206.4	83.83	-2.74×10^{-5}	5.45×10^{-14}	5.09×10^{-14}
Mg_2Zn_{11}	206.7	83.85	-2.73×10^{-5}	5.45×10^{-14}	5.08×10^{-14}
Mg_2Zn_{11}	207.1	83.87	-2.73×10^{-5}	5.44×10^{-14}	5.08×10^{-14}
Mg_2Zn_{11}	207.4	83.88	-2.73×10^{-5}	5.43×10^{-14}	5.07×10^{-14}
Mg_2Zn_{11}	207.7	83.90	-2.73×10^{-5}	5.43×10^{-14}	5.07×10^{-14}
Mg_2Zn_{11}	208.1	83.92	-2.72×10^{-5}	5.42×10^{-14}	5.06×10^{-14}

Table 51: Reduced modulus and hardness of Mg solid solution as a function of composition obtained from 450°C diffusion anneal of Mg vs. Mg-3at.%Zn after 24 hours; Peak Load 5mN

Phase	at.%Zn	Reduced Modulus (GPa)		Hardness (GPa)	
		Avg.	Std. Dev.	Avg.	Std. Dev.
Mg(Zn)	0.00	35.00	1.70	0.50	0.00
Mg(Zn)	0.00	36.38	1.20	0.53	0.05
Mg(Zn)	0.00	35.60	1.57	0.50	0.06
Mg(Zn)	0.00	36.86	1.06	0.48	0.03
Mg(Zn)	0.00	39.37	2.87	0.53	0.06
Mg(Zn)	0.00	37.88	1.14	0.54	0.04
Mg(Zn)	0.00	36.81	1.24	0.53	0.00
Mg(Zn)	0.00	36.59	0.30	0.51	0.03
Mg(Zn)	0.00	37.77	1.24	0.52	0.02
Mg(Zn)	0.00	37.96	1.49	0.54	0.04
Mg(Zn)	0.00	38.08	2.34	0.52	0.06
Mg(Zn)	0.00	37.65	1.69	0.58	0.01
Mg(Zn)	0.00	40.63	1.06	0.60	0.03
Mg(Zn)	0.01	38.40	1.36	0.54	0.02
Mg(Zn)	0.01	38.33	1.30	0.52	0.02
Mg(Zn)	0.01	38.82	0.61	0.53	0.04
Mg(Zn)	0.01	37.50	0.60	0.55	0.04
Mg(Zn)	0.02	38.25	1.05	0.52	0.02
Mg(Zn)	0.02	36.85	1.24	0.52	0.03
Mg(Zn)	0.02	39.23	3.69	0.55	0.11
Mg(Zn)	0.03	41.47	0.58	0.59	0.01
Mg(Zn)	0.03	42.27	2.57	0.61	0.08
Mg(Zn)	0.04	41.42	1.53	0.55	0.01
Mg(Zn)	0.05	43.35	3.94	0.65	0.11
Mg(Zn)	0.06	45.58	2.12	0.72	0.05
Mg(Zn)	0.07	45.10	1.45	0.70	0.05
Mg(Zn)	0.08	43.03	0.38	0.64	0.03
Mg(Zn)	0.10	43.29	1.51	0.63	0.03
Mg(Zn)	0.12	41.61	1.03	0.64	0.01
Mg(Zn)	0.14	38.84	0.85	0.63	0.00
Mg(Zn)	0.17	38.98	1.39	0.61	0.01
Mg(Zn)	0.20	40.55	2.70	0.66	0.04
Mg(Zn)	0.24	40.67	0.45	0.65	0.02
Mg(Zn)	0.28	41.88	3.58	0.65	0.04

Phase	at.%Zn	Reduced Modulus (GPa)		Hardness (GPa)	
		Avg.	Std. Dev.	Avg.	Std. Dev.
Mg(Zn)	0.33	40.28	0.79	0.62	0.00
Mg(Zn)	0.38	42.08	0.65	0.68	0.01
Mg(Zn)	0.43	42.02	1.16	0.71	0.01
Mg(Zn)	0.49	40.61	0.82	0.68	0.02
Mg(Zn)	0.56	42.55	2.17	0.69	0.06
Mg(Zn)	0.62	42.47	0.52	0.71	0.02
Mg(Zn)	0.69	44.13	1.60	0.76	0.05
Mg(Zn)	0.77	45.24	1.43	0.81	0.04
Mg(Zn)	0.85	43.77	2.33	0.76	0.03
Mg(Zn)	0.93	44.44	1.64	0.80	0.07
Mg(Zn)	1.01	45.33	3.84	0.87	0.09
Mg(Zn)	1.09	45.08	0.94	0.82	0.02
Mg(Zn)	1.17	45.64	1.69	0.85	0.04
Mg(Zn)	1.24	46.11	0.39	0.84	0.02
Mg(Zn)	1.31	44.35	1.44	0.85	0.01
Mg(Zn)	1.37	44.70	0.73	0.88	0.03
Mg(Zn)	1.43	44.28	0.57	0.84	0.02
Mg(Zn)	1.48	48.25	1.80	0.91	0.05
Mg(Zn)	1.53	47.45	0.15	0.89	0.07
Mg(Zn)	1.58	48.64	0.45	0.87	0.06
Mg(Zn)	1.62	48.43	2.89	0.96	0.06
Mg(Zn)	1.66	48.26	1.43	0.96	0.10
Mg(Zn)	1.71	50.21	0.61	0.98	0.04
Mg(Zn)	1.75	49.39	0.27	0.98	0.06
Mg(Zn)	1.78	50.40	0.31	1.01	0.04
Mg(Zn)	1.82	48.03	1.44	1.01	0.07
Mg(Zn)	1.86	49.37	0.66	1.07	0.03
Mg(Zn)	1.89	50.84	3.54	1.13	0.20
Mg(Zn)	1.92	49.17	1.41	1.06	0.08
Mg(Zn)	1.95	49.43	1.99	1.09	0.09
Mg(Zn)	1.98	52.43	0.25	1.17	0.01
Mg(Zn)	2.01	52.36	0.51	1.09	0.03
Mg(Zn)	2.04	52.07	0.94	1.15	0.06
Mg(Zn)	2.06	51.15	1.40	1.09	0.08
Mg(Zn)	2.09	51.89	2.05	1.15	0.10
Mg(Zn)	2.11	51.18	0.79	1.06	0.08

Phase	at.%Zn	Reduced Modulus (GPa)		Hardness (GPa)	
		Avg.	Std. Dev.	Avg.	Std. Dev.
Mg(Zn)	2.13	52.36	1.32	1.12	0.13
Mg(Zn)	2.15	53.14	1.10	1.06	0.08
Mg(Zn)	2.17	52.48	1.35	1.12	0.06
Mg(Zn)	2.18	52.96	1.01	1.19	0.15
Mg(Zn)	2.20	53.42	0.68	1.13	0.07
Mg(Zn)	2.21	53.54	0.74	1.20	0.13
Mg(Zn)	2.22	52.85	0.59	1.14	0.04
Mg(Zn)	2.23	51.79	2.15	1.29	0.09
Mg(Zn)	2.24	52.46	0.72	1.21	0.02
Mg(Zn)	2.25	52.36	0.48	1.15	0.06
Mg(Zn)	2.26	50.33	1.68	1.19	0.01
Mg(Zn)	2.27	52.29	0.85	1.14	0.06
Mg(Zn)	2.27	51.95	0.86	1.10	0.02
Mg(Zn)	2.28	52.91	0.31	1.14	0.05
Mg(Zn)	2.28	53.29	1.55	1.22	0.08
Mg(Zn)	2.29	53.09	0.45	1.20	0.02
Mg(Zn)	2.29	53.70	1.31	1.19	0.04
Mg(Zn)	2.29	52.24	0.18	1.14	0.04
Mg(Zn)	2.29	53.19	0.65	1.17	0.02
Mg(Zn)	2.29	54.07	0.71	1.18	0.02
Mg(Zn)	2.29	52.90	2.25	1.15	0.08
Mg(Zn)	2.29	52.50	0.99	1.13	0.01
Mg(Zn)	2.29	54.61	6.38	1.31	0.32
Mg(Zn)	2.29	55.46	2.95	1.29	0.22
Mg(Zn)	2.29	52.98	1.36	1.16	0.04
Mg(Zn)	2.29	51.08	2.51	1.18	0.03
Mg(Zn)	2.29	52.27	1.39	1.14	0.06
Mg(Zn)	2.29	52.63	0.97	1.17	0.02
Mg(Zn)	2.29	53.18	2.16	1.38	0.14
Mg(Zn)	2.29	52.80	0.48	1.22	0.04
Mg(Zn)	2.29	53.19	0.12	1.24	0.01

Table 52: Reduced modulus and hardness of intermetallic compounds formed during 315°C diffusion anneal of Mg vs. Zn after 168 hours; Peak Load 7mN

Phase	at.%Zn	Reduced Modulus (GPa)		Hardness (GPa)	
		Avg.	Std. Dev.	Avg.	Std. Dev.
Mg_4Zn_7	58.2	78.91	3.41	4.91	0.30
Mg_4Zn_7	58.5	84.19	2.09	5.17	0.35
Mg_4Zn_7	58.8	81.87	1.95	4.83	0.25
Mg_4Zn_7	59.2	84.26	2.07	5.12	0.23
Mg_4Zn_7	59.5	87.19	4.68	5.58	0.60
Mg_4Zn_7	59.9	84.27	0.73	5.34	0.24
Mg_4Zn_7	60.2	85.55	0.47	5.38	0.23
Mg_4Zn_7	60.5	86.50	4.18	5.51	0.63
$MgZn_2$	63.3	78.95	3.52	4.03	0.37
$MgZn_2$	63.3	77.17	1.23	3.86	0.24
$MgZn_2$	63.3	77.98	3.85	3.86	0.74
$MgZn_2$	63.3	80.88	6.85	4.04	0.98
$MgZn_2$	63.4	81.45	3.71	4.67	0.54
$MgZn_2$	63.4	81.01	0.73	4.61	0.17
$MgZn_2$	63.4	83.91	0.39	4.82	0.08
$MgZn_2$	63.5	83.47	1.47	4.93	0.24
$MgZn_2$	63.5	84.24	3.42	4.90	0.41
$MgZn_2$	63.5	84.31	2.41	4.83	0.19
$MgZn_2$	63.5	83.50	0.60	4.68	0.18
$MgZn_2$	63.6	83.71	2.10	4.78	0.23
$MgZn_2$	63.6	84.38	0.17	4.91	0.11
$MgZn_2$	63.6	86.44	0.86	5.10	0.21
$MgZn_2$	63.6	84.56	2.38	4.91	0.19
$MgZn_2$	63.7	84.99	2.22	4.91	0.13
$MgZn_2$	63.7	85.79	3.66	5.10	0.33
$MgZn_2$	63.7	84.19	1.79	4.85	0.23
$MgZn_2$	63.7	84.23	0.97	4.87	0.20
$MgZn_2$	63.8	85.13	2.33	5.05	0.10
$MgZn_2$	63.8	85.34	0.53	5.04	0.25
$MgZn_2$	63.8	83.80	1.02	4.79	0.12
$MgZn_2$	63.8	86.47	1.72	5.13	0.08
$MgZn_2$	63.9	85.12	1.94	4.94	0.25
$MgZn_2$	63.9	85.09	1.25	4.93	0.09

Phase	at.%Zn	Reduced Modulus (GPa)		Hardness (GPa)	
		Avg.	Std. Dev.	Avg.	Std. Dev.
$MgZn_2$	63.9	84.73	3.93	4.83	0.35
$MgZn_2$	63.9	84.71	2.36	4.85	0.16
$MgZn_2$	64.0	85.45	1.24	5.04	0.04
$MgZn_2$	64.0	85.08	2.24	4.93	0.20
$MgZn_2$	64.0	85.96	2.23	5.04	0.21
$MgZn_2$	64.0	86.42	1.00	4.99	0.07
$MgZn_2$	64.1	86.10	1.92	4.96	0.18
$MgZn_2$	64.1	85.28	1.89	4.88	0.08
$MgZn_2$	64.1	86.96	2.94	5.00	0.23
$MgZn_2$	64.1	86.21	1.75	5.14	0.02
$MgZn_2$	64.2	85.88	1.22	5.05	0.16
$MgZn_2$	64.2	86.31	4.06	5.11	0.13
$MgZn_2$	64.2	86.31	2.93	5.16	0.31
$MgZn_2$	64.3	87.03	0.90	5.22	0.09
$MgZn_2$	64.3	85.26	3.28	5.00	0.37
$MgZn_2$	64.3	88.02	1.27	5.29	0.21
$MgZn_2$	64.3	84.21	0.94	5.01	0.08
$MgZn_2$	64.4	86.34	3.28	5.17	0.39
$MgZn_2$	64.4	87.64	4.67	5.35	0.48
$MgZn_2$	64.4	85.07	3.58	5.06	0.28
$MgZn_2$	64.4	84.20	0.79	5.07	0.06
$MgZn_2$	64.5	83.83	4.58	5.05	0.62
Mg_2Zn_{11}	82.3	91.79	5.93	3.87	0.19
Mg_2Zn_{11}	82.6	94.09	3.27	3.99	0.22
Mg_2Zn_{11}	83.9	91.65	4.27	3.63	0.36

B.6 Mg-Al-Zn Ternary System

Table 53: Interdiffusion flux and interdiffusion coefficients in Mg solid solution as a function of composition obtained from 400°C diffusion anneal of Mg-9at.%Al vs. Mg-3at.%Zn after 8 hours; Matano plane, $x_o = 0$

Position (μm)	EPMA Line Scan	Concentration (at.%)		Flux $\left(\frac{\mu m \cdot at.frac.}{sec}\right)$		Hall Interdiffusion Coefficient (m^2/sec)	
		Al	Zn	Al	Zn	Al	Zn
-126.1	LS1	9.08	0.00	0	0		
-123.1	LS1	9.08	0.00	0	-8.17×10^{-9}		
-120.0	LS1	9.08	0.00	0	-7.67×10^{-8}		3.42×10^{-14}
-117.0	LS1	9.08	0.00	0	-1.62×10^{-7}		3.42×10^{-14}
-114.0	LS1	9.08	0.01	0	-2.62×10^{-7}		3.42×10^{-14}
-110.9	LS1	9.08	0.01	0	-3.79×10^{-7}		3.42×10^{-14}
-107.9	LS1	9.08	0.02	0	-5.11×10^{-7}		3.42×10^{-14}
-104.8	LS1	9.08	0.03	0	-6.58×10^{-7}		3.42×10^{-14}
-101.8	LS1	9.08	0.03	0	-8.19×10^{-7}		3.42×10^{-14}
-98.7	LS1	9.08	0.04	0	-9.93×10^{-7}		3.42×10^{-14}
-95.7	LS1	9.08	0.05	0	-1.18×10^{-6}		3.42×10^{-14}
-92.7	LS1	9.08	0.07	0	-1.38×10^{-6}		3.42×10^{-14}
-89.6	LS1	9.08	0.08	0	-1.59×10^{-6}		3.42×10^{-14}
-86.6	LS1	9.08	0.09	0	-1.82×10^{-6}		3.42×10^{-14}
-83.5	LS1	9.08	0.11	8.43×10^{-8}	-2.05×10^{-6}		3.42×10^{-14}
-80.5	LS1	9.07	0.12	1.69×10^{-7}	-2.29×10^{-6}		3.42×10^{-14}
-77.4	LS1	9.06	0.14	2.54×10^{-7}	-2.54×10^{-6}		3.42×10^{-14}
-74.4	LS1	9.06	0.16	3.42×10^{-7}	-2.80×10^{-6}		3.41×10^{-14}
-71.4	LS1	9.05	0.18	4.43×10^{-7}	-3.06×10^{-6}		3.41×10^{-14}
-68.3	LS1	9.04	0.20	5.66×10^{-7}	-3.33×10^{-6}		3.41×10^{-14}
-65.3	LS1	9.03	0.23	7.19×10^{-7}	-3.60×10^{-6}		3.41×10^{-14}
-62.2	LS1	9.02	0.25	9.08×10^{-7}	-3.88×10^{-6}		3.41×10^{-14}
-59.2	LS1	9.00	0.28	1.14×10^{-6}	-4.15×10^{-6}		3.41×10^{-14}
-56.2	LS1	8.98	0.30	1.41×10^{-6}	-4.43×10^{-6}		3.41×10^{-14}
-53.1	LS1	8.95	0.33	1.73×10^{-6}	-4.71×10^{-6}		3.41×10^{-14}
-50.1	LS1	8.91	0.36	2.10×10^{-6}	-4.98×10^{-6}		3.41×10^{-14}
-47.0	LS1	8.87	0.40	2.51×10^{-6}	-5.25×10^{-6}		3.41×10^{-14}
-44.0	LS1	8.82	0.43	2.97×10^{-6}	-5.51×10^{-6}		3.41×10^{-14}
-40.9	LS1	8.75	0.47	3.46×10^{-6}	-5.77×10^{-6}		3.41×10^{-14}
-37.9	LS1	8.68	0.50	4.00×10^{-6}	-6.02×10^{-6}		

Position (μm)	EPMA Line Scan	Concentration (at.%)		Flux $\left(\frac{\mu m \cdot at.frac.}{sec}\right)$		Hall Interdiffusion Coefficient (m^2/sec)	
		Al	Zn	Al	Zn	Al	Zn
-34.9	LS1	8.60	0.54	4.57×10^{-6}	-6.26×10^{-6}		
-31.8	LS1	8.50	0.58	5.20×10^{-6}	-6.48×10^{-6}		
-28.8	LS1	8.38	0.63	5.89×10^{-6}	-6.69×10^{-6}		
-25.7	LS1	8.23	0.67	6.63×10^{-6}	-6.89×10^{-6}		
-22.7	LS1	8.06	0.72	7.41×10^{-6}	-7.07×10^{-6}		
-19.6	LS1	7.84	0.77	8.21×10^{-6}	-7.23×10^{-6}		
-16.6	LS1	7.59	0.82	9.00×10^{-6}	-7.36×10^{-6}		
-13.6	LS1	7.29	0.87	9.73×10^{-6}	-7.48×10^{-6}		
-10.5	LS1	6.94	0.92	1.04×10^{-5}	-7.56×10^{-6}		
-7.5	LS1	6.53	0.98	1.09×10^{-5}	-7.63×10^{-6}		
-4.4	LS1	6.06	1.04	1.11×10^{-5}	-7.66×10^{-6}		
-1.4	LS1	5.52	1.10	1.11×10^{-5}	-7.65×10^{-6}		
1.6	LS1	4.92	1.16	1.07×10^{-5}	-7.62×10^{-6}		
4.7	LS1	4.24	1.23	9.97×10^{-6}	-7.55×10^{-6}		
7.7	LS1	3.53	1.30	8.82×10^{-6}	-7.43×10^{-6}		
10.8	LS1	2.81	1.37	7.35×10^{-6}	-7.27×10^{-6}		
13.8	LS1	2.12	1.44	5.68×10^{-6}	-7.07×10^{-6}		
16.9	LS1	1.50	1.52	3.99×10^{-6}	-6.81×10^{-6}		
19.9	LS1	0.96	1.60	2.47×10^{-6}	-6.49×10^{-6}	2.27×10^{-15}	
22.9	LS1	0.56	1.68	1.29×10^{-6}	-6.12×10^{-6}	2.20×10^{-15}	
26.0	LS1	0.28	1.77	4.52×10^{-7}	-5.71×10^{-6}	2.13×10^{-15}	
29.0	LS1	0.10	1.86	0	-5.28×10^{-6}	2.07×10^{-15}	
32.1	LS1	0.01	1.94	0	-4.83×10^{-6}	1.98×10^{-15}	
35.1	LS1	0.00	2.02	0	-4.39×10^{-6}		
38.2	LS1	0.00	2.08	0	-3.97×10^{-6}		
41.2	LS1	0.00	2.15	0	-3.57×10^{-6}		
44.2	LS1	0.00	2.20	0	-3.20×10^{-6}		
47.3	LS1	0.00	2.25	0	-2.85×10^{-6}		
50.3	LS1	0.00	2.29	0	-2.52×10^{-6}		
53.4	LS1	0.00	2.32	0	-2.22×10^{-6}		
56.4	LS1	0.00	2.36	0	-1.95×10^{-6}		
59.4	LS1	0.00	2.38	0	-1.71×10^{-6}		
62.5	LS1	0.00	2.41	0	-1.49×10^{-6}		
65.5	LS1	0.00	2.43	0	-1.28×10^{-6}		
68.6	LS1	0.00	2.44	0	-1.10×10^{-6}		

Position (μm)	EPMA Line Scan	Concentration (at.%)		Flux $\left(\frac{\mu m \cdot at.frac.}{sec}\right)$		Hall Interdiffusion Coefficient (m^2/sec)	
		Al	Zn	Al	Zn	Al	Zn
71.6	LS1	0.00	2.46	0	-9.25×10^{-7}		
74.7	LS1	0.00	2.47	0	-7.72×10^{-7}		
77.7	LS1	0.00	2.48	0	-6.35×10^{-7}		
80.7	LS1	0.00	2.49	0	-5.15×10^{-7}		
83.8	LS1	0.00	2.50	0	-4.11×10^{-7}		
86.8	LS1	0.00	2.51	0	-3.21×10^{-7}		
89.9	LS1	0.00	2.51	0	-2.44×10^{-7}		
92.9	LS1	0.00	2.52	0	-1.79×10^{-7}		
96.0	LS1	0.00	2.52	0	-1.24×10^{-7}		
99.0	LS1	0.00	2.53	0	-7.78×10^{-8}		
102.0	LS1	0.00	2.53	0	-3.72×10^{-8}		
105.1	LS1	0.00	2.53	0	-1.71×10^{-10}		
108.1	LS1	0.00	2.53	0	0		
-119.2	LS3	9.06	0.00	0	0		
-116.1	LS3	9.06	0.00	0	-3.74×10^{-8}		
-113.1	LS3	9.06	0.00	0	-1.18×10^{-7}		3.28×10^{-14}
-110.0	LS3	9.06	0.01	0	-2.13×10^{-7}		3.28×10^{-14}
-107.0	LS3	9.06	0.01	0	-3.24×10^{-7}		3.27×10^{-14}
-104.0	LS3	9.06	0.02	0	-4.49×10^{-7}		3.27×10^{-14}
-100.9	LS3	9.06	0.02	0	-5.89×10^{-7}		3.27×10^{-14}
-97.9	LS3	9.06	0.03	0	-7.43×10^{-7}		3.27×10^{-14}
-94.8	LS3	9.06	0.04	0	-9.10×10^{-7}		3.27×10^{-14}
-91.8	LS3	9.06	0.05	0	-1.09×10^{-6}		3.27×10^{-14}
-88.8	LS3	9.06	0.06	0	-1.29×10^{-6}		3.27×10^{-14}
-85.7	LS3	9.06	0.08	0	-1.49×10^{-6}		3.27×10^{-14}
-82.7	LS3	9.06	0.09	0	-1.71×10^{-6}		3.27×10^{-14}
-79.6	LS3	9.06	0.11	0	-1.94×10^{-6}		3.27×10^{-14}
-76.6	LS3	9.06	0.12	0	-2.17×10^{-6}		3.27×10^{-14}
-73.6	LS3	9.06	0.14	0	-2.42×10^{-6}		3.26×10^{-14}
-70.5	LS3	9.06	0.16	0	-2.67×10^{-6}		3.26×10^{-14}
-67.5	LS3	9.06	0.18	4.23×10^{-8}	-2.93×10^{-6}		3.26×10^{-14}
-64.4	LS3	9.06	0.20	1.26×10^{-7}	-3.20×10^{-6}		3.26×10^{-14}
-61.4	LS3	9.05	0.23	2.59×10^{-7}	-3.47×10^{-6}		3.26×10^{-14}
-58.4	LS3	9.04	0.25	4.46×10^{-7}	-3.74×10^{-6}		3.26×10^{-14}
-55.3	LS3	9.02	0.28	6.90×10^{-7}	-4.02×10^{-6}		3.26×10^{-14}

Position (μm)	EPMA Line Scan	Concentration (at.%)		Flux $\left(\frac{\mu m \cdot at.frac.}{sec}\right)$		Hall Interdiffusion Coefficient (m^2/sec)	
		Al	Zn	Al	Zn	Al	Zn
-52.3	LS3	8.99	0.31	$9.94x10^{-7}$	$-4.29x10^{-6}$		$3.26x10^{-14}$
-49.2	LS3	8.96	0.34	$1.36x10^{-6}$	$-4.57x10^{-6}$		$3.26x10^{-14}$
-46.2	LS3	8.91	0.38	$1.78x10^{-6}$	$-4.84x10^{-6}$		$3.25x10^{-14}$
-43.2	LS3	8.86	0.41	$2.26x10^{-6}$	$-5.11x10^{-6}$		$3.25x10^{-14}$
-40.1	LS3	8.79	0.45	$2.78x10^{-6}$	$-5.37x10^{-6}$		$3.25x10^{-14}$
-37.1	LS3	8.71	0.49	$3.35x10^{-6}$	$-5.62x10^{-6}$		$3.25x10^{-14}$
-34.0	LS3	8.62	0.53	$3.98x10^{-6}$	$-5.86x10^{-6}$		
-31.0	LS3	8.51	0.57	$4.66x10^{-6}$	$-6.09x10^{-6}$		
-28.0	LS3	8.38	0.62	$5.40x10^{-6}$	$-6.31x10^{-6}$		
-24.9	LS3	8.22	0.66	$6.20x10^{-6}$	$-6.51x10^{-6}$		
-21.9	LS3	8.02	0.71	$7.03x10^{-6}$	$-6.69x10^{-6}$		
-18.8	LS3	7.78	0.76	$7.87x10^{-6}$	$-6.85x10^{-6}$		
-15.8	LS3	7.50	0.82	$8.69x10^{-6}$	$-6.99x10^{-6}$		
-12.7	LS3	7.17	0.87	$9.44x10^{-6}$	$-7.11x10^{-6}$		
-9.7	LS3	6.79	0.93	$1.01x10^{-5}$	$-7.20x10^{-6}$		
-6.7	LS3	6.34	0.99	$1.05x10^{-5}$	$-7.25x10^{-6}$		
-3.6	LS3	5.83	1.06	$1.07x10^{-5}$	$-7.28x10^{-6}$		
-0.6	LS3	5.25	1.12	$1.06x10^{-5}$	$-7.27x10^{-6}$		
2.5	LS3	4.60	1.19	$1.02x10^{-5}$	$-7.22x10^{-6}$		
5.5	LS3	3.89	1.26	$9.27x10^{-6}$	$-7.13x10^{-6}$		
8.5	LS3	3.17	1.34	$8.04x10^{-6}$	$-7.00x10^{-6}$		
11.6	LS3	2.46	1.41	$6.55x10^{-6}$	$-6.83x10^{-6}$		
14.6	LS3	1.81	1.48	$4.94x10^{-6}$	$-6.62x10^{-6}$		
17.7	LS3	1.23	1.56	$3.41x10^{-6}$	$-6.37x10^{-6}$		
20.7	LS3	0.77	1.63	$2.14x10^{-6}$	$-6.08x10^{-6}$	$2.31x10^{-15}$	
23.7	LS3	0.45	1.71	$1.18x10^{-6}$	$-5.76x10^{-6}$	$2.25x10^{-15}$	
26.8	LS3	0.23	1.78	$5.39x10^{-7}$	$-5.41x10^{-6}$	$2.19x10^{-15}$	
29.8	LS3	0.10	1.85	$1.77x10^{-7}$	$-5.04x10^{-6}$	$2.14x10^{-15}$	
32.9	LS3	0.03	1.92	$2.64x10^{-8}$	$-4.66x10^{-6}$	$2.10x10^{-15}$	
35.9	LS3	0.00	1.99	$2.00x10^{-9}$	$-4.27x10^{-6}$	$2.04x10^{-15}$	
38.9	LS3	0.00	2.05	0	$-3.88x10^{-6}$		
42.0	LS3	0.00	2.10	0	$-3.50x10^{-6}$		
45.0	LS3	0.00	2.15	0	$-3.13x10^{-6}$		
48.1	LS3	0.00	2.20	0	$-2.76x10^{-6}$		
51.1	LS3	0.00	2.24	0	$-2.41x10^{-6}$		

Position (μm)	EPMA Line Scan	Concentration (at.%)		Flux $\left(\frac{\mu m \cdot at.frac.}{sec}\right)$		Hall Interdiffusion Coefficient (m^2/sec)	
		Al	Zn	Al	Zn	Al	Zn
54.1	LS3	0.00	2.28	0	-2.08×10^{-6}		
57.2	LS3	0.00	2.31	0	-1.77×10^{-6}		
60.2	LS3	0.00	2.34	0	-1.47×10^{-6}		
63.3	LS3	0.00	2.37	0	-1.20×10^{-6}		
66.3	LS3	0.00	2.39	0	-9.49×10^{-7}		
69.3	LS3	0.00	2.42	0	-7.23×10^{-7}		
72.4	LS3	0.00	2.43	0	-5.24×10^{-7}		
75.4	LS3	0.00	2.45	0	-3.50×10^{-7}		
78.5	LS3	0.00	2.46	0	-2.01×10^{-7}		
81.5	LS3	0.00	2.47	0	-7.72×10^{-8}		
84.5	LS3	0.00	2.48	0	0		

Table 54: Interdiffusion flux and interdiffusion coefficients in Mg solid solution as a function of composition obtained from 450°C diffusion anneal of Mg-9at.%Al vs. Mg-3at.%Zn after 4 hours; Matano plane, $x_o = 0$

Position (μm)	Concentration (at.%)		Flux $\left(\frac{\mu m \cdot at.frac.}{sec}\right)$		Hall Interdiffusion Coefficient (m^2/sec)	
	Al	Zn	Al	Zn	Al	Zn
-204.9	9.10	0.00	0	0		
-200.8	9.10	0.00	0	-1.06×10^{-7}		
-196.8	9.10	0.00	0	-2.53×10^{-7}		1.48×10^{-13}
-192.7	9.10	0.00	0	-3.68×10^{-7}		1.48×10^{-13}
-188.7	9.10	0.01	0	-4.58×10^{-7}		1.48×10^{-13}
-184.6	9.10	0.01	0	-5.33×10^{-7}		1.48×10^{-13}
-180.6	9.10	0.01	0	-5.97×10^{-7}		1.48×10^{-13}
-176.6	9.10	0.01	0	-6.58×10^{-7}		1.48×10^{-13}
-172.5	9.10	0.01	0	-7.23×10^{-7}		1.49×10^{-13}
-168.5	9.10	0.01	0	-7.96×10^{-7}		1.49×10^{-13}
-164.4	9.10	0.01	0	-8.84×10^{-7}		1.49×10^{-13}
-160.4	9.10	0.01	0	-9.89×10^{-7}		1.49×10^{-13}
-156.3	9.10	0.02	0	-1.12×10^{-6}		1.49×10^{-13}
-152.3	9.10	0.02	0	-1.28×10^{-6}		1.49×10^{-13}
-148.2	9.10	0.02	0	-1.46×10^{-6}		1.49×10^{-13}
-144.2	9.10	0.03	0	-1.68×10^{-6}		1.49×10^{-13}
-140.2	9.10	0.03	0	-1.94×10^{-6}		1.49×10^{-13}
-136.1	9.10	0.03	0	-2.24×10^{-6}		1.49×10^{-13}
-132.1	9.10	0.04	0	-2.58×10^{-6}		1.49×10^{-13}
-128.0	9.10	0.05	0	-2.96×10^{-6}		1.49×10^{-13}
-124.0	9.10	0.06	0	-3.38×10^{-6}		1.49×10^{-13}
-119.9	9.10	0.07	0	-3.85×10^{-6}		1.49×10^{-13}
-115.9	9.10	0.08	0	-4.36×10^{-6}		1.49×10^{-13}
-111.9	9.10	0.09	0	-4.91×10^{-6}		1.49×10^{-13}
-107.8	9.10	0.11	0	-5.50×10^{-6}		1.49×10^{-13}
-103.8	9.10	0.12	0	-6.13×10^{-6}		1.49×10^{-13}
-99.7	9.10	0.14	1.90×10^{-8}	-6.79×10^{-6}		1.49×10^{-13}
-95.7	9.10	0.16	1.19×10^{-7}	-7.48×10^{-6}		1.49×10^{-13}
-91.6	9.09	0.18	3.29×10^{-7}	-8.18×10^{-6}		1.49×10^{-13}
-87.6	9.09	0.20	6.71×10^{-7}	-8.90×10^{-6}		1.49×10^{-13}
-83.6	9.08	0.23	1.16×10^{-6}	-9.62×10^{-6}		1.50×10^{-13}

Position (μm)	Concentration (at.%)		Flux $\left(\frac{\mu m \cdot at.frac.}{sec}\right)$		Hall Interdiffusion Coefficient (m^2/sec)	
	Al	Zn	Al	Zn	Al	Zn
-79.5	9.06	0.25	1.82×10^{-6}	-1.04×10^{-5}		1.50×10^{-13}
-75.5	9.03	0.28	2.65×10^{-6}	-1.11×10^{-5}		1.50×10^{-13}
-71.4	9.00	0.31	3.65×10^{-6}	-1.18×10^{-5}		1.50×10^{-13}
-67.4	8.96	0.34	4.84×10^{-6}	-1.25×10^{-5}		1.50×10^{-13}
-63.3	8.91	0.37	6.19×10^{-6}	-1.32×10^{-5}		1.50×10^{-13}
-59.3	8.84	0.40	7.71×10^{-6}	-1.39×10^{-5}		1.50×10^{-13}
-55.2	8.77	0.44	9.41×10^{-6}	-1.45×10^{-5}		1.50×10^{-13}
-51.2	8.68	0.47	1.13×10^{-5}	-1.51×10^{-5}		1.50×10^{-13}
-47.2	8.56	0.51	1.34×10^{-5}	-1.57×10^{-5}		
-43.1	8.43	0.54	1.57×10^{-5}	-1.63×10^{-5}		
-39.1	8.27	0.58	1.82×10^{-5}	-1.68×10^{-5}		
-35.0	8.08	0.62	2.07×10^{-5}	-1.72×10^{-5}		
-31.0	7.86	0.66	2.33×10^{-5}	-1.77×10^{-5}		
-26.9	7.60	0.70	2.59×10^{-5}	-1.80×10^{-5}		
-22.9	7.30	0.75	2.84×10^{-5}	-1.83×10^{-5}		
-18.9	6.95	0.79	3.07×10^{-5}	-1.86×10^{-5}		
-14.8	6.56	0.84	3.26×10^{-5}	-1.88×10^{-5}		
-10.8	6.13	0.88	3.41×10^{-5}	-1.90×10^{-5}		
-6.7	5.63	0.93	3.50×10^{-5}	-1.90×10^{-5}		
-2.7	5.09	0.98	3.51×10^{-5}	-1.90×10^{-5}		
1.4	4.53	1.02	3.45×10^{-5}	-1.90×10^{-5}		
5.4	3.96	1.07	3.30×10^{-5}	-1.89×10^{-5}		
9.4	3.40	1.12	3.10×10^{-5}	-1.87×10^{-5}		
13.5	2.88	1.17	2.84×10^{-5}	-1.84×10^{-5}		
17.5	2.41	1.21	2.57×10^{-5}	-1.81×10^{-5}		
21.6	2.00	1.26	2.28×10^{-5}	-1.77×10^{-5}		
25.6	1.66	1.31	2.00×10^{-5}	-1.73×10^{-5}		
29.7	1.36	1.35	1.72×10^{-5}	-1.68×10^{-5}		
33.7	1.11	1.40	1.46×10^{-5}	-1.62×10^{-5}		
37.7	0.90	1.44	1.22×10^{-5}	-1.56×10^{-5}	5.01×10^{-14}	
41.8	0.72	1.49	9.89×10^{-6}	-1.50×10^{-5}	5.08×10^{-14}	
45.8	0.57	1.53	7.78×10^{-6}	-1.44×10^{-5}	5.14×10^{-14}	
49.9	0.45	1.57	5.90×10^{-6}	-1.37×10^{-5}	5.20×10^{-14}	
53.9	0.34	1.60	4.25×10^{-6}	-1.30×10^{-5}	5.25×10^{-14}	
58.0	0.26	1.64	2.85×10^{-6}	-1.23×10^{-5}	5.30×10^{-14}	

Position (μm)	Concentration (at.%)		Flux $\left(\frac{\mu m \cdot at.frac.}{sec}\right)$		Hall Interdiffusion Coefficient (m^2/sec)	
	Al	Zn	Al	Zn	Al	Zn
62.0	0.19	1.67	1.71×10^{-6}	-1.16×10^{-5}	5.34×10^{-14}	
66.1	0.14	1.70	6.50×10^{-7}	-1.09×10^{-5}	5.38×10^{-14}	
70.1	0.10	1.74	3.09×10^{-7}	-1.01×10^{-5}	5.42×10^{-14}	
74.1	0.07	1.76	1.00×10^{-7}	-9.43×10^{-6}	5.45×10^{-14}	
78.2	0.06	1.79	0	-8.73×10^{-6}	5.47×10^{-14}	
82.2	0.05	1.82	0	-8.05×10^{-6}	5.49×10^{-14}	
86.3	0.04	1.84	0	-7.40×10^{-6}	5.50×10^{-14}	
90.3	0.04	1.86	0	-6.78×10^{-6}	5.51×10^{-14}	
94.4	0.03	1.88	0	-6.20×10^{-6}	5.52×10^{-14}	
98.4	0.03	1.90	0	-5.66×10^{-6}	5.52×10^{-14}	
102.4	0.03	1.91	0	-5.16×10^{-6}	5.53×10^{-14}	
106.5	0.02	1.93	0	-4.70×10^{-6}	5.54×10^{-14}	
110.5	0.02	1.94	0	-4.27×10^{-6}	5.55×10^{-14}	
114.6	0.02	1.95	0	-3.87×10^{-6}	5.56×10^{-14}	
118.6	0.02	1.96	0	-3.51×10^{-6}	5.57×10^{-14}	
122.7	0.01	1.97	0	-3.16×10^{-6}	5.58×10^{-14}	
126.7	0.01	1.98	0	-2.84×10^{-6}	5.59×10^{-14}	
130.7	0.01	1.98	0	-2.54×10^{-6}	5.61×10^{-14}	
134.8	0.00	1.99	0	-2.24×10^{-6}	5.63×10^{-14}	
138.8	0.00	2.00	0	-1.94×10^{-6}	5.66×10^{-14}	
142.9	0.00	2.00	0	-1.65×10^{-6}	5.71×10^{-14}	
146.9	0.00	2.01	0	-1.36×10^{-6}		
151.0	0.00	2.01	0	-1.08×10^{-6}		
155.0	0.00	2.02	0	-8.20×10^{-7}		
159.1	0.00	2.02	0	-5.81×10^{-7}		
163.1	0.00	2.03	0	-3.73×10^{-7}		
167.1	0.00	2.03	0	-2.04×10^{-7}		
171.2	0.00	2.03	0	-8.09×10^{-8}		
175.2	0.00	2.04	0	-1.20×10^{-8}		
179.3	0.00	2.04	0	0		

Table 55: Interdiffusion flux and interdiffusion coefficients in Mg solid solution as a function of composition obtained from 400°C diffusion anneal of Mg-3at.%Al vs. Mg-1at.%Zn after 20 hours; Matano plane, $x_o = 0$

Position (μm)	EPMA Line Scan	Concentration (at.%)		Flux $\left(\frac{\mu m \cdot at.frac.}{sec}\right)$		Hall Interdiffusion Coefficient (m^2/sec)	
		Al	Zn	Al	Zn	Al	Zn
-93.4	LS1	0.00	2.71	0	0		
-90.4	LS1	0.00	2.71	0	-2.09x10^{-10}		
-87.3	LS1	0.00	2.71	0	-4.00x10^{-9}		4.61x10^{-15}
-84.3	LS1	0.00	2.71	0	-8.68x10^{-9}		4.65x10^{-15}
-81.2	LS1	0.00	2.71	0	-1.42x10^{-8}		4.67x10^{-15}
-78.2	LS1	0.00	2.71	0	-2.09x10^{-8}		4.68x10^{-15}
-75.1	LS1	0.00	2.71	0	-2.94x10^{-8}		4.69x10^{-15}
-72.0	LS1	0.01	2.71	0	-4.05x10^{-8}		4.71x10^{-15}
-69.0	LS1	0.01	2.71	0	-5.44x10^{-8}		4.72x10^{-15}
-65.9	LS1	0.01	2.71	0	-7.18x10^{-8}		4.73x10^{-15}
-62.9	LS1	0.01	2.71	0	-9.29x10^{-8}		4.74x10^{-15}
-59.8	LS1	0.02	2.71	0	-1.18x10^{-7}		4.76x10^{-15}
-56.8	LS1	0.03	2.71	0	-1.47x10^{-7}		4.77x10^{-15}
-53.7	LS1	0.03	2.71	0	-1.80x10^{-7}		4.79x10^{-15}
-50.7	LS1	0.04	2.71	0	-2.18x10^{-7}		4.81x10^{-15}
-47.6	LS1	0.05	2.71	0	-2.58x10^{-7}		4.83x10^{-15}
-44.6	LS1	0.07	2.71	0	-3.03x10^{-7}		4.84x10^{-15}
-41.5	LS1	0.08	2.71	1.64x10^{-9}	-3.50x10^{-7}		4.87x10^{-15}
-38.5	LS1	0.10	2.71	1.69x10^{-8}	-4.00x10^{-7}		4.89x10^{-15}
-35.4	LS1	0.12	2.71	3.61x10^{-8}	-4.52x10^{-7}		4.91x10^{-15}
-32.4	LS1	0.14	2.70	5.17x10^{-8}	-5.05x10^{-7}		4.94x10^{-15}
-29.3	LS1	0.17	2.69	6.59x10^{-8}	-5.58x10^{-7}		4.97x10^{-15}
-26.3	LS1	0.19	2.68	8.95x10^{-8}	-6.11x10^{-7}		5.00x10^{-15}
-23.2	LS1	0.23	2.67	9.85x10^{-8}	-6.22x10^{-7}		5.04x10^{-15}
-22.6	LS1	0.23	2.66	1.30x10^{-7}	-6.62x10^{-7}		5.05x10^{-15}
-20.2	LS1	0.26	2.64	1.90x10^{-7}	-7.10x10^{-7}		5.08x10^{-15}
-17.1	LS1	0.30	2.60	2.69x10^{-7}	-7.54x10^{-7}		5.13x10^{-15}
-14.1	LS1	0.34	2.52	3.62x10^{-7}	-7.93x10^{-7}		5.18x10^{-15}
-11.0	LS1	0.39	2.41	4.59x10^{-7}	-8.25x10^{-7}		5.25x10^{-15}
-7.9	LS1	0.43	2.26	5.47x10^{-7}	-8.48x10^{-7}		5.32x10^{-15}
-4.9	LS1	0.49	2.06	6.21x10^{-7}	-8.60x10^{-7}		5.42x10^{-15}
-1.8	LS1	0.54	1.74	6.34x10^{-7}	-8.61x10^{-7}		

Position (μm)	EPMA Line Scan	Concentration (at.%)		Flux $\left(\frac{\mu m \cdot at.frac.}{sec}\right)$		Hall Interdiffusion Coefficient (m^2/sec)	
		Al	Zn	Al	Zn	Al	Zn
1.2	LS1	0.60	1.14	5.92×10^{-7}	-8.56×10^{-7}		
3.2	LS1	0.63	0.86	5.90×10^{-7}	-8.56×10^{-7}		
3.2	LS1	0.63	0.85	5.54×10^{-7}	-8.52×10^{-7}		
4.3	LS1	0.65	0.71	4.35×10^{-7}	-8.34×10^{-7}	1.65×10^{-15}	
7.3	LS1	0.70	0.41	3.38×10^{-7}	-8.12×10^{-7}	2.29×10^{-15}	
10.4	LS1	0.73	0.25	2.75×10^{-7}	-7.90×10^{-7}	2.65×10^{-15}	
13.4	LS1	0.76	0.17	2.26×10^{-7}	-7.67×10^{-7}	2.84×10^{-15}	
16.5	LS1	0.78	0.12	1.93×10^{-7}	-7.45×10^{-7}	2.98×10^{-15}	
19.5	LS1	0.80	0.10	1.68×10^{-7}	-7.22×10^{-7}	3.06×10^{-15}	
22.6	LS1	0.82	0.08	1.44×10^{-7}	-6.97×10^{-7}	3.13×10^{-15}	
25.6	LS1	0.83	0.07	1.21×10^{-7}	-6.70×10^{-7}	3.18×10^{-15}	
28.7	LS1	0.85	0.05	1.01×10^{-7}	-6.41×10^{-7}	3.24×10^{-15}	
31.7	LS1	0.86	0.04	8.19×10^{-8}	-6.10×10^{-7}	3.29×10^{-15}	
34.8	LS1	0.87	0.04	6.53×10^{-8}	-5.78×10^{-7}	3.34×10^{-15}	
37.8	LS1	0.89	0.03	5.10×10^{-8}	-5.45×10^{-7}	3.38×10^{-15}	
40.9	LS1	0.90	0.02	3.87×10^{-8}	-5.11×10^{-7}	3.42×10^{-15}	
43.9	LS1	0.91	0.02	2.82×10^{-8}	-4.76×10^{-7}	3.45×10^{-15}	
47.0	LS1	0.92	0.02	1.92×10^{-8}	-4.40×10^{-7}	3.49×10^{-15}	
50.0	LS1	0.93	0.01	1.11×10^{-8}	-4.05×10^{-7}	3.52×10^{-15}	
53.1	LS1	0.94	0.01	3.24×10^{-9}	-3.70×10^{-7}	3.54×10^{-15}	
56.1	LS1	0.95	0.01	0	-3.35×10^{-7}	3.57×10^{-15}	
59.2	LS1	0.96	0.01	0	-3.00×10^{-7}	3.61×10^{-15}	
62.3	LS1	0.97	0.00	0	-2.66×10^{-7}	3.66×10^{-15}	
65.3	LS1	0.98	0.00	0	-2.33×10^{-7}	3.72×10^{-15}	
68.4	LS1	0.98	0.00	0	-2.02×10^{-7}	3.79×10^{-15}	
71.4	LS1	0.99	0.00	0	-1.72×10^{-7}	3.85×10^{-15}	
74.5	LS1	1.00	0.00	0	-1.44×10^{-7}	3.89×10^{-15}	
77.5	LS1	1.00	0.00	0	-1.17×10^{-7}		
80.6	LS1	1.01	0.00	0	-9.23×10^{-8}		
83.6	LS1	1.01	0.00	0	-6.95×10^{-8}		
86.7	LS1	1.02	0.00	0	-4.85×10^{-8}		
89.7	LS1	1.02	0.00	0	-2.93×10^{-8}		
92.8	LS1	1.02	0.00	0	-1.20×10^{-8}		
95.8	LS1	1.02	0.00	0	0		
-127.1	LS2	2.73	0.00				1.41×10^{-14}

Position (μm)	EPMA Line Scan	Concentration (at.%)		Flux $\left(\frac{\mu m \cdot at.frac.}{sec}\right)$		Hall Interdiffusion Coefficient (m^2/sec)	
		Al	Zn	Al	Zn	Al	Zn
-124.1	LS2	2.73	0.00				$1.38x10^{-14}$
-121.0	LS2	2.73	0.00				$1.36x10^{-14}$
-118.0	LS2	2.73	0.00				$1.35x10^{-14}$
-114.9	LS2	2.73	0.00				$1.35x10^{-14}$
-111.9	LS2	2.73	0.00				$1.34x10^{-14}$
-108.8	LS2	2.73	0.01				$1.33x10^{-14}$
-105.8	LS2	2.73	0.01				$1.33x10^{-14}$
-102.7	LS2	2.73	0.01				$1.32x10^{-14}$
-99.7	LS2	2.73	0.01				$1.31x10^{-14}$
-96.6	LS2	2.73	0.01				$1.31x10^{-14}$
-93.6	LS2	2.73	0.01				$1.31x10^{-14}$
-90.5	LS2	2.73	0.02				$1.30x10^{-14}$
-87.5	LS2	2.73	0.02				$1.30x10^{-14}$
-84.4	LS2	2.73	0.02				$1.29x10^{-14}$
-81.4	LS2	2.73	0.02				$1.29x10^{-14}$
-78.3	LS2	2.73	0.02				$1.29x10^{-14}$
-75.3	LS2	2.73	0.02				$1.28x10^{-14}$
-72.2	LS2	2.73	0.02				$1.28x10^{-14}$
-69.2	LS2	2.73	0.03				$1.28x10^{-14}$
-66.1	LS2	2.73	0.03				$1.28x10^{-14}$
-63.1	LS2	2.73	0.03				$1.27x10^{-14}$
-60.0	LS2	2.73	0.03				$1.27x10^{-14}$
-57.0	LS2	2.73	0.03				$1.26x10^{-14}$
-53.9	LS2	2.73	0.04				$1.26x10^{-14}$
-50.9	LS2	2.73	0.04				$1.25x10^{-14}$
-47.8	LS2	2.73	0.05				$1.24x10^{-14}$
-44.8	LS2	2.73	0.06				$1.23x10^{-14}$
1.0	LS2	1.20	0.59			$9.27x10^{-16}$	
4.1	LS2	0.59	0.68			$1.58x10^{-15}$	
7.1	LS2	0.34	0.74			$1.80x10^{-15}$	
10.2	LS2	0.24	0.77			$1.90x10^{-15}$	
13.2	LS2	0.19	0.80			$1.95x10^{-15}$	
16.3	LS2	0.16	0.81			$1.98x10^{-15}$	
19.3	LS2	0.13	0.83			$2.02x10^{-15}$	
22.4	LS2	0.11	0.84			$2.05x10^{-15}$	

Position (μm)	EPMA Line Scan	Concentration (at.%)		Flux $\left(\frac{\mu m \cdot at.frac.}{sec}\right)$		Hall Interdiffusion Coefficient (m^2/sec)	
		Al	Zn	Al	Zn	Al	Zn
25.4	LS2	0.09	0.85			2.08×10^{-15}	
28.5	LS2	0.07	0.86			2.11×10^{-15}	
31.5	LS2	0.05	0.88			2.14×10^{-15}	
34.6	LS2	0.04	0.89			2.17×10^{-15}	
37.6	LS2	0.03	0.90			2.20×10^{-15}	
40.7	LS2	0.02	0.91			2.23×10^{-15}	
43.7	LS2	0.01	0.93			2.25×10^{-15}	
46.8	LS2	0.01	0.94			2.29×10^{-15}	
49.8	LS2	0.00	0.95			2.32×10^{-15}	
52.9	LS2	0.00	0.96			2.36×10^{-15}	
55.9	LS2	0.00	0.96			2.41×10^{-15}	

Table 56: Interdiffusion flux and interdiffusion coefficients in Mg solid solution as a function of composition obtained from 450°C diffusion anneal of Mg-3at.%Al vs. Mg-1at.%Zn after 5 hours; Matano plane, $x_o = 0$

Position (μm)	EPMA Line Scan	Concentration (at.%)		Flux $\left(\frac{\mu m \cdot at.frac.}{sec}\right)$		Hall Interdiffusion Coefficient (m^2/sec)	
		Al	Zn	Al	Zn	Al	Zn
-184.2	LS1	2.77	0.00	0	0		
-178.2	LS1	2.77	0.00	0	-8.50×10^{-9}		
-172.1	LS1	2.77	0.00	0	-2.24×10^{-8}		6.41×10^{-14}
-166.0	LS1	2.77	0.00	0	-4.00×10^{-8}		6.44×10^{-14}
-160.0	LS1	2.77	0.00	0	-6.18×10^{-8}		6.46×10^{-14}
-153.9	LS1	2.77	0.00	0	-8.74×10^{-8}		6.47×10^{-14}
-147.9	LS1	2.77	0.00	0	-1.17×10^{-7}		6.49×10^{-14}
-141.8	LS1	2.77	0.00	0	-1.55×10^{-7}		6.50×10^{-14}
-135.7	LS1	2.77	0.00	0	-2.10×10^{-7}		6.51×10^{-14}
-129.7	LS1	2.77	0.01	0	-2.92×10^{-7}		6.53×10^{-14}
-123.6	LS1	2.77	0.01	0	-4.08×10^{-7}		6.55×10^{-14}
-117.6	LS1	2.77	0.01	0	-5.66×10^{-7}		6.57×10^{-14}
-111.5	LS1	2.77	0.02	0	-7.68×10^{-7}		6.60×10^{-14}
-105.4	LS1	2.77	0.02	0	-1.02×10^{-6}		6.63×10^{-14}
-99.4	LS1	2.77	0.03	0	-1.32×10^{-6}		6.66×10^{-14}
-93.3	LS1	2.77	0.04	0	-1.67×10^{-6}		6.69×10^{-14}
-87.3	LS1	2.77	0.06	0	-2.06×10^{-6}		6.73×10^{-14}
-81.2	LS1	2.77	0.07	0	-2.51×10^{-6}		6.77×10^{-14}
-75.2	LS1	2.77	0.09	0	-2.98×10^{-6}		6.81×10^{-14}
-69.1	LS1	2.77	0.12	1.25×10^{-8}	-3.50×10^{-6}		6.86×10^{-14}
-63.0	LS1	2.77	0.15	7.83×10^{-8}	-4.03×10^{-6}		6.92×10^{-14}
-57.0	LS1	2.77	0.18	1.80×10^{-7}	-4.56×10^{-6}		6.97×10^{-14}
-50.9	LS1	2.76	0.21	3.04×10^{-7}	-5.08×10^{-6}		7.04×10^{-14}
-46.2	LS1	2.75	0.24	5.45×10^{-7}	-5.67×10^{-6}		7.10×10^{-14}
-44.9	LS1	2.75	0.25	1.21×10^{-6}	-6.60×10^{-6}		7.11×10^{-14}
-38.8	LS1	2.73	0.29	2.46×10^{-6}	-7.42×10^{-6}		7.19×10^{-14}
-32.7	LS1	2.69	0.34	4.45×10^{-6}	-8.11×10^{-6}		7.28×10^{-14}
-26.7	LS1	2.60	0.38	7.02×10^{-6}	-8.66×10^{-6}		7.38×10^{-14}
-20.6	LS1	2.42	0.43	9.59×10^{-6}	-9.05×10^{-6}		7.50×10^{-14}
-14.6	LS1	2.15	0.48	1.14×10^{-5}	-9.27×10^{-6}		7.63×10^{-14}
-8.5	LS1	1.78	0.53	1.19×10^{-5}	-9.33×10^{-6}		
-2.4	LS1	1.39	0.57	1.13×10^{-5}	-9.24×10^{-6}		

Position (μm)	EPMA Line Scan	Concentration (at.%)		Flux $\left(\frac{\mu m \cdot at.frac.}{sec}\right)$		Hall Interdiffusion Coefficient (m^2/sec)	
		Al	Zn	Al	Zn	Al	Zn
3.6	LS1	1.02	0.62	$1.00x10^{-5}$	$-9.04x10^{-6}$		
9.7	LS1	0.75	0.66	$8.45x10^{-6}$	$-8.73x10^{-6}$	$1.99x10^{-14}$	
15.7	LS1	0.56	0.69	$6.61x10^{-6}$	$-8.36x10^{-6}$	$2.30x10^{-14}$	
21.8	LS1	0.40	0.73	$4.72x10^{-6}$	$-7.92x10^{-6}$	$2.56x10^{-14}$	
27.9	LS1	0.26	0.76	$3.06x10^{-6}$	$-7.44x10^{-6}$	$2.79x10^{-14}$	
33.9	LS1	0.15	0.78	$1.88x10^{-6}$	$-6.92x10^{-6}$	$2.98x10^{-14}$	
40.0	LS1	0.08	0.81	$1.19x10^{-6}$	$-6.38x10^{-6}$	$3.15x10^{-14}$	
46.0	LS1	0.05	0.83	$8.30x10^{-7}$	$-5.81x10^{-6}$	$3.27x10^{-14}$	
52.1	LS1	0.03	0.85	$5.97x10^{-7}$	$-5.23x10^{-6}$	$3.34x10^{-14}$	
58.2	LS1	0.02	0.87	$4.12x10^{-7}$	$-4.62x10^{-6}$	$3.39x10^{-14}$	
64.2	LS1	0.02	0.89	$2.68x10^{-7}$	$-3.98x10^{-6}$	$3.43x10^{-14}$	
70.3	LS1	0.01	0.90	$1.63x10^{-7}$	$-3.30x10^{-6}$	$3.47x10^{-14}$	
76.3	LS1	0.01	0.92	$8.70x10^{-8}$	$-2.56x10^{-6}$	$3.50x10^{-14}$	
82.4	LS1	0.01	0.93	$2.98x10^{-8}$	$-1.77x10^{-6}$	$3.53x10^{-14}$	
88.5	LS1	0.00	0.95	0	$-9.35x10^{-7}$	$3.55x10^{-14}$	
94.5	LS1	0.00	0.97	0	$-6.34x10^{-8}$	$3.57x10^{-14}$	
100.6	LS1	0.00	0.98	0	0	$3.59x10^{-14}$	
106.6	LS1	0.00	1.00	0	0	$3.62x10^{-14}$	
112.7	LS1	0.00	1.01	0	0	$3.64x10^{-14}$	
118.8	LS1	0.00	1.03	0	0	$3.67x10^{-14}$	
124.8	LS1	0.00	1.04	0	0	$3.69x10^{-14}$	
130.9	LS1	0.00	1.05	0	0	$3.73x10^{-14}$	
136.9	LS1	0.00	1.06	0	0	$3.78x10^{-14}$	
143.0	LS1	0.00	1.06	0	0		
-129.9	LS2	2.77	0.00	0	0		
-123.8	LS2	2.77	0.00	0	$-5.97x10^{-8}$		
-117.8	LS2	2.77	0.00	0	$-1.64x10^{-7}$		$4.98x10^{-14}$
-111.7	LS2	2.77	0.01	0	$-3.17x10^{-7}$		$5.02x10^{-14}$
-105.6	LS2	2.77	0.01	0	$-5.24x10^{-7}$		$5.06x10^{-14}$
-99.6	LS2	2.77	0.02	0	$-7.86x10^{-7}$		$5.09x10^{-14}$
-93.5	LS2	2.77	0.03	0	$-1.10x10^{-6}$		$5.13x10^{-14}$
-87.5	LS2	2.77	0.04	$5.91x10^{-8}$	$-1.48x10^{-6}$		$5.16x10^{-14}$
-81.4	LS2	2.76	0.06	$1.21x10^{-7}$	$-1.90x10^{-6}$		$5.20x10^{-14}$
-75.3	LS2	2.76	0.08	$1.84x10^{-7}$	$-2.38x10^{-6}$		$5.24x10^{-14}$
-69.3	LS2	2.76	0.10	$2.48x10^{-7}$	$-2.89x10^{-6}$		$5.29x10^{-14}$

Position (μm)	EPMA Line Scan	Concentration (at.%)		Flux $\left(\frac{\mu m \cdot at.frac.}{sec}\right)$		Hall Interdiffusion Coefficient (m^2/sec)	
		Al	Zn	Al	Zn	Al	Zn
-63.2	LS2	2.75	0.13	$3.41x10^{-7}$	$-3.43x10^{-6}$		$5.33x10^{-14}$
-57.2	LS2	2.75	0.16	$5.21x10^{-7}$	$-3.97x10^{-6}$		$5.39x10^{-14}$
-51.1	LS2	2.74	0.19	$8.25x10^{-7}$	$-4.49x10^{-6}$		$5.45x10^{-14}$
-45.0	LS2	2.71	0.23	$1.27x10^{-6}$	$-4.97x10^{-6}$		$5.51x10^{-14}$
-39.0	LS2	2.68	0.28	$1.85x10^{-6}$	$-5.41x10^{-6}$		$5.58x10^{-14}$
-32.9	LS2	2.62	0.32	$2.53x10^{-6}$	$-5.78x10^{-6}$		$5.65x10^{-14}$
-26.9	LS2	2.53	0.36	$3.37x10^{-6}$	$-6.08x10^{-6}$		$5.73x10^{-14}$
-20.8	LS2	2.41	0.41	$4.38x10^{-6}$	$-6.31x10^{-6}$		$5.82x10^{-14}$
-14.7	LS2	2.20	0.45	$5.43x10^{-6}$	$-6.45x10^{-6}$		$5.92x10^{-14}$
-8.7	LS2	1.88	0.50	$6.08x10^{-6}$	$-6.52x10^{-6}$		$6.03x10^{-14}$
-2.6	LS2	1.47	0.54	$6.04x10^{-6}$	$-6.52x10^{-6}$		
3.4	LS2	1.05	0.59	$5.45x10^{-6}$	$-6.45x10^{-6}$		
9.5	LS2	0.72	0.63	$4.76x10^{-6}$	$-6.32x10^{-6}$	$1.64x10^{-14}$	
15.6	LS2	0.52	0.66	$4.12x10^{-6}$	$-6.14x10^{-6}$	$1.68x10^{-14}$	
21.6	LS2	0.40	0.70	$3.41x10^{-6}$	$-5.91x10^{-6}$	$1.71x10^{-14}$	
27.7	LS2	0.30	0.73	$2.69x10^{-6}$	$-5.65x10^{-6}$	$1.74x10^{-14}$	
33.7	LS2	0.21	0.76	$1.98x10^{-6}$	$-5.35x10^{-6}$	$1.76x10^{-14}$	
39.8	LS2	0.14	0.79	$1.32x10^{-6}$	$-5.02x10^{-6}$	$1.78x10^{-14}$	
45.9	LS2	0.09	0.82	$7.54x10^{-7}$	$-4.65x10^{-6}$	$1.80x10^{-14}$	
51.9	LS2	0.05	0.85	$2.89x10^{-7}$	$-4.26x10^{-6}$	$1.82x10^{-14}$	
58.0	LS2	0.02	0.87	$2.66x10^{-8}$	$-3.85x10^{-6}$	$1.84x10^{-14}$	
64.0	LS2	0.00	0.90	0	$-3.42x10^{-6}$		
70.1	LS2	0.00	0.92	0	$-2.99x10^{-6}$		
76.2	LS2	0.00	0.94	0	$-2.56x10^{-6}$		
82.2	LS2	0.00	0.96	0	$-2.15x10^{-6}$		
88.3	LS2	0.00	0.98	0	$-1.76x10^{-6}$		
94.3	LS2	0.00	0.99	0	$-1.40x10^{-6}$		
100.4	LS2	0.00	1.00	0	$-1.07x10^{-6}$		
106.5	LS2	0.00	1.02	0	$-7.59x10^{-7}$		
112.5	LS2	0.00	1.03	0	$-4.80x10^{-7}$		
118.6	LS2	0.00	1.04	0	$-2.27x10^{-7}$		
124.6	LS2	0.00	1.04	0	$-7.00x10^{-10}$		
130.7	LS2	0.00	1.05	0	0		

Table 57: Interdiffusion coefficients in Mg solid solution as a function of composition obtained from 350°C diffusion anneal of Mg vs. Mg-3at.%Al-0.5at.%Zn after 168 hours

EPMA Line Scan	Concentration (at.%)		Hall Interdiffusion Coefficient (m^2/sec)	
	Al	Zn	Al	Zn
LS1	0.00	0.00		$7.35x10^{-16}$
LS1	0.00	0.00		$7.53x10^{-16}$
LS1	0.00	0.02		$6.56x10^{-16}$
LS1	0.00	0.02		$6.41x10^{-16}$
LS1	0.00	0.02		$6.56x10^{-16}$
LS1	0.02	0.03	$7.79x10^{-17}$	$6.21x10^{-16}$
LS1	0.08	0.03	$7.67x10^{-17}$	$6.24x10^{-16}$
LS1	0.17	0.04	$7.58x10^{-17}$	$5.86x10^{-16}$
LS1	0.71	0.08	$7.18x10^{-17}$	$4.65x10^{-16}$
LS2	0.01	0.00	$4.55x10^{-16}$	$5.04x10^{-16}$
LS2	0.03	0.01	$4.10x10^{-16}$	$4.06x10^{-16}$
LS2	0.07	0.02	$3.71x10^{-16}$	$3.89x10^{-16}$
LS2	0.06	0.02	$3.74x10^{-16}$	$3.91x10^{-16}$
LS2	0.06	0.02	$3.75x10^{-16}$	$3.83x10^{-16}$
LS2	0.13	0.03	$3.26x10^{-16}$	$3.38x10^{-16}$
LS2	0.30	0.03	$2.30x10^{-16}$	$3.39x10^{-16}$

Table 58: Interdiffusion flux and interdiffusion coefficients in Mg solid solution as a function of composition obtained from 400°C diffusion anneal of Mg vs. Mg-3at.%Al-0.5at.%Zn after 24 hours; Matano plane, $x_o = 0$

Position (μm)	EPMA Line Scan	Concentration (at.%)		Flux $\left(\frac{\mu m \cdot at.frac.}{sec}\right)$		Hall Interdiffusion Coefficient (m^2/sec)	
		Al	Zn	Al	Zn	Al	Zn
-151.9	LS1	0.00	0.00	0	0		
-143.8	LS1	0.00	0.00	0	-4.23x10^{-9}		
-135.7	LS1	0.00	0.00	0	-1.08x10^{-8}		
-127.6	LS1	0.00	0.00	0	-1.93x10^{-8}		2.06x10^{-14}
-119.5	LS1	0.00	0.00	0	-2.97x10^{-8}		2.06x10^{-14}
-111.5	LS1	0.00	0.00	0	-4.20x10^{-8}		2.06x10^{-14}
-103.4	LS1	0.00	0.01	0	-5.60x10^{-8}		2.05x10^{-14}
-95.3	LS1	0.00	0.01	0	-7.23x10^{-8}		2.05x10^{-14}
-87.2	LS1	0.00	0.01	0	-9.22x10^{-8}		2.05x10^{-14}
-79.1	LS1	0.00	0.02	0	-1.16x10^{-7}		2.05x10^{-14}
-71.0	LS1	0.00	0.02	-8.41x10^{-9}	-1.45x10^{-7}		2.05x10^{-14}
-63.0	LS1	0.00	0.03	-4.63x10^{-8}	-1.77x10^{-7}	3.95x10^{-15}	2.04x10^{-14}
-54.9	LS1	0.01	0.04	-1.01x10^{-7}	-2.13x10^{-7}	3.76x10^{-15}	2.04x10^{-14}
-46.8	LS1	0.03	0.05	-1.68x10^{-7}	-2.49x10^{-7}	3.63x10^{-15}	2.04x10^{-14}
-38.7	LS1	0.06	0.06	-2.45x10^{-7}	-2.83x10^{-7}	3.50x10^{-15}	2.03x10^{-14}
-30.6	LS1	0.10	0.08	-3.29x10^{-7}	-3.11x10^{-7}	3.38x10^{-15}	2.03x10^{-14}
-22.5	LS1	0.15	0.10	-4.31x10^{-7}	-3.32x10^{-7}	3.23x10^{-15}	2.02x10^{-14}
-14.4	LS1	0.25	0.12	-7.10x10^{-7}	-3.44x10^{-7}	3.02x10^{-15}	2.01x10^{-14}
-6.4	LS1	0.71	0.14	-8.28x10^{-7}	-3.47x10^{-7}		2.00x10^{-14}
1.7	LS1	1.58	0.16	-6.02x10^{-7}	-3.40x10^{-7}		
9.8	LS1	2.26	0.18	-3.86x10^{-7}	-3.25x10^{-7}		
17.9	LS1	2.53	0.20	-2.85x10^{-7}	-3.03x10^{-7}		
26.0	LS1	2.61	0.22	-2.20x10^{-7}	-2.76x10^{-7}		
34.1	LS1	2.65	0.23	-1.55x10^{-7}	-2.45x10^{-7}		
42.1	LS1	2.68	0.24	-9.51x10^{-8}	-2.12x10^{-7}		
50.2	LS1	2.70	0.26	-4.27x10^{-8}	-1.76x10^{-7}		
58.3	LS1	2.72	0.27	-1.04x10^{-9}	-1.40x10^{-7}		
66.4	LS1	2.73	0.28	0	-1.05x10^{-7}		
74.5	LS1	2.73	0.29	0	-7.01x10^{-8}		
82.6	LS1	2.73	0.30	0	-3.67x10^{-8}		
90.6	LS1	2.73	0.30	0	-5.28x10^{-9}		
98.7	LS1	2.73	0.31	0	-1.83x10^{-9}		

Position (μm)	EPMA Line Scan	Concentration (at.%)		Flux $\left(\frac{\mu m \cdot at.frac.}{sec}\right)$		Hall Interdiffusion Coefficient (m^2/sec)	
		Al	Zn	Al	Zn	Al	Zn
106.8	LS1	2.73	0.31	0	-2.25×10^{-10}		
114.9	LS1	2.73	0.31	0	0		
-149.3	LS2	0.00	0.00	0	0		
-140.8	LS2	0.00	0.00	0	-2.36×10^{-9}		
-132.2	LS2	0.00	0.00	0	-6.43×10^{-9}		
-123.6	LS2	0.00	0.00	0	-1.13×10^{-8}		
-115.1	LS2	0.00	0.00	0	-1.74×10^{-8}		
-106.5	LS2	0.00	0.00	0	-2.77×10^{-8}		
-97.9	LS2	0.00	0.00	0	-4.60×10^{-8}		1.14×10^{-14}
-89.4	LS2	0.00	0.01	0	-7.40×10^{-8}		1.14×10^{-14}
-80.8	LS2	0.00	0.01	0	-1.09×10^{-7}		1.14×10^{-14}
-72.2	LS2	0.00	0.02	0	-1.47×10^{-7}		1.14×10^{-14}
-63.7	LS2	0.00	0.03	0	-1.86×10^{-7}		1.14×10^{-14}
-55.1	LS2	0.00	0.04	0	-2.23×10^{-7}		1.14×10^{-14}
-46.5	LS2	0.00	0.05	0	-2.56×10^{-7}		1.14×10^{-14}
-38.0	LS2	0.00	0.07	-3.21×10^{-8}	-2.86×10^{-7}		1.14×10^{-14}
-29.4	LS2	0.02	0.08	-3.41×10^{-7}	-3.13×10^{-7}	8.28×10^{-16}	1.14×10^{-14}
-20.8	LS2	0.23	0.10	-7.23×10^{-7}	-3.35×10^{-7}	8.04×10^{-16}	1.14×10^{-14}
-12.2	LS2	0.63	0.13	-9.60×10^{-7}	-3.48×10^{-7}	7.77×10^{-16}	1.14×10^{-14}
-3.7	LS2	1.14	0.15	-9.41×10^{-7}	-3.47×10^{-7}	7.37×10^{-16}	
4.9	LS2	1.69	0.18	-6.89×10^{-7}	-3.34×10^{-7}		
13.5	LS2	2.16	0.20	-3.85×10^{-7}	-3.13×10^{-7}		
22.0	LS2	2.46	0.22	-1.72×10^{-7}	-2.87×10^{-7}		
30.6	LS2	2.60	0.24	-4.91×10^{-8}	-2.57×10^{-7}		
39.2	LS2	2.66	0.25	-3.38×10^{-9}	-2.26×10^{-7}		
47.7	LS2	2.68	0.27	0	-1.92×10^{-7}		
56.3	LS2	2.68	0.28	0	-1.57×10^{-7}		
64.9	LS2	2.68	0.29	0	-1.20×10^{-7}		
73.4	LS2	2.68	0.30	0	-8.26×10^{-8}		
82.0	LS2	2.68	0.31	0	-4.97×10^{-8}		
90.6	LS2	2.68	0.31	0	-2.59×10^{-8}		
99.1	LS2	2.68	0.32	0	-1.35×10^{-8}		
107.7	LS2	2.68	0.32	0	-1.12×10^{-8}		
116.3	LS2	2.68	0.32	0	0		

Table 59: Interdiffusion flux and interdiffusion coefficients in Mg solid solution as a function of composition obtained from 450°C diffusion anneal of Mg vs. Mg-3at.%Al-0.5at.%Zn after 4 hours; Matano plane, $x_o = 0$

Position (μm)	EPMA Line Scan	Concentration (at.%)		Flux $\left(\frac{\mu m \cdot at.frac.}{sec}\right)$		Hall Interdiffusion Coefficient (m^2/sec)	
		Al	Zn	Al	Zn	Al	Zn
91.3	LS1	0.00	0.00				6.02×10^{-14}
81.3	LS1	0.00	0.00				6.01×10^{-14}
71.3	LS1	0.00	0.01				5.99×10^{-14}
61.3	LS1	0.00	0.03				5.96×10^{-14}
51.3	LS1	0.00	0.03				5.96×10^{-14}
41.3	LS1	0.04	0.06			4.08×10^{-14}	5.93×10^{-14}
31.3	LS1	0.08	0.08			3.51×10^{-14}	5.91×10^{-14}
21.3	LS1	0.08	0.09			3.51×10^{-14}	5.89×10^{-14}
11.3	LS1	0.16	0.11			2.70×10^{-14}	5.87×10^{-14}
114.1	LS2	0.00	0.00	0	0		
101.9	LS2	0.00	0.00	0	0		5.35×10^{-14}
89.8	LS2	0.00	0.00	0	5.73×10^{-9}		5.35×10^{-14}
77.7	LS2	0.00	0.00	0	3.97×10^{-8}		5.35×10^{-14}
65.6	LS2	0.00	0.01	0	1.24×10^{-7}		5.36×10^{-14}
53.5	LS2	0.00	0.03	0	3.70×10^{-7}		5.36×10^{-14}
41.3	LS2	0.00	0.05	0	7.14×10^{-7}		5.36×10^{-14}
29.2	LS2	0.05	0.07	0	1.01×10^{-6}	5.34×10^{-15}	5.36×10^{-14}
17.1	LS2	0.42	0.11	0	1.30×10^{-6}	5.83×10^{-15}	5.36×10^{-14}
5.0	LS2	1.59	0.15	0	1.58×10^{-6}	7.49×10^{-15}	5.37×10^{-14}
-7.2	LS2	2.52	0.20	2.00×10^{-6}	1.75×10^{-6}		
-19.3	LS2	2.73	0.24	1.65×10^{-6}	1.73×10^{-6}		
-31.4	LS2	2.78	0.27	6.96×10^{-7}	1.54×10^{-6}		
-43.5	LS2	2.80	0.29	2.18×10^{-7}	1.28×10^{-6}		
-55.6	LS2	2.80	0.30	0	1.03×10^{-6}		
-67.8	LS2	2.80	0.32	0	7.80×10^{-7}		
-79.9	LS2	2.80	0.33	0	5.09×10^{-7}		
-92.0	LS2	2.80	0.33	0	2.31×10^{-7}		
-104.1	LS2	2.80	0.33	0	2.55×10^{-8}		
-116.2	LS2	2.80	0.33	0	0		

Table 60: Interdiffusion flux in Mg solid solution as a function of composition obtained from 400°C diffusion anneal of Mg-1at.%Al vs. Mg-1at.%Zn after 24 hours; Matano plane, $x_o = 0$

Position (μm)	EPMA Line Scan	Concentration (at.%)		Flux $\left(\frac{\mu m \cdot at.frac.}{sec}\right)$	
		Al	Zn	Al	Zn
-182.5	LS1	0.85	1.11	0	0
-176.5	LS1	0.85	1.11	2.11×10^{-9}	0
-170.4	LS1	0.85	1.11	5.11×10^{-9}	8.94×10^{-8}
-164.3	LS1	0.85	1.11	9.03×10^{-9}	1.85×10^{-7}
-158.3	LS1	0.85	1.10	1.39×10^{-8}	2.87×10^{-7}
-152.2	LS1	0.85	1.08	1.97×10^{-8}	3.95×10^{-7}
-146.2	LS1	0.85	1.07	2.63×10^{-8}	5.08×10^{-7}
-140.1	LS1	0.85	1.06	3.39×10^{-8}	6.25×10^{-7}
-134.0	LS1	0.84	1.04	4.24×10^{-8}	7.45×10^{-7}
-128.0	LS1	0.84	1.03	5.17×10^{-8}	8.67×10^{-7}
-121.9	LS1	0.84	1.01	6.17×10^{-8}	9.91×10^{-7}
-115.9	LS1	0.84	0.99	7.25×10^{-8}	1.11×10^{-6}
-109.8	LS1	0.84	0.97	8.40×10^{-8}	1.24×10^{-6}
-103.7	LS1	0.84	0.95	9.60×10^{-8}	1.36×10^{-6}
-97.7	LS1	0.83	0.93	1.09×10^{-7}	1.47×10^{-6}
-91.6	LS1	0.83	0.91	1.22×10^{-7}	1.59×10^{-6}
-85.6	LS1	0.83	0.89	1.35×10^{-7}	1.69×10^{-6}
-79.5	LS1	0.83	0.87	1.49×10^{-7}	1.80×10^{-6}
-73.4	LS1	0.82	0.84	1.64×10^{-7}	1.89×10^{-6}
-67.4	LS1	0.82	0.82	1.78×10^{-7}	1.99×10^{-6}
-61.3	LS1	0.82	0.80	1.92×10^{-7}	2.07×10^{-6}
-55.3	LS1	0.81	0.77	2.06×10^{-7}	2.14×10^{-6}
-49.2	LS1	0.81	0.75	2.20×10^{-7}	2.21×10^{-6}
-43.1	LS1	0.80	0.72	2.33×10^{-7}	2.27×10^{-6}
-37.1	LS1	0.80	0.69	2.45×10^{-7}	2.32×10^{-6}
-31.0	LS1	0.79	0.67	2.57×10^{-7}	2.36×10^{-6}
-24.9	LS1	0.78	0.64	2.83×10^{-7}	2.40×10^{-6}
-18.9	LS1	0.76	0.62	3.24×10^{-7}	2.42×10^{-6}
-12.8	LS1	0.72	0.59	3.72×10^{-7}	2.44×10^{-6}
-6.8	LS1	0.63	0.57	3.97×10^{-7}	2.44×10^{-6}
-0.7	LS1	0.52	0.54	3.79×10^{-7}	2.44×10^{-6}

Position (μm)	EPMA Line Scan	Concentration (at.%)		Flux $\left(\frac{\mu m \cdot at.frac.}{sec}\right)$	
		Al	Zn	Al	Zn
5.4	LS1	0.39	0.51	$3.19x10^{-7}$	$2.42x10^{-6}$
11.4	LS1	0.26	0.49	$2.32x10^{-7}$	$2.40x10^{-6}$
17.5	LS1	0.16	0.46	$1.37x10^{-7}$	$2.37x10^{-6}$
23.5	LS1	0.08	0.44	$6.30x10^{-8}$	$2.34x10^{-6}$
29.6	LS1	0.03	0.42	$2.15x10^{-8}$	$2.29x10^{-6}$
35.7	LS1	0.01	0.39	$5.31x10^{-9}$	$2.24x10^{-6}$
41.7	LS1	0.00	0.37	$5.41x10^{-10}$	$2.18x10^{-6}$
47.8	LS1	0.00	0.35	0	$2.12x10^{-6}$
53.8	LS1	0.00	0.32	0	$2.05x10^{-6}$
59.9	LS1	0.00	0.30	0	$1.97x10^{-6}$
66.0	LS1	0.00	0.28	0	$1.89x10^{-6}$
72.0	LS1	0.00	0.26	0	$1.80x10^{-6}$
78.1	LS1	0.00	0.24	0	$1.71x10^{-6}$
84.1	LS1	0.00	0.22	0	$1.62x10^{-6}$
90.2	LS1	0.00	0.20	0	$1.52x10^{-6}$
96.3	LS1	0.00	0.19	0	$1.43x10^{-6}$
102.3	LS1	0.00	0.17	0	$1.33x10^{-6}$
108.4	LS1	0.00	0.15	0	$1.23x10^{-6}$
114.4	LS1	0.00	0.14	0	$1.12x10^{-6}$
120.5	LS1	0.00	0.12	0	$1.02x10^{-6}$
126.6	LS1	0.00	0.11	0	$9.25x10^{-7}$
132.6	LS1	0.00	0.09	0	$8.28x10^{-7}$
138.7	LS1	0.00	0.08	0	$7.33x10^{-7}$
144.7	LS1	0.00	0.07	0	$6.42x10^{-7}$
150.8	LS1	0.00	0.06	0	$5.55x10^{-7}$
156.9	LS1	0.00	0.05	0	$4.72x10^{-7}$
162.9	LS1	0.00	0.04	0	$3.96x10^{-7}$
169.0	LS1	0.00	0.03	0	$3.26x10^{-7}$
175.1	LS1	0.00	0.03	0	$2.64x10^{-7}$
181.1	LS1	0.00	0.02	0	$2.10x10^{-7}$
187.2	LS1	0.00	0.01	0	$1.65x10^{-7}$
193.2	LS1	0.00	0.01	0	$1.31x10^{-7}$
199.3	LS1	0.00	0.01	0	$1.07x10^{-7}$
205.4	LS1	0.00	0.01	0	$9.62x10^{-8}$
211.4	LS1	0.00	0.00	0	0

Position (μm)	EPMA Line Scan	Concentration (at.%)		Flux $\left(\frac{\mu m \cdot at.frac.}{sec}\right)$	
		Al	Zn	Al	Zn
-168.9	LS2	0.87	1.11	0	
-162.8	LS2	0.87	1.11	0	$1.36x10^{-8}$
-156.8	LS2	0.87	1.11	0	$4.38x10^{-8}$
-150.7	LS2	0.87	1.11	0	$9.17x10^{-8}$
-144.6	LS2	0.87	1.10	0	$1.58x10^{-7}$
-138.6	LS2	0.87	1.09	0	$2.41x10^{-7}$
-132.5	LS2	0.87	1.08	0	$3.37x10^{-7}$
-126.5	LS2	0.87	1.07	0	$4.45x10^{-7}$
-120.4	LS2	0.87	1.05	0	$5.61x10^{-7}$
-114.3	LS2	0.87	1.04	0	$6.83x10^{-7}$
-108.3	LS2	0.87	1.02	0	$8.10x10^{-7}$
-102.2	LS2	0.87	1.00	0	$9.38x10^{-7}$
-96.2	LS2	0.87	0.97	0	$1.07x10^{-6}$
-90.1	LS2	0.87	0.95	0	$1.19x10^{-6}$
-84.0	LS2	0.87	0.92	$9.70x10^{-9}$	$1.32x10^{-6}$
-78.0	LS2	0.87	0.90	$2.02x10^{-8}$	$1.44x10^{-6}$
-71.9	LS2	0.87	0.87	$3.15x10^{-8}$	$1.55x10^{-6}$
-65.9	LS2	0.87	0.84	$4.38x10^{-8}$	$1.65x10^{-6}$
-59.8	LS2	0.86	0.81	$5.68x10^{-8}$	$1.75x10^{-6}$
-53.7	LS2	0.86	0.78	$7.05x10^{-8}$	$1.84x10^{-6}$
-47.7	LS2	0.85	0.75	$8.45x10^{-8}$	$1.92x10^{-6}$
-41.6	LS2	0.85	0.72	$1.02x10^{-7}$	$1.99x10^{-6}$
-35.6	LS2	0.84	0.69	$1.34x10^{-7}$	$2.05x10^{-6}$
-29.5	LS2	0.82	0.66	$1.83x10^{-7}$	$2.09x10^{-6}$
-23.4	LS2	0.79	0.63	$2.45x10^{-7}$	$2.13x10^{-6}$
-17.4	LS2	0.74	0.60	$3.01x10^{-7}$	$2.15x10^{-6}$
-11.3	LS2	0.67	0.57	$3.40x10^{-7}$	$2.17x10^{-6}$
-5.2	LS2	0.59	0.54	$3.51x10^{-7}$	$2.17x10^{-6}$
0.8	LS2	0.50	0.51	$3.31x10^{-7}$	$2.16x10^{-6}$
6.9	LS2	0.41	0.48	$2.80x10^{-7}$	$2.15x10^{-6}$
12.9	LS2	0.33	0.46	$2.04x10^{-7}$	$2.12x10^{-6}$
19.0	LS2	0.24	0.43	$1.14x10^{-7}$	$2.09x10^{-6}$
25.1	LS2	0.17	0.41	$2.19x10^{-8}$	$2.05x10^{-6}$
31.1	LS2	0.12	0.38	0	$2.00x10^{-6}$
37.2	LS2	0.07	0.36	0	$1.95x10^{-6}$

Position (μm)	EPMA Line Scan	Concentration (at.%)		Flux $\left(\frac{\mu m \cdot at.frac.}{sec}\right)$	
		Al	Zn	Al	Zn
43.2	LS2	0.04	0.33	0	1.89×10^{-6}
49.3	LS2	0.02	0.31	0	1.82×10^{-6}
55.4	LS2	0.01	0.29	0	1.75×10^{-6}
61.4	LS2	0.00	0.27	0	1.68×10^{-6}
67.5	LS2	0.00	0.25	0	1.60×10^{-6}
73.5	LS2	0.00	0.23	0	1.51×10^{-6}
79.6	LS2	0.00	0.21	0	1.43×10^{-6}
85.7	LS2	0.00	0.19	0	1.34×10^{-6}
91.7	LS2	0.00	0.17	0	1.25×10^{-6}
97.8	LS2	0.00	0.16	0	1.16×10^{-6}
103.8	LS2	0.00	0.14	0	1.07×10^{-6}
109.9	LS2	0.00	0.13	0	9.76×10^{-7}
116.0	LS2	0.00	0.11	0	8.86×10^{-7}
122.0	LS2	0.00	0.10	0	7.97×10^{-7}
128.1	LS2	0.00	0.09	0	7.09×10^{-7}
134.1	LS2	0.00	0.08	0	6.24×10^{-7}
140.2	LS2	0.00	0.07	0	5.42×10^{-7}
146.3	LS2	0.00	0.06	0	4.63×10^{-7}
152.3	LS2	0.00	0.05	0	3.88×10^{-7}
158.4	LS2	0.00	0.04	0	3.18×10^{-7}
164.4	LS2	0.00	0.03	0	2.54×10^{-7}
170.5	LS2	0.00	0.02	0	1.95×10^{-7}
176.6	LS2	0.00	0.02	0	1.43×10^{-7}
182.6	LS2	0.00	0.01	0	9.78×10^{-8}
188.7	LS2	0.00	0.01	0	6.03×10^{-8}
194.8	LS2	0.00	0.01	0	3.12×10^{-8}
200.8	LS2	0.00	0.00	0	1.09×10^{-8}
206.9	LS2	0.00	0.00	0	0

APPENDIX C: LIST OF PUBLICATIONS AND PRESENTATIONS

C.1 Peer Reviewed Publications

Kammerer, C.C., Fu M., Zhou L., Keiser, Jr. D.D., Sohn Y.H., "Interdiffusion and Reaction between Pure Magnesium and Aluminum Alloy 6061," *Defects and Diffusion Forum*, vol. 364 (2015) pp. 174-181. Print.

Kammerer, C. C., Kulkarni, N. S., Warmack, R. J., & Sohn, Y. H., "Interdiffusion and impurity diffusion in polycrystalline Mg solid solution with Al or Zn," *Journal of Alloys and Compounds*, vol. 617 (2014) pp. 968-974. Print.

Huang, K. K., Kammerer, C. C., Keiser, D. D., & Sohn, Y. H., "Diffusion Barrier Selection from Refractory Metals (Zr, Mo and Nb) Via Interdiffusion Investigation for U-Mo RERTR Fuel Alloy," *Journal of Phase Equilibria and Diffusion*, vol. 35 (2014) pp. 146-156. Print.

Kammerer, C., N. Kulkarni, R. Warmack, K. Perry, I. Belova, G. Murch and Y. Sohn. (2014). Impurity Diffusion Coefficients of Al and Zn in Mg Determined from Solid-to-Solid Diffusion Couples. Magnesium Technology 2014, John Wiley & Sons, Inc.: 505-509. Print.

Kammerer C, Kulkarni N, Warmack R, Sohn Y. (2014). Al and Zn Impurity Diffusion in Binary and Ternary Magnesium Solid-Solutions. Magnesium Technology 2014, John Wiley & Sons, Inc.: 407-411. Print.

Kammerer, C. C. (2013). Interdiffusion and impurity diffusion in magnesium solid solutions [electronic resource] / by Catherine C. Kammerer. Materials Science and Engineering. Orlando, FL, University of Central Florida. MS.

Sohn, Y. H., Patterson, T. T., Hofmeister, C. C., Kammerer, C. C., Mohr, W. W., Bergh, M. M., & Cho, K. K. "Tailoring Microstructure and Properties of Hierarchical Aluminum Metal Matrix Composites Through Friction Stir Processing," *JOM*, vol. 64 (2012) pp. 234-238. Print.

Yao, B., C. Kammerer, B. Simkin, B. Majumdar, C. Smith, M. v. d. Bergh, K. Cho and Y. H. Sohn. (2012). Grain Growth Behavior of Nanocrystalline Aluminum in Trimodal Metal Matrix Composite During Thermomechanical Processing. SAMPE 2012 - 57th International SAMPE Symposium 2012, Society for the Advancement of Materials & Process Engineering. Print.

Gordon, A. P., Drilling, B., Williams, K., Hebert, J. S., Kammerer, C. C., and Baldwin, F. (2011) "Optimization of Re-Torque and Relaxation Parameters of the GUCP" Proceedings of the ASME Conference on Pressure Vessels and Piping, Baltimore, Maryland, July 15th-23rd.

C.C. Kammerer, N.S. Kulkarni, R.J. Warmack, Y.H. Sohn, "Interdiffusion in Ternary Magnesium Solid Solutions of Aluminum and Zinc," *Journal of Phase Equilibria and Diffusion*, In Review.

C.C. Kammerer, S. Behdad, L. Zhou, F. Betancor, M. Gonzalez, B. Boesl, Y.H. Sohn, "Diffusion Kinetics, Mechanical Properties, and Crystallographic Characterization of Intermetallic Compounds in the Mg-Zn Binary System," *Intermetallics*, In Review.

L. Zhou, C.C. Kammerer, A. Giri, K. Cho, Y.H. Sohn, "Microstructural development and ternary interdiffusion in Ni-Mn-Ga alloys," *Metallurgical and Materials Transactions A*, In Review.

C.C. Kammerer, L. Zhou, M. Schneider, F. Betancor, Y. Park, K. Cho, Y.H. Sohn, "Mg-Gd Binary Phase Diagram Investigation via the Diffusion Couple Technique," *Scripta Materialia*, In Preparation.

C.C. Kammerer, K. Bermudez, R. Newell, Y.H. Sohn, "Diffusion Kinetics in the Mg-Y Binary System," In Preparation.

C.2 Conference Presentations

C.C. Kammerer, B. Warmack, N. Kulkarni, Y.H. Sohn, "Ternary Interdiffusion Coefficients in Mg-Rich Mg-Al-Zn Solid Solutions," To Be Presented at Materials Science & Technology 2015 Conference & Exhibition (MS&T'15), October 4-8, 2015, Columbus, OH.

C.C. Kammerer, B. Warmack, N. Kulkarni, Y.H. Sohn, "Interdiffusion in Ternary Magnesium Solid Solutions of Aluminum and Zinc," Presented at the 144th Annual Meeting & Exhibition TMS2015, March 15-19, Orlando, FL.

C.C. Kammerer, L. Zhou, K. Cho, Y.H. Sohn, "The Mg-Gd System: Characterization of Interdiffusion and Reaction Products," Presented at the 144th Annual Meeting & Exhibition TMS2015, March 15-19, Orlando, FL.

C.C. Kammerer, "Characterization of Reaction Products in the Mg-Gd System: A Combinatorial Approach," Presented at the Florida US-Korea Conference on Biomedical, Nanosciences, Engineering and Systems Technology (Florida BNEST 2015), February 21, 2015, Orlando, FL.

Y.H. Sohn, C. Kammerer, L. Zhou, Y. Park, "Next Chapter of Diffusion Couple Experiments: Materials Genome Development," Presented at the 2014 International Conference on Diffusion in Materials (DIMAT 2014), August 17-22, 2014, Munster, Germany.

C.C. Kammerer, S.T. Brennan, Y.H. Sohn, "Diffusion and Intermetallic Growth in the Mg-Zn System," Presented at the 10th International Conference on Diffusion in Solids and Liquids (DSL-2014), June 23-27, 2014, Paris, France.

C.C. Kammerer, L. Zhou, M. Fu, D.D. Keiser, Y.H. Sohn, "Diffusion Reactions Between Pure Mg and AA6061," Presented at the 10th International Conference on Diffusion in Solids and Liquids (DSL-2014), June 23-27, 2014, Paris, France.

C.C. Kammerer, B. Warmack, D. Leonard, N. Kularni, Y.H. Sohn, "The Influence of Solute Concentration on Impurity Diffusion in Magnesium Solid Solutions," Presented at the 25th Annual Conference and Exposition on Aerospace Materials (AeroMat 2014), June 16-19, 2014, Orlando, FL.

C.C. Kammerer, N. Kulkarni, B. Warmack, Y.H. Sohn, "Al and Zn Impurity Diffusion in Binary and Ternary Magnesium Solid-Solutions," Presented at the 143rd Annual Meeting & Exhibition TMS2014, February 16-20, San Diego, CA.

M. Fu, C.C. Kammerer, L. Zhou, D.D. Keiser, Y.H. Sohn, "Interdiffusion of Mg and AA6061," Presented at the 143rd Annual Meeting & Exhibition TMS2014, February 16-20, San Diego, CA.

C.C. Kammerer, N. Kulkarni, B. Warmack, K. Perry, I. Belova, G. Murch, Y.H. Sohn, "Impurity Diffusion Coefficients of Al and Zn in Mg Determined from Solid-to-Solid Diffusion Couples," Presented at the 142nd Annual Meeting & Exhibition TMS2013, March 3-7, 2013, San Antonio, TX.

Y.H. Sohn, B. Yao, C. Hofmeister, C.C. Kammerer, B. Majumdar, A. Giri, K. Cho, "Nano-Scale Grain Size Effects Observed on Aluminum Metal Matrix Composites: Strengthening, Stability and Growth," Presented at the 142nd Annual Meeting & Exhibition TMS2013, March 3-7, 2013, San Antonio, TX.

Y.H. Sohn, D. Shin, C.C. Kammerer, S. Brennan, K. Bermudez, J. Hamilton, "Diffusion Database for the Development of Magnesium Alloys and Their Hierarchical Composites," Presented at the 142nd Annual Meeting & Exhibition TMS2013, March 3-7, 2013, San Antonio, TX.

C.C. Kammerer, N. Kulkarni, B. Warmack, I. Belova, G. Murch, Y.H. Sohn, "Diffusion in Dilute Magnesium Alloys," Presented at Materials Science & Technology 2012 Conference & Exhibition (MS&T'12), October 7-11, 2012, Pittsburgh, PA.

LIST OF REFERENCES

1. Easton, M., A. Beer, M. Barnett, C. Davies, G. Dunlop, Y. Durandet, S. Blacket, T. Hilditch, and P. Beggs, *Magnesium alloy applications in automotive structures.* JOM, 2008. **60**(11): p. 57-62.
2. Friedrich, H.E. and B.L. Mordike, *Magnesium technology: metallurgy, design data, automotive applications*. 2006: Springer.
3. Agnew, S.R. and J.F. Nie, *Preface to the viewpoint set on: The current state of magnesium alloy science and technology.* Scripta Materialia, 2010. **63**: p. 671-671.
4. Luo, A.A., R.K. Mishra, B.R. Powell, and A.K. Sachdev, *Magnesium Alloy Development for Automotive Applications.* Materials Science Forum, 2012. **706**(1): p. 69.
5. Hirsch, J. and T. Al-Samman, *Superior light metals by texture engineering: Optimized aluminum and magnesium alloys for automotive applications.* Acta Materialia, 2013. **61**(3): p. 818-843.
6. Luo, A.A., *Magnesium casting technology for structural applications.* Journal of Magnesium and Alloys, 2013. **1**(1): p. 2-22.
7. Deutsche Gesellschaft für, M. and K.U. Kainer, *Magnesium alloys and their applications*. 2000, Weinheim ; Chichester: Wiley-VCH.
8. Li, X., F. Jiao, T. Al-Samman, and S. Ghosh Chowdhury, *Influence of second-phase precipitates on the texture evolution of Mg–Al–Zn alloys during hot deformation.* Scripta Materialia, 2012. **66**: p. 159-162.
9. *Metals Handbook*. Vol. 2. 1992: American Society for Metals.
10. Sandlöbes, S., Z. Pei, M. Friák, L.F. Zhu, F. Wang, S. Zaefferer, D. Raabe, and J. Neugebauer, *Ductility improvement of Mg alloys by solid solution: Ab initio modeling, synthesis and mechanical properties.* Acta Materialia, 2014. **70**: p. 92-104.
11. Peng, Q., J. Meng, Y. Li, Y. Huang, and N. Hort, *Effect of yttrium addition on lattice parameter, Young's modulus and vacancy of magnesium.* Materials Science and Engineering A, 2011. **528**: p. 2106-2109.
12. Park, J.S. and Y.W. Chang, *The Effect of Alloying Elements on the c/a Ratio of Magnesium Binary Alloys.* Advanced Materials Research, 2007. **26**(1): p. 95.
13. Rokhlin, L.L., *Magnesium alloys containing rare earth metals: structure and properties*. 2003, New York: Taylor & Francis.
14. Ball, E.A. and P.B. Prangnell, *Tensile-compressive yield asymmetries in high strength wrought magnesium alloys.* Scripta Metallurgica et Materialia, 1994. **31**(2): p. 111-116.
15. Bohlen, J., M.R. Nürnberg, J.W. Senn, D. Letzig, and S.R. Agnew, *The texture and anisotropy of magnesium–zinc–rare earth alloy sheets.* Acta Materialia, 2007. **55**(6): p. 2101-2112.
16. Smola, B., I. Stulikova, F. von Buch, and B.L. Mordike, *Structural aspects of high performance Mg alloys design.* Materials Science and Engineering, 2002. **A324**: p. 113-117.

17. Nie, J.F., *Precipitation and Hardening in Magnesium Alloys.* Metallurgical and Materials Transactions a-Physical Metallurgy and Materials Science, 2012. **43A**(11): p. 3891-3939.
18. *Integrated Computational Materials Engineering: A Transformational Discipline for Improved Competitiveness and National Security*. 2008: The National Academies Press.
19. Lu, X.-G., Z. Wang, Y. Cui, and Z. Jin, *Computational thermodynamics, computational kinetics, and materials design.* Chinese Science Bulletin, 2014. **59**(15): p. 1662-1671.
20. Dieter, G.E., *Mechanical Metallurgy*. 1986, Boston: McGraw Hill.
21. Nie, J.F. and B.C. Muddle. *Design of magnesium alloy microstructures for higher strength*. in *Materials 98*. 1998. Wollongog.
22. Tammann, G. and H.J. Rocha, *Die Diffusion zweier Metalle ineinander unter Bildung intermetallischer Verbindung.* Zeitschrift für Anorganische und Allgemeine Chemie, 1931. **199**(1): p. 289.
23. Clark, J.B. and F.N. Rhines, *Layer growth in Al-Mg-Zn.* Transactions of The American Society For Metals, 1959. **51**: p. 199-221.
24. Hall, L.D., *An Analytical Method of Calculating Variable Diffusion Coefficients.* The Journal of Chemical Physics, 1953: p. 87-89.
25. Matano, C., *On the Relation between the Diffusion-Coefficients and Concentrations of Solid Metals (The Nickel-Copper System).* Japanese Journal of Physics, 1933. **8**: p. 109.
26. Mehrer, H., *Diffusion in Solids: Fundamentals, Methods, Materials, Diffusion-Controlled Processes*. 2007, Berlin: Springer-Verlag.
27. Wagner, C., *The evaluation of data obtained with diffusion couples of binary single-phase and multiphase systems.* Acta Metallurgica, 1969. **17**(2): p. 99-107.
28. Kirkaldy, J.S., *DIFFUSION IN MULTICOMPONENT METALLIC SYSTEMS: I. PHENOMENOLOGICAL THEORY FOR SUBSTITUTIONAL SOLID SOLUTION ALLOYS.* Canadian Journal of Physics, 1958. **36**(7): p. 899-906.
29. Zhao, J.C., M.R. Jackson, L.A. Peluso, and L.N. Brewer, *A diffusion-multiple approach for mapping phase diagrams, hardness, and elastic modulus.* JOM, 2002. **54**(7): p. 42-45.
30. Manning, J.R., *Diffusion Kinetics for Atoms in Crystals*. 1968, Princeton: Van Nostrand.
31. Kodentsov, A.A., G. F. Bastin, and F. J.J. van Loo, *Chapter six - Application of diffusion couples in phase diagram determination*, in *Methods for Phase Diagram Determination*, J.C. Zhao, Editor. 2007, Elsevier Science Ltd: Oxford. p. 222-245.
32. van Loo, F.J.J., *Multiphase diffusion in binary and ternary solid-state systems.* Progress in Solid State Chemistry, 1990. **20**: p. 47-99.
33. Bermudez, K., S. Brennan, and Y.H. Sohn, *Intermetallic Phase Formation and Growth in the Mg-Y System*, in *Magnesium Technology 2012*. 2012, John Wiley & Sons, Inc. p. 145-148.
34. Brennan, S., K. Bermudez, N. Kulkarni, and Y. Sohn, *Interdiffusion in the Mg-Al System and Intrinsic Diffusion in β-Mg2Al3.* Metallurgical and Materials Transactions A, 2012. **43**(11): p. 4043-4052.

35. Brennan, S., K. Bermudez, N. Kulkarni, and Y.H. Sohn, *Diffusion Couple Investigation of the Mg-Zn System*, in *Magnesium Technology 2012*. 2012, John Wiley & Sons: Hoboken. p. 323-327.
36. Brennan, S., K. Bermudez, and Y.H. Sohn, *Intermetallic Growth and Interdiffusion in the Mg-Nd System*. 2012, 2012-07.
37. Giannuzzi, L.A. and F.A. Stevie, *A review of focused ion beam milling techniques for TEM specimen preparation.* Micron, 1999. **30**(3): p. 197-204.
38. Kempshall, B. and L.A. Giannuzzi, *In-Situ Lift-Out FIB Specimen Preparation for TEM of Magnetic Materials.* Microscopy and Microanalysis, 2002. **8**(Supplement S02): p. 390-391.
39. Oliver, W.C. and G.M. Pharr, *An improved technique for determining hardness and elastic modulus using load and displacement sensing indentation experiments.* Journal of Materials Research, 1992. **7**(06): p. 1564-1583.
40. Oliver, W.C. and G.M. Pharr, *Nanoindentation in materials research: Past, present, and future.* MRS Bulletin, 2010. **35**(11): p. 897-907.
41. Oliver, W.C. and G.M. Pharr, *Measurement of hardness and elastic modulus by instrumented indentation: Advances in understanding and refinements to methodology.* Journal of Materials Research, 2004. **19**(01): p. 3-20.
42. Philibert, J.M., *Atom movements - Diffusion and mass transport in solids*. 1991: EDP Sciences.
43. Huang, K., Y. Park, A. Ewh, B.H. Sencer, J.R. Kennedy, K.R. Coffey, and Y.H. Sohn, *Interdiffusion and reaction between uranium and iron.* Journal of Nuclear Materials, 2012. **424**: p. 82-88.
44. Dayananda, M.A., *Average Effective Interdiffusion Coefficients in Binary and Multicomponent Alloys.* Diffusion and Defect Forum, 1993: p. 521-536.
45. Boltzmann, L., Ann. Physik und Chem. Wied., 1894. **53**: p. 959.
46. Dayananda, M.A. and C.W. Kim, Metallurgical and Materials Transactions A, 1979: p. 1333-1339.
47. Sauer, F. and V. Freise, *DIFFUSION IN BINAREN GEMISCHEN MIT VOLUMENANDERUNG.* Zeitschrift fur elektrochemie, 1962. **66**(4): p. 353-363.
48. Dayananda, M.A. and Y.H. Sohn, *Average effective interdiffusion coefficients and their applications for isothermal multicomponent diffusion couples.* Scripta Materialia, 1996. **35**(6): p. 683-688.
49. Darken, L.S., *Diffusion, Mobility and Their Interrelation through Free Energy in Binary Metallic Systems (Reprinted from vol 175, pg 184, 1948)*.
50. Kammerer, C.C., *Interdiffusion and impurity diffusion in magnesium solid solutions [electronic resource] / by Catherine C. Kammerer*. 2013: Orlando, Fla. : University of Central Florida, 2013.
51. Sarafianos, N., *An analytical method of calculating variable diffusion coefficients.* Journal of Materials Science, 1986: p. 2283-2288.
52. Onsager, L., *Reciprocal Relations in Irreversible Processes I.* Phys. Rev., 1931. **37**: p. 405-426.

53. Onsager, L., *Reciprocal Relations in Irreversible Processes II.* Phys. Rev., 1931. **38**: p. 2265-2279.
54. Kirkaldy, J.S., *Diffusion in Multicomponent Metallic Systems.* Canadian Journal of Physics, 1957: p. 435-440.
55. Kirkaldy, J.S., R.J. Brigham, and D.H. Weichert, *Diffusion interactions in cu-zn-sn as determined from infinite and finite diffusion couples.* Acta Metallurgica, 1965. **13**(8): p. 907-915.
56. Kirkaldy, J.S., D. Weichert, and Z.-U. Haq, *DIFFUSION IN MULTICOMPONENT METALLIC SYSTEMS: VI. SOME THERMODYNAMIC PROPERTIES OF THE D MATRIX AND THE CORRESPONDING SOLUTIONS OF THE DIFFUSION EQUATIONS.* Canadian Journal of Physics, 1963. **41**(12): p. 2166-2173.
57. Whittle, D.P. and A. Green, *The measurement of diffusion coefficients in ternary systems.* Scripta Metallurgica, 1974. **8**: p. 883-884.
58. Dayananda, M. and C. Kim, *Zero-flux planes and flux reversals in Cu–Ni–Zn diffusion couples.* Metallurgical transactions. Part A: Physical Metallurgy & Materials Science, 1979. **10**(9): p. 1333.
59. Ziebold, T.O. and J.A.R. Cooper, *Atomic mobilities and multicomponent diffusion.* Mobilites atomiques et diffusion en systeme a constituants multiples (French), 1965. **13**: p. 465-470.
60. Ziebold, T.O. and R.E. Ogilvie, *Ternary Diffusion in Copper-Silver-Gold Alloys.* Trans. TMS-AIME, 1967. **239**: p. 942-953.
61. Balluffi, R.W., S.M. Allen, and W.C. Carter, *Kinetics of Materials*. 2005, Hoboken: John Wiley & Sons, Inc.
62. Balluffi, R.W., S.M. Allen, and W.C. Carter, *Kinetics of Materials*. 2005, Hoboken, New Jersey: John Wiley & Sones. 645.
63. Čermák, J. and I. Stoukal, *Diffusion of 65Zn in Mg and in Mg-xAl solid solutions.* Physica Status Solidi (a), 2006: p. 2386–2392.
64. Zener, C., *Theory of Do for Atomic Diffusion in Metals.* Journal of Applied Physics, 1951. **22**(4): p. 372-375.
65. Kammerer, C.C., N.S. Kulkarni, R.J. Warmack, and Y.H. Sohn, *Interdiffusion and impurity diffusion in polycrystalline Mg solid solution with Al or Zn.* Journal of Alloys and Compounds, 2014. **617**: p. 968-974.
66. Neumann, G. and C. Tuijn, *Self-Diffusion and Impurity Diffusion in Pure Metals*. 2009, London: Elsevier.
67. Hardie, D. and R.N. Parkins, *Lattice spacing relationships in magnesium solid solutions.* Philosophical Magazine, 1959. **4**(43): p. 815-825.
68. Xie, Y.-P., Z.-Y. Wang, and Z.F. Hou, *The phase stability and elastic properties of MgZn2 and Mg4Zn7 in Mg–Zn alloys.* Scripta Materialia, 2013. **68**(7): p. 495-498.
69. Ganeshan, S., S.L. Shang, Y. Wang, and Z.K. Liu, *Effect of alloying elements on the elastic properties of Mg from first-principles calculations.* Acta Materialia, 2009. **57**(13): p. 3876-3884.
70. Reed-Hill, R.E. and R. Abbaschian, *Physical Metallurgy Priciples*. 1992, Boston: PWS-Kent Publishing.

71. Ganeshan, S., L.G. Hector Jr., and Z.-K. Liu, *First-principles calculations of impurity diffusion coeefficients in dilute Mg alloys using the 8-frequency model.* Acta Materialia, 2011. **59**: p. 3214-3228.
72. Shin, D. and C. Wolverton, *First-principles study of solute–vacancy binding in magnesium.* Acta Materialia, 2010. **58**(2): p. 531-540.
73. Rao, A.R. and C. Suryanarayana, *Solute-vacancy binding energies in magnesium alloys.* physica status solidi (a), 1978. **45**(2): p. K131-K133.
74. Vydyanath, H.R., D.H. Sastry, and K.I. Vasu, *On the Kinetics of Clustering in a Magnesium-3%Zinc Alloy.* physica status solidi (b), 1968. **29**(2): p. K137-K140.
75. Hardie, D., *The elastic properties of magnesium solid solutions.* Acta Metallurgica, 1971. **19**(7): p. 719-723.
76. Busk, R.S., *Lattice parameters of magnesium alloys.* Journal of Metals (1949), 1950. **2**: p. Trans-1464.
77. Brennan, S., A.P. Warren, K.R. Coffey, N. Kulkarni, P. Todd, M. Kilmov, and Y.H. Sohn, *Aluminum Impurity Diffusion in Magnesium.* Journal of Phase Equilibria and Diffusion, 2012: p. 121-125.
78. Combronde, J. and G. Brebec, *Heterodiffusion de Ag, Cd, In, Sn et Sb dans le magnesium.* Acta Metallurgica, 1972. **20**(1): p. 37-44.
79. Das, S., Y.-M. Kim, T. Ha, R. Gauvin, and I.-H.i.-h.j.m.c. Jung, *Anisotropic Diffusion Behavior of Al in Mg: Diffusion Couple Study Using Mg Single Crystal.* Metallurgical & Materials Transactions. Part A, 2013. **44**(6): p. 2539-2547.
80. Das, S.K., N. Brodusch, R. Gauvin, and I.-H. Jung, *Grain boundary diffusion of Al in Mg.* Scripta Materialia, 2014. **80**: p. 41-44.
81. Das, S.K., Y.B. Kang, T. Ha, and I.H. Jung, *Thermodynamic modeling and diffusion kinetic experiments of binary Mg-Gd and Mg-Y systems.* Acta Materialia, 2014. **71**: p. 12.
82. Das, S.K., Y.-M. Kim, T.K. Ha, and I.-H. Jung, *Investigation of anisotropic diffusion behavior of Zn in hcp Mg and interdiffusion coefficients of intermediate phases in the Mg-Zn system.* Calphad, 2013: p. 51.
83. Fujikawa, S.I., *Tracer diffusion of magnesium in pseudo-binary Al-Mg2Si alloys.* Defect and diffusion forum/journal, 1997. **143**: p. 403-408.
84. Fujikawa, S.I. and Y. Takada, *Interdiffusion between aluminum and Al-Mg alloys.* Defect and diffusion forum/journal, 1997. **143**: p. 409-414.
85. Funamizu, Y. and K. Watanabe, *Interdiffusion in the Al–Mg System.* Transactions of the Japan Institute of Metals, 1972. **13**(4): p. 278-283.
86. Huber, L., I. Elfimov, J. Rottler, and M. Militzer, *Ab initio calculations of rare-earth diffusion in magnesium.* Physical Review B: Condensed Matter & Materials Physics, 2012. **85**(14): p. 1-7.
87. Kammerer, C., N. Kulkarni, R. Warmack, K. Perry, I. Belova, G. Murch, and Y. Sohn, *Impurity Diffusion Coefficients of Al and Zn in Mg Determined from Solid-to-Solid Diffusion Couples*, in *Magnesium Technology 2014*. 2014, John Wiley & Sons, Inc. p. 505-509.

88. Kammerer, C., N. Kulkarni, R. Warmack, and Y. Sohn, *Al and Zn Impurity Diffusion in Binary and Ternary Magnesium Solid-Solutions*, in *Magnesium Technology 2014*. 2014, John Wiley & Sons, Inc. p. 407-411.
89. Lal, K., *Diffusion of Some Elements in Magnesium*, in *CEA Report R-3136*. 1967, Saclay. p. 54.
90. Mostafa, A. and M. Medraj, *On the atomic interdiffusion in Mg–{Ce, Nd, Zn} and Zn–{Ce, Nd} binary systems.* Journal of Materials Research, 2014. **29**(13): p. 1463-1479.
91. Sohn, Y., *13 - Diffusion in metals*, in *Smithells Metals Reference Book (Eighth Edition)*, W.F.G.C. Totemeier, Editor. 2004, Butterworth-Heinemann: Oxford. p. 1-120.
92. Das, S.K., Y.M. Kim, T.K. Ha, and I.H. Jung, *Investigation of anisotropic diffusion behavior of Zn in hcp Mg and interdiffusion coefficients of intermediate phases in the Mg-Zn system*. 2013.
93. Wang, K., H. Wang, F. Liu, and H. Zhai, *Morphological stability analysis for planar interface during rapidly directional solidification of concentrated multi-component alloys.* Acta Materialia, 2014. **67**: p. 220-231.
94. Yao, J., Y.W. Cui, H. Liu, H. Kou, J. Li, and L. Zhou, *Diffusional mobility for fcc phase of Al–Mg–Zn system and its applications.* CALPHAD, 2008. **32**(3): p. 602-607.
95. Beke, D., I. Gödeny, F.J. Kedves, and G. Groma, *Diffusion of 65Zn in dilute AlZn, AlMg, AlZnMg and AlZnFe alloys.* Acta Metallurgica, 1977. **25**(5): p. 539-550.
96. Takahashi, T., Y. Minamino, K. Hirao, and T. Yamane, *Quaternary Diffusion in the alpha Solid Solutions of Al-Zn-Mg-Cu Alloys.* Materials Transactions, JIM, 1999. **40**(9): p. 997-1004.
97. Takahashi, T., Y. Minamino, and T. Yamane, *Quaternary Diffusion in 7000 Aluminum Alloys.* MATERIALS TRANSACTIONS, 2002. **43**(2): p. 232-238.
98. Malik, M.T. and D. Bergner, *Methods for Determination of Effective Diffusion Coefficients in Ternary Alloys.* Cryst. Res. Technol., 1985: p. 1283-1300.
99. Okamoto, H., *Supplemental Literature Review of Binary Phase Diagrams: Cs-In, Cs-K, Cs-Rb, Eu-In, Ho-Mn, K-Rb, Li-Mg, Mg-Nd, Mg-Zn, Mn-Sm, O-Sb, and Si-Sr.* Journal of Phase Equilibria and Diffusion, 2013. **34**(3): p. 251-263.
100. Gao, X. and J.F. Nie, *Characterization of strengthening precipitate phases in a Mg-Zn alloy.* Scripta Materialia, 2007(8): p. 645.
101. Ghosh, P., M. Mezbahul-Islam, and M. Medraj, *Critical assessment and thermodynamic modeling of Mg-Zn, Mg-Sn, Sn-Zn and Mg-Sn-Zn systems.* Calphad, 2012: p. 28.
102. Cerný, R. and G. Renaudin, *The intermetallic compound Mg21Zn25.* Acta Crystallographica. Section C, Crystal Structure Communications, 2002. **58**(Pt 11): p. i154-i155.
103. Yarmolyuk, Y.R., P.I. Kripyakevich, and E.V. Melink, *Crystal Structure of the Compound Mg_4Zn_7.* Sov. Phys. Crystallogr., 1975. **20**(3): p. 329-331.
104. Sakakura, T. and S. Sugino, *Fundamental study on interdiffuison in H.C.P. Alloys. Part 2: Magnesium-Zinc system.* Memories Suzuka Coll. Technol., 1977. **10**: p. 141-153.
105. Carpenter, P., *Electron-Probe Microanalysis (EPMA): An Overview for Beginners and a Status Report for Experts.* Microscopy and Microanalysis, 2008. **14**(SupplementS2): p. 1150-1151.

106. Khan, Y., *Dynamic Temperature Crystallization Behavior of Amorphous and Liquid Mg70zn30 Alloy.* Journal of Materials Science, 1989. **24**(3): p. 963-973.
107. Gao, X. and J.F. Nie, *Structure and thermal stability of primary intermetallic particles in an Mg–Zn casting alloy.* Scripta Materialia, 2007. **57**(7): p. 655-658.
108. De Negri, S., M. Skrobańska, S. Delfino, and A. Saccone, *The Mg–Zn–Si system: Constitutional properties and phase formation during mechanical alloying.* Intermetallics, 2010. **18**(9): p. 1722-1728.
109. Takei, T., *The equilibrium diagram of the system magnesium-zinc.* Kinzoku-no Kenkyu, 1929. **6**: p. 177-183.
110. Laves, F., *Zur Konstitution der Magnesium-Zink-Legierungen.* Naturwissenschaften, 1939. **27**(26): p. 454-455.
111. Clark, J.B. and F.N. Rhines, *Central region of the magnesium–zinc phase diagram.* Journal of Metals, 1957. **9**: p. 425-430.
112. Okamoto, H., *Comment on Mg-Zn (magnesium-zinc).* Journal of Phase Equilibria, 1994. **15**(1): p. 129.
113. Samson, S., *The crystal structure of Mg2Zn11: isomorphism between Mg2Zn11 and Mg2Cu6Al5.* Acta Chemica Scandinavica, 1949. **3**: p. 835–843.
114. Vegard, L., *Die Konstitution der Mischkristalle und die Raumfüllung der Atome.* Zeitschrift für Physik, 1921. **5**(1): p. 17.
115. Eichler, K., H. Kubsch, T. Müller, and P. Paufler, *Änderung von Verformungseigenschaften der intermetallischen Verbindung MgZn2 im Homogenitätsbereich.* Kristall & Technik, 1976. **11**(11): p. 1185.
116. Ohba, T., Y. Kitano, and Y. Komura, *The charge-density study of the Laves phases, MgZn2 and MgCu2.* Acta Crystallographica Section C, 1984. **40**(1): p. 1-5.
117. Lal, K. and V. Levy, Comptes Rendus Acad. Sci. Paris, 1966. **262**: p. 107-109.
118. Zhao, H.D., G.W. Qin, Y.P. Ren, W.L. Pei, D. Chen, and Y. Guo, *The maximum solubility of Y in alph-Mg and composition ranges of Mg24Y5–x and Mg2Y1-x intermetallic phases in Mg-Y binary system.* Journal of Alloys and Compounds, 2011. **509**: p. 627-631.
119. Okamoto, H., *Mg-Y (Magnesium-Yttrium).* Journal of Phase Equilibria and Diffusion, 2010. **31**(2): p. 199-199.
120. Zanicchi, G., V. Contardi, R. Marazza, D. Mazzone, and R. Ferro, *On some lanthanide and pseudolanthanide magnesium alloys.* Journal of The Less-Common Metals, 1988. **142**: p. L31-L36.
121. Smith, J., D. Bailey, D. Novotny, and J. Davison, *Thermodynamics of formation of yttrium-magnesium intermediate phases.* Acta Metallurgica, 1965. **13**(8): p. 889-895.
122. Kripyakevich, P.I. and V.I. Evdokimenko, *CRYSTAL STRUCTURES OF MAGNESIUM-RICH COMPOUNDS IN THE SYSTEMS Er-Mg, Dy-Mg AND Y-Mg.* Journal Name: Dopovidi Akad. Nauk Ukr. RSR; Journal Volume: Vol: No. 12; Other Information: Orig. Receipt Date: 31-DEC-63, 1962: p. Medium: X; Size: Pages: 1610-12.
123. Flandorfer, H., M. Giovannini, A. Saccone, R. Rogi, and R. Ferro, *The Ce-Mg-Y system.* Metallurgical and Materials Transactions A, 1997(2): p. 265.

124. Sviderskaya, Z. and E. PADEZHNOUA, *PHASE EQUILIBRIA IN THE MAGNESIUM-YTTRIUM AND MAGNESIUM-YTTRIUM-MANGANESE SYSTEMS.* IZV AKAD NAUK SSSR METALLY, NOV-DEC. 1968,--6--, 183-190, 1968.
125. Mezbahul-Islam, M., A.O. Mostafa, and M. Medraj, *Essential Magnesium Alloys Binary Phase Diagrams and Their Thermochemical Data.* Journal of Materials, 2014. **2014**: p. 33.
126. Paul, A., T. Laurila, V. Vuorinen, and S.V. Divinski, *Thermodynamics, Diffusion & the Kirkendall Effect in Solids*. 2014, Switzerland: Springer International Publishing. 543.
127. Kozubski, R., S. Czekaj, M. Kozłowski, E. Partyka, and K. Zapała, *Dynamics of superstructure formation in intermetallic compounds.* Journal of Alloys and Compounds, 2004. **378**(1–2): p. 302-307.
128. Mehrer, H., *Diffusion in intermetallics.* Materials transactions jim, 1996. **37**(6): p. 1259-1280.
129. Ghosh, C., *Study on important diffusion parameters of binary NiSn phase.* Journal of Materials Science: Materials in Electronics, 2013. **24**(7): p. 2558-2561.
130. Guo, C., Z. Du, and C. Li, *A thermodynamic description of the Gd–Mg–Y system.* Calphad, 2007. **31**: p. 75-88.
131. Hampl, M., C. Blawert, M.R. Silva Campos, N. Hort, Q. Peng, K.U. Kainer, and R. Schmid-Fetzer, *Thermodynamic assessment and experimental study of Mg–Gd alloys.* Journal of Alloys and Compounds, 2013. **581**: p. 166-177.
132. Manfrinetti, P. and J.K.A. Gschneidner, *Phase equilibrium in the La-Mg (0 – 65 at.% Mg) and Gd-Mg systems.* Journal of The Less-Common Metals, 1986. **123**: p. 267-275.
133. Okamoto, H., *Gd-Mg (Gadolinium-Magnesium).* Journal of Phase Equilibria, 1993. **14**(4): p. 534.
134. Rokhlin, L.L., *Structure and Properties of Alloys of the Mg-REM System.* Matal Science and Heat Treatment, 2006. **48**(11-12): p. 487-490.
135. Goldstein, J., *Scanning electron microscopy and X-ray microanalysis : a text for biologists, materials scientists, and geologists*. 1981: New York : Plenum Press, c1981.
136. Harris, I.R., C.C. Koch, and G.V. Raynor, *The room-temperature lattice spacings of some intra rare-earth binary systems.* Journal of The Less-Common Metals, 1966. **11**: p. 436-454.
137. Iandelli, A. and A. Palenzona, *Atomic size of rare earths in intermetallic compounds. MX compounds of CsCl type.* Journal of The Less-Common Metals, 1965. **9**: p. 1-6.
138. Fornasini, M.L., P. Manfrinetti, and K.A. Gschneidner, *GdMg5: a complex structure with a large cubic cell.* Acta Crystallographica: Section C (Wiley-Blackwell), 1986. **42**(2): p. 138.
139. Gibbs, G.B., *Diffusion layer growth in a binary system.* Journal of Nuclear Materials, 1966. **20**(3): p. 303-306.
140. Kidson, G.V., *Some aspects of the growth of diffusion layers in binary systems.* Journal of Nuclear Materials, 1961. **3**(1): p. 21-29.
141. Shewmon, P.G. and F.N. Rhines, *Trans.* AIME, 1954. **200**: p. 1021.
142. Butt, M.Z. and P. Feltham, *Solid-solution hardening.* Journal of Materials Science, 1993. **28**: p. 2557-2576.

143. Mata, M., M. Anglada, and J. Alcalá, *Contact Deformation Regimes Around Sharp Indentations and the Concept of the Characteristic Strain.* Journal of Materials Research, 2002. **17**(05): p. 964-976.
144. Li, H., A.H.W. Ngan, and M.G. Wang, *Continuous strain bursts in crystalline and amorphous metals during plastic deformation by nanoindentation.* Journal of Materials Research, 2005. **20**(11): p. 3072-3081.
145. Yilmaz, A., *The Portevin-Le Chatelier effect: a review of experimental findings.* SCIENCE AND TECHNOLOGY OF ADVANCED MATERIALS, 2011. **12**(6): p. 16.
146. Chinh, N.Q., G. Horváth, Z. Kovács, A. Juhász, G. Bérces, and J. Lendvai, *Kinematic and dynamic characterization of plastic instabilities occurring in nano- and microindentation tests.* Materials Science and Engineering: A, 2005. **409**(1–2): p. 100-107.
147. Horváth, G., N.Q. Chinh, J. Gubicza, and J. Lendvai, *Plastic instabilities and dislocation densities during plastic deformation in Al–Mg alloys.* Materials Science and Engineering: A, 2007. **445–446**(0): p. 186-192.
148. Dierke, H., F. Krawehl, S. Graff, S. Forest, J. Šachl, and H. Neuhäuser, *Portevin–LeChatelier effect in Al–Mg alloys: Influence of obstacles – experiments and modelling.* Computational Materials Science, 2007. **39**: p. 106-112.
149. Rodriguez, P., *Serrated plastic flow.* Bulletin of Materials Science, 1984. **6**(4): p. 653-663.
150. Wolfram, *ElementData*. 2014.
151. Gupta, N., D.D. Luong, and P.K. Rohatgi, *A method for intermediate strain rate compression testing and study of compressive failure mechanism of Mg-Al-Zn alloy.* Journal of Applied Physics, 2011. **109**(10): p. -.
152. Wei, S., T. Zhu, M. Hodgson, and W. Gao, *Effects of lead addition on the microstructure and mechanical properties of as-cast Mg–4Zn alloys.* Materials Science and Engineering: A, 2012. **550**(0): p. 199-205.
153. Sánchez-Martín, R., M.T. Pérez-Prado, J. Segurado, J. Bohlen, I. Gutiérrez-Urrutia, J. Llorca, and J.M. Molina-Aldareguia, *Measuring the critical resolved shear stresses in Mg alloys by instrumented nanoindentation.* Acta Materialia, 2014. **71**(0): p. 283-292.
154. Wu, M.-M., L. Wen, B.-Y. Tang, L.-M. Peng, and W.-J. Ding, *First-principles study of elastic and electronic properties of MgZn2 and ScZn2 phases in Mg–Sc–Zn alloy.* Journal of Alloys and Compounds, 2010. **506**: p. 412-417.
155. Seidenkranz, T. and E. Hegenbarth, *Single-crystal elastic constants of MgZn2 in the temperature range from 4.2 to 300 K.* physica status solidi (a), 1976. **33**(1): p. 205-210.
156. Tang, B.-Y., P. Chen, D.-L. Li, J.-X. Yi, L. Wen, L.-M. Peng, and W.-J. Ding, *First-principles investigation of the structural and mechanical properties of β″ phase in Mg–Gd alloy system.* Journal of Alloys and Compounds, 2010. **492**(1–2): p. 416-420.
157. Liu, Y., W.C. Hu, D.J. Li, X.Q. Zeng, C.S. Xu, and X.J. Yang, *Structural, electronic and thermodynamic properties of BiF3-type Mg3Gd compound: A first-principle study.* Physica b-condensed matter, 2014. **432**: p. 33-39.

158. Zhang, J., C. Mao, C.G. Long, J. Chen, K. Tang, M.J. Zhang, and P. Peng, *Phase stability, elastic properties and electronic structures of Mg–Y intermetallics from first-principles calculations.* Journal of Magnesium and Alloys, 2015.
159. Xu, Y., L.S. Chumbley, G.A. Weigelt, and F.C. Laabs, *Analysis of interdiffusion of Dy, Nd, and Pr in Mg.* J. Mater. Res., 2001. **16**(11): p. 3287-3292.
160. Müller, T.H. and P. Paufler, *Yield strength of the monocrystalline intermetallic compound MgZn2.* physica status solidi (a), 1977. **40**(2): p. 471-477.
161. Blake, A.H. and C.H. Cáceres, *Solid-solution hardening and softening in Mg–Zn alloys.* Materials Science & Engineering A, 2008. **483**: p. 161-163.
162. von Batchelder, F.W. and R.F. Raeuchle, *Lattice Constants and Brillouin Zone Overlap in Dilute Magnesium Alloys.* Physical Review, 1957. **105**(1): p. 59-61.
163. Pauling, L., *General chemistry*. 1988: New York : Dover Publications, Inc., 1988.
164. Boyce, C., *Using logic to define the Aufbau–Hund–Pauli relation: a guide to teaching orbitals as a single, natural, unfragmented rule-set.* Foundations of Chemistry, 2014. **16**(2): p. 93-106.
165. Gao, L., R.S. Chen, and E.H. Han, *Effects of rare-earth elements Gd and Y on the solid solution strengthening of Mg alloys.* Journal of Alloys and Compounds, 2009. **481**(1–2): p. 379-384.
166. Gao, L., J. Zhou, Z. Sun, R. Chen, and E. Han, *Electronic origin of the anomalous solid solution hardening of Y and Gd in Mg: A first-principles study.* Chinese Science Bulletin, 2011. **56**(10): p. 1038-1042.
167. Miura, S., S. Imagawa, T. Toyoda, K. Ohkubo, and T. Mohri, *Effect of Rare-Earth Elements Y and Dy on the Deformation Behavior of Mg Alloy Single Crystals.* MATERIALS TRANSACTIONS, 2008. **49**(5): p. 952-956.
168. Ninomiya, R., H. Yukawa, M. Morinaga, and K. Kubota, *An electronic approach to the prediction of the mechanical properties of magnesium alloys.* Journal of Alloys and Compounds, 1994. **215**(1–2): p. 315-323.
169. Kumar, V., A. Gupta, D. Lahiri, and K. Balani, *Serrated yielding during nanoindentation of thermomechanically processed novel Mg–9Li–7Al–1Sn and Mg–9Li–5Al–3Sn–1Zn alloys.* Journal of Physics D: Applied Physics, 2013. **46**(14): p. 145304.
170. Hadorn, J., K. Hantzsche, S. Yi, J. Bohlen, D. Letzig, and S.a.v.e. Agnew, *Effects of Solute and Second-Phase Particles on the Texture of Nd-Containing Mg Alloys.* Metallurgical & Materials Transactions. Part A, 2012. **43**(4): p. 1363-1375.
171. Ma, N., Q.M. Peng, X.J. Li, H. Li, J.H. Zhang, and Y.J. Tian, *Influence of Scandium on Corrosion Properties and Electrochemical Behaviour of Mg Alloys in Different Media.* International journal of electrochemical science, 2012. **7**(9): p. 8020-8034.
172. Ryabov, D.K., N.I. Kolobnev, and S.V. Samohvalov, *Effect of scandium addition on mechanical properties and corrosion resistance of medium strength Al-Zn-Mg(-Cu) alloy.* Materials Science Forum, 2014. **794-796**: p. 241.